Illuminating the function of AMPA receptors with fluorescent probes

Inaugural-Dissertation

to obtain the academic degree

Doctor rerum naturalium (Dr. rer. nat)

submitted to the Department of Biology, Chemistry and Pharmacy

of Freie Universität Berlin

by

Ljudmila Katchan

from Grodno, Belarus

2016

The thesis was conducted in the period 01.02.2012 – 16.08.2016

1st reviewer : <u>Dr. Andrew Plested</u>

2nd reviewer: <u>Prof. Stephan Sigrist</u>

Date of defence: _____November 22 2016_____

Summary

The family of ionotropic glutamate receptors (iGluRs) mediates the majority of fast excitatory synaptic transmission in the central nervous system. Their implication in higher brain function and life-threatening neurological disorders makes this protein family the target of numerous investigations. Despite immense progress in unraveling the structure and function of iGluRs, central questions remain unanswered. What conformational changes accompany and enable the sub-millisecond activation rates of the receptors? Which sites of the receptor are central for function and regulation? Although structural details are available for all iGluR subtypes through crystallographic and electron microscopy studies, little evidence exists to support the theories of the dynamic structural rearrangements within the receptor during the gating cycle. Furthermore, as the intracellular C-terminal tail and loops are unresolved in all structures available to date, structural and dynamic information about this region of the receptor is limited.

In the present study AMPA receptor subunits were labelled with variants of green fluorescent protein (GFP) through genetic incorporation into various insertion sites in both the extracellular and the intracellular regions of the receptor. Fluorescence resonance energy transfer (FRET) signals between these strategically positioned fluorophores were combined with simultaneous electrophysiological measurements to record conformational rearrangements during receptor gating in real time.

On the level of the intracellular domains, insertion of yellow and cyan fluorescent proteins (YFP and CFP, respectively) in the loop connecting the M1 and M2 transmembrane helices and the C-terminal tail enabled us to measure conformational rearrangements in response to an extracellularly-binding allosteric modulator cyclothiazide (CTZ), which blocks receptor desensitisation. Following the lead of the conformational changes of this region, FRET between single YFP insertions in the two intracellular positions and a membrane bound quencher showed state-dependent changes during receptor gating, and allowed us to map the positions of the insertion sites relative to the membrane in the receptor resting, desensitised and active states.

Fluorescent insertions within the extracellular domains of the AMPA receptor allowed us to probe both lateral and orthogonal movements of the ligand binding and amino terminal domains. Additionally, genetically labelling a transmembrane AMPA receptor regulatory protein (TARP) with

an acceptor fluorophore enabled direct visualisation of complex association and dynamics, which could be functionally confirmed through simultaneous electrophysiological recordings.

In summary, these experiments gave – for the first time – a concurrent visualisation of structure-function correlation of AMPA receptors, and could ultimately lead to optically active glutamate receptors capable of reporting their own activity.

Zusammenfassung

Die Familie von ionotropen Glutamatrezeptoren (iGluRs) vermittelt die Mehrzahl der schnellen exzitatorischen synaptischen Transmission im Zentralnervensystem. Ihre Verwicklung in höheren Gehirnfunktion und lebensbedrohlichen neurologischen Störungen macht diese Proteinfamilie das Ziel zahlreicher Untersuchungen. Trotz immensen Fortschritte in der Struktur und Funktion von iGluRs entwirren, zentrale Fragen bleiben unbeantwortet. Welche Konformationsänderungen begleiten und ermöglichen die Untermillisekunde Aktivierungsraten der Rezeptoren? Welche Websites des Rezeptors sind für Funktion und Regulation zentraler? Obwohl strukturelle Details für alle iGluR Subtypen durch kristallographische und Elektronenmikroskopie-Studien verfügbar sind, gibt es wenig Beweise für die Theorien der dynamischen Strukturänderungen innerhalb des Rezeptors während des Gating-Zyklus zu unterstützen. Ferner ist, wie die intrazelluläre C-terminale Schwanz und Schleifen in allen Strukturen verfügbar bisher ungelöst sind, strukturelle und dynamische Informationen über diese Region des Rezeptors ist begrenzt.

In der vorliegenden Studie AMPA-Rezeptor-Untereinheiten wurden mit Varianten des Green Fluorescent Protein (GFP), durch genetische Einarbeitung in unterschiedliche Insertionsstellen markierten sowohl in der extrazellulären und intrazellulären Regionen des Rezeptors. Fluoreszenz-Resonanz-Energie-Transfer (FRET) Signale zwischen diesen strategisch positionierte Fluorophore wurden bei gleichzeitiger elektrophysiologischen Messungen kombiniert, um Konformationsänderungen während Rezeptor-Gating in Echtzeit aufnehmen.

Auf der Ebene der intrazellulären Domänen, Insertion von Gelb und Cyan fluoreszierende Proteine (YFP und CFP sind) in der Schleife, die M1 und M2 Transmembran-Helices und den C-terminalen Schwanz verbindet es uns ermöglicht, Konformationsänderungen in Reaktion auf eine extracellularly- zu messen Bindung allosterischer Modulator Cyclothiazid (CTZ), die Blöcke Rezeptor Desensibilisierung. Nach dem Vorbild der Konformationsänderungen dieser Region, FRET zwischen einzelnen YFP Einfügungen in den beiden intrazellulären Positionen und eine Membran gebundenen Quencher zeigte zustandsabhängigen Veränderungen während der Rezeptor-Gating und erlaubt es uns, die Positionen der Insertionsstellen in Bezug auf die Membran zu kartieren in dem Rezeptor ruhende, desensibilisiert und aktive Zustände.

Fluorescent Einfügungen innerhalb der extrazellulären Domänen des Rezeptors AMPA erlaubt uns sowohl lateral als auch orthogonale Bewegungen der Ligandenbindung und aminoterminalen Domänen zu untersuchen. Zusätzlich Kennzeichnung genetisch ein Trans AMPA-Rezeptor-

Regulatorprotein (TARP) mit einem Akzeptor-Fluorophor direkte Visualisierung komplexer Assoziation und Dynamik ermöglicht, die funktionell durch gleichzeitige elektrophysiologischen Ableitungen bestätigt werden konnte.

Zusammenfassend ergaben diese Experimente - zum ersten Mal - eine gleichzeitige Visualisierung von Struktur-Funktions-Beziehung von AMPA-Rezeptoren und letztendlich zu optisch aktiven Glutamat-Rezeptoren fähig berichten ihre eigene Aktivität führen könnte.

1. Introduction

1.1 AMPA receptors – physiology

1.1.1 The basics

In the central nervous system (CNS) the fast excitatory neurotransmission is predominantly mediated by ionotropic glutamate receptors (iGluRs). The family of iGluRs consists of three functionally distinct classes: the AMPA (α-amino-3-hydroxyl-5-methyl-4-isoxazole-propionate acid) receptors – which react as the first responders to presynaptically released glutamate, NMDA (*N*-methyl-*D*-aspartate) – which exhibit relatively slower kinetics, and kainate receptors – which contribute to the postsynaptic responses and can modulate presynaptic neurotransmitter release.

During excitatory neurotransmission the iGluRs, which are expressed at roughly 80% of the brain synapses, transduce the presynaptic chemical signals into postsynaptic electrical signals (Traynelis et al., 2010). In response to glutamate binding the iGluRs undergo a rapid conformational change allowing cations to flow through the open ion channel pore and generate the postsynaptic excitatory currents (EPSCs).

Maintenance of the complexity of neuronal signalling requires a remarkable level of regulation and control. One of the most distinguished features of ionotropic glutamate receptors is the diversity of gating kinetics between and within receptor subtypes, which defines the time course of synaptic transmission (Traynelis et al. 2010). AMPA receptors assemble into tetrameric complexes of highly homologous subunits GluA1-4 (Dingledine et al., 1999; Anggono and Huganir, 2012). While NMDA receptors are obligate heteromers, the AMPA and kainate receptors are not and form fully functional homomers. In native complexes, however, AMPARs form heteromeric tetramers of varying subunit composition (Wenthold et al., 1996; Lerma et al., 1994; Traynelis et al., 2010). The variable subunit composition dictates the trafficking (Shi et al., 2001; Passafaro et al., 2001) and the biophysical properties of the AMPARs (Isaac et al., 2007) in this way diversifying the synaptic responses. In particular the presence or absence of the GluA2 subunit in receptor heterotetramers can dramatically alter the synaptic transmission by influencing the AMPAR properties (Derkach et al., 2007). AMPAR subunits exist in two alternative splice variants the "flip" and "flop" versions (Fig. 1 A), which modulate the functionality of the receptor complexes, such as receptor kinetics

and sensitivity to allosteric modulators (Sommer et al., 1991; Partin et al., 1994; Partin et al., 1996). Additionally, native GluA2 subunits in the adult brain are subjected to RNA editing to substitute the glutamine (Q) at residue 607 in the pore lining transmembrane helix 2 (M2) for an arginine (R) (Fig. 1 A), a modification shown to be critical for a number of functional features of GluA2 containing AMPAR complexes (Jonas and Burnashev, 1995). Firstly, the Q/R editing determines the Ca^{2+} permeability of the receptors, such that receptors with a GluA2(R) subunit are rendered impermeable to divalent cations, whereas receptors with GluA2(Q) or lacking the GluA2 subunit all together show high calcium permeability (Burnashev et al., 1992; Hume et al., 1991; Dingledine et al., 1992, Hollmann et al., 1991). Secondly, calcium impermeable channels have significantly lower single channel conductance (Swanson et al., 1997) and are not blocked by intracellular polyamines in a voltage-dependent manner (Bowie and Mayer, 1995). Consequently the GluA2 is a critical subunit in determining AMPAR function and is present in the vast majority of native complexes (Lu et al., 2009).

One of the main structural and functional divergence between the GluA subunits is found in the C-terminal tails (Derkach et al., 2007; Mallow and Malena, 2002) which serve as targets for post translational modifications (Swope et al., 1992; Roche et al., 1996; Hayashi et al., 2005), multiple intracellular signal transduction pathways (Collingridge et al., 2004)) and interaction with scaffolding proteins (Kim and Sheng, 2004) and auxiliary subunits (Nicoll et al., 2006). Through the multiple modifications and interactions the AMPA receptors in their multi protein complexes serve to shape the synaptic efficacy and strength. Modulation of receptor kinetics by the family of auxiliary proteins (Nicoll et al., 2006, see *Introduction* 1.4) determines the timescale of the fast response of the synapse, whereas subunit specific association with intracellular protein complexes drives the dynamic distribution of the AMPARs. Perhaps most importantly, the changes in composition and density of AMPARs at the synapse are tightly regulated by dynamic receptor trafficking and underlie the long term strengthening and weakening of the synaptic responses (Malinow and Malenka, 2002).

1.1.2 AMPA receptors in synaptic plasticity

Synaptic plasticity in the form of long-term potentiation (LTP, strengthening of the synapse) or depression (LTD, weakening of the synapse) is reliant on the activity dependent increase or

decrease of AMPARs at the postsynaptic density, and forms the molecular basis for higher cognitive functions such as learning and memory (Traynelis et al., 2010). Conductance of AMPARs following presynaptically released glutamate results in depolarisation of the postsynaptic terminal which relieves the Mg^{2+} block of NMDA receptors allowing Ca^{2+} to enter the cell. In turn, the influx of Ca^{2+} ions triggers a number of signalling cascades ultimately altering the composition of the synapse. The density of AMPARs at synaptic sites is activity dependent and showed an activity induced redistribution in cultured hippocampal neurons leading to a decrease in the numbers of AMPARs (Lissin et al., 1998; Lissin et al., 1999) and subsequently the amplitudes of AMPAR induced post-synaptic currents (O'Brien et al., 1998). Conversely inhibition of excitatory synaptic transmission led to an increase in the amplitudes of AMPAR currents and a corresponding increase in APMAR accumulation at the synapse (O'Brien et al., 1998). Upon LTP induction in hippocampal slice cultures the initial step to increase the number of surface AMPA receptors was proposed to be the activity dependent delivery of GFP-GluA1 to the synapse (Shi et al., 1999). Stabilisation of the surface receptor numbers is thought to occur through rapid cycling of the GluA2/A3 containing receptors, which are thought to replace the newly inserted A1/A2 heteromers (Passafaro et al., 2001; Shi et al., 2001).

In addition to intrinsic modulatory effects of the presence or absence of the GluA2 subunit in receptor tetramers, subunit composition affects synaptic plasticity through mechanisms involving receptor phosphorylation (Derkach et al., 2007). Phosphorylation of the GluA1 subunit proved to be critical for the generation of LTP and LTD and memory consolidation in mice (Lee et al., 2003; Whitlock et al., 2006).

1.1.3 AMPA receptors in pathophysiological conditions

Given the crucial role the iGluRs play in maintaining the basic function of the CNS through excitatory neurotransmission, the involvement of these proteins in pathophysiological conditions of the nervous system and their potential as therapeutic targets is not unexpected. Stroke induced neuronal death, for instance, is attributed primarily to the disfunction of glutamate homeostasis. Accumulation of glutamate at the synaptic cleft, due to glutamate transporter impairment, leads to over-activation of NMDA receptors and subsequent excitotoxicity, making NMDAR and AMPAR

antagonists a possible target for treatment, as they have been shown to produce neuro-protective effects (Danysz and Parsons, 2003; Furukawa et al., 2003; Traynelis, 2010).

An impairment of glutamatergic signalling has also been associated with the neurodegenerative processes involved in Alzheimers disease (AD) (Parsons et al., 2013). In AD the NMDA receptors are thought to be perpetually over-activated leading to a sustained influx of Ca^{2+} ions and a slow form of excitotoxicity (Danysz and Parsons, 2003; Parsons et al., 2013). Based on this notion, the voltage dependent NMDAR antagonist Memantine, which has fast on and off kinetics, has been approved for treatment of moderate AD (Danysz and Parsons, 2003; Parsons and Gilling., 2007; Parsons et al., 2013).

Psychiatric illnesses such as schizophrenia have also been associated with a decreased glutamate activity in limbic brain structures involving postsynaptic NMDA and AMPA receptors (Rubio et al., 2012; Lakhan et al., 2013).

1.2 AMPA receptor structure

All AMPA receptor subunits possess a modular structure consisting of four semiautonomous domains: the extracellular amino terminal domain (ATD) – responsible for receptor assembly, trafficking and localisation – and the ligand binding domain (LBD) – with the binding sites for agonists, antagonists and multiple modulators; the transmembrane domain (TMD) – forming the ion channel pore; and the intracellular C-terminal domain (CTD) – a target for numerous intracellular regulatory proteins (Traynelis et al., 2010). Receptor subunits assemble into tetrameric complexes (Rosenmund et al., 1998) and form the distinct extracellular domain layers and the ion channel pore. There has been a surge of high resolution full-length structures of iGluRs in the recent years, starting with the first crystal structure of the GluA2 homomeric receptor solved in 2009 (Sobolevsky et al., 2009; Dürr et al., 2014; Chen et al., 2014; Meyerson et al., 2014; Yelshanskaya et al., 2014; Karakas and Furukawa, 2014; Lee et al., 2014; Herguedas et al., 2016).

The first full length structure of an AMPA receptor was solved in 2009 with a 3.6 Å resolution (PDB 3kg2, Sobolevsky et al., 2009) and confirmed previous findings – from studies of isolated ATDs and LBDs (Armstrong et al., 1998; Armstrong and Gouaux, 2000; Armstrong et al., 2006; Sun et al., 2002; Jin et al., 2005; Clayton et al., 2009; Jin et al., 2009; Sukumaran et al., 2011) – that the AMPA receptor subunits assemble as a tetramer in a dimer of dimers conformation. Perhaps the
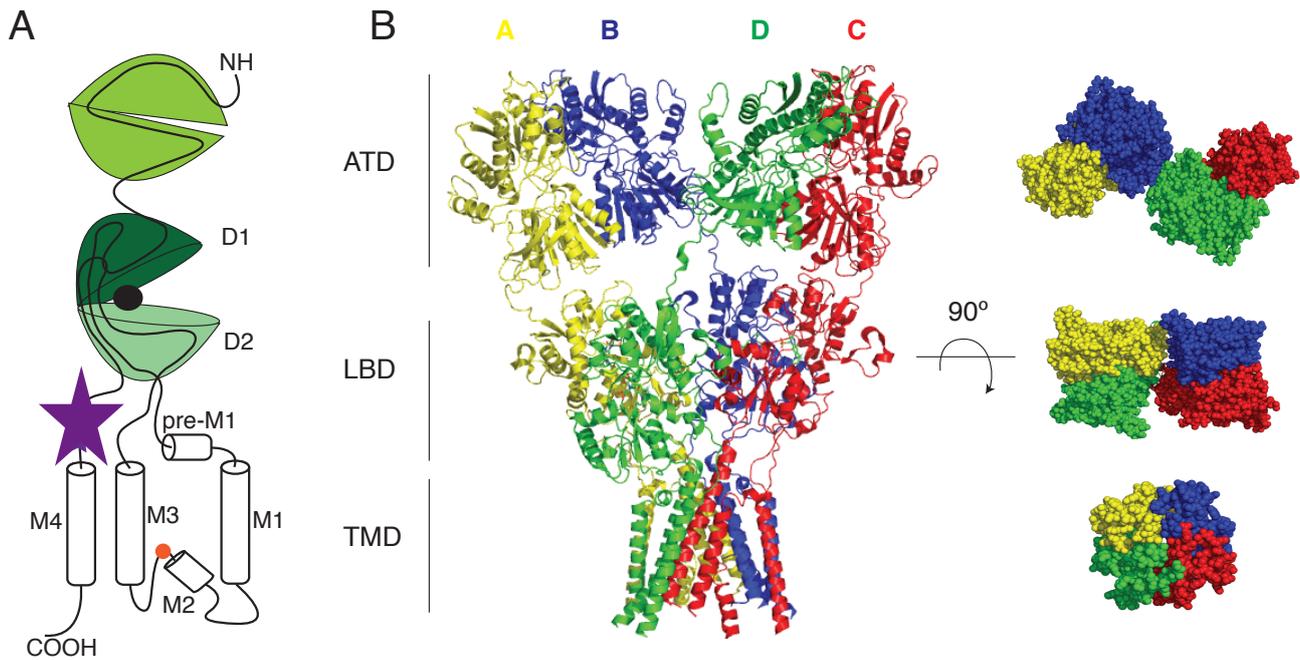
Figure 1 Structure of the homomeric rat GluA2 (PDB 3kg2) A A schematic representation of a single GluA2 subunit with the polypeptide chain traced through the distinct domains. ATD is shown in light green. The two segments S1 and S2 form the upper (D1, dark green) and the lower (D2, light green) lobes of the LBD. Glutamate (black sphere) binds between the two LBD lobes. TMD is composed of the M1, M3-4 helices and the M2 forms the pore loop and contains the Q/R editing site (orange sphere). The flip/flop region is indicated by the purple star. **B** Full-length structure of the homomeric GluA2 (Sobolevsky et al., 2009). Each subunit is assigned a colour. The separate domains (right panel) from top view show the two-fold symmetrical arrangement of the ATDs (with subunits A/B and C/D forming dimers); the LBDs with subunits A/D and B/C forming dimer interactions and the four-fold symmetrical arrangement of the TMD.

most unexpected feature of the complete tetramer was the subunit crossover between the extracellular domains and the apparent symmetry mismatch between the 2-fold rotational symmetry of the extracellular domains and the 4-fold symmetry of the transmembrane domain (Sobolevsky et al., 2009) (Fig. 1 B). On the level of the ATD dimers form between subunits A/B and C/D, whereas in the LBD layer subunits A/D and B/C form the dimers. The mismatch between the two-fold rotational symmetry of the extracellular domains and the four-fold rotational symmetry of the TMD is resolved on the level of the LBD-TMD linkers and is thought to underlie the essential functional properties of the receptor activation mechanism.

1.2.1 Amino terminal domain

Among all the domains the ATDs possess the least primary sequence homology between the iGluR subtypes (approximately 20-25 % between AMPA and Kainate; and virtually none between AMPA and NMDA receptors) and between the subunits within each family (approximately 55 % among GluA1 – 4) (Furukawa, 2012). Aside from the involvement in receptor assembly and heteromerisation (Leuschner et al., 1999; Ayalon et al., 2001; Ayalon et al., 2005) the functional role of the ATD is still not entirely clear. Subunits lacking the ATD were able to form functional channels without largely influencing receptor kinetics (Pasternack et al., 2002). It has been demonstrated that the ATDs are the initial domains for receptor dimerisation prior to tetrameric assembly, as ATD deleted mutants showed no dimer intermediates compared to their full length counterparts when ran on SDS-PAGE and BN-PAGE (Kim et al., 2010). As opposed to the NMDA receptor ATDs (Paoletti and Neyton, 2007) the AMPA receptors are not allosterically modulated by Zinc ions, protons or modulatory compound interactions within the ATDs (Traynelis et al., 2010). There is some conflicting information about the arrangement of the AMPAR ATDs in the context of a full length receptor (Chen et al., 2014; Sobolevsky et al., 2009; Herguedas et al., 2016). The full length structure in complex with a dimeric snail toxin, which binds tightly to the LBDs preventing receptor desensitisation, shows a separation of the ATD and LBD layers, as has been shown for the majority of homomeric AMPAR structures (Chen et al., 2014). In contrast, a GluA2/GluA3 heteromeric full length structure showed tightly stacked ATD and LBD layers with virtually no distance in between (Herguedas et al., 2016). This result is difficult to reconcile with the fact that the snail toxin has no binding interface with the bottom of the ATD layer (Chen et al., 2014) and affects native AMPARs in hippocampal slices (Walker et al., 2009), which are almost certainly heteromers (Traynelis et al., 2010).

1.2.2 Ligand binding domain

In contrast to the ATDs the LBD sequence is highly conserved between the subfamilies of iGluRs (Traynelis et al., 2010). LBDs of all receptor families are shaped as a clamshell with the agonist binding site located in the cleft between the upper (D1) and the lower (D2) lobes (Armstrong et al., 1998; Armstrong and Gouaux, 2000; Sobolevsky et al., 2009). Whereas the ATD consists of a single

uninterrupted polypeptide chain, the LBDs are made out of segments S1, located between the ATD and the M1 transmembrane helix and S2, located between the M3 and M4 transmembrane helices (Fig. 1 A). Agonist binding induces a closure of the cleft – facilitated by a movement of the D2 lobe – the degree of which is dependent on the size of the ligand (Armstrong et al., 1998; Armstrong and Gouaux, 2000). Consequently the efficacy of a ligand is partly determined by the degree of cleft closure its binding induces in the LBD. Connected to both the amino terminal and the transmembrane domains the LBDs drive the receptor into the functional states in response to an initial agonist application. In the LBD layer the dimers are mainly stabilised by the D1-D1 interface and are arranged in a back to back manner with a 2-fold rotational symmetry (Armstrong et al., 1998).

1.2.3 Transmembrane domain

Each transmembrane domain of an AMPA receptor consists of 3 membrane-spanning helices (M1, 3 and 4) and a pore-forming helix (M2) (Sobolevsky et al., 2009) (Fig. 1 A). In a tetrameric assembly the TMD displays a 4-fold rotational symmetry, in contrast to the 2-fold symmetry of the extracellular domains – a mismatch that is thought to underlie the opening and closing of the ion channel during gating. This symmetry mismatch is resolved on the level of the linkers connecting the LBD to the TMD (Sobolevsky et al., 2009). A polypeptide segment leading from the lower lobe of the LBD to the M1 transmembrane helix displays a kink and a short membrane parallel helical formation (pre-M1) just prior to the TMD, which in a tetrameric receptor forms a cuff around the centre of the TMD. The ion channel pore is lined by the M3 helices which in the antagonist-bound (closed channel) conformation cross at the top of the TMD (Sobolevsky et al., 2009). The transmembrane domains of iGluRs and voltage-gated K^+ channels share surprisingly high sequence homology, with the exception of the M4 transmembrane segment (Wood et al., 1995; Sobolevsky et al., 2009). Truncations on the level of the M4 helix fail to produce functional receptors of both AMPA (Salussolia et al., 2011; Salussolia et al., 2013) and NMDA (Schorge et al., 2003) receptor families, highlighting the importance of the interactions between the transmembrane segments of each subunit.

Due to the transient nature of the open channel state – presumably originating in the energetically unfavourable conformation on a global receptor scale – all crystal structures to date have captured

the TMD in a closed conformation (Sobolevsky et al., 2009; Dürr et al., 2014; Meyerson et al., 2014; Yelshanskaya et al., 2014; Chen et al., 2014; Herguedas et al., 2016).

1.2.4 C-terminal domain

The C-terminal tail of the AMPAR subunits has been excised in crystallographic structures to date, and thus there is no structural information about this particular domain. Functionally, the CTD is involved in multiple protein interactions, receptor stabilisation at the synaptic sites and is subjected to a number of post-translational modifications (Traynelis et al., 2010). AMPA receptor subunits differ in their cytoplasmic tails and the associated proteins between GluA1/A4 and A2/A3. All subunits contain PDZ binding motifs at the C-termini which facilitate interaction with proteins within the postsynaptic density (PSD) (Malinow and Malenka, 2002), with the GluA1 and A4 subunits binding to type I PDZ and GluA2 and A3 subunits interacting with type II PDZ (Malinow and Malenka, 2002; Song and Huganir, 2002; Bredt and Nicoll, 2003; Traynelis, 2010). An interaction of the GluA2 subunit with the synaptic protein GRIP was shown through the yeast two-hybrid system (Dong et al., 1997). This interaction was localised at the PDZ binding motif of the Glua2 C-terminal domain, similar to the ones present in the NMDARs and K^+ channels. Furthermore the association of AMPA receptors with the GRIP and GRIP2 proteins is thought to be involved in receptor trafficking to the synapses (Dong et al., 1999). Splice variants of GluA2 subunits producing short C-terminal tails were shown to interact with the PICK1 protein, known to bind protein kinase Cα, through the same PDZ motif as described for the GRIP protein, located at the extreme of the C-terminus (Dev et al., 1999). The PICK1 interaction was further confirmed by co-localisation studies and was suggested to play a role in AMPA receptor clustering at the synapses (Xia et al., 1999).

Post translational modifications of the AMPAR C-terminal domain, such as phosphorylation and palmitoylation, are implicated in the regulation of AMPA receptor function and maintenance (Traynelis, 2010). Several phosphorylation sites in the C-terminal domain of the GluA1 subunit have been identified (Roche et al., 1996) and the phosphorylation of these by PKA has been shown to enhance receptor response to glutamate, suggesting the role of intracellular modifications in receptor function. It was subsequently proposed that LTP and LTD reversibly modify the phosphorylation of the GluA1 subunit such that induced potentiation leads to dephosphorylation of

the calcium/calmodulin-dependent protein kinase II (CamKII) site and the induction of LTD results in the dephosphorylation of the cyclic-AMP-dependent protein kinase (PKA) (Lee et al., 2000), demonstrating the tightly coupled functional modification of the C-terminal domain of the AMPA receptors. During cerebellar long term depression phosphorylation of the GluA2 Ser880 by PKC (Linden and Connor, 1991; De Zeeuw et al., 1998) was shown to be necessary (Chung et al., 2003). This process is thought to proceed through several steps involving phosphorylation driven disruption of GluA2-GRIP and GRIP2 interactions and promotion of GluA2 binding to PICK1 (Chung et al., 2003; Xia et al., 2000). Using a new method for quantitative assessment of the degree of phosphorylation, the Phos-tag SDS-PAGE, it was shown that only a minuscule percentage of synaptically expressed GluA1 subunits are actually phosphorylated in native hippocampal tissue (Hosokawa et al., 2015). This finding was in a sharp contrast to the notion that AMPA receptor phosphorylation plays a role in plasticity mechanisms, and encouraged a reconsideration of the mechanism by which the C-terminally located phosphorylation sites are involved in synaptic plasticity (Lee et al., 2003). In fact, whether the C-terminal tail is necessary for synaptic plasticity is under general speculation, as it has been found that there is no requirement of the GluA1 C-terminal domain in LTP formation or in GluA1 subunit in general (Granger and Nicoll, 2014).

Due to the multiple interactions the C-terminal domain of the AMPA receptor, as for many other transmembrane proteins, is likely to be disordered (Minezaki et al., 2007; Cortese et al., 2008). Modifying the disorder of the C-terminal domain of the NMDA receptors for instance results in partial attenuation of the inhibition by extracellular Zn^{2+} ions (Choi et al., 2013).

1.3 Mechanisms of AMPA receptor gating

AMPA receptors are marked by their ultra fast (sub-millisecond) activation and deactivation in response to brief pulses of glutamate, which shape the fast component of excitatory neuronal signalling. Another essential feature of these receptors is the rapid desensitisation in prolonged presence of agonist. This state is characterised by a bound agonist in the ligand binding core and a closed ion channel pore. Understanding of the molecular mechanisms underlying AMPAR gating has been greatly facilitated by crystal structures of both isolated domains and full length protein in complex with numerous full and partial agonists and antagonists. **Figure 2** shows a simplified cartoon representation of the proposed mechanisms of action of the AMPA receptor.
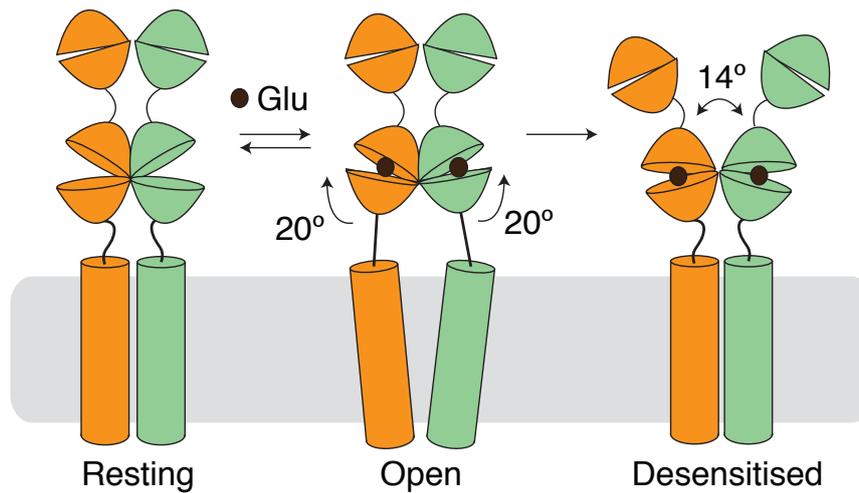
Figure 2 Structural transitions during AMPA receptor gating A cartoon representation of the mobility of the AMPAR domains during the transitions from receptor resting (left panel) to active state (middle panel) and to desensitised state (right panel).

1.3.1 Activation

Agonist binding within the LBD cleft is secured through 7 ion pair and hydrogen bond interactions of domains 1 and 2 of the LBD clamshell to the α-carboxyl and α-amino groups of a glutamate molecule (Armstrong and Gouaux, 2000). In the isolated LBD S1S2 structure the binding of full agonists induces a rigid body "screw-axis" movement of approximately 20º of the D2 lobe towards a closed cleft conformation (Armstrong and Gouaux, 2000) (Fig. 2). Additionally, distinct degrees of D1-D2 separation in presence of competitive antagonist DNQX, no ligand (apo state) and agonists (AMPA, kainate, glutamate and quisqualate) were observed, suggesting that the closure of the cleft is the primary driving force of channel opening (Armstrong and Gouaux, 2000; Jin et al., 2002). In a similar manner the partial agonists of the willardiine family induced distinct cleft closures, all smaller than that produced by the full agonists, depending on their size, suggesting that the degree of D2 movement is directly proportional to the degree of channel opening (Jin et al., 2003). The smaller domain closure in presence of partial agonists has also been confirmed on the scale of a full length receptor (Dürr et al., 2014). Whether or not the cleft closure directly determines the efficacy of a ligand is still subjected to reasonable doubt, as ligand binding domains with a mutated residue in the agonist binding core exhibit changed efficacy but not a distinguishable

cleft closure (Birdsey-Benson et al., 2010). In the case of NMDA receptors partial agonism is also not associated with distinct cleft closures of the LBDs (Inanobe et al., 2005).

In context of a full length receptor tetramer the binding of agonist is proposed to cause structural rearrangements on the level of the LBD dimers (Meyerson et al., 2014). The active state of the homomeric GluA2 is proposed to lead to an approximately 7 Å vertical contraction between the ATD and LBD layers compared to the receptor in its resting state. Within the LBD tetramer, agonist binding induces an inequivalent downward movement of the upper lobes of the proximal (A and C) and distal (B and D) subunits, by 10 and 4 Å, respectively (see Fig. 1B for subunit nomenclature). In addition to this movement the lower lobes of the LBDs separate upon activation, leading to a net corkscrew motion of the LBD dimers. The largest conformational changes produced by this motion are visible in the M3-D2 linkers and include a 33º anticlockwise rotation of the proximal subunits and a 20º clockwise rotation of the distal subunits.

In addition to the distinct active conformation, the LBDs likely visit numerous transient intermediate states during receptor activation depending on the occupancy of the binding sites. These states can be captured by various cross linking techniques and illustrate the dynamic nature of the structural conformation of the receptor (Lau et al., 2013; Baranovic et al., 2016).

As all structures of full length AMPA receptors solved thus far present a closed ion channel pore, little evidence exists of the arrangement and orientation of the four-fold symmetric TMD in the active state of the channel. To model the movements of the receptor subunits during gating molecular dynamics simulations were used on ATD deleted constructs (Dong and Zhou, 2011). In the resting state the channel pore is blocked at three positions along the M3 helices (Sobolevsky et al., 2009). During simulations, in which the LBDs of a tetramer were forced to move from the antagonist-bound to an agonist bound conformation, the positions in the pore were no longer blocked and the agonist-bound conformation of the LBDs led to an upward movement of the M3 transmembrane helices (and TMD as a whole) of approximately 5 Å towards the D1 lobes of the LBDs (Dong and Zhou, 2011). These LBD-driven gating motions had distinct components from the proximal and the distal subunits, such that agonist binding to the proximal subunits lifted the D2 lobes and the closely connected D2-M3 linkers, whereas agonist binding to the distal subunits lifted the D2 lobe to a lesser extent but moved them away from the central axis of the receptor. This inequality in subunit contribution is translated to the transmembrane helices, where the tilt angles of

the proximal and distal M3 helices changed in opposite directions during receptor activation, decreasing in the proximal pair and increasing in the distal pair.

1.3.2 Desensitisation

Because the open state of the ion channel is not energetically favourable due to the strain exerted on the linkers connecting the LBDs to the TMDs, agonist induced activation results in a rapid conformational change to a closed state through either deactivation or desensitisation. Most ligand gated ion channels undergo desensitisation, a state characterised by bound agonist and closed pore (Jones and Westbrook, 1996). Exactly how desensitisation contributes to the size and frequency of postsynaptic responses is still unclear. Desensitising AMPA receptors could potentially be involved in shaping of the synaptic response and induction of synaptic depression (Trussel et al., 1993). AMPA receptors undergo a rapid and profound desensitisation not only in saturating, but also at low concentrations of glutamate (Kiskin et al., 1986; Trussell and Fischbach, 1989; Colquhoun et al., 1992; Geiger et al., 1995; Otis et al., 1996a). Although only valid for some neuronal cell types, the similarity of AMPAR desensitisation rates – which vary by almost 10 fold depending on the preparation (Colquhoun et al., 1992; Hestrin, 1993; Geiger et al., 1995) – to the decay of synaptic currents raises the question whether the AMPARs desensitise during synaptic activity (Otis et al., 1996b). Under certain conditions the desensitisation may limit the mean channel burst duration during synaptic activation and thus is able to ensure the brief time course of miniature excitatory postsynaptic currents (mEPSC) in cases where repetitive firing, restricted diffusion or poor uptake prolongs the time course of glutamate in the synaptic cleft (Trussel and Fischbach, 1989; Barbour et al., 1994). Since AMPAR in regions with rapid glutamate clearance is largely resistant to desensitisation, it has been suggested that the desensitisation may be tuned to produce different patterns of short term plasticity at synapses that undergo repetitive activation or delayed glutamate uptake (DiGregorio et al., 2007). An example of such short term plasticity is the depression of excitatory synaptic transmission, which occurs at high frequencies of firing of the presynaptic neurone, in which the slow recovery from desensitisation of the AMPARs is thought to play a role (Trussel and Fischbach, 1989; Colquhoun et al., 1992; Rozov et al., 2001).

Dimer interfaces between the D1 lobes of adjacent subunits play a crucial role in the gating cycle of the AMPARs (Sun et al., 2002; Horning and Mayer, 2004; Armstrong et al., 2006), as disruption of

this interface leads to markedly increased desensitisation rates and its increased stabilisation by either the L483Y mutation or the binding of the positive allosteric modulator cyclothiazide (CTZ), which blocks receptor desensitisation and traps the receptor in an active conformation (Sun et al., 2002). Receptor activation through structural rearrangements of the lower lobes of the LBD, puts strain on the D1-D1 interface of the LBD dimers, which may be relieved by either deactivation and restoration of closed channel and open LBD cleft, or by desensitisation through the disruption of the dimer interface. As a consequence desensitisation leads to an approximately 14 degree separation of the D1 lobes towards the D2 lobes and a decrease in distance between the D2 lobes (Armstrong et al., 2006; Plested and Mayer, 2009) (Fig. 2). In the light of recent full length structures of iGluRs in desensitised state new mechanisms of receptor desensitisation have been proposed involving substantial rearrangements on the level of both the LBD and ATD layers (Nakagawa et al., 2005; Schauder et al., 2013; Meyerson et al., 2014; Dürr et al., 2014). Using cryo-EM two separate studies resolved the structures of a desensitised full length AMPAR bound to either partial agonists fluorowillardiine (FW) or kainate (Dürr et al., 2014) or full agonist quisqualate (Meyerson et al., 2014). During receptor desensitisation the two-fold rotational symmetry of the LBD domains as described for the antagonist bound conformation (Sobolevsky et al., 2009) is thought to transition into a four-fold symmetric assembly through a rotation of the individual LBDs and a disruption of dimer interfaces (Meyerson et al., 2014; Dürr et al., 2014). This rotation is thought to relieve the strain in the LBD-TMD linkers, allowing the ion pore to close. A similar phenomenon of the LBDs was shown for the kainate receptor in desensitised state (Schauder et al., 2013).

On the level of the ATDs even larger structural rearrangements are proposed. The cryo-EM density maps of several classes of desensitised AMPAR molecules showed various degrees of ATD dimer separation, a reversible and seemingly AMPAR-specific feature, as the desensitised Kainate receptors did not exhibit the same rearrangements (Meyerson et al., 2014). These conformational changes were explained to be the result of tension applied by the LBDs, which the ATD dimer interfaces – being rather weak – cannot withstand. Interestingly, the receptor bound to a partial agonist S-5-Nitrowillardiine (NOW), presumably captured in a deep desensitised state, does not display the same level of LBD displacement or any separation of the ATD dimers (Yelshanskaya et al., 2014), highlighting the possibility of numerous transient conformations visited by the receptor domains.

1.4 Association of AMPARs with auxiliary proteins

Native AMPA receptors are in majority found in complexes with transmembrane AMPA receptor regulatory proteins (TARPs) – integral membrane proteins, which regulate receptor trafficking and synaptic targeting as well as modulate the kinetic properties of AMPARs (Traynelis et al., 2010). The first prototypical TARP, stargazin, was discovered in stargazer mice, which due to a mutation in the *stg* gene exhibited seizures typical of epilepsy (Letts et al., 1998). Subsequent studies showed that the stg mutation resulted in diminished AMPAR mediated excitatory postsynaptic currents (EPSC) leaving the NMDA mediated slow component of the EPSC unaffected, suggesting an involvement of stargazin in AMPAR regulation (Hashimoto et al., 1999) and that stargazin directly interacts with the AMPARs at the synapse (Chen et al., 2000). A whole family of stargazin (γ-2) related TARPs comprising the canonical type I γ-3, γ-4 and γ-8 (Tomita et al., 2003) and type II γ-5 and γ-7 (Kato et al., 2007; Kato et al., 2008) which distinctly regulate the native AMPARs have been described since. The discovery of the TARP family has helped to reconcile the functional differences seen between heterologousely expressed and native AMPARs (Jackson and Nicoll, 2011).

Within the complexes of AMPA receptors and their associated TARPs the interaction sites have been subject to investigation. It was proposed that several interaction sites are responsible for the diverse effects of TARP association, with interactions between the intracellular C-terminal domains of the receptor largely responsible for the enhanced trafficking of the AMPARs to the surface produced by TARPs and extracellular interactions being responsible for the modulatory effects on receptor gating (Tomita et al., 2004; 2005). On the extracellular level, the regulation of AMPA receptor gating was shown to be dependent on interactions between the stargazin and the ligand binding domain of the AMPA receptors, and not dependent on the presence of the ATDs (Tomita et al., 2006). In contrast to this finding, a map of AMPA - TARP interaction was created using peptide arrays, and proposed that large areas of the ATDs may be involved in TARP association in a state dependent manner (Cais et al., 2014). These AMPAR ATD – TARP interaction sites were proposed to be dependent on the structural rearrangements occurring during receptor desensitisation, which were suggested by structural studies (see *Introduction 1.3.2*).

Structures of GluA2 AMPA receptor in complex with stargazin have been recently solved by single particle cryo-EM by two separate groups (Zhao et al., 2016; Twomey et al., 2016). The former study

shows a full length antagonist-bound homomer in complex with four stargazin molecules at a resolution of approximately 7Å (Zhao et al., 2016). The TARPs are arranged in a four-fold symmetry around the TMD of the receptor and the structure proposes that the interactions between the TARPs and the receptor are composed of two components: one between the transmembrane regions of the receptor and stargazin and one between the extracellular loop of stargazin and the bottom of the LBD clamshell. The interactions between the transmembrane segments obey the overall four-fold symmetry of the AMPA receptor TMD, whereas the interactions on the level of the LBD, not directly visible due to either the poor resolution of the complex or the functional state of the antagonist-bound receptor, display non-equivalence between the dimer of dimers of the AMPAR LBDs. This symmetry mismatch mimics the one found between the LBD and TMD layers in the isolated receptors (Sobolevsky et al., 2009), and is manifested by a closer proximity of the B/D subunit LBDs to a TARP molecule than that of the A/C subunit LBDs (Fig. 1 for subunit nomenclature).

The second study uses a tandem between the N-terminus of stargazin and the C-terminus of GluA2 to elucidate the complex structure (Twomey et al., 2016). In contrast to the fully occupied receptor reported by Zhao et al., the majority of cryo-EM particles of the tandem show a single molecule of stargazin associated with the AMPAR. The main interaction between GluA2 and the single bound stargazin is mediated by a substantial interface formed by the transmembrane helices 3 and 4 of stargazin and the M1 and M4 of the AMPAR. The extracellular portion of the stargazin molecule is conveniently positioned in close proximity to the lower lobe of the LBD clamshell, in agreement with the study by Zhao et al., and suggests that these regions of the complex interact.

In summary, the interaction sites reported by the two studies are in agreement with one another and are concentrated in two regions: the transmembrane segments of the receptor and stargazin and the extracellular loop and the LBD. As further evidence for AMPA TARP interaction at the lower D2 lobe of the LBD, mutations of Lys-Gly-Lys residues located on the lower D2 lobe, a KGK motif conserved among all AMPAR subunits, to residues present in the kainate receptors, abolished stargazin modulation of receptor gating, such as decreased desensitisation and deactivation rates (see *Introduction 1.4.2*) (Dawe et al., 2016). Interestingly, introducing the KGK motif into kainate receptor D2 lobes did not produce any changes in receptor kinetics in presence of stargazin, suggesting that these residues are not sufficient to induce functional modulation of KARs by TARPs.

Whilst evidence is building up for the interaction sites between TARPs and AMPARs, the stoichiometry of the complex is still under question, as one study reports a saturated AMPAR with 4 stargazin protomers associated per complex (Zhao et al., 2016) and another suggests a variable amount of stargazin molecules per complex, with a single stargazin protomer associated in the complex as a preferred arrangement (Twomey et al., 2016). Ironically, the structure of the receptor fused to stargazin displays a lower stoichiometric ratio compared to freely associated AMPAR-TARP complex, perhaps indicative of the non-physiological nature of the fusion complex.

1.4.1 Membrane trafficking and anchoring of AMPARs at the synapse

Stargazin and other members of the type I TARP family facilitate AMPA receptor trafficking in both heterologous systems and in neurons, increasing the surface expression and localisation of the receptors (Chen et al., 2000; Tomita et al., 2003; Tomita et al., 2004). In neurons the localisation of AMPARs to the synapse is critically dependent on a direct interaction between the stargazin C-terminal PDZ binding motif and PSD-95 protein (Schnell et al., 2002; Bats et al., 2007, Opazo et al., 2010).

An interesting phenomenon induced by the presence of stargazin is the auto-inactivation of steady state currents of the AMPA receptors at high concentrations of agonist (Morimoto-Tomita et al., 2009). Heterologousely expressed AMPA receptors without stargazin display a sigmoid dose-response curve for glutamate whereas in the presence of stargazin the curve becomes bell-shaped (Morimoto-Tomita et al., 2009). This feature of stargazin was explained to be linked to activity dependent complex dissociation, which was also shown to occur during long term exposure to high concentrations of glutamate (Tomita et al., 2004; Morimoto-Tomita et al., 2009). Receptor complexes were further investigated by uPAINT single-molecule tracking of fluorescently labeled antibodies specific to the extracellular domain of GluA2 on the surface of neurons in culture (Constals et al., 2015). Receptor mobility, presumably linked to association with TARPs at the synapse, was increased during desensitising conditions, suggesting that the dissociation of AMPAR - TARP complexes occurs when the receptors enter the desensitised state, rendering them more mobile and allowing them to exit the synapse.

1.4.2 Modulation of AMPAR functional properties by TARPs

Aside from their roles as receptor chaperones to and in the postsynaptic density, all TARPs are involved in the modulation of receptor function to some degree (Jackson and Nicoll, 2011, Straub and Tomita, 2012).

Stargazin, arguably the most studied member of the TARP family, has been shown to induce an increase in the steady state current, a decrease in deactivation and desensitisation rates and an increase in kainate efficacy in HEK 293 cells and oocytes (Priel et al., 2005; Tomita et al., 2005; Turetsky et al., 2005; Bedoukian et al., 2006). Other members of type I TARPs, such as γ-3, γ-4 and γ-8 have displayed similar kinetic modulation of AMPARs, but to varying degrees (Tomita et al., 2005; Milstein et al., 2007; Cho et al., 2007; Korber et al., 2007). Swapping the domains of type I TARPs and TARP II γ-5 showed that the channel gating of AMPARs is modified through the interactions of the extracellular loop of the TARPs, whereas the increased trafficking is mediated largely by the intracellular domains of the TARPs (Tomita et al., 2005; Milstein et al., 2007). Calcium permeable AMPA receptors are voltage dependently blocked by intracellular polyamines showing strong inward rectification (Bowie and Mayer, 1995). An essential modification of AMPA receptor properties regulated by TARPs is their sensitivity to polyamine block, which is relived by the association of TARPs (Soto et al., 2007). To this end, considering that the majority of AMPARs in an adult brain is made of GluA2 containing heteromers and in complex with TARPs (Tomita et al., 2003; Fukata et al., 2005), the polyamine sensitivity as a measure of A2 subunit abundance in complexes, which has been used a long time, is somewhat misleading (Jackson and Nicoll, 2011). The measure of the relief of the polyamine block in heterologous systems is however a good indicator of TARP association.

1.5 FRET

1.6.1 General FRET theory

Förster resonance energy transfer was first described in 1948 by Theodor Förster (Förster, 1948) and is the phenomenon of non-radiative energy transfer between a donor and acceptor fluorescent molecules through dipole-dipole interactions. The acceptor may, but need not, be fluorescent (Jares-Erijman and Jovin, 2003). Energy may be transferred from a donor molecule in an excited state to an acceptor molecule in the ground state, given that a number of conditions are met (Fig. 3):

1. Donor emission and acceptor absorption spectra must overlap.

2. The donor and acceptor molecules must be in close proximity (< 100 Å).

3. The orientation of the dipoles between the donor and acceptor must be non-perpendicular.
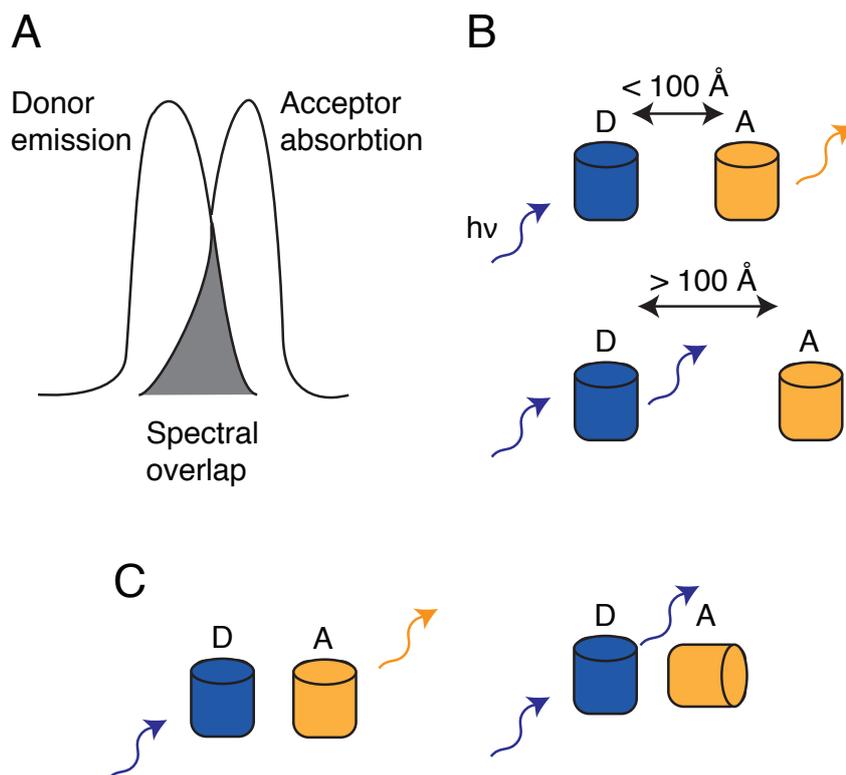
Figure 3 FRET conditions to be met by a donor (D) and acceptor (A) molecules A Arbitrary spectra of donor emission and acceptor absorption with the overlap integral J(λ) shown in grey. **B** Distance dependence of energy transfer. When donor and acceptor molecules are in close proximity to one another, energy from the excited donor molecule will be transferred to the acceptor molecule. **C** Orientation of the donor and acceptor molecules must be non-perpendicular for energy transfer to take place.

When these conditions are met, the relationship between the donor and acceptor distance and the efficiency of energy transfer of the donor-acceptor pair is given by:

Equation 1
$$E = \frac{R_0^6}{R_0^6 + r^6}$$

where R_0 is the Förster distance for a given donor-acceptor pair at which transfer efficiency is 50% and r is the distance between the donor and acceptor fluorophores. FRET efficiency is steeply dependent on the distance separating the donor and acceptor molecules, and will rapidly approach 1 as the distance r decreases below the value of R_0, and consequently approach 0 as r increases beyond. Each pair of FRET donor and acceptor molecules will have a distinct R_0 value which is dependent on the spectral overlap of the donor and acceptor pair (the overlap integral $J(\lambda)$) (Fig. 3 A), the quantum yield of the donor (Q_D) and the relative orientation in space of the transition dipoles of the donor and acceptor molecules (described by κ^2). Dependent on the spectral properties of the donor and acceptor molecules the spectral overlap is given as:

Equation 2
$$J(\lambda) = \int_0^\infty F_D(\lambda)\varepsilon_A(\lambda)\lambda^4 d\lambda$$

where $F_D(\lambda)$ is the fluorescence intensity of the donor in the wavelength range λ to $\lambda + d\lambda$ normalised to unity and the ε_A is the extinction coefficient of the acceptor at a given wavelength (Jares-Erijman and Jovin, 2003). With the known spectral properties of the fluorescent donor and acceptor molecules the R_0 for a given pair is calculated as:

Equation 3
$$R_0 = 0.211(\kappa^2 n^{-4} Q_D J(\lambda))^{1/6}$$

with the wavelength given in nm and the F_D in units of $M^{-1}cm^{-1}$ and n being the refractive index of the medium. Normally the reflective index is assumed to be 1.4 and the κ^2 is usually set to be equal 2/3 (Dale et al., 1979). From Eq. 3 it follows that the larger the spectral overlap of the donor and acceptor molecules the higher does the R_0 value become, making the FRET measurements highly

versatile. As a summary, Table 2 shows a number of commonly used FRET pairs and their respective R_0s.

1.6.2 FRET measurements

Energy transfer from a donor to an acceptor molecule can be measured in a number of ways. In practice, these measurements meet several technical and physical complications. Among the complication is the issue of bleed through or crosstalk between the donor and acceptor fluorescence. First, the acceptor may potentially be excited directly by the donor excitation wavelength, leading to a signal of a non-FRET origin. Secondly, donor fluorescence may leak into the channel of acceptor emission wavelength, resulting in a misleading signal. The solution to these issues, although not complete, is to uncouple the fluorescence channels by either the choice of donor-acceptor pair with high spectral separation or by using highly specific fluorescence excitation and emission filters (Piston and Cremers, 2007). Although spectral separation of the donor and acceptor molecules reduces the crosstalk between the channels it also simultaneously leads to a decrease of the overlap integral $J(\lambda)$ and subsequently the R_0, resulting in a diminished dynamic range of the measurements. A number of drawbacks in FRET measurements is associated with the chosen labelling technique. Genetic labelling with fluorescent proteins, although versatile, is accompanied by a number of limitations. First, because the spectra of the FPs are rather broad, the issue of donor to acceptor channel crosstalk is enhanced. As mentioned previously, this can be corrected by filtering system to a certain degree. Secondly, the size of the fluorescent protein (approximately 24 Å in diameter of the barrel structure (Ormö et al., 1996)) is a limiting factor in distance probing, as it occupies a large part of the effective distances that can be measured by FRET. Modifications of the existing variants of the green fluorescent protein (GFP) have led to FRET pairs with improved qualities such as the quantum yield and the Förster distance, for mCerulean (Rizzo et al., 2004; Markwardt et al., 2011) and mVenus (Nagai et al., 2002).

Several methodologies for detecting FRET interactions have been devised (Clegg, 1995; Clegg, 1996; Pepperkok et al., 1999; Piston and Cremers, 2007; Jares-Erijman and Jovin, 2003; Sekar and Periasamy, 2003; Cardullo and Purpa, 2003) to overcome the inherent optical and physical limitations, among others the bleed-through of donor and acceptor channels and the arbitrary inter — and intramolecular stoichiometry of donor and acceptor distributions. The methodologies can be

divided into four subcategories, defined by the acquisition characteristics: i) measurements of donor fluorescence (Donor quenching or lifetime measurements), ii) measurements of acceptor fluorescence (sensitised emission), iii) spectral measurements of both donor and acceptor and iv) anisotropy measurements. Some of the most commonly used techniques to measure FRET are described in the following paragraphs.

Fluorescence lifetime imaging

One of the most widely used approach to measure FRET through donor is the fluorescence life-time imaging technique (FLIM). This approach provides direct evidence of physical interaction of a donor and acceptor molecule by measuring the nanosecond decay kinetics of the electronic exited state of a donor chromophore characterised by the fluorescence lifetime **τ** (Bastiaens and Squire, 1999). In the absence of non-radiative reactions a donor chromophore will decay from its excited state at a given rate (Cardullo and Purpa, 2003). When non-radiative processes, such as FRET, occur the decay time (the lifetime of the fluorophore) will be decreased. This process can be translated directly into the efficiency of the energy transfer:

Equation 4
$$E = 1 - \frac{\tau_{DA}}{\tau_D}$$

where **τ**$_{DA}$ is the donor lifetime in presence of acceptor and **τ**$_{DA}$ is the lifetime of the donor without the acceptor. Measuring the lifetime of a chromophore is advantageous as it is directly coupled to the reactions occurring in its exited state and is independent of donor concentrations and donor acceptor channel crosstalk. On the downside, because of the large number of photons needed for reliable calculation of the fluorophore lifetime, this method tends to be slow and not thus not appropriate for measurements of kinetically fast processes, such as protein dynamics.

Donor quenching and sensitised emission

Alternative to measuring fluorescence lifetimes, which requires complex instrumentation, fluorescence intensity based techniques can be used. Energy transfer can be quantified by measuring the decrease of donor fluorescence (quenching) or an increase in acceptor fluorescence
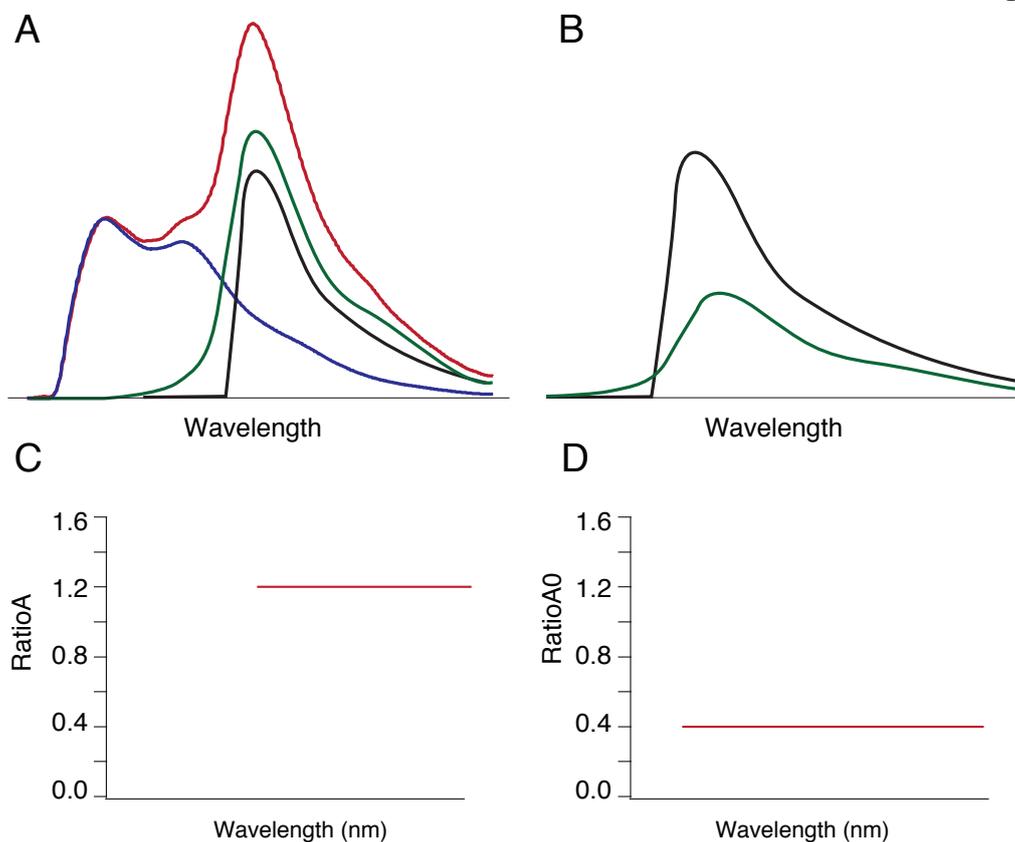
Figure 4 Spectrum based FRET efficiency measurements A Spectra collected from donor and acceptor labelled samples. The colour coding is as follows: red, emission with donor excitation; black, emission with direct donor excitation; blue, donor emission; green, extracted acceptor emission. **B** Spectra from samples with acceptor alone. Colour code is as in **A**. **C** RatioA as a function of wavelength, calculated from spectra in **A** (ratio of green and black lines). **D** RatioA$_0$ as a function of wavelength, calculated from spectra in **B**.

(sensitised emission) (Cardullo and Parpura, 2003). Donor quenching can be used in cases where the acceptor molecule is not fluorescent, such as in cases of organic fluorescence quenchers (Fernandez et al., 1983; Chanda et al., 2005a; Chanda et al., 2005b; DiFranco et al., 2007; Zimmermann et al., 2008; Wang et al., 2010) and requires a measure of donor intensity in presence and absence of acceptor. In a proximity of an acceptor molecule the donor fluorescence intensity will decrease, indicating energy transfer. If the donor fluorescence intensity in presence and absence of an acceptor is measured in a single sample, as is the case with the use of quenchers, the uncertainty and errors arising from variable donor intensities in separated control samples are eliminated (Shrestha et al., 2015).

Quantifying the sensitised emission of the acceptor is another fluorescence intensity based approach to measure FRET. The intensity of fluorescence in the acceptor channel during donor wavelength excitation will be dependent on and composed of: i) the amount of energy transfer, ii) the amount of

direct excitation of the acceptor by donor excitation wavelength and iii) the component of donor emission. To account and correct for the mixture of the signal in the acceptor emission channel ratios of donor and acceptor fluorescence intensities may be used, as will be described in the following section.

Ratiometric FRET

Spectral based ratiometric approach to measuring FRET provides a way to eliminate some of the inherent errors in fluorescence intensity measurements, such as the contamination of the signal by direct excitation of the acceptor by donor wavelength and donor emission in the acceptor channel (Zheng et al., 2002; Zheng and Zagotta, 2003). This approach relies on the collection of three different sets of spectra: i) donor and acceptor (FRET containing) spectra, ii) donor spectra and iii) acceptor spectra at both donor and acceptor excitation wavelengths (Fig. 4).

Donor spectra in absence of acceptor are scaled and subtracted from the FRET containing spectra, leaving the acceptor signal, which includes both FRET and direct excitation components. The ratio between the extracted acceptor signal and acceptor spectra collected through acceptor wavelength excitation is denoted RatioA (Fig. 4 A):

Equation 5
$$RatioA = \frac{F_D}{F_A}$$

where F_D is acceptor fluorescence at donor excitation wavelength and F_A is acceptor fluorescence at acceptor excitation wavelength.

To address the component of direct excitation of the acceptor by donor excitation wavelength spectra are also collected from acceptor only samples excited with both donor and acceptor wavelengths (Fig. 4 B):

Equation 6
$$RatioA_0 = \frac{F_D^{direct}}{F_A}$$

where F_D^{direct} is the direct component of acceptor emission arising from donor excitation.

Taking the ratio between the two separately collected ratios surpasses the errors associated with uneven donor/acceptor distributions, stoichiometry and crosstalk and leads to the so-called FRET ratio (FR) (Zheng et al., 2003; Zheng and Zagotta, 2003):

Equation 7
$$FR = \frac{RatioA}{RatioA_0}$$

which in turn relates the collected spectral information to the efficiency of energy transfer by:

Equation 8
$$E = \frac{\varepsilon_A}{\varepsilon_D}(FR - 1)$$

where ε_A is the extinction coefficient of the acceptor at donor excitation wavelength and ε_D is the extinction coefficient of the donor molecule at the same wavelength (Erickson et al., 2001).

1.6.3 FRET in iGluRs

Resonance energy transfer has been widely used to study functional conformational changes in ionotropic glutamate receptors. The following paragraph will provide an overview of the most influential studies on both AMPARs, KARs and NMDARs using various RET techniques.

NMDARs

In one of the first reports of LRET in full length NMDA receptors the arrangement potential zinc induced dynamic of the GluN1 and GluN2A ATDs and the conformational rearrangements of the GluN2A ATD binding cleft were probed using cysteine labelling with LRET donor terbium chelate, whose lifetime is well defined, and either Alexa Fluor 555 or Ni(NTA)$_2$Cy3 as acceptor molecules (Sirrieh et al., 2013). A compact arrangement of the ATD dimers described by crystallography (Karakas et al., 2011; Karakas and Furukawa, 2014), as compared to the AMPAR ATDs (Sobolevsky et al., 2009), was confirmed by distance measurements using the terbium chelate donor lifetime in presence of acceptors (Sirrieh et al., 2013). Furthermore, the LRET data showed no

agonist driven movement of the ATDs relative to each other during receptor activation or desensitisation and an increased closure of the GluN2A ATD cleft in presence of zinc ion as compared to the unbound state. Single molecule FRET (smFRET) between Alexa Fluor 555 and 647 attached to the upper and lower lobes of an isolated NMDA receptor LBDs the dynamics of the clamshell upon glycine binding were detected on a millisecond time scale and showed to be considerably slower than receptor open state transitions (Cooper et al., 2015).

Using FLIM measurements of GluN1 subunits C-terminally labelled with GFP and mCherry in cultured hippocampal neurons, conformational transitions of the C-terminal domain of an intact NMDA receptor heterotetramer were demonstrated (Dore et al., 2015). Firstly, a significant change in the lifetime of GFP was observed in the neuronal spines as compared to nearby dendritic compartments, suggesting a distinct conformation of the CTD in presence of synaptic proteins associated with the NMDA receptor. Secondly, a relatively fast reduction in FRET was measured during agonist binding, showing a translation of ligand binding into a conformational rearrangement of the C-terminal domain. These experiments were done in presence of a channel blocker, and thus no current was measured, showing a unidirectional propagation of a signal from the extracellular to the intracellular layer of the receptor. In an accompanying study involving FRET FLIM measurements between NMDA CTDs and labelled PP1 and CamKII, following the report of fast C-terminal transitions in absence of ion flow, an explanation of the purpose of these intracellular conformational rearrangements was proposed, which involved a CTD mediated change in interaction between NMDAR and PP1 to allow a further interaction with the phosphorylated CamK II (Aow et a., 2015).

AMPARs

Conformational dynamics of the ligand binding domain, isolated as well as in modified receptors (ATD deleted) have been studied using FRET. In the modified receptors, the amino terminal domain of the GluA4 subunit was removed and the functionality of the remaining homomeric receptor complexes was shown to be preserved (Du et al., 2005; Gonzalez et al., 2008, 2010). FRET was first measured between genetically attached GFP acceptor molecule in the N-terminal end of the D1 lobe and terbium chelate chemically attached to a mutated cysteine residue in the D2 lobe and confirmed the clamshell dynamics of the isolated (S1S2) ligand binding domain (Armstrong and

Gouaux, 2000) in response to agonist binding, as it showed a decrease in donor acceptor distances upon binding of glutamate which was larger than that observed during the binding of the partial agonist kainate. A similar observation was made during measurement of FRET within isolated LBDs (Ramanoudjame et al., 2006). Acceptor molecules nitrilotriacetic acid chelate of nickel or fluorescein were attached to a histidine or mutated cysteine residue on the N-terminal end of the S1S2 LBD, respectively, and residue S652 of the lower lobe of the LBD was labelled with either diethylenetriaminepentaacetic acid chelate of terbium (DTPA-Tb) or triethylenetetraaminehexaacetic acid chelate of terbium (TTHA-Tb) donors. FRET between the labelled D1 and D2 lobes upon binding of full and partial agonists showed a decrease in donor acceptor distances which followed the trend of cleft closure described previously (Armstrong and Gouaux, 2000): apo > kainate > glutamate ≈ AMPA (Ramanoudjame et al., 2006). Using a smaller acceptor tag in the place of N-terminally positioned GFP, which is of roughly the same size as the LBD, another study monitored ligand driven conformational rearrangements of the LBD cleft closure in an ATD deleted GluA4 homomer in membrane preparations (Gonzalez et al., 2008). With the same approach, chemical labelling of cysteine residues on the D1 lobe of a modified (ATD deleted) GluA4 receptor, the interface between the ligand binding domains in a homomeric receptor was probed in receptor resting, active and desensitised states (Gonzalez et al., 2010). It was proposed that in a resting conformation the dimer interface is less constrained, compared to an active state, and that the binding of agonist brings the D1 lobes of LBD dimers to closer proximity with each other, whereas the disruption of the interface proceeds as previously thought (Armstrong et al., 2006, Gonzalez et al., 2010).

So far studies directly correlating the structural dynamics through optical readouts with functional measurements of intact AMPA receptors in living cells are lacking. This issue will be addressed in the current study, where patch clamp fluorometry on fluorescently labelled AMPARs was applied (see *Results*).

1.6.4 Voltage clamp and patch clamp fluorometry

A combination of fluorescence measurements and electrophysiology has been termed voltage-clamp fluorometry (VCF) and was first applied on the Shaker potassium channels (Mannuzzu et al., 1996) to directly monitor the dynamics of the voltage sensing S4 domain of the ion channel during

activation. A core advantage of the technique is the possibility to optically correlate structural rearrangements with functional states of the ion channels under investigation, which has been missing in the separated structural (crystallography, cryo-EM) and functional (electrophysiology) studies (Kusch and Zrifarelli, 2014). Following the first reports of simultaneous optical and electrophysiological measurements of the dynamics of the Shaker channel the technique was broadened to the use of multiple environmentally sensitive dyes (Cha et al., 1997), FRET (Glauner et al., 1999) and lanthanide resonance energy transfer (LRET) (Cha et al., 1999). Using the environmentally sensitive dyes such as Tetramethylrhodamine maleimide (TMRM) the first study was able to distinguish site specific movements of the S2 and S4 segments of the ion channel as the labelled cysteine residues were either exposed or hidden from the extracellular aqueous environment (Cha et al., 1997). The latter two studies accomplished to measure distances and conformational changes of an ion channel for the first time, proposing a possible mechanism of voltage sensing. As the FRET distances were measured between moving domains, this information provided insight into the dynamic of the voltage sensing domain, but not to the movements relative to the plasma membrane of the cell. To overcome this VCF using donor (sulphorhodamine dye) quenching by the voltage sensitive membrane bound dipicrylamine (DPA) was applied in cut open oocyte configuration to study the translocation of the S4 segment within the membrane during voltage sensing (Chanda et al., 2005). Although VCF was originally a combination between two techniques: i) oocyte based two electrode voltage clamp (TEVC) and ii) scanning cysteine accessibility mutagenesis (SCAM) (Ghandi and Olcese, 2008), the basic principle behind it allows for high variability in the use of both electrophysiological and optical approaches. VCF has been implemented in both oocytes and mammalian cells (Blunck et al., 2004) using fluorescence quenching, LRET and FRET to monitor optical responses (Table 1). Originating from the VCF technique the patch clamp fluorometry (PCF) approach was first described by the group of William Zagotta (Zheng and Zagotta, 2000, 2003). This method measures the fluorescence from cell-excised patches, and thus overcomes some of the limitations accompanying cellular measurements, such as background and auto-fluorescence, limited access to intracellular positions and relatively low temporal resolution.

Optical readouts of structural dynamics in combination with functional recordings have been applied to study the structure-function relationship of multiple channels (Table 1). CFP and YFP are a popular FRET pair in PCF recordings and has been used in the study of both cyclic nucleotide

gated (CNG) channels (Zheng et al., 2003) and BK channels (Miranda et al., 2013). In the former study PCF from inside out patches from oocytes expressing CFP and YFP tagged CNG channel subunits was used to show a direct interaction between the N- and C-terminal domains of neighbouring subunits at study state conditions. Furthermore the disruption of this interaction was visualise in real time through the binding of Ca^{2+}-calmodulin to the N-terminal domain. In the study of BK channel dynamics YFP and CFP were attached to instinct positions within the intracellular gating ring region of the ion channel and Ca^{2+} and voltage dependent structural rearrangements were monitored through changes in FRET efficiency. Surprisingly the PCF recordings showed that not only are the motions of the gating ring far larger than previously thought, the distinct regions of fluorescent protein attachment respond differently to voltage. The CNG channels, which are activated by the binding of cyclic nucleotides to an intracellular C-terminal ligand binding domain, are among the most well-studied by the PCF technique (Zheng and Zagotta, 2000; Zheng et al., 2003; Trudeau and Zagotta, 2004; Taraska and Zagotta , 2007; Puljung and Zagotta, 2013). In one study PCF with labelled C-terminal region of CNG channels expressed in oocytes with both GFP and Alexa dyes was able to distinguish between movements orthogonal and parallel to the plasma membrane by a combination of donor quenching and FRET approaches (Taraska and Zagotta, 2007). It was shown that no orthogonal motions during cyclic nucleotides binding exist within the C-terminal region by using a membrane bound non-fluorescent quencher DPA and C-terminally attached GFP and Alexa488. In contrast, parallel movements relative to the membrane were measured between the C-linker and the C-terminal during gating using FRET between Alexa568 and GFP.

From the superfamily of ligand gated ion channels, the cys-loop receptors such as nAChR, GABA and glycine receptors have been studied using the PCF and VCF techniques (Pless and Lynch, 2008). Labelling of loop 5, located extracellularly at the interface between neuronal nAChR alpha and beta subunits close to agonist binding site, with TMRM dye showed fluorescence changes in presence of ligand suggesting a dynamic of the labelled domain during gating mechanism (Mourot et al., 2008). In a similar fashion VCF with another environmentally sensitive dye MTSR attached at the M2 transmembrane segment of the beta subunit of the muscular nAChR showed conformational rearrangements of the helix and sequential transitions of the subunits during receptor gating cycle (Dahan et al., 2004).

In the GABA receptors labelling of extracellular cysteine-replaced residues within the interface between subunits and simultaneous electrophysiological recordings showed agonist and antagonist driven conformational changes (Chang et al., 2002). VCF with various environmentally sensitive dyes in the vicinity of the GABA$_A$ binding pocket showed distinct fluorescence changes in active desensitised and inactive states, providing insights into the receptor structural dynamic (Muroi et al., 2006).

Channel	Electrophysiology	Fluorescence	Reference
Shaker voltage gated potassium channel	Cut open oocyte VCF	Environmentally sensitive dyes (TMRM, fluorescein-5-maleimide (FM) and Oregon green	Cha et al., 1997
	VCF whole cell oocyte	TMRM	Cha and Bezanilla, 1998 Cha et al., 1999a Mannuzzu et al., 1996 Claydon et al., 2007 Pathak et al., 2005 Pathak et al., 2007
		Fluorescein maleimide FM and TMRM FRET	Glauner et al., 1999
Cyclic nucleotide gated channels (CNG)	PCF inside out patch (oocyte)	CFP-YFP FRET	Zheng et al. 2003
		Alexa488 +Iodide (Quenching)	Zheng and Zagotta, 2000
		Donor quenching by DPA and FRET	Taraska and Zagotta, 2007
		FRET transition metal ion	Trudeau and Zagotta, 2004
		Transition metal ion FRET (tmFRET)	Puljung and Zagotta, 2013
Shaker potassium channel	VCF oocyte	ANAP	Kalstrup and Blunck, 2013
Kv1.2		TMRM	Horne et al., 2010
BK channels	PCF Inside out patch (Oocyte)	CFP-YFP FRET	Miranda et al., 2013

Voltage gated Na$^+$ channels	Cut open oocyte VCF	TMRM	Cha et al., 1999b Chanda and Bezanilla, 2002 Chanda et al., 2004
Nicotinic acetylcholine receptor (nAChR)	VCF oocyte	sulforhodamine methanethiosulfonate (MTSR) TMRM	Dahan et al., 2004 Mourot et al., 2008
GABA receptors	VCF (oocyte)	Alexa546 maleimide Alexa546 maleimide, MTSR and TMRM	Chang et al., 2002 Muroi et al., 2006
NMDA receptors	PCF	single molecule (sm)FRET between NMDA antibody-Atto-594 and Glycine-Alexa-532	Sasmal et al., 2014 Sasmal et al., 2016

Table 1 Overview of studies employing voltage clamp or patch clamp fluorometry in ion channels. The table is divided by the ion channel studied; the electrophysiological technique used (voltage clamp fluorometry, VCF; patch clamp fluorometry, PCF) and the cell type in which the recording were made; the fluorescent molecules used for optical readouts. References are provided for each individual study.

2. Materials and methods

2.1 Cell culture

2.1.1 Buffers and solutions

Complete minimum essential medium (MEM)

All components were purchased from Biochrom AG/Millipore (Berlin, Germany). MEM Earle's was supplemented with 10% fetal bovine serum (FBS) and 5% penicillin/streptomycin. The complete medium was stored at 4ºC.

Kynurenic acid solution

The kynurenic acid solution contained (in mM): 50 kynurenic acid (MW 207,19; Abcam Biochemicals, Cambridge, UK) and 100 $MgCl_2$ ($MgCl_2$ x $6H_2O$ MW 203.30) The solution was titrated with NaOH to pH 7.2 and filter-sterilized using a 0.22 μm Nylon filter (Nalgene). Aliquots were stored at -20ºC.

2xHEPES-buffered saline

The 2xHBS contained (in mM): 283 NaCl (MW 58.44), 1.5 Na_2HPO_4 (MW 142) and 50 HEPES (MW 238.3). The buffer was titrated with NaOH to pH 7.2 and filter-sterilised using a 0.22 μm Nylon filter (Nalgene).

$CaCl_2$ solution

The $CaCl_2$ solution contained (in mM): 340 $CaCl_2$ x $2H_2O$ (MW 147)

2.1.2 Cell cultivation

HEK-293 (human embryonic kidney) cells were used for over-expression of glutamate receptors for electrophysiological recordings. The cells were purchased from Leibniz Institute DSMZ (German Collection of Microorganisms and Cell Cultures GmbH, Braunschweig). The cells were maintained

in complete MEM at 37 ºC and 5% CO_2. The cells were passaged twice a week as follows. The confluent cells were washed with sterile PBS (Biochrom AG/Millipore) (pre-warmed to 37ºC) and incubated in 0.05% Trypsin in PBS (Biochrom AG/Millipore) for 2 min at 37ºC. The detached cells were collected with 10mL MEM, transferred into a 15 mL Falcon tube and centrifuged at 400xg for 4 min. The cell pellet was resuspended and the cells were plated in new flasks containing fresh MEM in a dilution of 1:5-1:7. All dishes and flasks were purchased from NUNC™/Thermo Fisher Scientific (Schwerte, Germany).

2.1.3 Preparation of coverslips

For electrophysiological recordings HEK 293 cells were plated on 10 mm diameter glass coverslips (Hartenstein, Würrtzburg, Germany). Before usage the coverslips were placed in 70% Ethanol in 50 mL Falcon tubes (Sarstedt, Nümbrecht, Germany) and sonicated for 10 min. The coverslips were subsequently stored in 99% Ethanol at room temperature. Before cell plating the coverslips were flame-sterilised and placed into sterile Nunclon™ 3.5 cm dishes (Thermoscientific, Roskilde, Denmark). Following the passaging procedure the cells were into the dishes containing the coverslips at a dilution of 1:80 to 1:100 to achieve approximate confluence of 70% at the day of transfection.

2.1.4 DNA transfection

The cells were transfected using $CaPO_4$ precipitation method 24 hours post passaging and plating. 1.5 mL Eppendorf tubes with 60 µL of 2xHEBS were prepared for each dish of cells. In separate Eppendorf tubes a total of 3 µg of plasmid DNA (1 µg/ µL) were added to 57 µL of $CaCl_2$ solution and mixed briefly. The $CaCl_2$/DNA mixture was then added drop-wise to the 2xHEBS containing tube and the content was mixed by flicking the tube slightly. The mixture was incubated at room temperature for 30 min to obtain the DNA-$CaPO_4$ precipitate. The precipitate was then drop-wise added to the dish of cells and incubated for 6 hours in the dedicated cell incubator (37 ºC, 5% CO_2). After the incubation period the DNA mixture containing medium was removed, the cells were washed 2 times with sterile PBS and the medium was replaced by 2 mL fresh MEM. The medium was supplemented kynurenic acid solution to a final concentration of 1 mM, to avoid glutamate

mediated excitotoxicity due to over-expression of glutamate receptors (Prescott et al. 2006), and the cells were incubated until use, normally 48-74 hours.

2.2 Molecular biology

2.2.1 Expression vectors

The pRK5 expression vector encoding the flip splice variant of the Glua2 subunit unedited at the Q/R site was used for expression of homomeric glutamate receptor complexes (BiQG pRK5 GluA2 IRES EGFP). To create a non-fluorescent target vector the Internal Ribosome Entry Site (IRES) and the following EGFP were removed by overlap PCR, leaving the BiQG-pRK5-GluA2 expression vector ready for fluorescent protein fusion.

Expression vectors encoding GluA2 subunit with intracellular mVenus and mCerulean3 fusions (pCI expression vector) (denoted I6V, I10V, I6V-I10C) were provided by Linda Zachariassen and Anders Skov Kristensen (University of Copenhagen, Denmark).

2.2.2 Insertion of fluorescent proteins

According to the described permissive sites for insertions of fluorescent proteins (Sheridan, 2006) within the GluA2 subunit several fusion chimeras were created using overlap PCR (Table 2 for primers). The positions were denoted according to the number of the amino acid preceding the insertion site counting from the N-terminal position (Fig. 5). The numbering of the positions did not include the 21 amino acid signal peptide.

Monomeric versions of the fluorescent protein variants were used for fusion constructs, to avoid dimerisation of FPs and interference in the folding of the full fusion protein (Table 3). To create a monomeric version of EGFP the mutation A206K was introduced (Zacharias et al., 2002) by overlap PCR. Prior to insertion the fluorescent protein variants were modified as follows: each fluorescent protein was enclosed by a 9 amino acid linker at the N-terminal site (LSLIHIWRA) and a 12 amino acid linker at the C-terminal site (GGRARADVYKRQ). This modification was likewise done by overlap PCR simultaneously removing two amino acids from the N-terminal of the FP sequence (MV) and the stop codon from the C-terminal.

Insertion of a cpGFP (Marvin et al., 2013) into various positions in the GluA2 subunit was done in the same manner as described above with the exception of the connective linkers. The cpGFP was copied out of the template vector pCMV.iGluSnFR (Addgene) with overlap primers (Table 2). The cpGFP preserved its original linkers and was inserted into the receptor without further modifications.
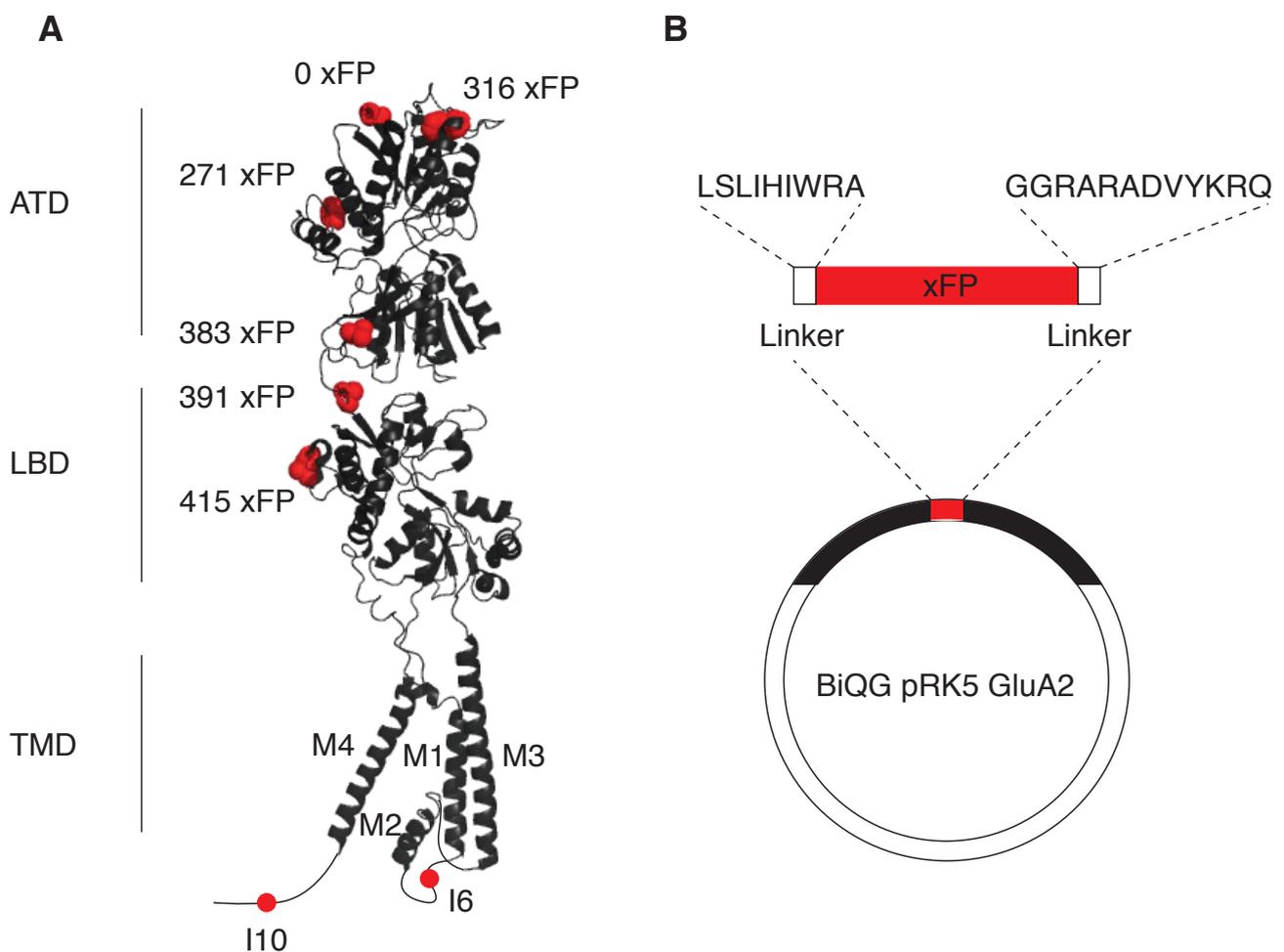
Figure 5 Genetic insertion of fluorescent proteins into the GluA2 subunit A A single subunit of the AMPA receptor with positions of fluorescent fusion sites indicated in re spheres. **B** A schematic representation of the expression vector of fluorescently fused AMPA receptors. Black filling indicates the sequence of a single subunit of the AMPA receptor. Red insertions represents the inserted fluorescent protein flanked by either a 9 amino acid linker on the 3' end or a 12 amino acid linker on the 5' end.

Position/ primer	FP	sequence 5' - 3'
271/ M1	mEGFP/Venus/mCerulean3	ggaagagaaagaataccctggagcacacaca**ctgtctctt atacacatc**
271/ M2	mEGFP/Venus/mCerulean3	**gatgtgtataagagacag**gcgacaattaagtatacttcggc c
271/ M3 (rev)	mEGFP/Venus/mCerulean3	CGTCAGGGCCGAAGTATACTTAATTG TCGC**CTGTCTCTTATACACATCTGC**
271/ M4 (rev)	mEGFP/Venus/mCerulean3	**GATGTGTATAAGAGACAG**TGTGTGT GCTCCAGGGTATTC
316/ M1	mEGFP/Venus/mCerulean3	AACCCAGCTGTGCCC**CTCTCCCTGA TTATGATTTG**
316 /M2	mEGFP/Venus/mCerulean3	TGGGGACAAGGGGTCGAAATAGAAA GGGC
316/ M3 (rev)	mEGFP/Venus/mCerulean3	GACCCCTTGTCCCCA**CTGCCGCTTG TACACGTCTGCCCG**
316/ M4 (rev)	mEGFP/Venus/mCerulean3	GGGCACAGCTGGGTTGGCCAAACAA T
383 /M1	mEGFP/Venus/mCerulean3	atggttgtcaccctaactgagctcccatca**ctgtctcttatac acatctggc**
383 /M2	mEGFP/Venus/mCerulean3	**gatgtgtataagagacag**gcgacaattaagtatacttcggc c
383/ M3 (rev)	mEGFP/Venus/mCerulean3	CTTGTTTTCAAGCCCAGACGTGTCAT TTCC**CTGTCTCTTATACAC**
383/ M4 (rev)	mEGFP/Venus/mCerulean3	**GATGTGTATAAGAGACAG**TGTGTGT GCTCCAGGGTATTC
391 /M1	mEGFP/Venus/mCerulean3	caggaaatgacacgtctgggcttgaa**ctgtctcttatacac atc**
391/ M2	mEGFP/Venus/mCerulean3	**tgtataagagacagcttgaa**aacaagactgtggtggtcac c
391 /M3 (rev)	mEGFP/Venus/mCerulean3	TGACCACCACAGTCTTGTT**TTCAAGC TGTCTCTTATACACATCTGC**
391 /M4 (rev)	mEGFP/Venus/mCerulean3	**GTGTATAAGAGACAG**TTCAAGCCCA GACGTGTCATT
415 /M1	mEGFP/Venus/mCerulean3	ccatatgttatgatg**ctgtctcttatacac**
415 /M2	mEGFP/Venus/mCerulean3	**gtgtataagagacag**aagaaaaatcatgaaatgc
415 /M3 (rev)	mEGFP/Venus/mCerulean3	TTCATGATTTTTCTT**CTGTCTCTTATA CAC**
415 /M4 (rev)	mEGFP/Venus/mCerulean3	**GTGTATAAGAGACAG**CATCATAACAT ATGG
383 /M1	cpGFP	actgagctcccaactctggtgAGCCACAACG
383 /M2	cpGFP	TTTAACaaCCCcggaaatgacacgtctgggc
383/ M3 (rev)	cpGFP	AGACGTGTCATTTCCGGGGTTGTTAA AGTTG
383/ M4 (rev)	cpGFP	GCTCACCAGAGTTGGGAGCTCAGT
391 /M1	cpGFP	caggaaatgacacgtctgggcttgaactggtgAGCCAC AACGTCTA
391/ M2	cpGFP	GGAGTACAACTTTAACaaCCCcaacaagac tgtggtggtcacc
391 /M3 (rev)	cpGFP	GGTGACCACCACAGTCTTGTTGGGGT TGTTAAAGTTGTACTC
391 /M4 (rev)	cpGFP	GACGTTGTGGCTCACCAGTTCAAGCC CAGACGTGTCATTTCC

Table 2 Primers for fluorescent protein fusion within the AMPA receptor using overlap PCR Each primer is given in 3' - 5' order. The reverse primers are reverse and complemented of the target sequence. Bold lettering indicates overlap regions with the fluorescent protein and the linkers. Reverse primers are in capital letters.

Fluorescent protein	Excitation (nm)	Emission (nm)	Extinction coefficient (10^3 $M^{-1}cm^{-1}$)	Origin	Reference
Venus	515	528	92.2	GFP	Nagai et al., 2002
mCerulean3	433	475	40	GFP	Markwardt et al., 2011
mEGFP	488	507	56	GFP	Zacharias et al., 2006
mTagRFP-T	555	584	81	eqFP578	Shaner et al., 2008

Table 3 Variants of fluorescent proteins used for fusions within the AMPA receptors The origin, extinction coefficients, excitation and emission maxima are indicated for each fluorescent protein variant.

2.3 Electrophysiology and voltage clamp fluorometry

2.3.1 Experimental setup

The experimental setup for voltage clamp fluorometry is illustrated in **figure 6** The IX-81 inverted microscope (Olympus) was mounted on a compressed air isolation table (TMC, Peabody, MA, USA). For recordings a coverslip with cells was placed in the Chamlide AC-PI chamber (Live Cell instrument, Seoul, Korea) where it was constantly perfused by extracellular solution. The outflow of the bath was connected to a low noise pump. An AgCl (Warner Instruments, USA) ground electrode was placed directly in the bath solution. Solutions were applied through a custom-made 4 barrel perfusion tool. The perfusion tool was connected to a gravity driven perfusion system of valve-controlled containers (BD Plastipak, Hartenstein). To ensure ultra fast solution exchange the motion of the tool was driven by a piezo-electric transducer (Physik Instrumente (PI), Palmbach, Germany), which was controlled by the piezo amplifier (PI) connected to the digitiser (Instrutech ITC-18, HEKA Instruments, Malsfeld, Germany). Patch pipettes were mounted in an ISO-S-1.5G micro-electrode holder (G23 Instruments, UK) attached to a head-stage (Axon Instruments). The movement of the head-stage was controlled by the Patchstar motorised micro-manipulator (Scientifica, Uckfield, UK). The resistance of the pipette was monitored on a two channel oscilloscope (Tektronix, Cologne, Germany). The current from either outside out patches or whole lifted cells was recorded through an Axopatch 200B patch clamp amplifier and the Axograph software (Axograph Scientific). A multi laser engine (iChrome MLE LFE) (Toptica Photonics, Munich, Germany) combined four diode lasers of the following wavelengths: 445, 488, 514 and 561 nm. The lasers were directed in an all-in-one PM/SM fiber output through the manual TIRF input of the microscope and focused to the back focal plane of a UCPLFLN 20x Olympus objective (1.8mm WD, 0.7 NA). The individual laser lines were controlled through the designated Toptica software (Topas iChrome MLE). Customised filter sets were mounted onto Olympus filter cubes and placed in the filter cube turret of the microscope to accommodate the corresponding laser lines. All filters were from Semrock manufacturer, unless otherwise stated, purchased at AHF Analysentechnik (Tübingen, Germany). For the 445nm laser the following set was used: Brightline™ HC 448/20 band pass excitation filter, RazorEdge™ LP 458 long pass emission filter and laser beamsplitter 442 RDC (Chroma). For the 488 laser line the following filters were used:
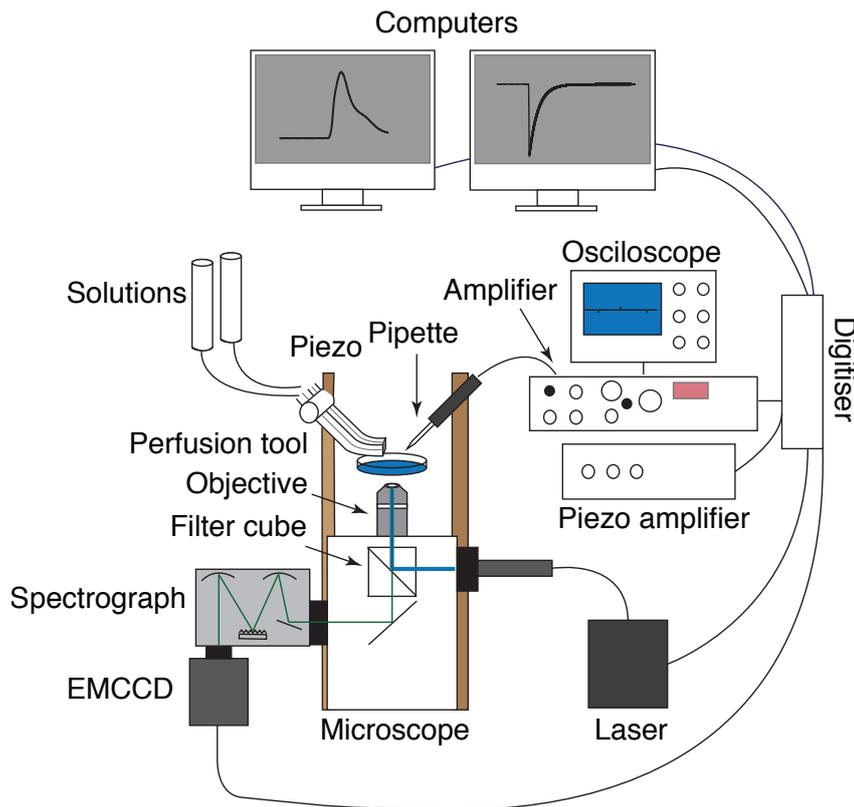
Figure 6 Experimental setup A schematic representation of the patch clamp fluorometry setup used for simultaneous acquisition of fluorescence and electrophysiological recordings.

bandpass excitation ET470/40x (Chroma), beamsplitter T495LPxR (Chroma) and long pass emission filter Edgebasic™ 488. For the 514 nm laser line the following filters were used: Brightline™ HC 512/18 band pass excitation filter, Edgebasic™ 514 long pass emission filter and Brightline™ single edge dichroic BSR 514. For the 561 nm laser the following filters were used: Brightline™ HC 561/14 band pass excitation filter, Edgebasic™ LP 561 long pass emission filter and laser beamsplitter 561 RDC (Chroma). The emitted light was passed through the slit of a spectrograph (SP2156, Princeton Instruments), onto a grating (300/500 nm) and the resulting spectra were imaged by a ProEm 512 electron multiplying CCD (EMCCD) camera (Princeton instruments, New Jersey). The EMCCD camera was controlled by manufacturer software (Lightfield). Camera shutter, laser, microscope and piezo were connected to a digitizer and controlled through the Axograph software. To accommodate automatic changing of the filter cube position inside the microscope during a recording the motorised filter cube turret was connected to an Arduino panel and put under computer control using a reverse engineered serial connection written in Python.

2.3.2 Solutions for electrophysiological recordings

Sodium extracellular "Ringer" solution

The 1 x solution contained (in mM): 150 NaCl (MW 58.44), 0.1 $MgCl_2$ (MW 203.3), 0.1 $CaCl_2$ (MW 110.99) and 5 HEPES (MW 283.3). The components were dissolved in MilliQ H_2O, the solution was titrated to pH 7.3 with NaOH, filtered using a 0.2 μm filter (Millipore) and stored at 4 °C. The solution was filtered using 0.2 μm nylon filter (Millipore).

Potassium extracellular solution

The 1 x solution contained (in mM): 158 NaCl (MW 58.44), 20 HEPES (MW 283.3), 3 KCl (MW 74.55) and 1 $CaCl_2$ (MW 110.99). The components were dissolved in MilliQ H_2O, the solution was titrated to pH 7.4 with NaOH, filtered using a 0.2 μm nylon filter and stored at 4 °C. The solution was filtered using 0.2 μm nylon filter (Millipore).

Sodium intracellular solution

The sodium intracellular solution contained (in mM): 115 NaCl (MW 58.44), 10 NaF (MW 41.99), 5 Na_4BAPTA (MW 564), 0.5 $CaCl_2$ (MW 110.99), 1 $MgCl_2$ (MW 203.3), 5 HEPES (MW 283.3) and 10 Na_2ATP (MW 551). The components were dissolved in MilliQ H_2O, the solution was titrated to pH 7.3 with NaOH and filtered using 0.2 μm nylon filter (Millipore).

Potassium intracellular solution

The potassium intracellular solution contained (in mM): 135 KCl (MW 74.55), 20 KF (MW 58.09), 20 HEPES (MW 283.3), 3 NaCl (MW 58.44), 1 $MgCl_2$ (MW 203.3) and 2 EGTA (MW 380.35). The components were dissolved in MilliQ H_2O, the solution was titrated to pH 7.3 with NaOH and filtered using 0.2 μm nylon filter (Millipore).

Glutamate solution

The stock solution contained (in M): 2 L-Glutamate (MW 147.1), 0.5 Sucrose (MW 342) and 1.5 NaOH (MW 40). The components were dissolved in MilliQ H_2O, the solution was titrated to pH 7.3 with NaOH and filtered using 0.2 μm nylon filter (Millipore). The glutamate solution of the desired

concentration (commonly 10 mM) was prepared freshly on the day of the experiment by dilution in the extracellular buffer and filtering with 0.2 µm nylon filter (Millipore).

Cyclothiazide solution

The positive allosteric modulator cyclothiazide (CTZ) (MW 389.88) was dissolved in DMSO to a final concentration of 50 mM. Aliquots were stored at –20ºC. Working solution of 100 µM CTZ was prepared freshly on the day of the experiment.

Dipicrylamine solution

Dipicrylamine (DPA) (MW 439.2) was dissolved in DMSO to a final concentration of 20 mM. Aliquots were stored at -20ºC. Working solution of 5 µM DPA was prepared freshly on the day of the experiment.

2.3.3 Preparation of perfusion tools

To make the base of the perfusion tool, square four-barrel glass tubes (Vitrocom, Mountain Lakes, NJ) were cut into 10 cm long pieces using a diamond pen. The cut tubes were pulled using a P-1000 Flaming/Brown micropipette puller (Sutter Instruments, Novato, USA) to produce a thin tip. A diamond pen was used to finalise the cut under the microscope. The tip of the tube was bent 30-40 degrees by applying heat from a filament. To minimise dead volume inside the perfusion tool, app. 0.6 cm of the tip was cut off and incubated in a drop of 48% Hydrofluoric acid for 22 min to etch the glass walls. After incubation period the tip was washed several times with NaOH diluted in MilliQ H_2O and pure MilliQ H_2O. Brown fine quartz filament capillaries (Agilent technologies, USA) with a diameter of 0.320 mm were cut into 10-12 cm long pieces and purified by sonification in 70% Ethanol for 10 min and subsequent wash in MilliQ H_2O. A single capillary was inserted into each barrel of the bottom part of the tool (not etched) and fitted to the tip of the perfusion tool (etched). Two-component glue (Araldite) was mixed and applied at the interface between the two pieces of the tool. Capillary action distributed the glue around the filaments. A drop of glue was also placed at the bottom of the tube, to secure the filaments further. The assembled perfusion tool was left to dry overnight at 42ºC and was used for a good few days until taken and blocked by other members of the group.

2.3.4 Preparation of patch pipettes

Thin wall borosilicate capillaries (Warner instruments, Hamden, USA) were pulled on the P1000 micropipette puller (Sutter Instruments) and polished using a heat filament to a final resistance of 3-5 MΩ for outside out patches and approximately 1 MΩ for whole cell recordings.

2.3.5 Fast-perfusion outside out patch clamp recordings

For kinetic characterisation of ion channels electrophysiological recordings were done on excised outside out patches. Pulled and polished micropipettes were backfilled with intracellular solution and mounted onto the micro-electrode holder. Positive pressure inside the pipette was applied manually by blowing into Teflon tubing connected to the micro-electrode holder. The pipette was placed into the bath solution and the resistance was monitored on the oscilloscope (Fig. 7). A camera connected to the bottom port of the microscope allowed visualisation of the cells in the bath. Once a cell with sufficient expression (as noted by the amount of fluorescence) was identified, the patch pipette was moved into a position above the cell using the micro-manipulator. During slow approach and constant manual application of positive pressure to the pipette, the increase in resistance could be monitored on the oscilloscope as the patch pipette came closer to the plasma membrane. When a gigaseal was reached, a point when the resistance of the pipette reaches at least 1GΩ, the plasma membrane of the cell was broken through by application of gentle negative pressure to the pipette. Slow movement of the pipette away from the cell resulted in formation of an outside out patch. The patch was moved to the interface between of the solutions flowing through the barrels of the perfusion tool and the current was recorded. Unless otherwise stated, the membrane potential of the patch was held at -60 mV.

2.3.6 Fast-perfusion lifted whole cell recordings

The procedure for obtaining the gigaseal was as described above. From the whole cell configuration (Fig. 7) the patched cell was lifted from the coverslip and moved to the perfusion tool. All

fluorescence recordings were done on lifted whole cells. The membrane voltage was clamped at -40 mV, due to large currents, unless otherwise stated.
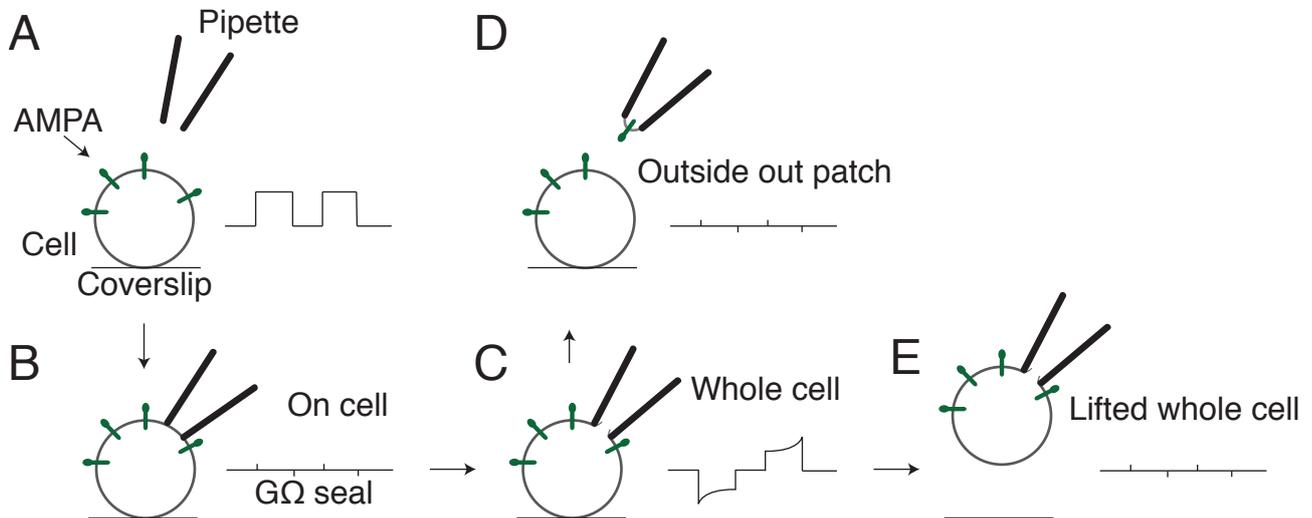
Figure 7 Electrophysiological recordings of HEK293 cells A schematic representation of the steps leading to either an outside-out patch or a lifted whole cell configurations. The HEK293 cells seeded growing on glass coverslips were expressing fluorescently labelled AMPA receptors (green) on the membrane. The patch pipette is shown in black. The patch pipette resistance following a test pulse as seen on the oscilloscope is shown for each configuration. A Patch pipette is lowered into the bath solution ready to approach a cell. **B** Cell attached configuration leads to an increase in patch pipette resistance. **C** Application of negative pressure results in the rupture of the cell membrane creating a whole cell configuration. **D** Pulling the patch pipette rapidly from the cell results in an outside-out patch, with the extracellular domains of the channel exposed to the bath solution. **E** Pulling the pipette slowly from the whole cell configuration results in a lifted whole cell.

2.3.7 Fluorescence recordings

As mentioned before the emitted fluorescence was passed through a spectrograph and collected on the chip of an EMCCD camera (name of cable by which the camera is connected to the Mac). To improve fluorescence acquisition rates a region of interest (ROI) was selected on the chip with a height of 25 and the width of 512 pixels. The lifted whole cell was positioned within the ROI during a recording. The camera acquisition settings were adjusted using the LightField software. Normally, the temperature of cooling system was set to -20 ºC and the EM gain to 25. The acquisition of fluorescence was controlled by a rising edge of a trigger. The trigger was produced by introducing
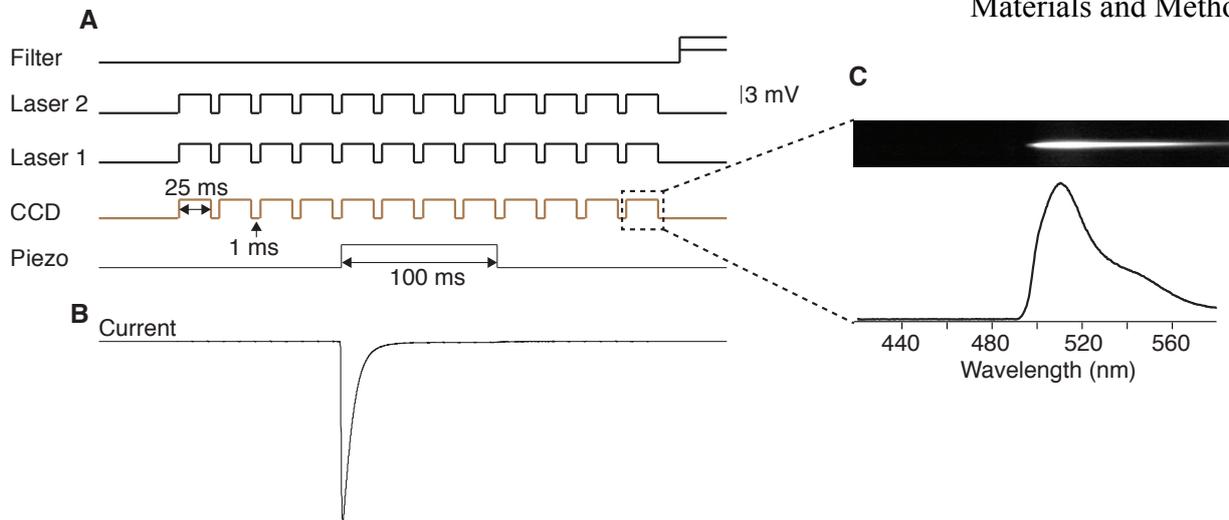
Figure 8 Patch clamp fluorometry recording protocol A schematic representation of the protocol used for simultaneous acquisition of currents and fluorescence spectra from HEK293 cells expressing fluorescently labelled AMPA receptors. **A** Recording protocols were created in Axograph. Normally the amount of channels would depend on the the number of different fluorescent proteins fused to the AMPA receptor. For FRET recordings a channel for a laser line exciting the donor fluorophore and the acceptor fluorophore would be added. Pulses within each channel would activate the lasers. The pulses were made of the same length as the fluorescence acquisition frames in the CCD channel, activating the shutter of the EMCCD camera. The piezo channel drives the movement of the perfusion tool. **B** The corresponding current evoked by application of glutamate following a pulse from the piezo. **C** The insert shows a fluorescence line-scan and the spectra from the average of the line-scan, here from YFP emission.

pulses of varying time length in the Axograph protocol. In this way the time point, frequency and duration of acquisition could all be set within a single protocol (Fig. 8). The frame triggers were spaced with 1ms latency to allow the readout of each frame by the camera chip (the readout time depended on the size of the ROI and on the readout mode selected in the software). Depending on the arbitrary fluorescence intensity of the cells and on the experiment the acquisition frames were set to be between 10 and 100ms in length (100 – 10 Hz) (Fig. 8 A). The data was saved in .spe file format. The lasers exciting donor and acceptor fluorescence were triggered by pulses of equivalent length as the acquisition frames. Donor and acceptor excitation was alternated by introducing a switch at the end of a pulse-train, which moved the corresponding filter-cube into position. A current was recorded during each episode (Fig. 8 B). Each frame of the CCD camera contained a line-scan (Fig 8 C). Averaging the intensities within the ROI resulted in the recorded spectra, which were used for subsequent data analysis (Fig 8. C)

Spectral FRET approach was used as described (Zheng and Zagotta, 2003) to measure FRET efficiency between a donor and acceptor fluorophore. Figure 4 (*Introduction*) summarises the theory behind this method.

2.4 Data analysis

2.4.1 Electrophysiology

Electrophysiological analysis was done using Axograph software. The rate of desensitization (k_{des}) was determined by fitting a single exponential function to the current decay during a long (100 ms) pulse of 10 mM glutamate. The rate of deactivation (k_{deact}) was determined by fitting a single exponential function to the decay following a brief (1 ms) pulse of 10 mM glutamate. Recovery from desensitisation was measured using a two-pulse protocol with variable interpulse intervals. The rate of recovery (k_{rec}) was determined by fitting the recovery data with a Hodgkin-Huxley-type function with a slope of 2. The time constants (ms) were converted into rate constants (s^{-1}) by dividing them by 1000.

2.4.2 Fluorescence

Processing of raw fluorescence data from the LightField software was done in IgorPro by automated procedures written in house. Summaries and statistics were usually performed in Excel. Figures were made by plotting summarised data into IgorPro.

FRET

During FRET recordings the acquisition alternated between donor and acceptor emission fluorescence trains. Analysis of the raw data was done in Igor (Appendix A2). Each .spe file contained data in the form: 512 (intensity) x number of frames x number of episodes. First the data was dimensioned into 3D stacks to resemble the recording protocol (Fig. 9). The Y dimension contained 512 points, representing the intensity values. The x dimension was of the same order as the number of frames in one episode. The z dimension contained the number of episodes recorded. The xy sheets of data were separated based on the excitation wavelength (donor and acceptor) and averaged in the z-dimension. A spectrum of donor fluorescence (loaded separately) was scaled to the peak of each donor-acceptor frame and subtracted. The resulting frames (containing mixture of FRET and direct excitation, Fig. 4) were divided by acceptor frames to obtain RatioA for each
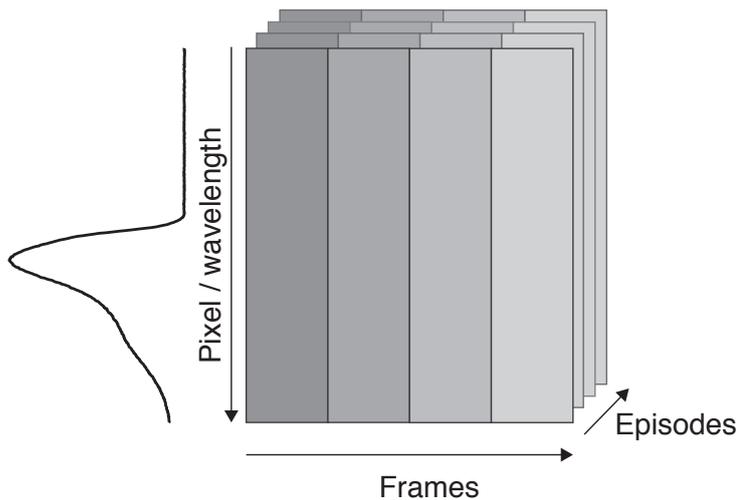
Figure 9 Analysis of FRET data A representation of the analysis procedure done in IGOR. The fluorescence data collected from the EMCCD camera were reorganised in order to have the fluorescence spectra from individual frames in columns, the frames acquired during a single electrophysiological episode in rows and each subsequent electrophysiological episode in layers.

frame. RatioA0 was measured in a similar manner using data recorded from cells expressing acceptor fluorophore only. The FRET-ratio (FR) and the FRET efficiency were calculated as described previously (Zheng and Zagotta, 2003, Ericsson et al., 2011, see *Introduction 1.6.2*).

Donor quenching

Data from experiments with a single fluorescence component (i.e. DPA quenching) was processed in the same manner as described above (**Appendix A4**) excluding the separation of wavelengths and spectral FRET calculations. Instead, following baseline and re-dimensioning procedures, the peak fluorescence values from each frame were collected. The quenching of a given fluorescent protein (F_Q) by DPA was calculated for each frame as:

Equation 9
$$F_Q = \frac{F_{DPA}}{F}$$

where F_{DPA} was the measured fluorescence intensity in presence of DPA and F was the fluorescence intensity measured before application of DPA.

The relative change in fluorescence during an electrophysiological recording was calculated as ΔF/F. The ΔF/F for the *j*th acquisition from in a set of n frames relative to the intensity measured in the first acquired frame in presence of DPA (F_1) was calculated according to:

Equation 10

$$\left[\Delta F / F\right]_j = \frac{F_j - F_1}{F_1}, j = 1...n$$

A background fluorescence signal was recorded using an identical protocol in absence of DPA and subtracted from each recording, in order to correct for minor optical artefacts arising from mechanical solution exchange.

2.4.3 Distance determination

FRET

Following the calculation of FRET efficiencies between donor and acceptor fluorophores the corresponding distances were calculated using an automated IgorPro procedure written in house (see **Appendix A3**). The relationship between the efficiency of energy transfer (E) and the distance separating the fluorophores is described by:

Equation 11

$$r = R_0 \left(\frac{1}{E} - 1\right)^{\frac{1}{6}}$$

where r is the distance in Angstroms and R_0 is the förster distance for a given donor-acceptor pair.

Donor quenching

In experiments were donor quenching was measured by DPA the distances of the fluorophores in various insertion sites were calculated as described previously (Wang et al., 2010; Zachariassen, Katchan et al., 2016). Distances of the intracellular insertion sites were determined following the voltage dependent quenching of the fluorophores in different receptor states (*Results* Fig. 24). DPA molecules were assumed to reside in either the inner or outer leaflet of the membrane, separated by approximately 25 Å. As described previously (Fernandez et al., 1983) the transverse distribution of DPA molecules could be described as a one-barrier model, spanning roughly 60 % of the membrane

electric field. For the concentration of DPA used in the experiments (5 µM) the total density in the membrane (σ_{tot}) was 1.25×10^{-4} Å^{-1} (Wang et al., 2010). The varying density of DPA at the inner leaflet of the membrane at room temperature with voltage was calculated as:

Equation 12
$$\sigma_{in} = \frac{\sigma_{tot}}{1 + \exp(\dfrac{-e\alpha(V - V_0)}{kT})}$$

taking $\alpha = 0.6$, $V_0 = -15$ mV, and $e/kT = 25.6$ mV.

The density of DPA at the outer membrane leaflet at a given voltage was the difference between the total density and the density at the inner leaflet:

Equation 13
$$\sigma_{out} = \sigma_{tot} - \sigma_{in}$$

DPA molecules were assumed to be distributed in a plane at the plasma membrane and the quenching probability for a donor fluorophore at a range of distances from the acceptor plane were calculated. The donor fluorophore is first placed at a distance R_z from a plane containing an infinitesimally thick ring of radius r, concentric with the projection of the fluorophore (Fig. 10).
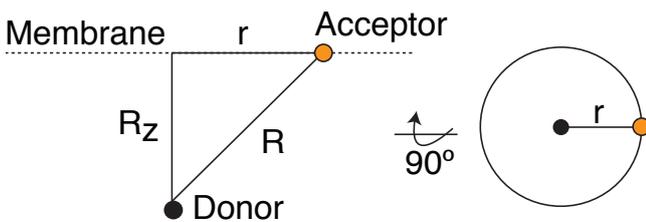
Figure 10 Geometric calculation of donor quenching at various distances from the membrane The membrane is represented as a dashed line with the acceptor (orange sphere) located in the plane of the membrane. R_z is the distance of the donor to the membrane plane, R is the distance of the donor to an acceptor located in the plane and r is the radius of the circular projection on the plane of the membrane concentric to the donor.

Donor acceptor distance (R) is given by:

Equation 14
$$R = \sqrt{R_z^2 + r^2}$$

FRET efficiency is related to the fluorophore distance:

Equation 15

$$E = \frac{1}{1+(\frac{r}{R_0})^6}$$

Substituting the distance R into the FRET efficiency formula gives:

Equation 16

$$E = \frac{1}{1+(\frac{R_z^2+r^2}{R_0^2})^3}$$

The probability of quenching of the donor by an acceptor residing inside the infinitesimally thick ring can be described as a product of the FRET efficiency, the density of DPA (σ) and the circumference of the ring:

Equation 17

$$q(r)dr = \frac{\sigma 2\pi r dr}{1+(\frac{R_z^2+r^2}{R_0^2})^3}$$

The probability of no quenching, P, of the donor by DPA within a disc with radius $r + dr$ can be expressed:

Equation 18

$$\frac{dP}{dr} = \frac{\sigma 2\pi r P}{1+(\frac{R_z^2+r^2}{R_0^2})^3}$$

which gives rise to the following differential equation:

Equation 19

$$P(r+dr) = P(r) \cdot (1 - q(r)dr)$$

The probability of no quenching is the solution to this differential equation evaluated at infinity:

Equation 20
$$P_{\infty} = \exp(-\sigma\pi R_0^2 \int\limits_{\frac{R_z^2}{R_0^2}}^{\infty} \frac{du}{1+u^3})$$

where the following substitution was made:

Equation 21
$$u = (\frac{R_z^2 + r^2}{R_0^2})$$

At positive and negative membrane potentials DPA resides at either outer or the inner leaflet of the membrane giving rise to two probe distances R_z or R_z + 25 Å. The probabilities were evaluated according to the voltage-dependent densities of DPA in each membrane plane and combined to give a net probability of quenching as a function of voltage and the displacement of the donor from the membrane (Zachariassen, Katchan et al., 2016). The probabilities at the limiting negative and positive voltages were used calculate the theoretical fluorescence intensity (F) and voltage-dependent change(ΔF) in intensity as a function of fluorophore distance (Fig. 26).

3. Results

3.1 Fluorescent labelling of AMPA receptors

3.2.1 Genetic labelling

According to the permissive sites described previously (Sheridan 2006), different variants of fluorescent proteins (FP) were genetically fused inline at distinct positions within the AMPA receptor subunit (see *Materials and methods* **Table 3** for summary of fluorescent proteins). **Figure 11 A** shows the position of FP fusion in a single AMPA subunit. Among the 7 insertion sites 5 positions were in the extracellular region of the receptor: 2 within the amino terminal domain
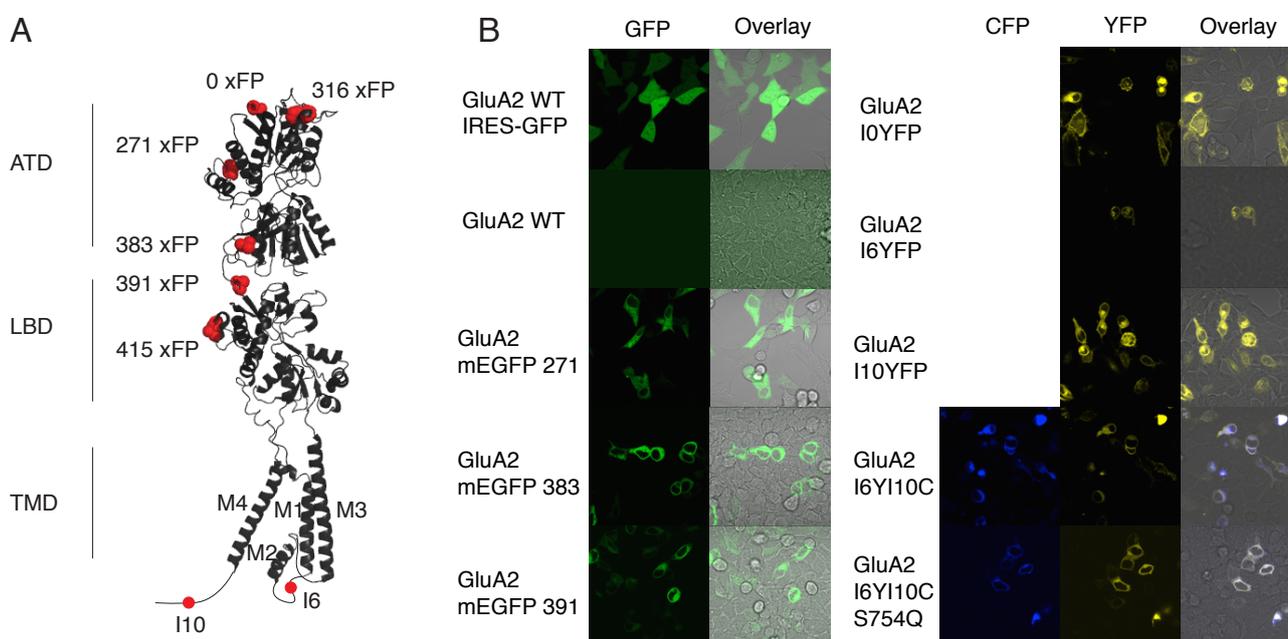
Figure 11 Genetic labelling of AMPARs A A single AMPA receptor subunit (PDB 3kg2, Sobolevsky et al., 2009) with positions for fluorescent protein fusion indicated by red spheres in the amino terminal domain (ATD), the ligand binding domain (LBD) and the intracellular region. The C-terminal domain and the intracellular loop were drawn by hand, as these regions are unresolved in the structure. **B** Confocal microscopy images of HEK293 cells expressing the fluorescently fused AMPA receptors. Receptors harbouring green fluorescent protein (GFP) at the indicated insertion sites in the extracellular domains were imaged following excitation by 488 nm laser, with the exception of I0, which was fused to a yellow fluorescent protein (YFP) and was excited by the 514 nm laser. The intracellular insertion sites contained YFP in single fusion constructs, and YFP and cyan fluorescent protein (CFP) fusions in the double labelled receptors. The CFP was excited by the 454 nm laser. All recordings are overlaid with the bright-field images to illustrate cell density and viability.

(ATD) (I0 and 271), 2 within the linker connecting the ATD to the ligand binding domain (383 and 391) and one within the ligand binding domain (415). The remaining two insertion sites were in the intracellular region of the receptor: one position in the intracellular loop connecting the M1M2 transmembrane helices (I6) and the second position within the C-terminal tail (I10). There are several aspects to consider when evaluating the functionality of the fluorescently fused receptors : i) the proper folding of the fluorescent protein, which can be assessed by fluorescence imaging; ii) the proper folding of the receptor, which can be assessed by electrophysiology and fluorescence imaging and iii) the proper maintenance of the kinetic properties of the receptor, which can be addressed by fast perfusion electrophysiology.

Firstly, to test the fluorescence expression of the fusion constructs transfected HEK293 cells were imaged on a confocal microscope (Fig. 11 B). As control the cells were transfected with a WT AMPA receptor plasmid expressing GFP through an IRES domain, to illustrate cytoplasmic staining of the cell. To confirm that the IRES-GFP deleted plasmid lacks any residual fluorescence cells expressing this construct were also imaged (GluA2 WT). To show specific membrane fluorescence a plasmid expressing GFP fused to a truncated k-ras membrane anchor sequence (Wang et al., 2010) was expressed (GFP-tk).

Overall the fluorescence signal from the fusion constructs was robust, but not limited to the plasma membrane, suggesting that the folding of the FP is not disturbed but that part of the labelled receptors are retained intracellularly. Electrophysiological recordings of whole cell currents of the fusion receptors thus provide a more precise readout of AMPAR expression and function.

3.2 Fluorescent insertions in the intracellular region

The structural information on glutamate receptors, and AMPA receptor in particular, has been rapidly expanding in the recent years (see *Introduction 1.2*). Despite the numerous solved structures, little is known about the arrangement of the intracellular domains of AMPA receptors, since these parts of the receptor were either unresolved or truncated. The intracellular region consists of loops connecting the transmembrane helices and the C-trminal tail. To asses the potential dynamic nature of the intracellular domains of the AMPAR, double labelled receptors with a YFP fusion in the M1M2 helix loop and a CFP fusion in the C-terminal domain and single YFP fusions at the two positions were used.

3.2.1 Membrane expression and functionality of AMPA receptors with intracellular fluorescent fusions

To test the functionality of the fluorescent fusion receptors the membrane expression in HEK293 cells was tested electrophysiologically. In a whole lifted cell configuration (see *Materials and methods*) 10 mM glutamate was applied for 100ms and the current was recorded. **Figure 12** shows a summary of whole cell peak currents of receptors with intracellular fusions, GluA2-6Y, -10Y, -6Y10C and -6Y10C S754Q compared to WT. Both the single and double fusion receptors had a similar membrane expression as untagged wild type AMPA receptor (Fig. 12 B). The averages of the absolute peak current values were (in nA, ± SEM): $I_{6Y} = 5.8 \pm 0.7$, n = 14; $I_{10Y} = 4.2 \pm 0.4$, n = 13; $I_{6Y10C} = 7.4 \pm 0.5$, n = 18; $I_{6Y10C\ S754Q} = 5.3 \pm 0.6$, n = 17 and $I_{WT} = 6.6 \pm 0.6$, n = 6. The near wild type expression of the fusion constructs confirms that the receptors containing YFP and CFP at the intracellular positions within the receptor are not hindered in trafficking to cell membrane and form functional tetramers.

Figure 12 Membrane expression of the intracellularly fused receptors A Cartoon representation of the intracellular insertion sites I6 and I10 with a single YFP (yellow), and the double CFP (blue) and YFP fusions. **B** Peak currents from lifted whole cells at –40mV in response to 10mM glutamate. The average values are given in the text.

3.2.2 Kinetic characterisation of AMPA receptors with intracellular fluorescent fusions

Because of the rapid kinetics of the AMPARs, membrane expression of the fusion receptors is not sufficient to confirm full functionality of these molecules. In order to verify that the fluorescently-tagged GluA2 constructs were a good surrogate for AMPARs with normal fast gating, the
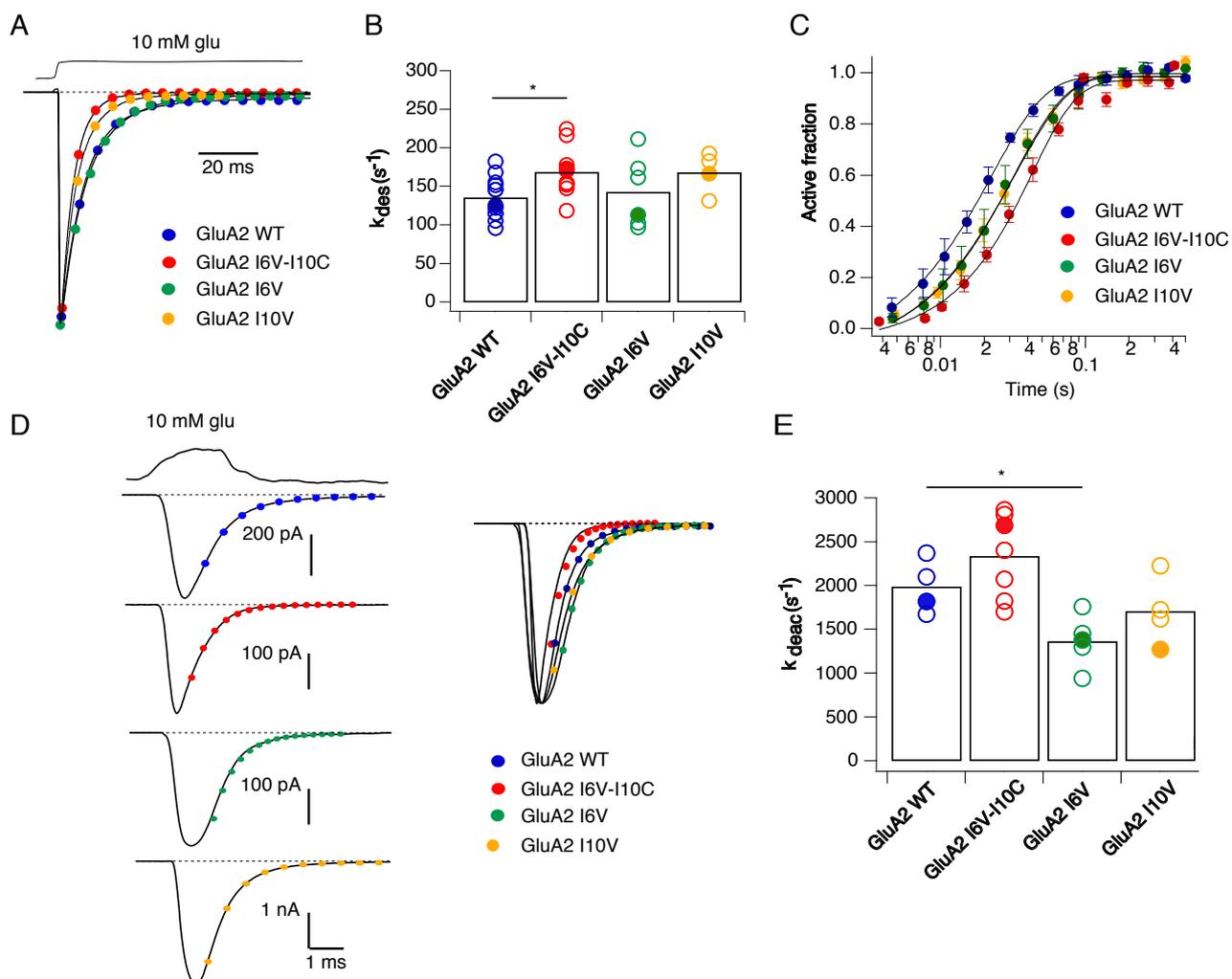
Figure 13 Kinetic characterisation of receptors with fluorescent intracellular fusions A Representative desensitising traces of the fusion receptors during a long (100 ms) pulse of 10 mM glutamate (here $k_{\text{des 6Y-10C}} = 173$ s^{-1}, red ; $k_{\text{des 6Y}} = 113$ s^{-1}, green; $k_{\text{des 10Y}} = 166$ s^{-1}, yellow; and $k_{\text{des WT}} = 122$ s^{-1}, blue). **B** A summary of desensitisation rates. Bars represent the mean. Individual recordings are shown as open circles, closed circles indicate the representative value in *A*. *p<0.05. Mean values are presented in the text. **C** Summary of recovery rates of the fusion receptors (*see Materials and Methods*). Mean values are presented in the text **D** Representative deactivation traces in response to a fast (1 ms) jump into 10 mM glutamate. Here deactivation rates from single exponential fits: $k_{\text{deact 6Y-10C}} = 2688$ s^{-1}, red; $k_{\text{deact 6Y}} = 1380$ s^{-1}, green; $k_{\text{deact 10Y}} = 1270$ s^{-1}, yellow and $k_{\text{deact WT}} = 1820$ s^{-1}, blue. **E** A summary of deactivation rates. Bars represent the mean. Individual recordings are shown as open circles, closed circles indicate the representative value in *D*. *$p < 0.05$. Mean values are presented in the text.

deactivation, desensitization and recovery from desensitization of GluA2-6Y-10C, GluA2-6Y and GluA2-10Y receptors were compared to that of WT GluA2 receptors expressed in HEK cells using fast perfusion patch-clamp electrophysiology. In outside-out patches, both dual fusion (GluA2-6Y-10C) and single fusion (GluA2-6Y and -10Y) receptors had similar kinetic properties to

WT GluA2 (Fig. 13, panels A-E). The desensitization rates of the fusion receptors during a long (100 ms) pulse of 10 mM glutamate ($k_{des\ 6Y\text{-}10C} = 168 \pm 31$ s^{-1}, n = 10; $k_{des\ 6Y} = 143 \pm 18$ s^{-1}, n = 6; $k_{des\ 10Y} = 168 \pm 13$ s^{-1}, n = 4) were close to WT GluA2 desensitization rates ($k_{des\ WT} = 135 \pm 26$ s^{-1}, $n = 12$; Fig. 13, A & B). For GluA2-6Y-10C, the rate of deactivation in response to a short (1 ms) pulse of glutamate ($k_{deact\ 6Y\text{-}10C} = 2300 \pm 230$ s^{-1}, n = 7; $k_{deact\ 6Y} = 1370 \pm 150$ s^{-1}, n = 5; $k_{deact\ 10Y} = 1700 \pm 150$ s^{-1}, n = 4) were likewise similar to that of wild type ($k_{deact\ WT} = 1990 \pm 150$ s^{-1}, $n = 4$). The rates of recovery from desensitization (Fig. 13 C) on the other hand showed that GluA2-6Y-10C recovered slightly slower ($k_{rec\ 6Y\text{-}10C} = 34 \pm 5$ s^{-1}, red, n = 6) than wild type ($k_{rec} = 57 \pm 6$ s^{-1}, blue, n = 5) whereas single fusions were essentially unaffected ($k_{rec\ 6Y} = 48 \pm 8$ s^{-1}, green, n = 6; $k_{rec\ 10Y} = 50 \pm 5$ s^{-1}, yellow, n = 6). In summary, these data show that GluA2 receptors with one or two inserted fluorophores at the I6 and I10 positions have a functional phenotype very similar to WT GluA2 receptors; maintaining fast activation and desensitization with a slightly slowed recovery from desensitization.

Taken together the fluorescence, membrane expression and kinetic characteristic of the fluorescent fusion AMPA receptors suggest that these receptors can be used as optical reporters of structural dynamics within the receptor.

3.2.3 FRET between the M1M2 loop inserted YFP and C-terminally inserted CFP

With functional and fluorescent AMPA receptors it was now possible to address the question of structural dynamics within the intracellular region. To accomplish this Förster resonance energy transfer (FRET) between a donor (CFP) and acceptor (YFP) of the double labelled GluA2 6Y10C was measured. Because of the steep distance dependence of the FRET signal, the donor and acceptor fluorophores have to be located at FRET enabling distances from one another. The R$_0$ of the CFP-YFP pair, the distance at which the FRET signal is at half maximum, is 52 Å (Markwardt et al., 2011).

Figure 14 shows spectra collected from HEK293 cells transfected with the double labelled GluA2 6Y10C receptor. The spectra exhibit a peak in the YFP (acceptor) emission window following CFP (donor) excitation (Fig 14 A, black line) indicating a FRET signal. Cells transfected with a receptor with a single CFP fusion in the C-terminal domain (Fig 14 A, blue line) produced CFP spectra without a YFP peak. To confirm that the FRET signal is located in the YFP emission, spectra were

collected from cells expressing receptors with a single YFP fusion at the M1M2 loop (GluA2 6Y) (Fig. 14 B).

3.2.4 Spectral FRET characterisation of GluA2 6Y10C at steady state

Following the spectral FRET approach (Zheng and Zagotta, 2003) spectra were collected from cells expressing three differently labelled receptors (for detailed explanation see *Introduction 1.6.2*). Cells expressing GluA2 10C were used to obtain the CFP spectra (Fig. 15 A, left panel, dashed blue line). Cells expressing GluA2 6Y were used for measuring the RatioA0 (Fig. 15 A, right panel and B). Cells expressing GluA2 6Y10C produced the spectra with a peak in both CFP and YFP emission range (Fig. 15 A, left panel, black line). To separate the YFP emission produced by CFP excitation the CFP spectra were subtracted (Fig. 15, left panel, solid blue line). RatioA was obtained by normalising the separated YFP spectra to YFP emission spectra from direct excitation at 514nm (Fig. 15 B). RatioA0 describes the direct excitation component and is obtained by normalising the direct excitation spectra (Fig 15 A, right panel, blue line) to the total acceptor emission (Fig 15 A, right panel, yellow line) of the control sample expressing only YFP fused receptors. Because the YFP emission is a mixture between a FRET signal and a direct excitation of YFP by the 445 nm
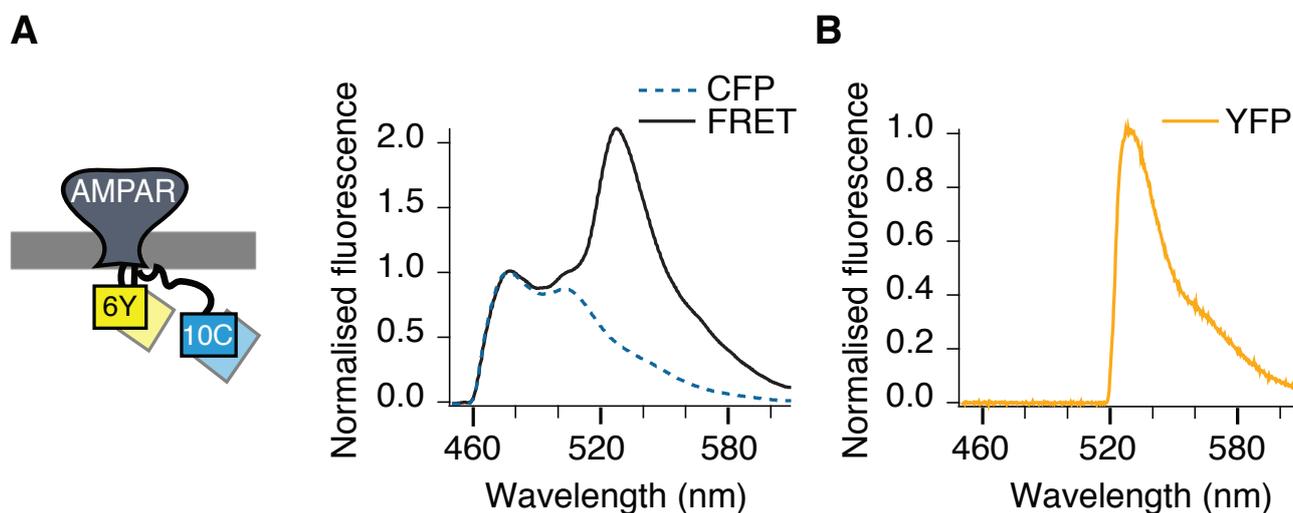
Figure 14 Spectral characterisation of GluA2 6Y10C receptor A A cartoon representation of the fluorescent fusions within the intracellular region of the AMPA receptor. YFP is inserted in the M1M2 transmembrane helix loop and the CFP is inserted into the C-terminal domain. **B** Spectra collected from HEK293 cells expressing GluA2 Y10C construct following excitation at 445 nm (black line) and from cells expressing GluA2 10C construct (dashed blue line). **C** Spectra collected from cells expressing GluA2 6Y construct fallowing excitation at 514 nm.

laser line, the quantitative measure of the FRET can be achieved by normalising the two ratios (RatioA and RatioA0) (Fig 15 B). For the GluA2 6Y10C construct the average RatioA was 1.4 ± 0.03, n = 9 and the average RatioA0 was measured to be 0.27 ± 0.02, n = 6.

FRET ratio and subsequent FRET efficiencies were calculated as described (*Materials and methods)* for each recorded cell and translated into distances using an IgorPro procedure written in house (see **Appendix A3**)*.* In steady state conditions the average FRET efficiency was calculated to be 0.34 ± 0.02, n = 9 (Fig. 15 C). FRET efficiencies calculated for each individual cell were fed into the FRET calculator to extract the corresponding distances. Calculation of distances showed an average separation of the donor and acceptor fluorophore of 58 ± 0.8 Å. The average FRET efficiency was plotted agains the corresponding average distance onto the theoretical FRET efficiency curve, calculated for the CFP – YFP FRET pair with the R_0 = 52 Å (Fig. 15 C, black line).

3.2.5 Extracellular binding produces changes in FRET in the intracellular region

The FRET signal described above was measured at steady state conditions, without any ligand present to activate the receptor. The high sensitivity of a FRET signal to the distance between the donor and acceptor makes the two inserted fluorophores ideal to monitor conformational changes within the intracellular region of the AMPA receptor. To do this the patch clamp fluorometry technique was used on cells expressing the GluA2 6Y10C receptors (Fig. 16 A). Saturating concentration of glutamate was applied to a lifted whole cell and the current was recorded. Concurrently fluorescence was acquired in 100 ms long frames (Fig. 16 B). The excitation was alternated after every episode between donor and acceptor wavelengths and averaged FRET signals of the GluA2 6Y10C were plotted (Fig. 16 C, left panel). To trap the receptor in an active state, the positive allosteric modulator cyclothiazide (CTZ), which blocks receptor desensitisation, was applied continuously with the ringer solution for some minutes before a new recording was made. There was a detectable difference between FRET in the desensitising and non-desensitising conditions (Fig. 16 C, left panel, green vs red lines, n = 8). There was however no change in FRET in response to glutamate. CTZ binds to the AMPAR at the inter-dimer interface between the D1 lobes of the ligand binding domain (Sun et al., 2002). To see if the extracellular binding of the modulator influenced the arrangement of the intracellularly attached donor and acceptor

fluorophores, a double labelled receptor with a mutated CTZ binding site was used (GluA2 6Y10C S754Q (Partin et al., 1996)). The apparent difference in FRET was not visible for this construct,
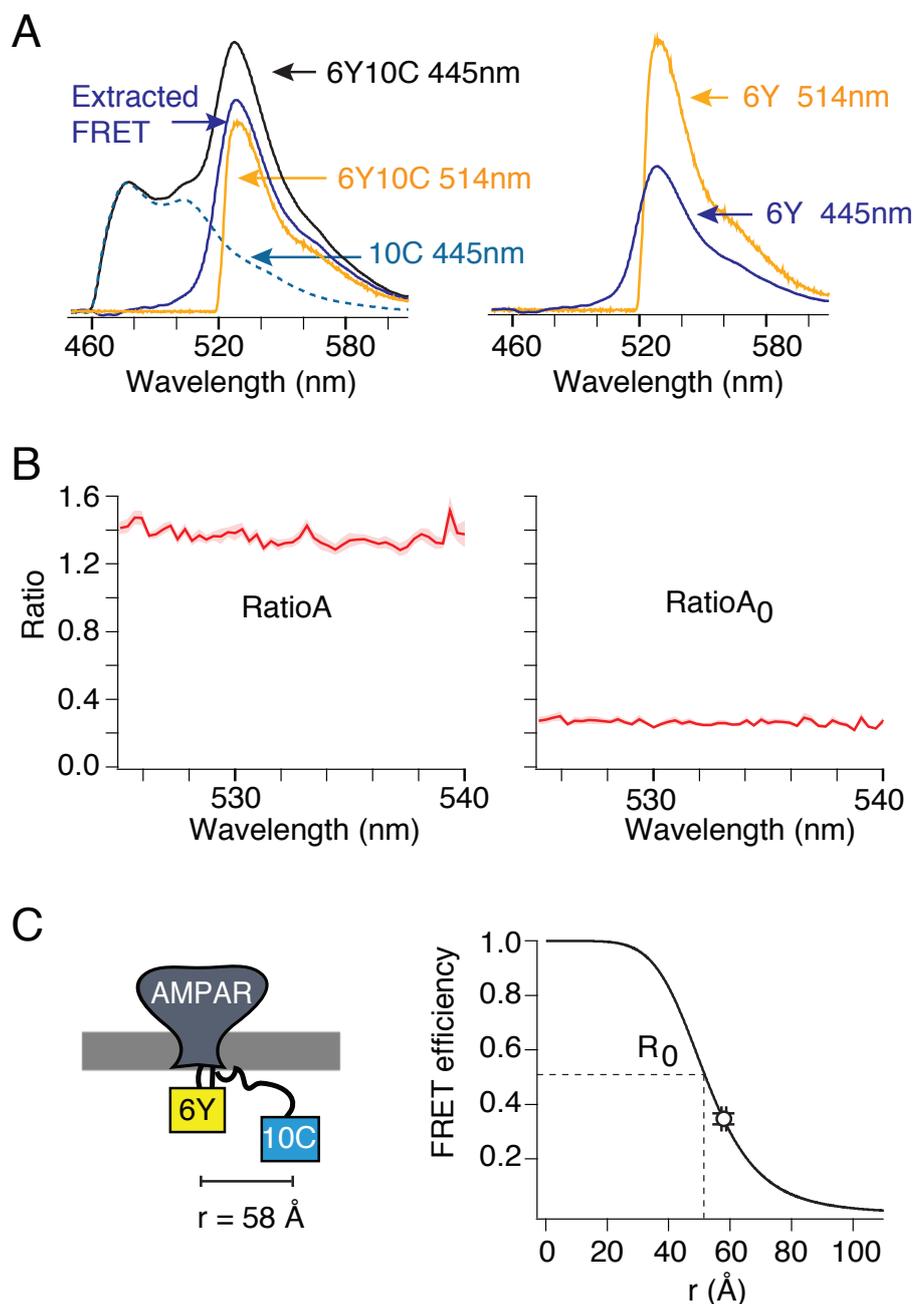
Figure 15 Spectral FRET calculation of GluA2 6Y10C A Representative example of spectra collected from a cell expressing GluA2 6Y10C construct for calculation of RatioA and of GluA2 6Y control for calculation of $RatioA_0$. Dark blue line represents acceptor emission spectra in the FRET channel. **B** Average values of RatioA and $RatioA_0$. Stand error of the mean (SEM) is indicated by the shaded area. **C** Calculated FRET efficiency plotted against the corresponding average distance (r) between CFP and YFP in the GluA2 6Y10C construct (circle). The error bars indicate the SEM values and are presented in the text. Dashed lines show the position of the value of the R_0 for the CFP-YFP FRET pair on the theoretical FRET curve.

suggesting that the CTZ binding is indeed affecting the intracellular regions of the receptor (Fig. 16 C, right panel, n = 5).
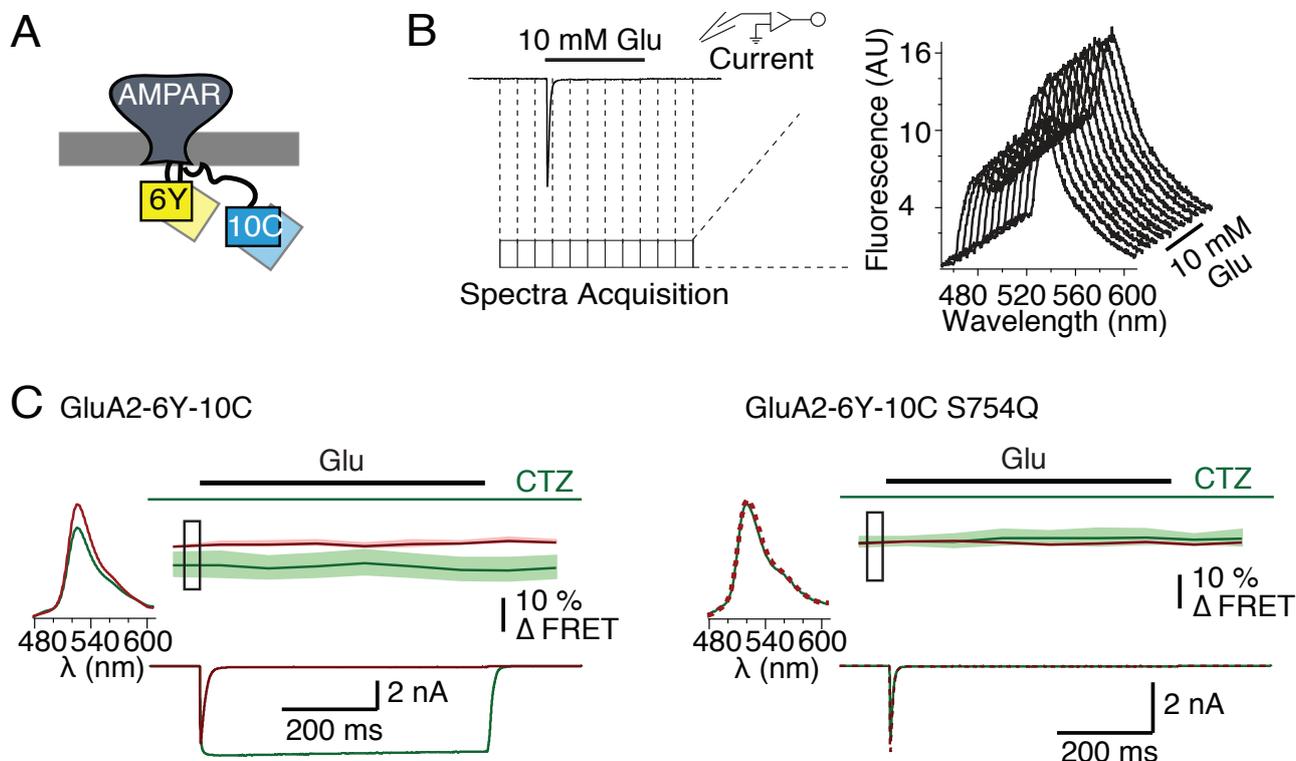
Figure 16 Whole cell patch clamp fluorometry of the GluA2 6Y10C receptors A A schematic representation of the intracellular positions of the FRET pair. **B** Concurrent electrophysiological and optical recording protocol. Fluorescence was acquired in frames of 100 ms length during electrophysiological recording of a lifted whole cell at –60 mV. A train of spectra collected following 445 nm excitation is shown in the insert. Application of glutamate is shown with a bar. **C** Averaged FRET traces, with SEM indicated by pale shading, and representative correlated current traces from cells expressing GluA2 6Y10C, left panel (n = 8) and the corresponding S754Q mutant 6Y10C S754Q, right panel, (n = 5). Traces were recorded in presence and absence of CTZ (green and red traces, respectively). Ratiometric FRET was calculated as described in *Materials & Methods*. The data were normalised on a frame-by-frame basis to the control condition (absence of CTZ) to allow comparison of the equilibrium values.

To measure the direct effect of CTZ binding on the FRET between the M1M2 loop and the C-terminal domain, spectra were collected during a prolonged application of CTZ to a naive cell (Fig. 17). Because the recording could only be done once to monitor the binding of CTZ directly with FRET, the excitation wavelength in this experiment was alternated during the episode (Fig. 17 A).
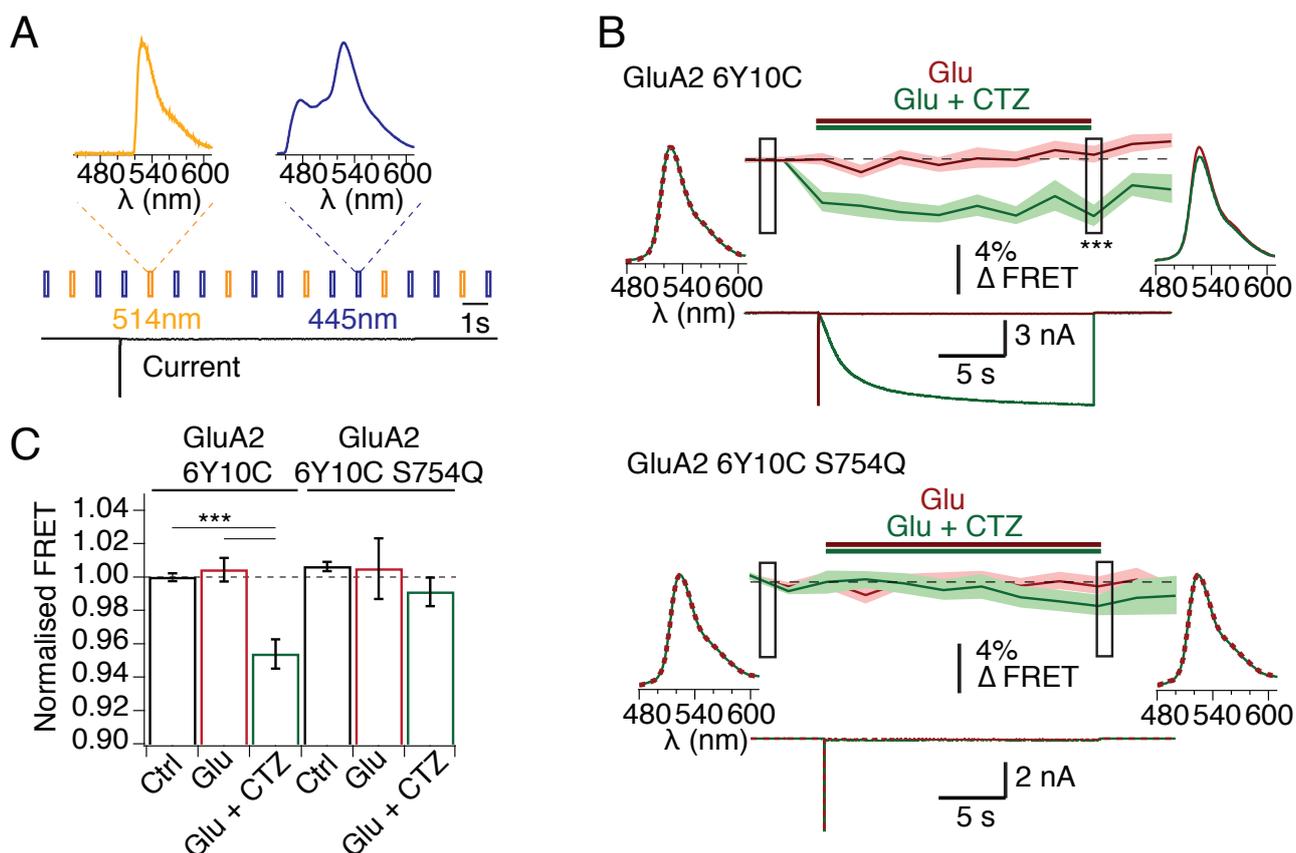
Figure 17 Visualisation of direct binding of CTZ through FRET A Schematic representation of the recording protocol. Spectra of 300 ms were acquired during alternating donor and acceptor excitation during long applications (20 s) of glutamate or glutamate with CTZ. The interval between frames was 1 s. **B** Average spectral FRET recording of GluA2 6Y-10C (*upper panel*) and GluA2 6Y-10C S754Q (*lower panel*) constructs in a total of 18 frames during a prolonged (20 s) exposure to glutamate (red traces) or glutamate and CTZ (green traces). The data were normalised to the baseline before the jump. Boxes indicate point of comparison between the two conditions. Averaged acceptor emission spectra following excitation at 445 nm are shown from the boxed points in the recording. In the upper panel unpaired two-tailed Student's t-test between the green and red trace gave p = 8E-05 for the last sample during CTZ application. **C** Averaged normalised FRET from spectra acquired at resting conditions (control) in presence of glutamate (red) and in presence of glutamate and CTZ (green) at the last frame during application. Error bars represent the SEM values and are presented in the text.

The alteration of excitation wavelength, which requires mechanical switching of the filter cube turret slowed down the frequency of fluorescence recording dramatically (1 s). The FRET ratio values were normalised to the average of the first two frames, recorded in control conditions while the receptor predominantly resides in a resting state. The binding of CTZ can be monitored on the current trace as the gradual block of desensitisation which began to develop 50ms after application (Fig. 17 B, upper panel). The corresponding FRET signal decreased by approximately 4% (p =

8E-05, Fig. 17 B, upper panel) during the application of CTZ as compared to no apparent change in FRET during application of glutamate.

The FRET levels did not return to baseline after the application, consistent with the slow unbinding of CTZ from the receptors. In the mutant receptor GluA2 6Y10C S754Q unable to bind CTZ both the functional effects and FRET change was absent during the same conditions (Fig. 17 B, lower panel). Averaged acceptor emission spectra arising from donor excitation are shown for all conditions (Fig. 17 B). Because the raw emission spectra are not normalised to the direct excitation of YFP in each frame, and are not corrected by RatioA0, the difference between the peaks doesn't fully compare to the calculated FRET difference. The quantified difference in FRET between the last recorded frame during glutamate/glutamate and CTZ application and the the first recorded frame in resting control condition is shown in figure 8C. For GluA2 6Y10C: $FRET_{Norm\ ctrl} = 1 \pm 0.002$; $FRET_{Norm\ Glu} = 1 \pm 0.007$; $FRET_{Norm\ Glu+CTZ} = 0.95 \pm 0.008$, $p = 8E-05$. For the S754Q mutant: $FRET_{Norm\ ctrl} = 1 \pm 0.002$; $FRET_{Norm\ Glu} = 1 \pm 0.02$; $FRET_{Norm\ Glu+CTZ} = 0.99 \pm 0.008$. The slight decrease of the FRET signal of the S754Q mutant in presence of CTZ does not indicate a specific change, as can be seen on the full fluorescence trace, but rather reflects a high variability of the FRET signal.

Application of the inactive D-isomer of glutamate to the double labelled GluA2 6Y10C or the S754Q mutant didn't provoke any changes in FRET (Fig. 18).
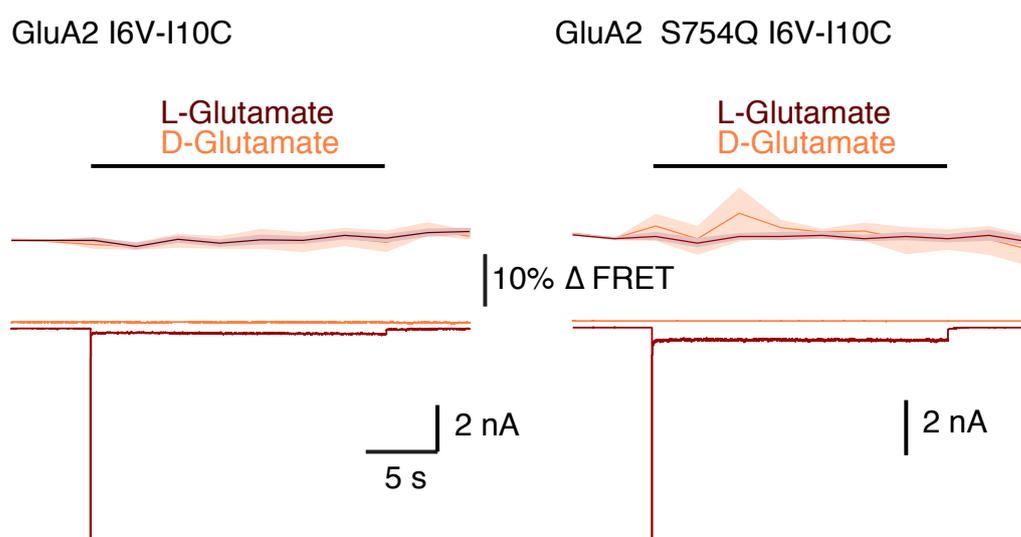
Figure 18 Spectral FRET during application of L- and D-glutamate Average spectral FRET recording of GluA2-6Y-10C (*left panel*) and GluA2-6Y-10C-S754Q (*right panel*) constructs in a total of 18 frames during a prolonged (20 s) exposure to *L*-glutamate (red traces) or *D*-glutamate (orange traces). Shaded area represents the SEM values. Each point of the FRET curve was normalised to the baseline before the jump.

The finding that extracellular binding of CTZ produces a change in FRET in the GluA2 6Y10C construct but fails to evoke any FRET change in the mutant lacking the CTZ binding site, suggest a a link between the arrangement of the intracellular region and extracellular parts of the receptor.

3.2.6 Correlation between the peak current, FRET ratio and the change in FRET

The calculated FRET ratio for the double labelled GluA2 6Y10C constructs in resting state did not correlate with the whole cell peak current $R^2 = 0.05$ (Fig. 19 A, n = 16). This lack of correlation is to be expected, as the distance between the donor and acceptor fluorophores should not be influenced by the amount of receptors present at the cell membrane and because intracellularly retained receptors will inevitably contribute to the overall fluorescence signal. Prolonged application of CTZ to a naïve cell resulted in a measurable decrease of the FRET. This change seemed to correlate moderately with the peak current of the recorded cell. The percentile change in FRET at the last point of CTZ application in the protocol shown in Fig. 12 gave $R^2 = 0.53$ (Fig. 19 B, n = 16). To some extent, this supports the idea that the binding of CTZ influences the
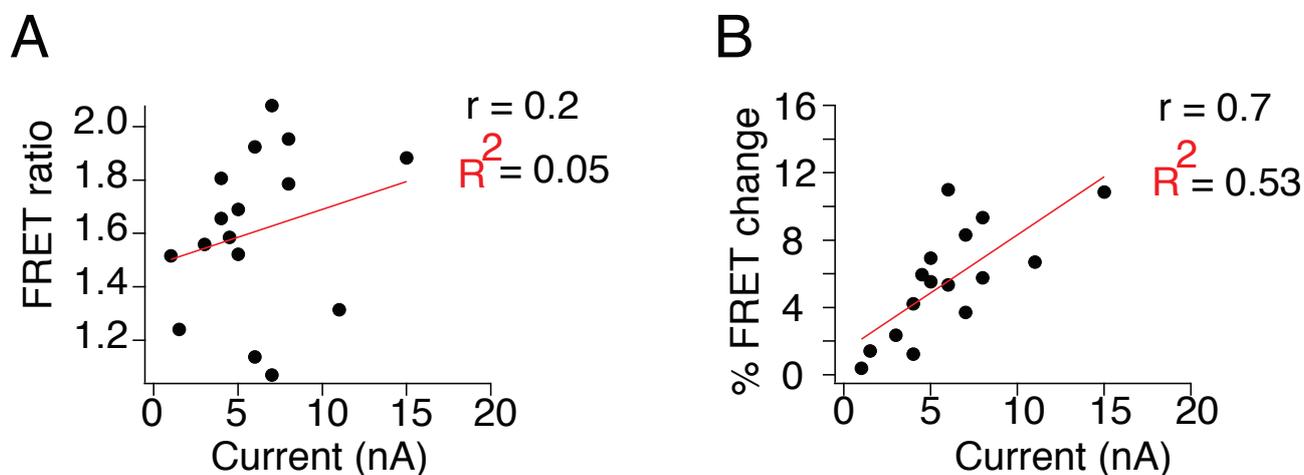
Figure 19 Correlation between whole cell peak current and spectral FRET A Correlation and linear regression analysis of the averaged FRET ratios calculated from cells expressing GluA2 6Y10C construct against the measured whole cell peak current. Linear correlation coefficient r = 0.2 and linear regression $R^2 = 0.05$, n = 16. **B** Correlation and linear regression analysis of the relative FRET change as measured in the last frame during glutamate and CTZ application (Fig. 8B, upper panel) calculated from cells expressing GluA2 6Y10C construct against the measured whole cell peak current. Linear correlation coefficient r = 0.7 and linear regression $R^2 = 0.53$, n = 16.

arrangement of the intracellular donor and acceptor molecules in receptors present at the cell membrane, and does not affect the intracellularly retained AMPARs, optimising the specificity of the signal.

3.2.7 YFP at positions I6 and I10 is quenched by a membrane bound probe

To date, any structural information about the intracellular region of the AMPA receptor is lacking. While the intracellular loops connecting the transmembrane helices are unresolved in every full length crystal structure available so far (Sobolevsky et al., 2009; Dürr et al., 2014; Meyerson et al., 2014; Yelshanskaya et al., 2014; Herguedas et al., 2016), the C-terminal domain is deleted all together. FRET between the M1M2 loop and the C-terminal tail illustrated that the extracellular domains and the intracellular region are dynamically coupled. The connection between receptor function, such as activation and desensitisation, evoked primarily by rearrangements of the extracellular domains, and the dynamics of the intracellular region is, however, still unclear. To address this and to determine the arrangement of the intracellular region, single YFP fusions of AMPA receptors were used. The M1M2 loop insertion (I6) and the C-terminal insertion (I10), were combined with a non-fluorescent membrane bound quencher, dipicrylamine (DPA), in a single component FRET system. Because of spectral overlap between DPA excitation and emission of blue-green FPs, it has previously been used as a component of a voltage sensor (Chanda et al., 2005; DiFranco et al., 2007; Wang et al., 2010) and as a reference point for orthogonal movements of CNG ion channels (Taraska et al., 2007).

To test the single component FRET system, it was necessary to assure that the distances between the donor (YFP) and acceptor (DPA) were sufficient for FRET to occur, taking into consideration that the R_0 of this pair is 31 Å. Initially fluorescence emission of the GluA2 6Y and GluA2 10Y constructs was recorded in lifted whole cells clamped at -40 mV in 5μM DPA. As the DPA is highly voltage sensitive (Fernandez et al., 1983; Chanda et al., 2005a; Chanda et al., 2005b) it preferentially resides in the outer leaflet of the cell membrane at this potential (Fig. 20 A). GluA2 6Y emission spectra showed a large reduction of the peak fluorescence during continuous profusion by DPA (Fig. 20 B), showing that this insertion site is in close enough proximity to the membrane and subsequently to the DPA molecules to be quenched. The GluA2 I10 was likewise quenched by DPA but to a lesser extent (Fig. 20 C) suggesting a more distant position of the C-terminal insertion

relative to the membrane. As controls, emission spectra of membrane bound GFP and YFP (see *Materials and methods*) were recorded in presence and absence of DPA. On average the normalised fluorescence was: $F_{Norm, I6} = 0.41 \pm 0.02$, n = 27; $F_{Norm, I10} = 0.7 \pm 0.02$, n = 18; $F_{Norm, YFP-tk} = 0.5 \pm 0.08$, n = 3, $F_{Norm, GFP-tk} = 0.27 \pm 0.02$, n = 3.
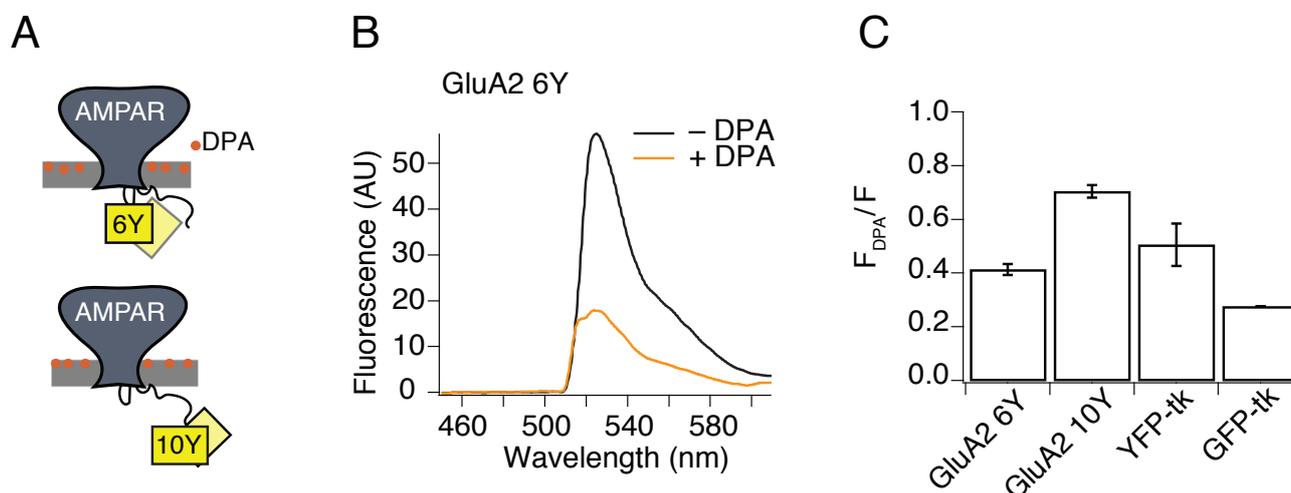
Figure 20 Quenching of YFP at 6Y and 10Y positions by DPA A cartoon representation of the single intracellular YFP insertions into the AMPAR. **B** representative spectra from lifted whole cells expressing GluA2 6Y construct in presence (orange) and absence (black) of 5μM DPA following excitation at 514 nm. **C** Averaged fluorescence in presence of 5μM DPA normalised to total fluorescence in absence of DPA from cells expressing GluA2 6Y, 10Y, YFP-tk and GFP-tk. Error bars represent the SEM values and are presented in the text. The normalised fluorescence values are presented in the text.

3.2.8 State dependent quenching of YFP at positions I6 and I10 by DPA

Taking into account the initial quenching of the YFP at the intracellular positions, spectra were collected at 20Hz from cells expressing GluA2 6Y and 10Y during prolonged (5s) application of glutamate in presence or absence of the desensitisation blocker CTZ. To avoid any artefacts arising from the in-equilibrium of DPA concentration at the cell membrane during fast solution exchange, 5μM DPA was present in both the Ringer buffer and in the glutamate solutions applied to the recorded cell. During receptor desensitisation the relative fluorescence of YFP increased by approximately 11% for I6 and 7% for I10 (Fig. 21 A, red lines). In presence of CTZ, however, a condition trapping the receptor in active state, the fluorescence of YFP decreased by 10% and 6% in

I6 and I10 positions, respectively (Fig. 21 A, green lines). The corresponding currents show the rapid desensitisation and the block thereof in presence of CTZ (Fig. 21 A, red an green lines, respectively, bottom). The onset and recovery of the fluorescence signals generated by long applications were considerably slower than receptor gating kinetics, with following time constants: $\tau_{on\_des\,6Y} = 1.3 \pm 0.2$ s, $\tau_{off\_des\,6Y} = 0.9 \pm 0.03$ s, and $\tau_{on\_des\,10Y} = 1.1 \pm 0.4$ s, $\tau_{off\_des\,10Y} = 1.2 \pm 0.1$ s, for the desensitised state of GluA2-6Y and GluA2-10Y, and $\tau_{on\_act\,6Y} = 1 \pm 0.1$ s, $\tau_{off\_act\,6Y} = 3 \pm 1$ s, and $\tau_{on\_act\,10Y} = 0.7 \pm 0.1$ s, $\tau_{off\_act\,10Y} = 1.6 \pm 0.1$ s, for the active state. Calculated from the average of the last three frames of glutamate application the maximal ΔF/F in the different states was: $\Delta F/F_{des\,I6} = 0.11 \pm 0.02$, n = 11; $\Delta F/F_{act\,I6} = -0.11 \pm 0.02$, n = 9; $\Delta F/F_{des\,I10} = 0.07 \pm 0.01$, n = 6; $\Delta F/F_{act\,I10} = -0.06 \pm 0.02$, n = 8 (Fig. 21 B). The state dependent changes in fluorescence of YFP suggest a difference of the arrangement of the given positions relative to the plasma membrane, a closer proximity during activation and an increase in distance during desensitisation.
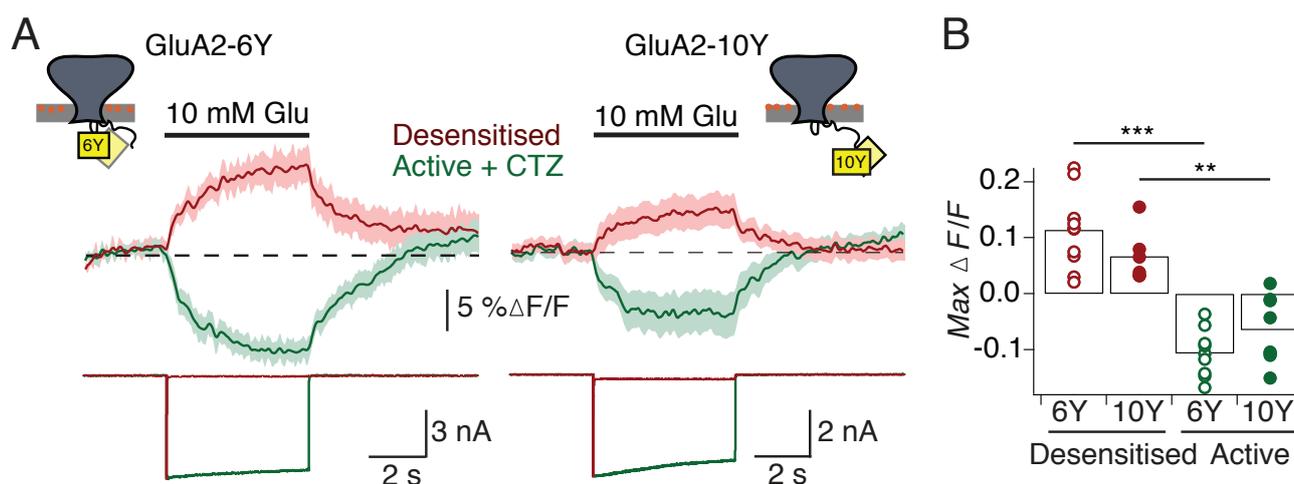
Figure 21 State dependent quenching of YFP at intracellular insertion sites by DPA A Upper panels show averaged peak fluorescence emission of GluA2-6Y (left) and GluA2-10Y (right) recorded at 20 Hz from whole cells during long (5 s) exposures of glutamate (10 mM) in the presence (*green*) and absence (*red*) of CTZ (100 µM). Cells were clamped at –40 mV under constant DPA perfusion. Pale shading indicates the SEM. Lower panels show representative simultaneous current recordings with the same colour scheme. For calculation of *ΔF / F*, see *Materials and Methods*. **B** Summary of maximal changes in the peak of the fluorescence (the average of the final three samples during the glutamate application) in response to a 5 s glutamate application in absence (*red*) and presence (*green*) of CTZ. Changes in fluorescence in absence of CTZ represent receptor transition from resting to the desensitised state, whereas the changes in fluorescence in presence of CTZ represent the transition to the active state. Points indicate responses from individual cells and the bars represent the mean. The mean values are shown in the text.

3.2.9 State dependent quenching of YFP at position I6 follows receptor gating kinetics

Because of the higher relative change in fluorescence the I6 position was chosen for further investigation. To resolve the fluorescence change kinetics the rate of acquisition was increased to 100Hz. Spectra were collected as above, from whole cells expressing the GluA2-6Y receptors. To further ensure that the fluorescence changes were gating specific, sub-saturating concentrations of glutamate (100 µM) were applied. Fast applications of glutamate (100 ms) showed concentration dependent responses of both fluorescence and current in presence of CTZ (Fig. 22 A).
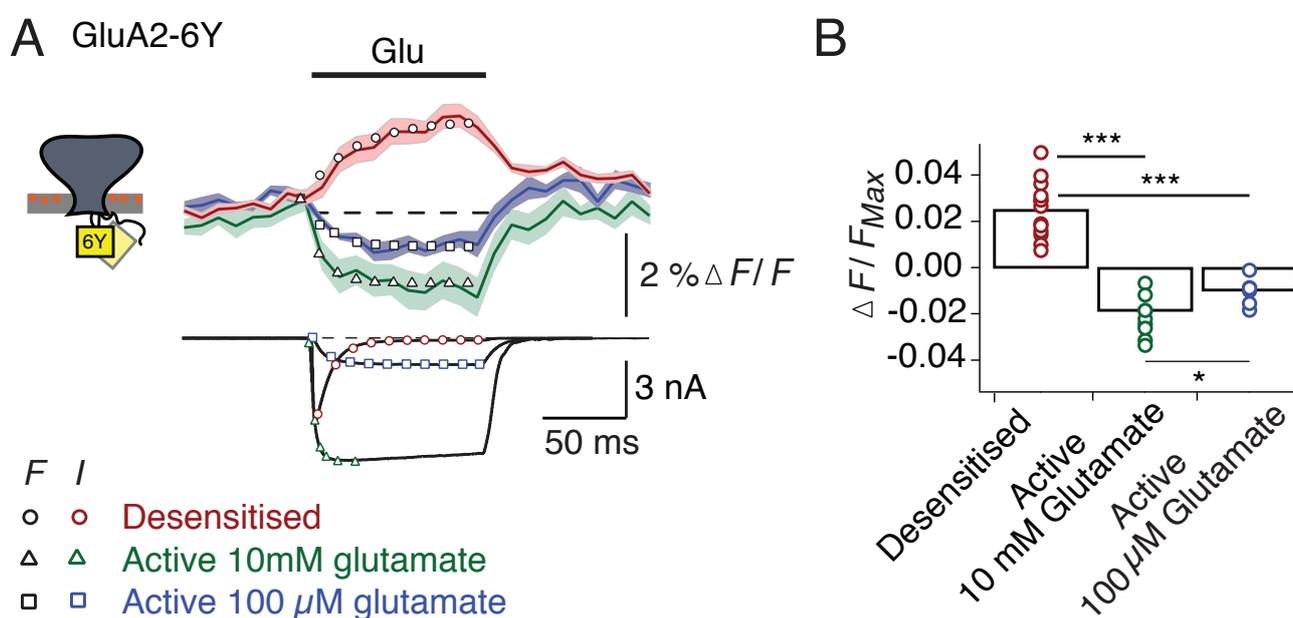
Figure 22 100 Hz recording of GluA2 6Y fluorescence quenching A Fluorescence emission and membrane current from cells expressing GluA2-6Y in presence of DPA, in response to brief (100 ms) stimulus with saturating concentration of glutamate (10 mM) (*red*), saturating concentration of glutamate (10 mM) and CTZ (100 µM) (*green*) and sub-saturating concentration of glutamate (0.1 mM) (*purple*). The fluorescence signal was recorded at 100 Hz. Average fluorescence changes and individual currents were independently fit with single exponentials, yielding the time constants for fluorescence (black geometrical figures) and for current (coloured geometrical figures) presented in the text. **B** Summary of the maximum change in fluorescence during fast fluorescence acquisition. The maximum normalised fluorescence change, $[\Delta F / F]_{Max}$ was calculated from the average peak intensity of the 3 final frames during the glutamate application in all three conditions. Points indicate responses from individual cells and the bars represent the SEM. The mean values are shown in the text.

Application of sub-saturating concentrations of glutamate in presence of CTZ gave rise to a decreasing fluorescence response which developed with $\tau_{F,\ act}$ = 13 ms, corresponding to the current activated with τ_{act} = 8.5 ms (Fig. 22 A; *black vs purple squares*). Saturating concentrations of glutamate (10 mM) evoked fluorescence signals which developed with $\tau_{F,\ act}$ = 10 ms, compared to the time constant for current onset τ_{act} = 3.5 ms (Fig. 22 A; *black vs green triangles*). Under desensitising conditions the time constant for fluorescence signal onset was $\tau_{F,des}$ = 29 ms, considerably slower than the rate of desensitisation τ_{des} = 9.4 ms (Fig. 22 A; *black vs red circles*). This discrepancy could be attributed to the fluorescence signal in desensitised conditions containing a mixture of both activation and desensitisation, slowing down the onset. In figure 16 B the maximum normalised fluorescence change, $[\Delta F / F]_{Max}$, was calculated from the average peak intensity of the 3 final frames during the glutamate application in all three conditions. $[\Delta F / F]_{Max}$ (desensitised, red circles) = 0.025 ± 0.003, n = 13, p = 1.8E-09 (red vs. green circles) and p = 8.9E-08 (red vs. purple circles); $[\Delta F / F]_{Max}$ (Active, 10mM, green circles) = -0.021 ± 0.003, n = 9, p = 0.006 (green vs. purple circles); $[\Delta F / F]_{Max}$ (Active, 100 µM, purple circles) = 0.009 ± 0.002, n = 6. With the kinetics of the fluorescence signal similar to those of receptor gating, the measurements show that the M1M2 loop undergoes conformational changes during receptor activation and desensitisation. It is also conceivable that a conformation in desensitised state, different to resting state, exists for the intracellular loop.

3.2.10 Quenching of YFP in intracellular positions is voltage sensitive

The DPA molecules, due to their negative charge, are highly voltage sensitive (Chanda et al., 2005). This characteristic has been exploited in development of genetically encoded voltage sensors, with changes in fluorescence intensity of a fluorescent protein as the sensor readout (Chanda et al., 2005; Wang et al., 2010). Depending on the potential, the DPA will be distributed either in outer or the inner leaflet of the membrane (Fig. 23 A). The transition of the DPA between the membrane leaflets in response to voltage changes will result in a distance change between the donor and acceptor in a single component FRET system. To see if applications of different voltages to a lifted whole cell expressing single intracellular YFP fusion had any effect on YFP quenching, voltage ramps from -120 mV to 120mV were introduced to the recording protocols. Spectra were acquired before, during and after the ramp (Fig. 23 B). As expected, the YFP fluorescence at I6 position was voltage
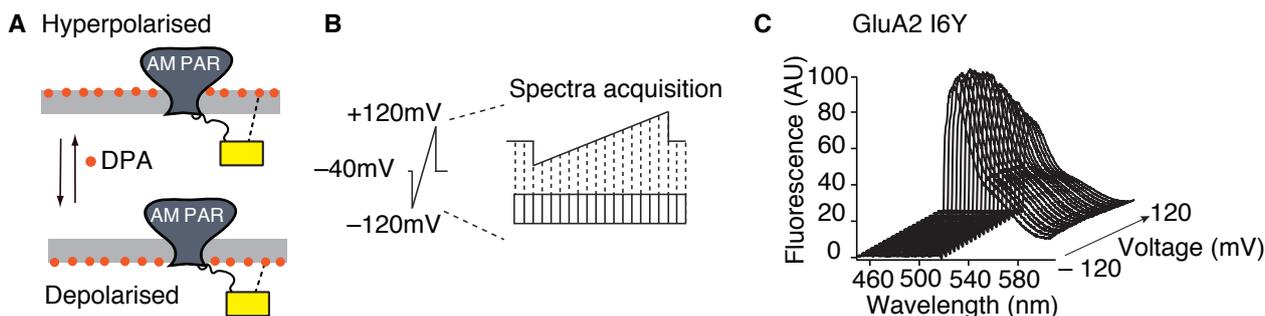
Figure 23 Voltage sensitive quenching of intracellular YFP insertions by DPA A A schematic representation of voltage dependent DPA distribution in the plasma membrane. **B** An example voltage ramp inserted into a recording protocol with simultaneous collection of spectra in 50 ms frames. **C** A representative train of spectra collected during a voltage ramp ranging from −120 to 120 mV from cells expressing GluA2 6Y.

dependent, showing how switching to positive potentials shifts the acceptor (DPA) closer to the donor (YFP) (Fig. 23 C).

3.2.11 Voltage dependence of I6 and I10 positions in different receptor states

Because of the state dependent fluorescence changes of the intracellular insertions, the voltage sensitivity of DPA could be used to pinpoint the positions of the insertions relative to the membrane. The quenching of YFP in each insertion site would depend on the R_0 of the donor-acceptor pair (31 and 37 Å for YFP and GFP, respectively) and on the distance of the probe to the membrane. To test this hypothesis voltage ramps were positioned within a recording protocol to coincide with receptor resting (orange), desensitised (red) and active (green) states (Fig. 24 A). Spectra were collected from cells expressing GluA2 I6Y and I10Y constructs during long (5s) applications of glutamate in presence (active state) and absence (desensitised state) of CTZ. The fluorescence in each distinct state was normalised to that at -40mV (the holding voltage of the cell). To avoid any hysteresis effects arising from the depletion of DPA from the membrane, the ramps were run in both directions and the responses were averaged. The curves showed that the extent as well as the initial degree of quenching were state dependent and differed slightly between the two insertion sites (Fig. 24 B).
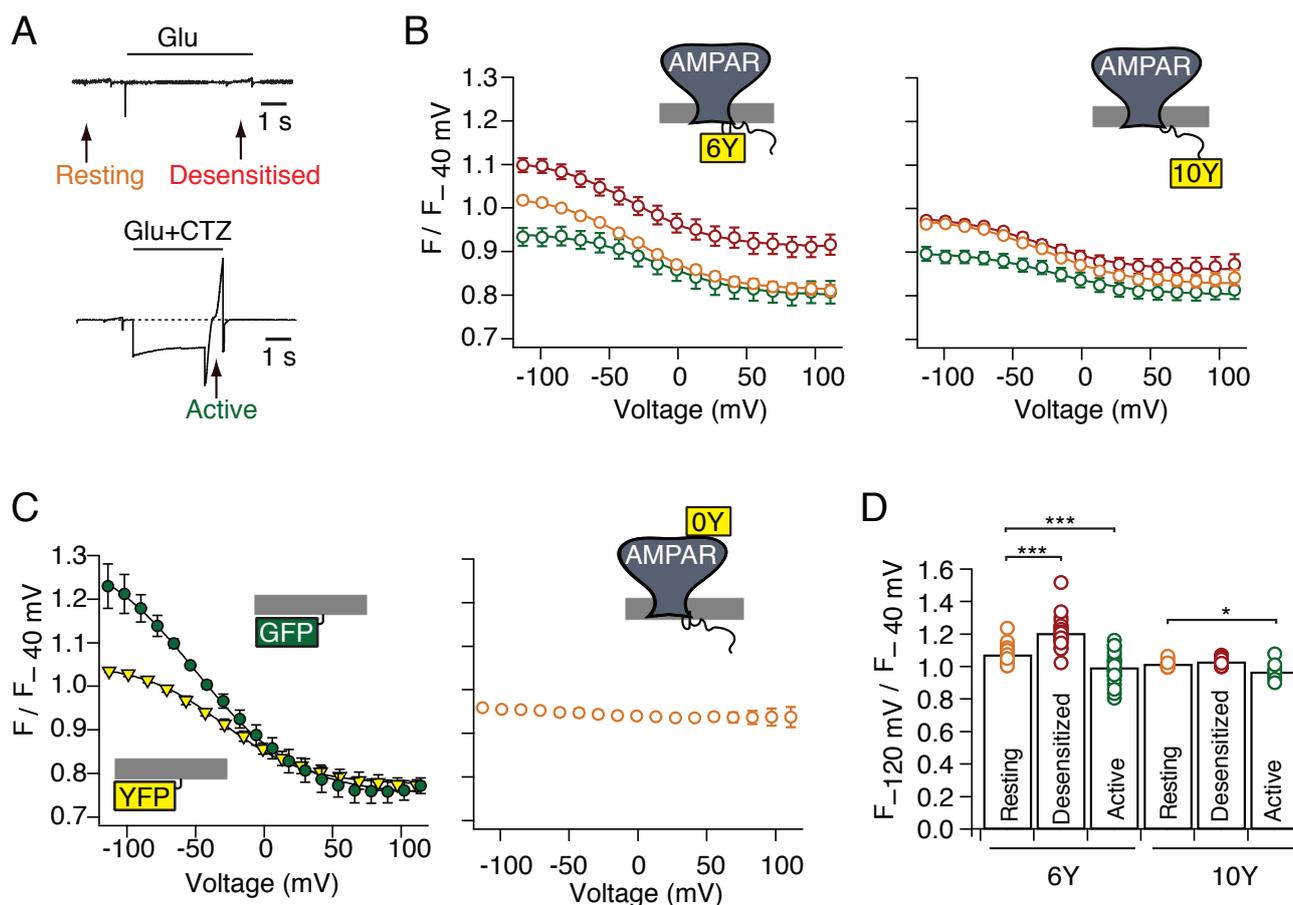
Figure 24 Voltage driven state dependent quenching of GluA2 6Y and 10Y A A schematic representation of the protocol with incorporated voltage ramps used to drive DPA translocation across the membrane. The ramps were timed to trap the receptor in the resting state (before glutamate jump, orange), desensitised state (at the end of 5s application of glutamate, red) and active state (at the end of 5s application of glutamate in presence of CTZ, green). **B** Quenching of fluorescence of GluA2 6Y (*left panel*) and GluA2 10Y (*right panel*) in resting (*orange circles*), desensitised (*red circles*) and active (*green circles*) states. The acquired spectra were normalised to the fluorescence at –40mV in resting state. To eliminate hysteresis effects, data points are the average of responses to negative and positive-going ramps. Lines represent weighted sigmoid fits. **C** Voltage-dependent quenching of membrane bound GFP (green circles) and YFP (yellow triangles). **D** Summary of quenching at the hyperpolarising limit, normalised to quenching at –40 mV for GluA2 6Y and 10Y. Unpaired two-tailed student's t-test gave p = 9.6E-9 for 6Y, desensitised vs resting; p = 0.001 for 6Y, active vs resting; For 10Y, p = 0.008, active vs resting.

The degree of quenching at -120mV relative to holding potential (Fig. 24 C) was for the two insertion sites: $[F_{-120mV}/F_{-40mV}]_{rest\ I6}$ = 1.07 ± 0.009, n = 29; $[F_{-120mV}/F_{-40mV}]_{des\ I6}$ = 1.20 ± 0.02, n = 29, p = 4.5E-09 (orange vs. red circles); $[F_{-120mV}/F_{-40mV}]_{act\ I6}$ = 0.99 ± 0.02, n = 23, p = 0.001 (orange vs. green circles); $[F_{-120mV}/F_{-40mV}]_{rest\ I10}$ = 1.02 ± 0.006, n = 12; $[F_{-120mV}/F_{-40mV}]_{des\ I10}$ = 1.03 ± 0.008, n = 12, p = 0.18 (orange vs. red circles); $[F_{-120mV}/F_{-40mV}]_{act\ I10}$ = 0.97 ± 0.02, n = 10, p = 0.02 (orange vs. green circles). These differences confirm the state dependent arrangement of the

YFP in the two insertion sites. As the DPA is shifted further from the YFP as compared to the equilibrium at holding potential, the relative dequenching of YFP is different for each state. These measurement further confirm the tighter arrangement of the two insertion sites relative to the membrane in active state and a looser arrangement in desensitised state. Spectra from cells expressing membrane anchored YFP and GFP (see *Materials and methods*) showed similar quenching responses to voltage in presence of DPA (Fig. 24 D). Voltage ramps to cells expressing an extracellularly fused AMPA receptor, with a YFP at the N-terminal, did not elicit any voltage-dependent response (Fig. 24 D, right panel). Because the distance between the probe and the membrane (app. 100 Å) exceeds the R_0 of the donor-acceptor pair, no interaction between DPA and YFP was expected.

The half quenching voltage V_{Q50} and the maximal voltage dependent change in fluorescence ΔF were read of the curves and plotted for each state. The values for the half quenching voltage (Fig. 25 A) of the different states of the I6 insertion site were: $V_{Q50\,rest\,I6}$ = -35.1 ± 2.4 mV, n = 29; $V_{Q50\,des\,I6}$ = -51 ± 4 mV, n = 29, $p_{des\,vs\,rest}$ = 7.25E-04; $V_{Q50\,act\,I6}$ = -37 ± 3 mV, n = 23, $p_{act\,vs\,des}$ = 0.006, $p_{act\,vs\,rest}$ = 0.7. The half quenching voltages of the I10 insertion site were: $V_{Q50\,rest\,I10}$ = -30 ± 3 mV, n = 12; $V_{Q50\,des\,I10}$ = -35 ± 3 mV, n = 12, $p_{des\,vs\,rest}$ = 0.2; $V_{Q50\,act\,I10}$ = -21 ± 3 mV, n = 10, $p_{act\,vs\,rest}$ = 0.03, $p_{act\,vs\,des}$ = 0.004. The half quenching voltages for the membrane anchored GFP and YFP were: $V_{Q50\,GFP\text{-}tk}$ = -47 ± 7 mV, n = 5; $V_{Q50\,YFP\text{-}tk}$ = -29 ± 4 mV, n = 8. The difference in the quenching profile of the the two membrane bound control probes was likely due the difference in the R_0 (31 and 37 Å, for YFP and GFP, respectively). The half quenching voltages of the I10 and I6 insertion sites were similar to the ones obtained for the membrane bound YFP. Because of the shallowness of the quenching curves, likely due to the limited portion of the electric field travelled by the DPA molecules (0.6) (Fernandez), the values for V_{Q50} could not be used for determining precise state dependent distances of the probes from the membrane. The increasing V_{Q50} values of the YFP at position I10 suggest that overall the C-terminal tail must be further away from the membrane, as compared to the M1M2 loop. This is also emphasised by the fact that the maximal translocation of DPA molecules across the membrane, that is the shift in equilibrium, occurs at -15 mV (Fernandez et al., 1983) close to the values obtained for the I10 position.

A more reliable measure of the state dependent positions of the two insertion sites from the membrane was the maximal quenching occurring between –120 and 120 mV (Fig. 25 B). The values of ΔF_{Max} were gathered from individual sigmoid fits to the normalised quenching curves

presented in Fig. 24 B. For the GluA2 6Y expressing cells the extent of quenching following a voltage ramp was: $[\Delta F_{Max}]_{6Y\ rest} = 0.22 \pm 0.01$, n = 29; $[\Delta F_{Max}]_{6Y\ des} = 0.2 \pm 0.02$, n = 29; $[\Delta F_{Max}]_{6Y\ act} = 0.14 \pm 0.02$, n = 23. For the GluA2 10Y expressing cells the extent of quenching following a voltage ramp was: $[\Delta F_{Max}]10_{Y\ rest} = 0.15 \pm 0.008$, n = 12; $[\Delta F_{Max}]10_{Y\ des} = 0.12 \pm 0.01$, n = 12; $[\Delta F_{Max}]10_{Y\ act} = 0.09 \pm 0.01$, n = 10. The extents of quenching of membrane bound YFP and GFP were: $[\Delta F_{Max}]_{YFP-tk} = 0.27 \pm 0.01$, n = 8; $[\Delta F_{Max}]_{YFP-tk} = 0.56 \pm 0.09$, n = 5.

Surprisingly, the active states of both GluA2 6Y and 10Y shows a lower extent of quenching, compared to resting and desensitised states.
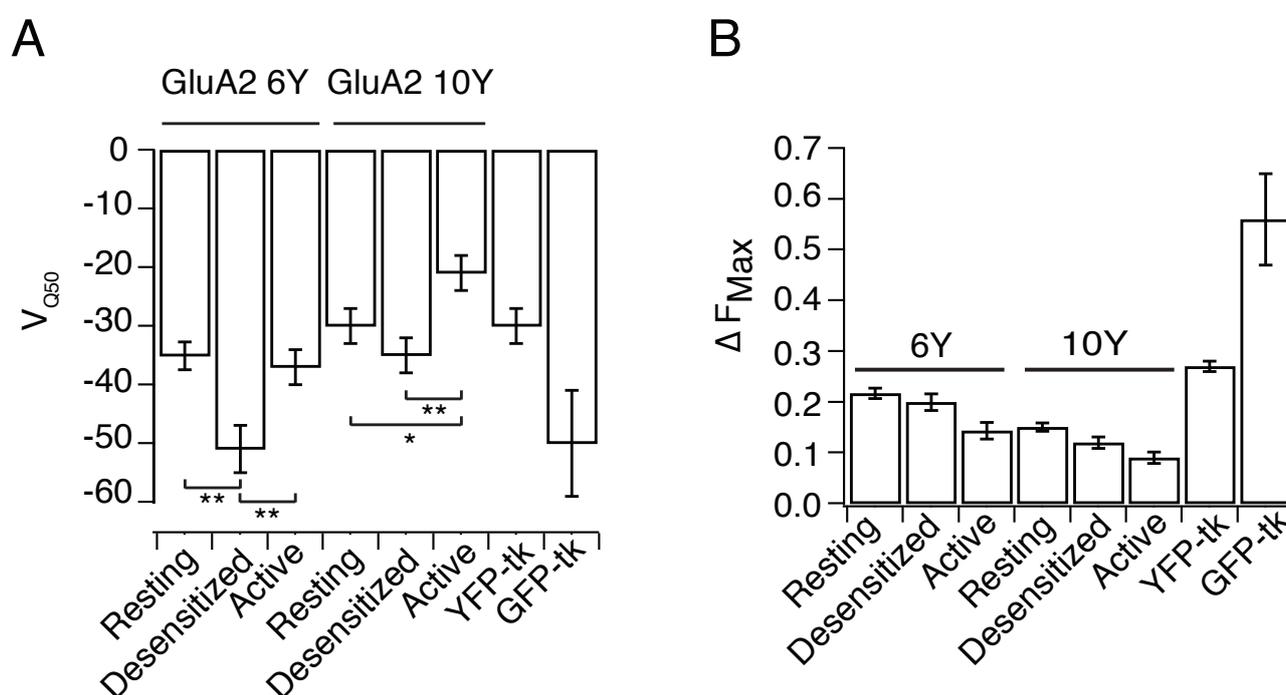
Figure 25 Measurement of half quenching voltage and extent of quenching for GluA2 6Y and 10Y A . Summary of half-maximal quenching voltages. Cells expressing either GluA2 6Y or GluA2 10Y fusions, or the membrane-tethered GFP or YFP were exposed to 5 μM DPA, and the membrane potential was ramped from –120 mV to +120 mV. The values are presented in the text. *$p < 0.05$, ** $p < 0.01$. **B** Summary of extent of quenching for the I6 and I10 positions in the different functional states compared to membrane bound YFP-tk and GFP-tk. The curve for the control position I0 was subtracted from all the quenching curves prior to fitting to a sigmoid function.

3.2.12 Distance determination of YFP in the intracellular insertion sites relative to the membrane

In an infinitely depolarised membrane DPA preferentially resides in the inner leaflet (Fig. 23 A). In this condition the donor fluorescence will reduce in a saturating manner before the FP is hindered by its size from further approach towards the membrane. At infinite negative membrane potentials DPA will be restricted to the outer leaflet (25 Å further away from the donor, compared to depolarised condition). In this situation, quenching only develops at closer FP distances, and cannot saturate. Closely following derivations described in Wang et al., 2010, the probability of quenching of a donor was calculated for a range of distances in both depolarising (Fig. 26 B, blue line) and hyperpolarising (Fig. 26 B, pink line) conditions (see *Materials and methods*). Based on the theoretical curves, which assume DPA to be a plane of acceptors, the predicted voltage-dependent ΔF is bell-shaped and peaks around 25Å from the membrane (Fig. 26 B, dashed line). Because the absolute scales of fluorescence, or of the background, are not known, the theoretical fluorescence intensity curves were corrected as described previously (Zachariassen, Katchan et al., 2016). For the the GluA2 I6Y insertion 69 % of background correction and a scaling factor of 1.15 was applied (Fig. 26 C). For the C-terminal GluA2 I10Y insertion a background of 80 % was subtracted from the theoretical curves (Fig. 26 C). Fluorescence intensity of each position in three different (resting (orange), desensitised (red) and active (green) states was read of off the voltage-dependent quenching curves (Fig. 24 B) and plotted onto the theoretical background-subtracted hyperpolarised curves (Fig. 26 C and D, open circles). Plotting the corresponding ΔF values (Fig. 25 B) onto the curve describing the predicted voltage-dependent change (from hyperpolarising to depolarising voltages) allowed us to read off the state dependent distances of the insertion sites relative to the membrane (Fig. 26 C and D, filled circles). The bell-shaped curve of the predicted ΔF shows that the measured values of ΔF in active and desensitised states lye on different sides of the peak, explaining why these values are smaller than those measured in resting state. According to the predicted ΔF curve, the distance between the YFP in position I6 and the membrane was 25 Å in resting state, 32 Å in desensitised state and 13 Å in active state. YFP in the C-terminal I10 position was separated from the membrane by 32 Å in resting state, 37 Å in desensitised state and 14 Å in active state.
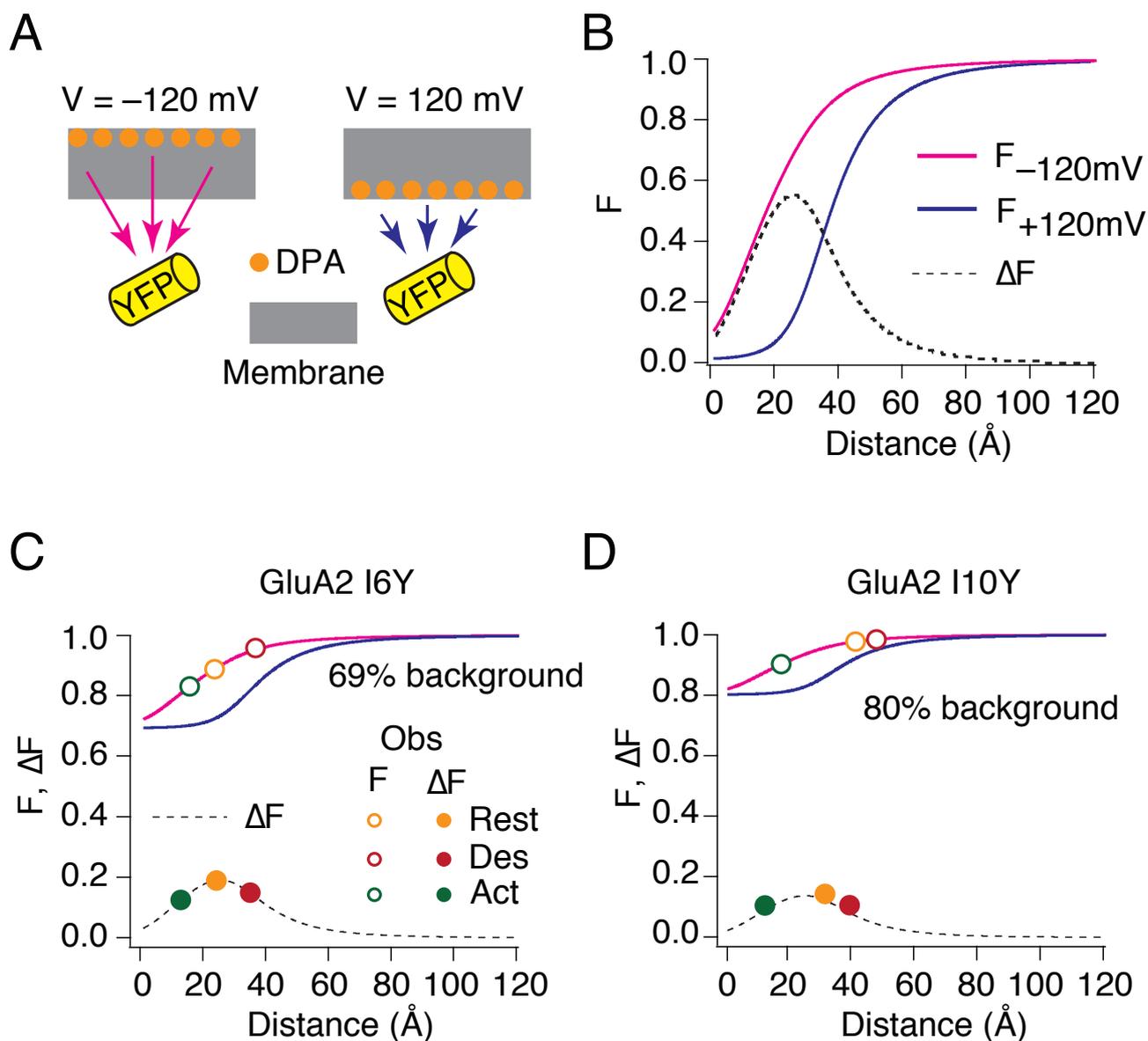
Figure 26 Determination of positions of the I6 and i10 fluorophores relative to the membrane A Cartoon of YFP quenching by a plane of DPA molecules residing in either the outer leaflet of the membrane at negative potentials or in the inner leaflet of the membrane at positive potentials. **B** Theoretical curves of the fluorescence intensity in the depolarising (blue) and hyperpolarising (pink) conditions. Donor quenching will saturate at positive membrane potentials, but not at negative potentials, due to the thickness of the membrane and the size of the fluorophore. This produces the hump in the predicted ΔF curve (the difference in fluorescence at positive and negative extremes of voltages). **C** and **D** Background subtracted curves with the same colour scheme for the two membrane voltages are shown for GluA2 I6Y and I10Y constructs. The observed F (at negative membrane potentials, open circles) and ΔF(closed circles) are plotted onto the corresponding theoretical curves in order to extract the distances of the fluorophores relative to the membrane in the different states.

73

Figure 27 shows a summarising cartoon of the membrane-relative positions of the intracellular I6 (yellow) and I10 (blue) insertion sites during the functional transitions of the receptor from its resting (orange) to active (green) and finally desensitised (red) states. A minimal change in the lateral separation of about 58 Å between the two positions is assumed, based on the lack of gating specific FRET change between YFP in I6 and CFP in I10.
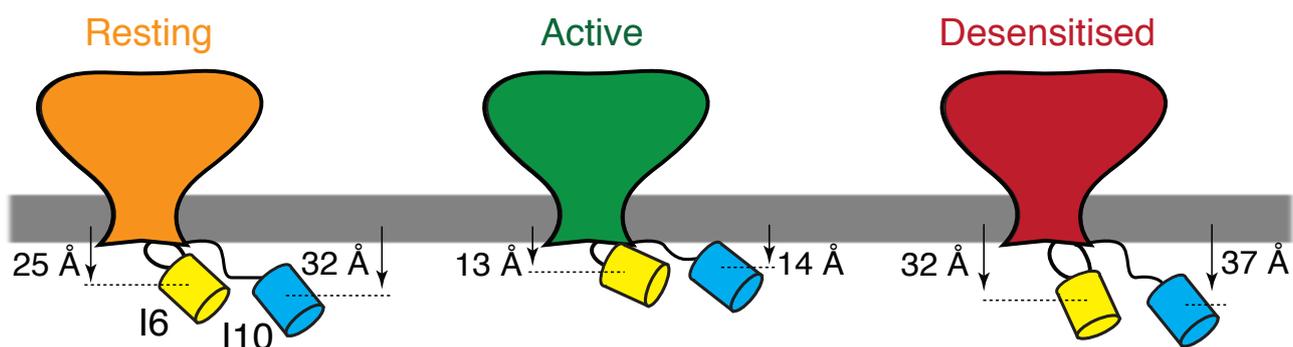
Figure 27 State dependent positions of the intracellular insertion sites A summarising cartoon of the I6 (yellow) and I10 (blue) insertion sites in resting (orange), active (green) and desensitised (red) states of the receptor.

3.3 Extracellular domains

The driving force for AMPA receptor activation is generated by structural rearrangements of the extracellular ligand binding domains. Here, the binding of neurotransmitter is translated into the motions necessary for the opening of ion channel pore and rapid activation of the receptor. It is also on the level of the extracellular domains that the rearrangements leading to receptor desensitisation and deactivation occur. The many structural studies have provided information on the arrangement of the distinct domain layers in the tetrameric receptor in a number of states (see *Introduction 1.2*). Because the structures capture a snapshot of the receptor in a given state, the dynamic nature of the receptor is not addressed. To measure the conformational changes that accompany the receptor transitions between its functional states we used various fluorescence approaches in combination with simultaneous electrophysiological recordings. AMPA receptors with genetically fused fluorescent proteins at various sites throughout the extracellular domains were used to assess both lateral and orthogonal motions of these regions. Additionally, the fluorescently labelled receptors allowed direct measurement of complex formation between the AMPA receptors and the transmembrane AMPAR regulatory proteins (TARPs) and enabled detection of complex dynamics.

3.3.1 Membrane expression and functionality of AMPA receptors with extracellular fluorescent fusions is dependent on fluorescent protein variant and insertion site

Confocal images of HEK293 cells expressing GFP at the various insertion sites in the extracellular domains are shown in Figure 5. To test the membrane expression of AMPA receptors fused to different fluorescent protein variants within the extracellular domains, currents were recorded from lifted HEK293 cells expressing either YFP, CFP, GFP or mTag-RFP-T (denoted as RFP for simplicity) at positions 271, 383 and 391 (Fig. 28). The insertions sites are indicated by magenta spheres in a single AMPA receptor subunit and include a position within the amino terminal domain (271) and two positions within the the linker connecting the ATD to the ligand binding domain (383 and 391) (Fig. 28 A). The membrane expression depended on both the insertion site and the fluorescent protein used (Fig. 28 B). Fusion of the red fluorescent protein (mTagRFP-T) did not produce any visible fluorescence (data not shown) or currents (Fig. 28 B). This can be due to the different origin of the fluorescent protein (Merzlyak et al., 2007) and its distinct folding properties,

which don't allow the inline fusion of the FP within a sequence of another protein. Whole cell peak currents were for position 271(in nA): $I_{Peak\ YFP} = 0.1 \pm 0.1$, n = 2; $I_{Peak\ GFP} = 0.6 \pm 0.3$, n = 4. For position 383, which overall showed higher tolerance of fluorescent protein insertion, the peak currents were (in nA): $I_{Peak\ YFP} = 5 \pm 0.4$, n = 11; $I_{Peak\ CFP} = 5 \pm 0.6$, n = 4; $I_{Peak\ GFP} = 3 \pm 0.4$, n = 8; $I_{Peak\ RFP} = 0$, n =3. Cells expressing fluorescent proteins fused in position 391 at the bottom of the ATD-LBD linker produced following whole cell currents (in nA): $I_{Peak\ YFP} = 8 \pm 0.5$, n = 11; $I_{Peak\ CFP} = 4 \pm 0.3$, n = 3; $I_{Peak\ GFP} = 5 \pm 0.3$, n = 16; $I_{Peak\ RFP} = 0$, n = 3. Despite a fluorescence signal (Fig. 11 B) fusion of either YFP or GFP in position 271 produced whole cell currents notably lower than the other insertion sites. This indicates that the insertion within the ATD, although accommodating for
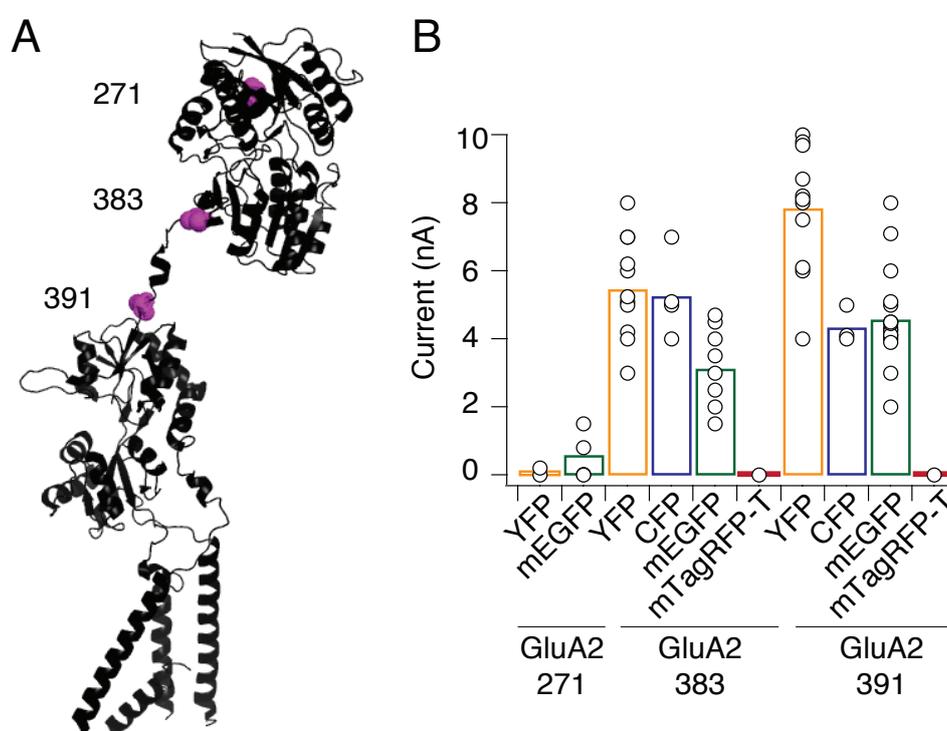
Figure 28 Functional expression of the AMPA receptors with extracellular insertions of different fluorescent protein variants A The structure of a single AMPA receptor subunit with the extracellular fluorescent protein insertion sites indicated in magenta spheres. **B** A summary of whole cell peak currents from cells expressing AMPA receptors with Venus (YFP, yellow), mCerulean3 (CFP, blue), mEGFP (green) and mTagRFP-T (red) inserted in either the 271, 383 or 391 positions. The circles represent peak current values from individual cells, bars represent the mean.

fluorescent protein folding, either does not allow proper assembly of the tetrameric receptor, perturbs receptor trafficking to the plasma membrane or in other ways hinders receptor function

(see *Discussion*). The remaining insertion sites (383 and 391) showed overall a robust membrane expression when fused to YFP, CFP and GFP.

3.3.2 Kinetic characterisation of AMPA receptors with extracellular YFP fusions

To verify that the fluorescent fusions at the two different positions in the ATD-LBD linker region maintained rapid AMPA receptor kinetics, desensitisation, deactivation and recovery from
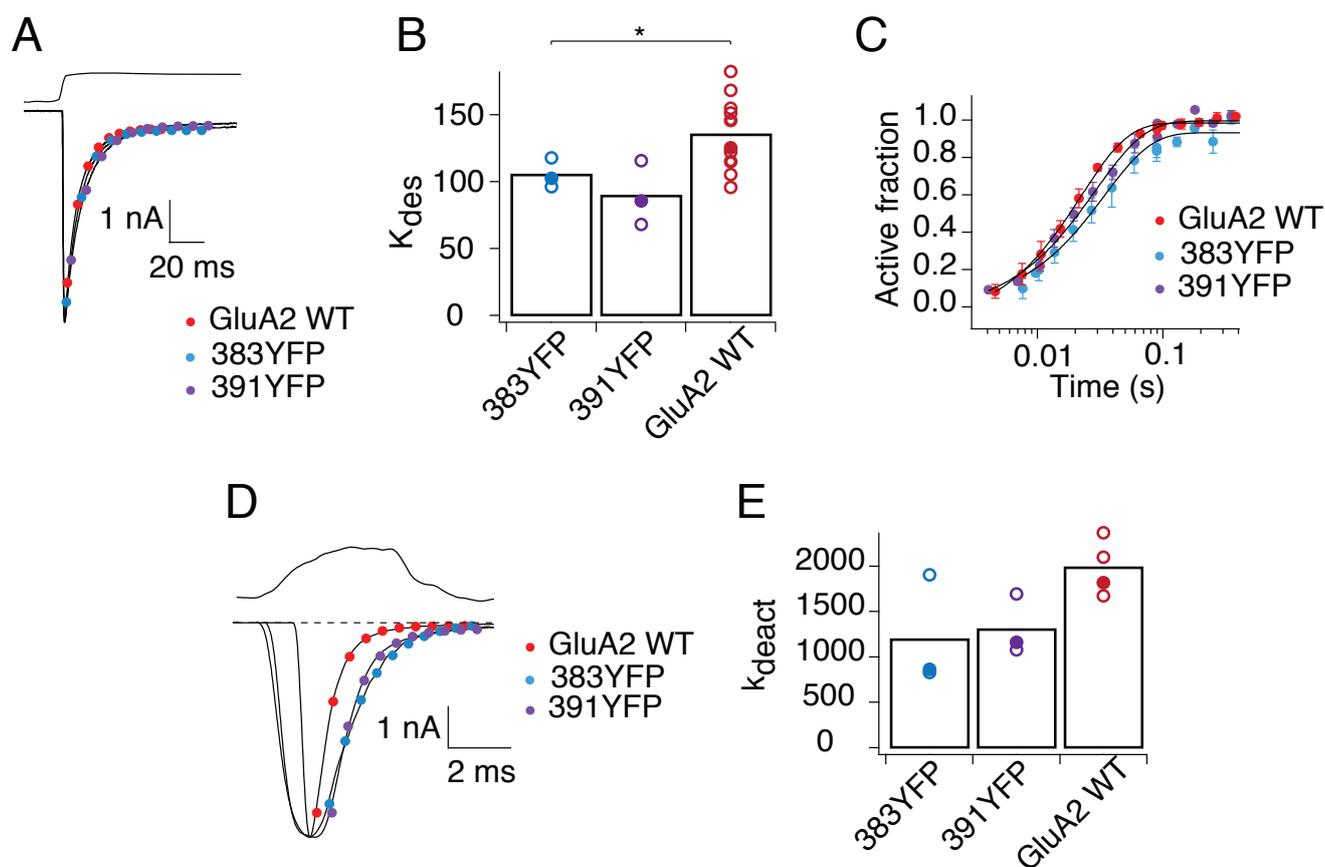
Figure 29 Kinetic characterisation of AMPA receptors with extracellular insertion of YFP A Representative desensitising traces of the fusion receptors during a long (100 ms) pulse of 10 mM glutamate (here $k_{des\ 383YFP} = 102$ s^{-1}, blue ; $k_{des\ 391YFP} = 85$ s^{-1}, purple and $k_{des\ WT} = 122$ s^{-1}, red). **B** A summary of desensitisation rates. Bars represent the mean. Individual recordings are shown as open circles, closed circles indicate the representative value in *A*. Mean values are presented in the text. *$p < 0.05$ **C** Summary of recovery rates of the fusion receptors (*see Materials and Methods*). Mean values are presented in the text. **D** Representative deactivation traces in response to a fast (1 ms) jump into 10 mM glutamate. Here deactivation rates from single exponential fits: $k_{deact\ 383YFP} = 865$ s^{-1}, blue; $k_{deact\ 391YFP} = 1163$ s^{-1}, purple and $k_{deact\ WT} = 1820$ s^{-1}, red. **E** A summary of deactivation rates. Bars represent the mean. Individual recordings are shown as open circles, closed circles indicate the representative value in *D*. Mean values are presented in the text.

desensitisation was measured in outside out patches from cells expressing GluA2 383YFP and GluA2 391YFP and compared to the GluA2 WT. YFP fused receptors were used for kinetic characterisation due to their superior expression as seen from whole cell recordings (Fig. 28 B). Receptors with fluorescent fusions in both insertion sites had similar kinetics to GluA2 WT (Fig. 29 panels A - E). The desensitisation rate of the GluA2 391YFP following a long (100 ms) 10 mM glutamate pulse ($k_{des\ 391YFP} = 90 \pm 13$ s^{-1}, n = 3) was comparable to WT desensitisation ($k_{des\ WT} = 135 \pm 7$ s^{-1}, n = 12) (Fig. 29 A and B). Desensitisation of the GluA2 383YFP was slightly slower than the WT ($k_{des\ 383YFP} = 105 \pm 6$ s^{-1}, n = 3, $p = 0.02$). The rates of deactivation following a brief (1 ms) pulse of 10 mM glutamate of both the 383YFP insertion ($k_{deact\ 383YFP} = 1200 \pm 353$ s^{-1}, n = 3) and 391 insertion ($k_{deact\ 391YFP} = 1312 \pm 192$ s^{-1}, n = 3) were close to WT receptor deactivation ($k_{deact\ WT} = 1990 \pm 153$ s^{-1}, n = 4) (Fig. 29 D and E). Recovery from desensitisation of GluA2 383YFP and 391YFP was essentially unaffected ($k_{rec\ 383YFP} = 43 \pm 11$ s^{-1}, n = 3; $k_{rec\ 391YFP} = 44 \pm 6$ s^{-1}, n = 3) compared to GluA2 WT ($k_{rec\ WT} = 57 \pm 6$ s^{-1}, n = 5) (Fig. 29 C). Taken together these results suggest a preserved rapid gating kinetics of AMPA receptors with fluorescent proteins fused at the 383 and 391 positions.

3.3.3 Quenching of extracellular GFP fusions by DPA

To assess the possible vertical movements of the extracellular domains during receptor gating, the membrane bound quencher DPA was used. Spectra were collected from cells expressing a monomeric GFP in the extracellular positions 383 and 391 of the AMPA receptor in presence and absence of 5 μM DPA (Fig. 30 B). Based on the dimensions of the extracellular domains (Sobolevsky et al., 2009) the distances of the FP insertion sites to the membrane are expected to be in the range of approximately 80-100 Å. To detect fluorescence quenching with optimal efficiency an FP with the highest R_0 with DPA was used (GFP, $R_0 = 37$ Å). The degree of quenching by DPA differed slightly for the the two insertions sites, with the GluA2 391GFP construct displaying lower relative fluorescence in presence of DPA (Fig. 30 B and C). The average normalised quenching of GFP fluorescence was: $[F_{DPA}/F]_{383GFP} = 0.95 \pm 0.05$, n = 4, $[F_{DPA}/F]_{391GFP} = 0.88 \pm 0.07$, n = 8 (Fig. 30 C). To compare the DPA dependent quenching the value of intracellular membrane bound GFP was included in the graph $[F_{DPA}/F]_{GFP-tk} = 0.27 \pm 0.02$, n = 3. The small degree of quenching of GFP in the extracellular positions is likely due to the distance between the donor GFP and the acceptor

DPA in the membrane. Based on the crystal structure dimensions (Sobolevsky et al., 2009) the length of the extracellular domains is approximately 120Å. The insertion sites are positioned roughly in the middle of the extracellular domains (the linker region) with the 391 position closer to the membrane than the 383 (Fig. 30 A) and considering the Förster distance between GFP and DPA ($R_0 = 37$Å) (Wang et al., 2010) it is not surprising that quenching by DPA of the two fusions is so unpronounced. Assuming that at the holding voltage of −60 mV a large fraction of DPA molecules will reside at the outer leaflet of the membrane, the probability of quenching of GFP by DPA was calculated following the procedure described in Zachariassen, Katchan et al., 2016 (see **Appendix A5**).
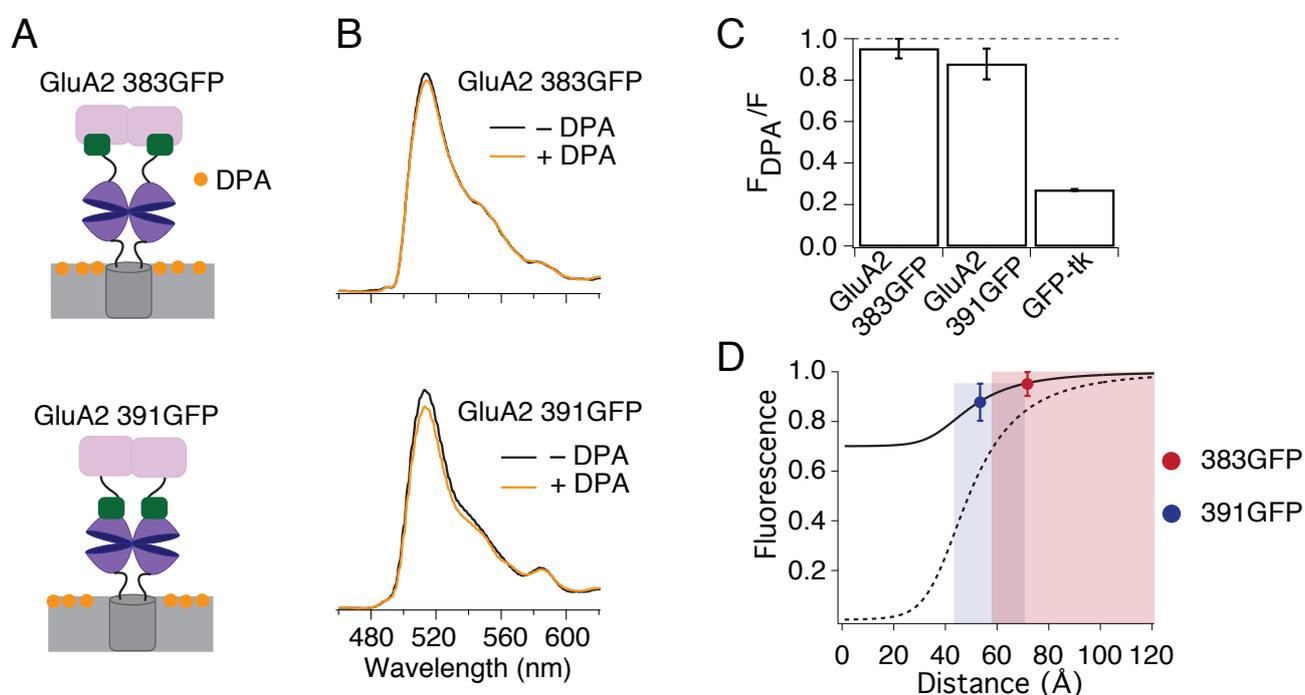
Figure 30 Quenching of extracellularly fused GFP by DPA A A cartoon representation of the AMPA receptor dimers with extracellularly inserted GFP (green squares). DPA is represented as orange spheres. The location of DPA molecules in the outer leaflet of the cell membrane is representative for the holding voltage of −60 mV. **B** GFP fluorescence emission spectra excited at 488 nm collected from cells expressing the GluA2 383GFP (upper panel) and GluA2 391GFP (lower panel) in presence (orange traces) and absence (black traces) of 5μM DPA. **C** Summary of normalised fluorescence emission from GFP at the two insertion sites as compared to an intracellular membrane attached GFP (GFP-tk). Error bars represent the SEM values and are presented in the text. **D** FRET efficiency calculated from the extent of DPA quenching of GFP at the two insertion sites. The distance (r) to the DPA of the GFP in positions 391 (blue circle) and 383 (red circle) is read off of the theoretical curve describing the probability of quenching at a given distance with R_0 set to 37Å. The shaded area shows the possible corresponding distances for the average values of quenching. See *Materials and methods* for details of calculations.

Quenching probability was plotted as a function of distance between the GFP molecule and a plane of DPA (Wang et al., 2010) for two conditions: 1) idealistic model, where no background fluorescence is assumed to be present (Fig. 30 D, dashed) and 2) a model, where a background of 70% is assumed (Zachariassen, Katchan et al., 2016) (Fig. 30 D, solid line). The experimental values of GFP quenching at the two extracellular insertion sites were then plotted onto the background subtracted curve in order to read out the possible distances between the FP insertion sites and the membrane bound plane of DPA molecules. The average distances between GFP molecules at position 383 and 391 were: $r_{383GFP-DPA}$ = 70 Å and $r_{391GFP-DPA}$ = 52 Å. Because of the shallowness of the background subtracted curve and the large separation between the extracellular insertion sites and the plasma membrane, the distances have a large variability and can only be approximated (see *Discussion*).

3.3.4 AMPA receptors with extracellular GFP fusions showed no state dependent quenching by DPA

Despite the large separation of the extracellular FP insertion sites from the membrane, movements of the ATDs relative to the membrane, which have been proposed by structural studies (Meyerson et al., 2014; Dürr et al., 2014), such as a 7 Å contraction of the ATD layer toward the membrane during activation (Meyerson et al., 2014) and an approximately 20 Å bend of the ATDs during desensitisation (Dürr et al., 2014), could potentially be detected by FRET. To asses these potential state dependent movements of the extracellular domain of AMPA receptors during gating spectra were collected at 20Hz from HEK293 cells expressing the GluA2 383GFP and GluA2 391GFP constructs during long (5 s) applications of 10 mM glutamate and under constant perfusion with 5 μM DPA. At the clamped voltage of – 60 mV, the DPA molecules will preferentially reside in the outer leaflet of the membrane (Chanda et al., 2005a). The normalised relative change in peak fluorescence was calculated for each collected frame (see *Materials and methods*) and plotted against the time of frame acquisition (Fig. 31 A).

To capture the fluorescence in different receptor states, the spectra were collected in desensitising (in absence of CTZ, red) and non-desensitising (presence of CTZ, green) conditions. To correct for any artefacts arising from solution exchange, the spectra collected in absence of DPA were subtracted as background from the spectra collected in presence of DPA.
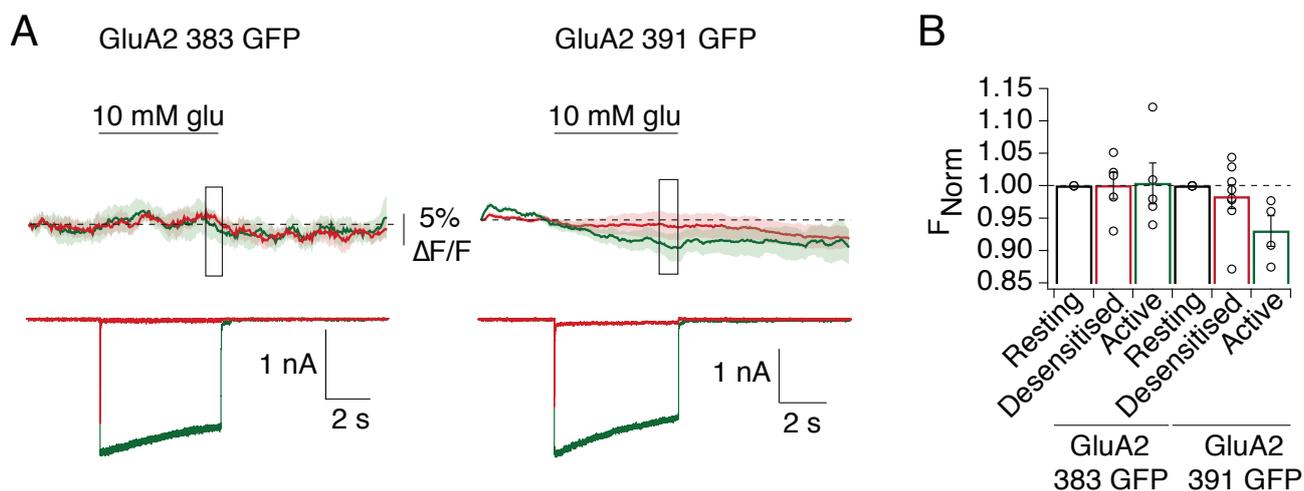
Figure 31 Quenching of extracellularly fused GFP by DPA in different receptor states A Upper panels show averaged relative change in peak fluorescence emission of GluA2 383GFP (left) and GluA2 391GFP (right) recorded at 20 Hz from lifted whole cells during long (5 s) applications of glutamate (10 mM) in the presence (*green*) and absence (*red*) of CTZ (100 µM). Cells were clamped at –60 mV under constant DPA perfusion. Pale shading indicates the standard deviation of the mean. Lower panels show representative simultaneous current recordings with the same colour scheme. For calculation of $\Delta F / F$, see *Materials and Methods*. Boxes indicate the regions of averaged values in B. **B** Averaged peak fluorescence from 7 frames at the end of glutamate application (boxed region in **A**) in the presence (*green*) and absence (*red*) of CTZ normalised to average peak fluorescence from 7 frames receptor resting state (black) before glutamate application. The normalised fluorescence is given for both the GluA2 383 and 391GFP insertions. The open circles represent normalised fluorescence of individual recorded cells. Bars represent the mean and the error bars show the standard deviation of the mean. The values are given in the text.

For both the GluA2 383GFP (Fig. 31 A, left panel) and the GluA2 391GFP (Fig. 31 A, right panel) the fluorescence of GFP did not show any significant state dependent changes. To quantify the degree of quenching by DPA in different receptor states the average fluorescence peaks from the boxed regions in figure 25A were normalised to the resting state (prior to application of glutamate) (Fig. 31 B). The normalised fluorescence intensity was: $[F_{Norm}]_{383GFP\ des} = 1 \pm 0.02$, n = 5; $[F_{Norm}]_{383GFP\ act} = 1 \pm 0.03$, n = 5; $[F_{Norm}]_{391GFP\ des} = 0.98 \pm 0.02$, n = 8; $[F_{Norm}]_{383GFP\ act} = 0.93 \pm 0.02$, n = 4. Despite not presenting any quantitative significance ($p_{393GFP\ act\ vs\ rest} = 0.05$) the slight decrease of the fluorescence in active state of the GluA2 391GFP construct might represent a small movement, which due to the high FRET donor-acceptor distance could not be resolved.

3.3.5 Measurement of intersubunit FRET with CFP and YFP pair

AMPA receptor gating is a highly dynamic process, with the domains of each subunit within the receptor tetramer sampling various arrangements during activation and desensitisation (Armstrong et al., 1998; Plested and Mayer, 2009; Lau et al., 2013; Meyerson et al., 2014; Dürr et al., 2014; Baranovic et al., 2016). To measure potential intersubunit movements, ratiometric spectral FRET was measured in cells expressing a 1:1 ratio of GluA2 CFP and GluA2 YFP insertions in either the 383 or 391 positions (Fig. 32 A). This was expected to yield tetrameric receptors harbouring donor and acceptor fluorophores at the two insertion sites for FRET to occur.
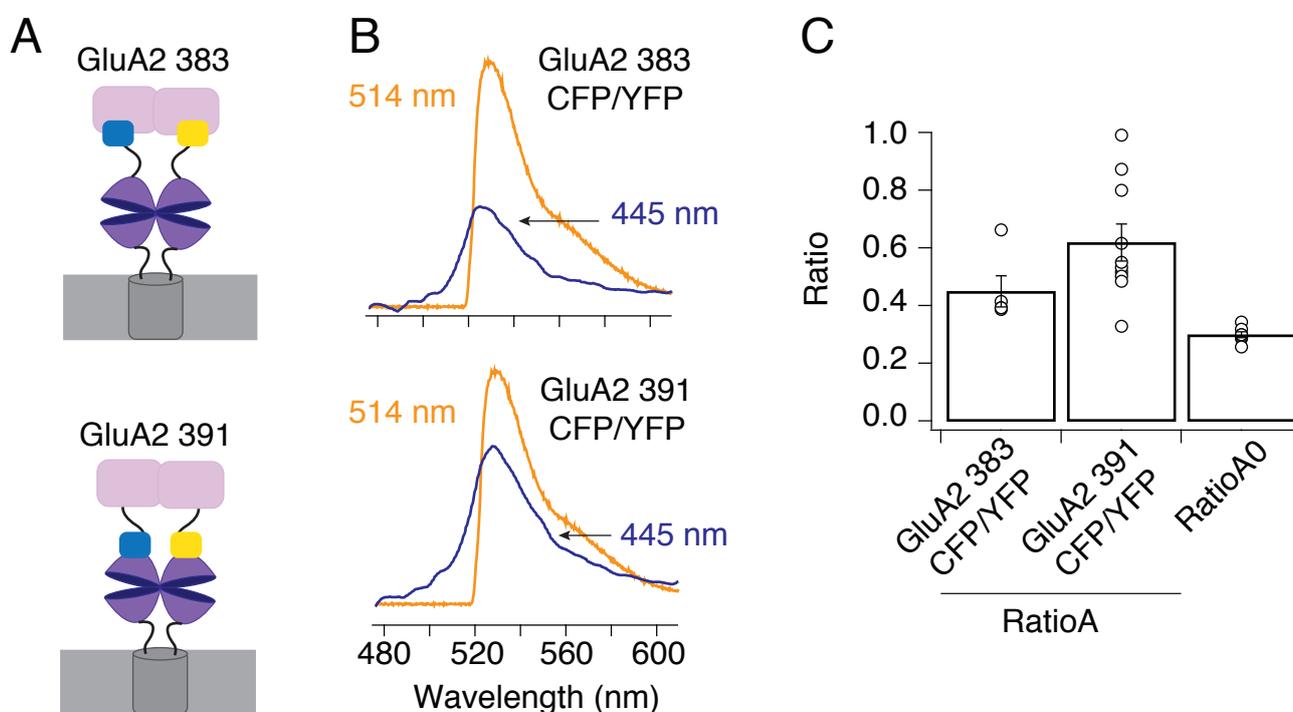
Figure 32 FRET between YFP and CFP inserted within AMPA receptor extracellular domains A Cartoon representation of an AMPA receptor dimer with a YFP or CFP inserted in a single subunit at either the 383 or 391 positions. **B** Representative fluorescence emission spectra collected from cells expressing GluA2 383YFP / GluA2 383CFP (top) and GluA2 391YFP/GluA2 391CFP (bottom) at a 1:1 DNA ratio. In the FRET channel 445 nm excitation was used and acceptor emission (blue) was extracted by subtracting the donor emission spectra (not shown). Direct acceptor excitation at 514 nm produced the emission spectra of YFP (yellow). **C** A summary of ratios A calculated as the extracted acceptor fluorescence (blue) normalised to direct acceptor fluorescence (yellow) from cells expressing GluA2 383YFP / GluA2 383CFP and GluA2 391YFP/GluA2 391CFP. RatioA$_0$ was calculated as the emission ratio of YFP excited at 445 nm and 514 nm from cells expressing YFP tagged AMPA receptors. Open circles represent values obtained from individual cells. Bars represent the mean. Error bars show the standard deviation from the mean.

Spectral FRET characterisation showed that the CFP and YFP in fact are positioned in close enough proximity to each other to undergo energy transfer (Fig. 32 B and C). The average ratioA values for the two insertion sites were: $\text{ratioA}_{\text{GluA2 383}} = 0.45 \pm 0.05$, n =5; $\text{ratioA}_{\text{GluA2 391}} = 0.61 \pm 0.06$, n =10 (Fig. 32 C). The ratioA_0 calculated by collecting spectra from cells expressing YFP labelled AMPA receptors at analogous laser intensities as for ratioA was: $\text{ratioA}_0 = 0.30 \pm 0.01$, n =7. The difference in the ratios suggests a higher separation of the donor and acceptor at the 383 position at the top of ATD-LBD connecting linker as compared to the 391 position at the bottom of the linker. With FRET efficiencies calculated from the obtained ratios for the two insertion sites it was possible to determine the approximate distances (r) between the donor and acceptor fluorophores, with R_0 for the YFP-CFP pair being 52 Å (Markwardt et al., 2011) (see *Materials and methods*). For the GluA2 383 insertion site the corresponding values were: $[\text{E}_{\text{FRET}}]_{\text{GluA2 383}} = 0.04 \pm 0.02$ and $r_{\text{GluA2 383}} = 90 \pm 4$ Å (Fig. 33, open circle). For the GluA2 391 insertion site the donor and acceptor were closer to each other: $[\text{E}_{\text{FRET}}]_{\text{GluA2 391}} = 0.10 \pm 0.02$ and $r_{\text{GluA2 391}} = 76 \pm 2.3$ Å (Fig. 33, filled circle).
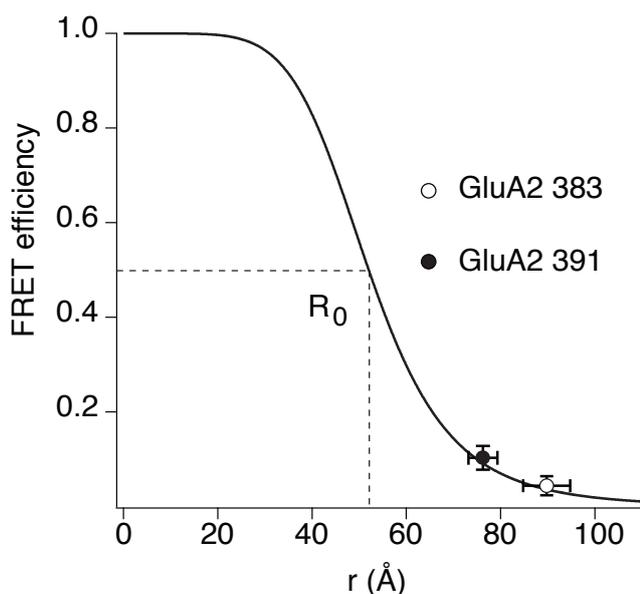
Figure 33 Determination of distances between the 383 and 391 positions of the AMPA receptor Averaged distances between the donor and acceptor at the positions 383 (open circle) and 391 (filled circle) in the AMPA receptor were determined based on the calculated FRET efficiencies (see *Materials and methods*). The line represents a theoretical relationship between FRET and distance r between CFP and YFP with the R_0 = 52Å. The error bars represent the standard deviation from the mean for both the FRET efficiencies and the corresponding distances (r). Dashed lines show where the R_0 is located on the curve.

3.3.6 FRET between CFP and YFP at extracellular sites in GluA2 was not state dependent

To monitor possible state dependent FRET changes between the CFP and YFP at extracellular insertion sites, alternating donor and acceptor spectra were recored from cells expressing a mixture of CFP and YFP fusions in GluA2 383 and 391 positions. The cells were recorded in presence and absence of 100 μM CTZ, to capture the active (green line) and desensitised (red line) states of the receptors, respectively (Fig. 34 A). During receptor gating there was no apparent change in the FRET between the CFP and YFP at either of the positions. The non-normalised values of the FRET efficiencies for the donor-acceptor pair at the two insertion sites in resting, desensitised and active states were: $[E_{FRET}]_{383\ rest} = 0.04 \pm 0.02$, n = 5; $[E_{FRET}]_{383\ des} = 0.04 \pm 0.2$, n = 5; $[E_{FRET}]_{383\ act} = 0.05 \pm 0.02$, n = 5; $[E_{FRET}]_{391\ rest} = 0.10 \pm 0.2$, n = 8; $[E_{FRET}]_{391\ des} = 0.10 \pm 0.2$, n = 8; $[E_{FRET}]_{391\ rest} = 0.15 \pm 0.3$, n = 7 (Fig. 34 B). The rather constant increase in FRET seen for the GluA2 391 insertion site can be explained by slight bleaching of the acceptor fluorophore, leading to an increase in the value of ratioA and subsequently the FRET efficiency.
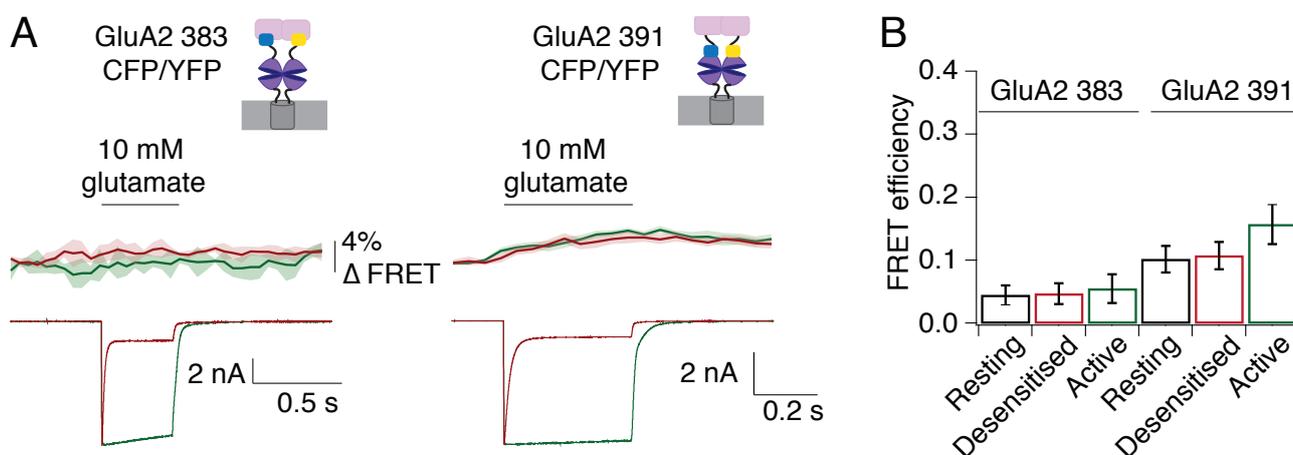
Figure 34 State dependence of FRET between YFP and CFP inserted within AMPA receptor extracellular domains A Upper panels show the average relative change in FRET calculated from fluorescence emission spectra of cells expressing either the GlA2383 CFP/YFP mixture (left) or the GluA2 391CFP/YFP mixture (right). FRET was recorded with an acquisition frequency of 20Hz in presence (green traces) and absence (red traces) of 100 μM CTZ. The shaded area represents the standard deviation of the mean. The lower panels show the corresponding current traces recorded simultaneously with the fluorescence emission spectra. **B** A summary of the average FRET efficiencies between the CFP and YFP in the GluA2 383 and GluA2 391constructs during receptor resting state (before application of glutamate) (black), desensitised state (red) and active state (green). Bars represent the averages (the values are given in the text). The error bars show the standard deviation of the mean.

In cells expressing a mixture of CFP and YFP labelled AMPA receptor subunits, the arrangement of the donor and acceptor fluorophores in a homotetrameric receptor may assemble in several FRET enabling patterns with one or multiple donors and acceptors in a single receptor (Fig. 35). The measured FRET efficiency will predominantly arise from donor and acceptor molecules at closest proximity to each other (Miranda et al., 2013).
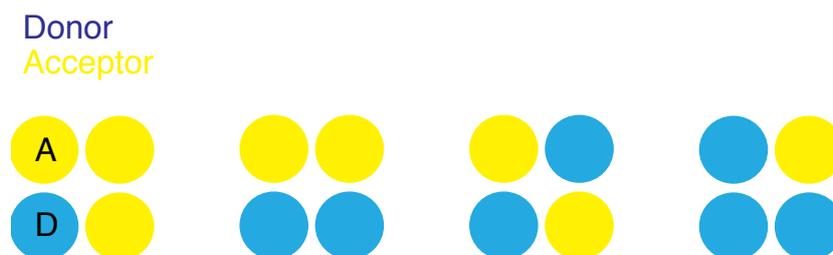
Figure 35 Possible arrangement of the donor and acceptor fluorophores in a homotetrameric receptor The donor (CFP, blue circles) and acceptor (YFP, yellow circles) each attached to a separate subunit of the AMPA receptor can be mixed in a number of ways during receptor assembly assuming a four fold symmetry for simplification.

To show the approximate arrangement of the fluorescent proteins within the receptor tetramer the structures of YFP and CFP (PDB 1ema) were docked onto the full length AMPAR (Sobolevsky et al., 2009, PDB 3kg2) at the insertion sites 383 and 391 (Fig. 36). According to the dimensions of the extracellular ATDs and LBDs only certain assemblies of labelled subunits would allow the detection of energy transfer. These assemblies will have the donor and acceptor separated by 76 and 90 Å for FPs inserted in positions 391 and 383, respectively. specific manipulation of receptor subunit assembly.
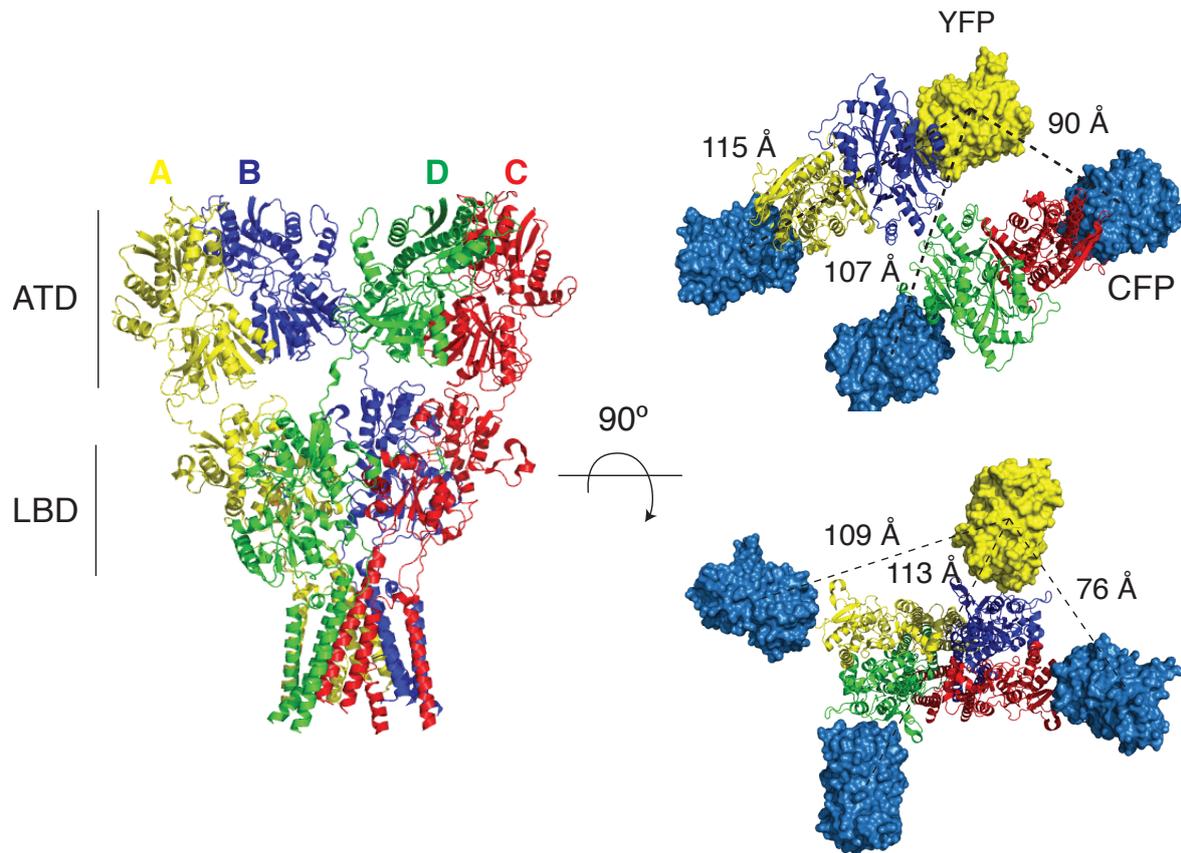
Figure 36 Possible arrangement of the donor and acceptor fluorophores in a hometetrameric receptor The donor (CFP, blue circles) and acceptor (YFP, yellow circles) each attached to a separate subunit of the AMPA receptor can be mixed in a number of ways during receptor assembly assuming a four fold symmetry for simplification.

3.4 Visualisation of AMPAR and Stargazin interaction with FRET

At native synapses the diversity of glutamatergic signalling can in part be ascribed to the modifications of the postsynaptic AMPA receptor trafficking, pharmacology and gating properties by the auxiliary transmembrane proteins (see *Introduction 1.4*). Among the members of the Transmembrane AMPA receptor Regulatory Proteins (TARPs), which are required for surface expression of mature native AMPA receptors, are stargazin (γ2), γ3, γ4 and γ8. Each TARP has a discrete expression patterns in the central nervous system and exhibit distinct modulation of AMPA receptor kinetics (Jackson and Nicoll, 2011). Among the functional properties influenced by the association of TARPs are the slowing of AMPA receptor desensitisation and deactivation (Priel et al., 2005; Tomita et al., 2005) and attenuation of intracellular polyamine block (Soto et al., 2007). To facilitate direct visualisation of AMPA receptor and TARP complexes the patch clamp fluorometry technique was used. For this AMPA receptors with extracellular GFP fusions at positions 383 and 391 were used as FRET donors and Stargazin carrying an extracellular mTAG-RFP-T label was used as a FRET acceptor. Stargazin consists of four transmembrane domains connected by linkers of various lengths (Straub and Tomita, 2012) and intracellular N- and C-termini. To create an extracellularly fluorescently labeled TARP the N-terminal tail of stargazin was fused to the C-terminal tail of the Neuropilin Tolloid like 2 protein (Neto 2), a single transmembrane domain auxiliary protein of the kainate receptors (Straub et al., 2011a and b) (see *Materials and methods*). The N-terminal domain of the stargazin-Neto2 chimera was subsequently genetically fused to an mTag-RFP-T, resulting in an extracellular FRET acceptor labeled TARP (Fig. 37 A).

3.4.1 Fluorescently labelled stargazin forms functional complexes with AMPA receptors

Firstly, to asses if the fluorescently labelled AMPA receptors and stargazin are able to assemble and form complexes, the functional modulation of AMPA receptors by stargazin was used as a readout. Currents were recorded from lifted whole HEK293 cells expressing the GluA2 383GFP or GluA2 391GFP alone or together with the wild-type or RFP labelled stargazin at different voltages to monitor the current to voltage relationship and the degree of intracellular polyamine block. At positive potentials the currents of AMPA receptors expressed alone should be blocked by the

intracellular polyamines, as was the case for both GluA2 383GFP and 391GFP constructs (Fig. 37 B, empty and filled red circles, respectively). Co-expression of labelled AMPA receptors with both labelled and WT stargazin resulted in a relief of the polyamine block for both the GluA2 383GFP construct (Fig. 37 B, upper panel) and GluA2 391GFP construct (Fig. 37 B, lower panel). The rectification indexes calculated as the whole cell peak current at 40 mV normalised to the peak current at -40 mV were: $RI_{gluA2\ 383\ +\ RFP\text{-}stg} = 0.32 \pm 0.05$, n = 7; $RI_{gluA2\ 383\ +\ WT\ stg} = 0.35 \pm 0.04$, n = 3; $RI_{gluA2\ 383} = 0.08 \pm 0.02$; n = 6; $RI_{gluA2\ 391\ +\ RFP\text{-}stg} = 0.25 \pm 0.04$, n = 11; $RI_{gluA2\ 391\ +\ WT\ stg} = 0.24 \pm$
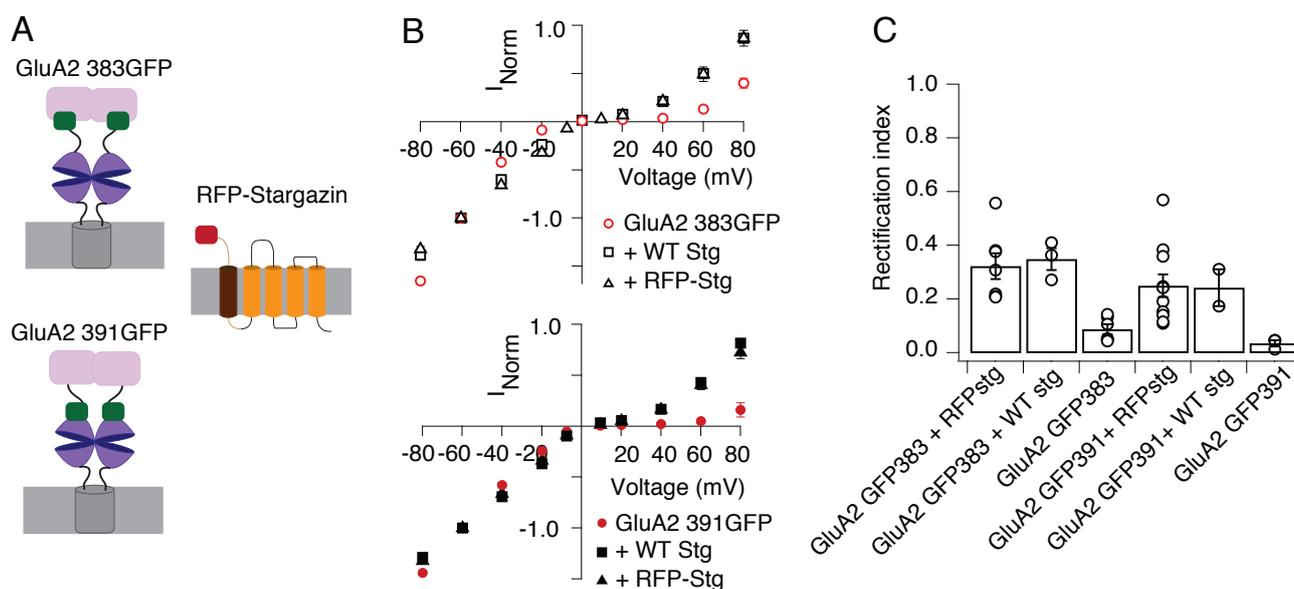
Figure 37 Functional characterisation of labelled AMPAR and TARP complexes A Cartoon representation of the AMPA receptor dimers with GFP inserted in the 383 (top) and 391 (bottom) positions and the topography of the Stargazin-Neto1 chimera with an extracellular mTagRFP-T fused to the N-terminal tail. The stargazin is presented as orange transmembrane segments. The Neto1 domain is shown as a brown transmembrane segment. The RFP tag is shown as a red square. **B** Averaged IV relationship obtained from whole cell peak currents at voltages ranging from -80 to 80 mV for GluA2 383GFP (top) and GluA2 391GFP (bottom). The IV was recorded in cells expressing the labelled AMPA receptors alone (red circles), in combination with WT unlabelled Stargazin (black squares) and in combination with the labelled RFP-Stargazin-Neto1 chimera (black triangles). **C** Average rectification indices calculated from whole cell peak currents at 40 mV normalised to peak currents recorded at –40 mV from cells expressing the labelled GluA2 383 and 391 GF alone or together with WT or RFP labelled Stargazin. Open circles show the values from individual cells, bars show the mean (presented in the text) and the error bars represent the standard deviation of the mean.

0.07, n = 2; $RI_{gluA2\ 391}$= 0.03 ± 0.01, n = 3 (Fig. 37 C). The relief of polyamine block caused by association of labelled stargazin was of a comparable degree as that induced by WT stargazin, suggesting that the extracellular labelled AMPA receptor carrying the donor fluorophore and the extracellularly tagged stargazin carrying the acceptor fluorophore form functional complexes at the cell membrane. Furthermore these results show that the modulation of AMPA receptor by stargazin is not disturbed by the inline insertion of fluorescent proteins.

3.4.2 FRET between RFP labelled stargazin and AMPA receptors with extracellular GFP fusions

The complexes between the AMPA receptors carrying the extracellular donor fluorophores and the acceptor labelled stargazin can be directly measured by FRET. The ratiometric spectral FRET approach was used once again, with spectra collected from three different samples to give the measures for the ratios A and A_0. To measure the ratioA spectra were collected from HEK293 cells transfected with a 2:1 DNA mixture of either the GluA2 383GFP or 391GFP encoding plasmids and mTagRFP-T Stargazin encoding plasmid. The emission spectra were collected following alternating excitation wavelengths between donor excitation at 488 nm (Fig. 38 A, black traces) and acceptor excitation at 561 nm (Fig. 38 A, red traces). Average spectra collected from cells expressing the GluA2 383GFP and 391GFP without stargazin (Fig. 38 A, dashed green traces) were used to extract the acceptor emission arising from donor excitation (Fig. 38 A, green traces). The ratioA was calculated as the ratio between the extracted acceptor emission (green traces) and acceptor emission following direct excitation at 561 nm (red traces). The average values of ratioA between the two AMPA receptor insertion sites and RFP stargazin at steady state conditions were: $ratioA_{GluA2\ 383GFP}$ = 0.80 ± 0.05, n = 8; $ratioA_{GluA2\ 391GFP}$ = 0.88 ± 0.03, n = 16 (Fig. 38 B). Emission spectra collected from cells expressing the RFP labelled stargazin were used to calculate $ratioA_0$ (see *Materials and methods*). The average values of $ratioA_0$ for RFP were $ratioA_{0\ RFP}$ = 0.65 ± 0.04, n = 6 (Fig. 38 B). The FRET efficiency was calculated using the ratios A and A_0 and the corresponding distances between the donor GFP molecules in AMPA receptor sites 383 and 391 and the RFP acceptor attached to the stargazin were extracted (see *Materials and methods*). The calculated FRET efficiencies (E) were plotted agains the distances on a theoretical GFP-RFP FRET curve using R_0 = 58 Å (Merzlyak et al., 20078) (Fig. 38 C). The values of the efficiencies and the distances between

the two insertion sites in the receptor and RFP-stargazin were: $E_{GluA2\ 383GFP} = 0.33 \pm 0.1$ and $r_{GluA2\ 383GFP} = 64 \pm 7$ Å (Fig. 38 C, empty circle); $E_{GluA2\ 391GFP} = 0.50 \pm 0.07$ and $r_{GluA2\ 383GFP} = 57 \pm 3$ Å (Fig. 38 C, filled circle).
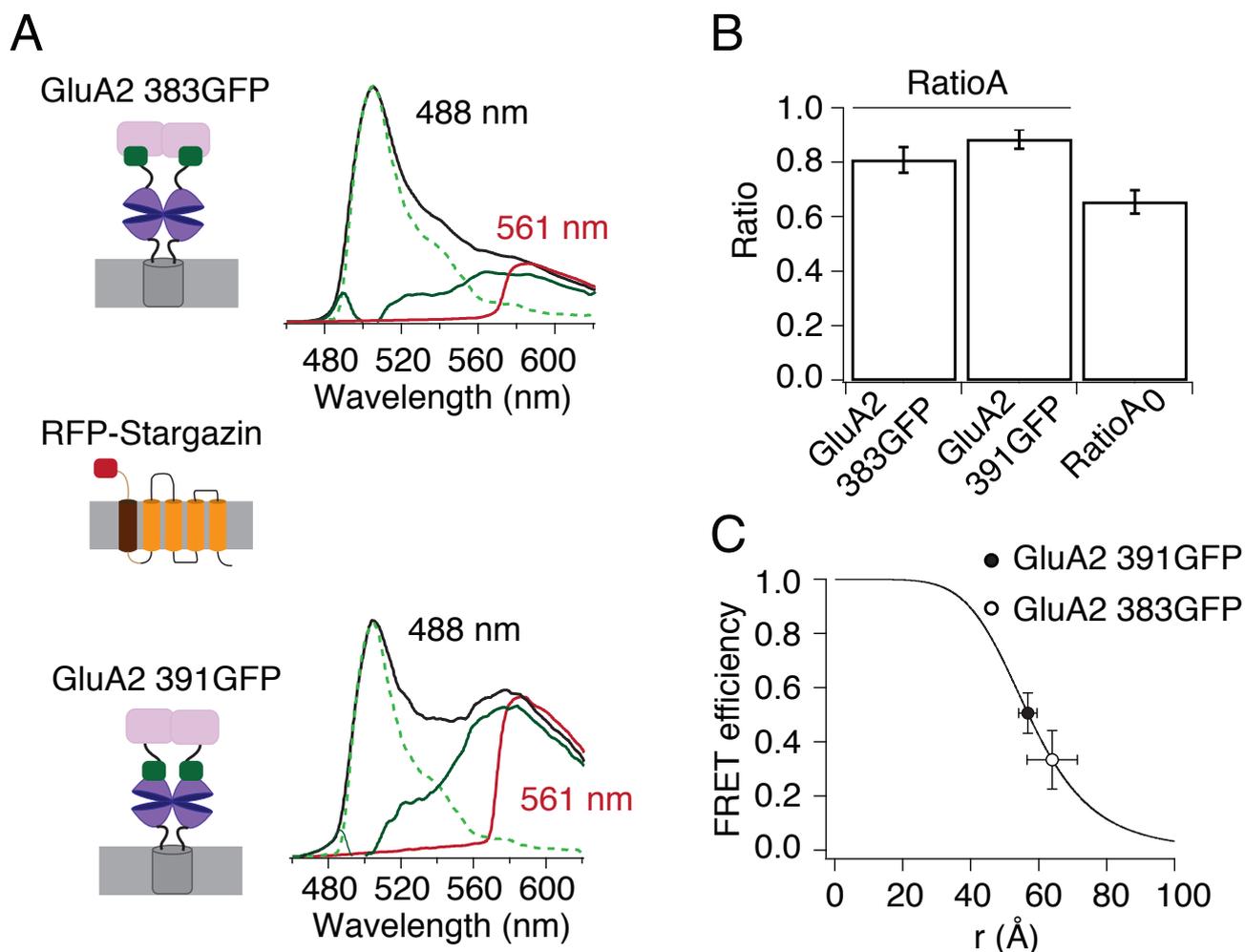
Figure 38 Spectral characterisation of labelled AMPAR and TARP complexes A Cartoon representation of the AMPA receptor dimers with GFP inserted in the 383 (top) and 391 (bottom) positions and the topography of the Stargazin-Neto1 chimera with an extracellular mTagRFP-T fused to the N-terminal tail. Representative emission spectra for calculation of ratioA are shown for the corresponding GluA2 constructs on the right side of the panel. **B** A summary of ratios A calculated as the extracted acceptor fluorescence (dark green) normalised to direct acceptor fluorescence (red) from cells expressing GluA2 383GFP and GluA2 391GFP in combination with RFP-Stargazin. RatioA0 was calculated as the emission ratio of RFP excited at 488 nm and 561 nm from cells expressing RFP tagged Stargazin. Bars represent the mean and the error bars show the standard deviation from the mean. **C** Averaged distances between the donor in the positions 383 (open circle) and 391 (filled circle) in the AMPA receptor and the acceptor on the Stargazin were determined based on the calculated FRET efficiencies (see *Materials and methods*). The line represents a theoretical relationship between FRET and distance r between GFP and RFP with the $R_0 = 57$ Å. The error bars represent the standard deviation from the mean in both x- and y axis.

The FRET measured between the GluA2 383GFP/ 391GFP and the RFP labelled stargazin suggests a higher separation between the donor in position 383, consistent with data from DPA measurements (Fig. 30). The concurrent functional recordings showing AMPA receptor modulation by stargazin, suggest that the FRET signal arrises from fully functional complexes of AMPA receptors and TARPs at the cell membrane.

3.4.3 Measuring state dependent FRET between AMPA receptors and stargazin

To address potential state dependent movements of the extracellular domains relative to the stargazin within the AMPA/TARP complex, spectral FRET was recorded simultaneously with currents in response to long (400 ms) applications of 10 mM glutamate in presence (active state, green traces) and absence (desensitised state, red traces) of 100 µM CTZ (Fig. 39). In desensitising conditions the relative FRET between the donor GFP at either position 383 or 391 and the stargazin attached RFP did not change significantly (Fig. 39 A and B, red).

GFP in position 383 (top of the ATD-LBD linker) showed a small increase in FRET against the RFP fused to stargazin in presence of CTZ (Fig. 39 A upper panel, green trace and B). The GFP in position 391, however, showed no activation dependent change in FRET (Fig. 39 A, lower panel). The FRET values, normalised to the average of the first three frames acquired, were for the different receptor states and insertion sites: $[FRET_{Norm}]_{383\ rest} = 1 \pm 0.004$, $n = 8$; $[FRET_{Norm}]_{383\ des} = 1.01 \pm 0.02$, $n = 8$; $[FRET_{Norm}]_{383\ act} = 1.05 \pm 0.03$, $n = 6$; $[FRET_{Norm}]_{391\ rest} = 1 \pm 0.004$, $n = 7$; $[FRET_{Norm}]_{391\ des} = 1.02 \pm 0.01$, $n = 7$; $[FRET_{Norm}]_{391\ act} = 1 \pm 0.01$, $n = 8$ (Fig. 39 B). The FRET increase between GFP in position 383 during receptor activation suggests that the interaction of AMPARs with TARPs in functional complexes may be dynamic.
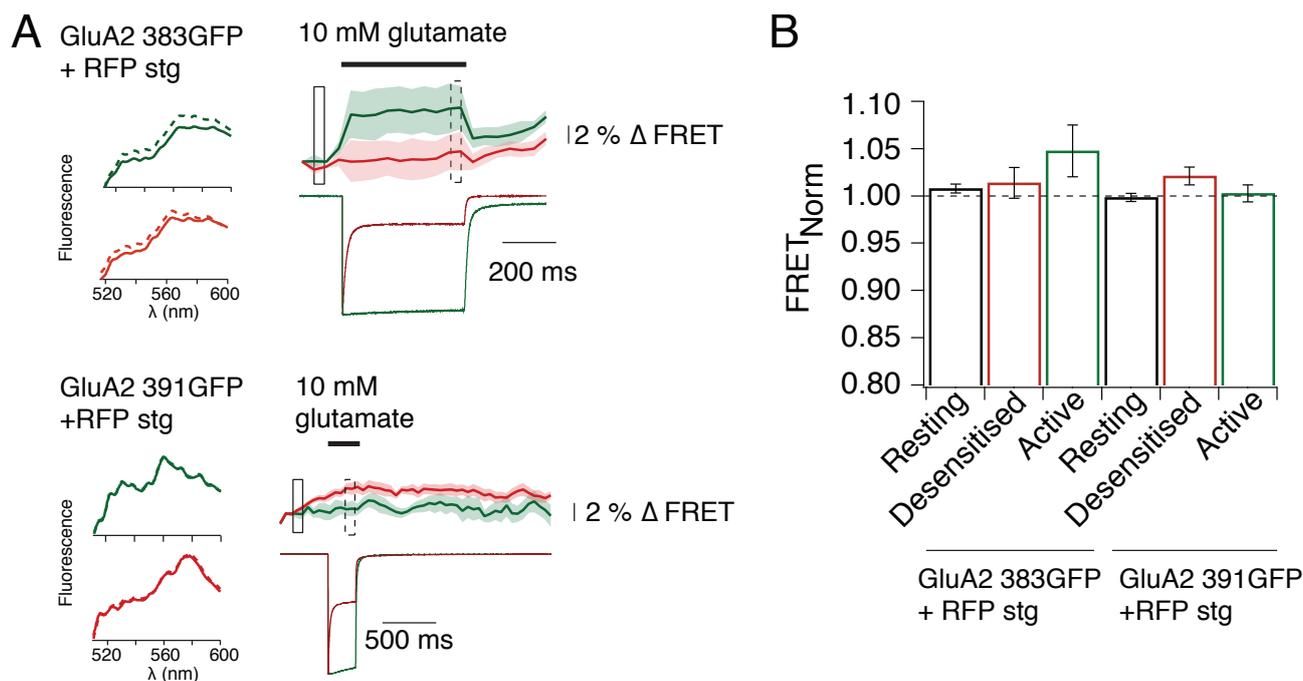
Figure 39 Spectral FRET between AMPAR and TARP complexes during receptor gating A Averaged relative changes in the FRET between GFP inserted in the extracellular domain of the AMPA receptor in position 383 (top) and 391 (bottom) and RFP-stargazin. FRET was recorded with an acquisition frequency of 20Hz in presence (green traces) and absence (red traces) of 100 μM CTZ. The shaded area represents the standard deviation of the mean. The lower panels show the corresponding current traces recorded simultaneously with the fluorescence emission spectra. An average of 3 frames of extracted acceptor emission spectra from the boxed regions in the recording are shown on the left. Spectra from desensitising conditions are shown in red and spectra collected in presence of CTZ are shown in green. The spectra collected before application of glutamate and at the end of glutamate application are compared (solid and dashed lines, respectively). **B** Summary of normalised FRET in the resting (black), desensitised (red) and active (green) receptor states for the GluA2 383 and 391GFP constructs in complex with RFP-Stargazin. The FRET values were taken from the boxed regions on the recordings in **A**. The bars represent the mean, with the exact values presented in the text, and the error bars show the standard deviation of the mean.

3.4.4 The dissociation of receptor-TARP complexes could not be seen with FRET

To see if the AMPAR-TARP complexes undergo dissociation on a measurable timescale, and if receptor desensitisation influences the dissociation (Cais et al., 2015), spectral FRET was recorded in cells expressing the GluA2 391GFP and RFP-stargazin during long (50 s) application of 10 mM glutamate. To have a functional readout of the potential dissociation of the complexes along side the optical, in the form of the measure of polyamine block, two voltage ramps ranging from -80 to 80 mV were placed in the recording, one at the beginning of the glutamate application and one at the end (Fig. 40 B). Additionally, two ramps were placed outside of the glutamate application, one before and one after. These were subsequently subtracted from the ramps recorded during the glutamate application. The modification of the AMPA receptors by stargazin did not seem to be altered during the long desensitising pulse of glutamate, as is evident from the comparison of the two I-V curves (Fig. 40 C). The average rectification index of the two ramps, calculated as the ratio of the peak currents at 40 mV to –60 mV was: $RI_{Ramp\ 1} = 0.29 \pm 0.07$ and $RI_{Ramp\ 1} = 0.34 \pm 0.06$, n = 4. The increase in the relief of polyamine block during the second ramp was insignificant ($p = 0.6$) and can be explained by the increase in the steady state current during long desensitising pulses (see *Discussion*). During the long pulse the FRET signal between the AMPA receptor and RFP-tagged stargazin decreased by approximately 5% as compared to FRET baseline before glutamate application (Fig. 40 E and F). The decrease of the FRET signal can be assigned to an increase in the donor acceptor distance, but is difficult to link to AMPA-TARP complex dynamic, since the change is not accompanied by any functional data supporting complex dissociation (see *Discussion*). It is also noteworthy that the FRET change does not seem to be gating specific and is on a timescale far beyond that of receptor kinetics.
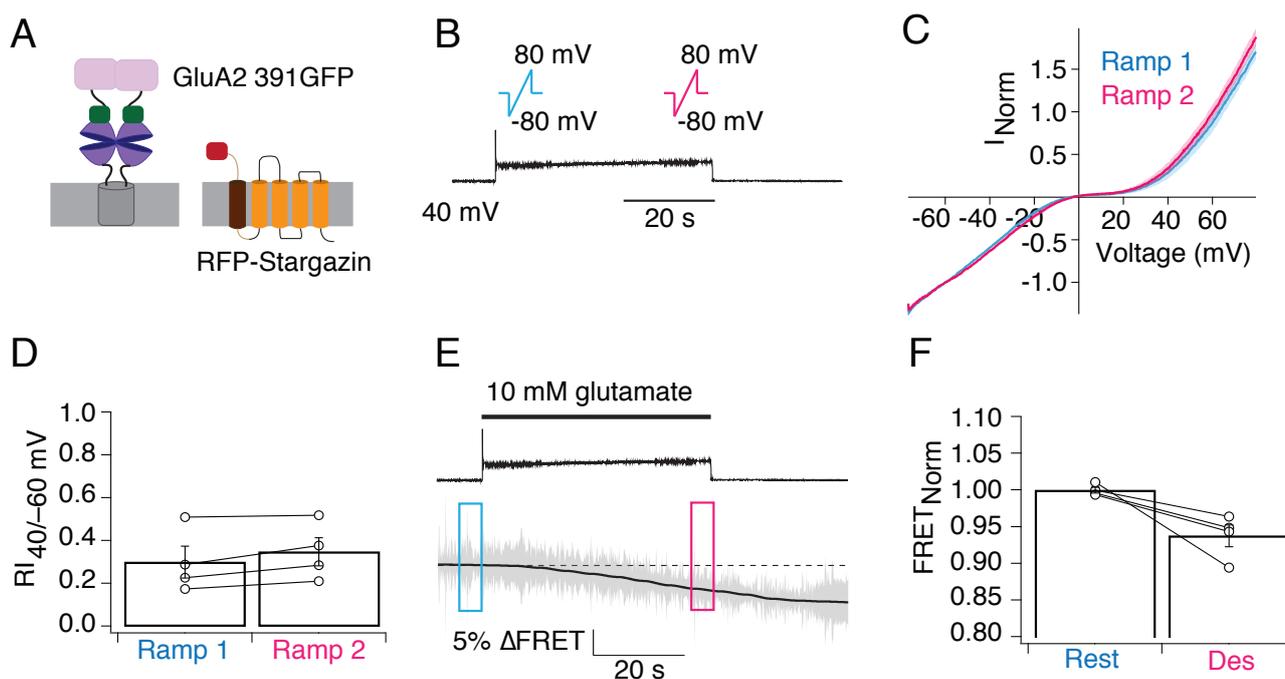
Figure 40 Spectral FRET between AMPAR and TARPs to visualise complex dissociation A Cartoon representation of the AMPA with a GFP inserted in position 391 and RFP-Stargazin. **B** An example current trace recorded at 40 mV during 50 s application of glutamate. Two voltage ramps from -80 to 80 mV were positioned in the beginning of the glutamate application (blue) and at the end (pink). **C** Comparison of the averaged IV relationship between the two ramps. The values of the ramp before the jump were subtracted from ramp 1 (blue) and the values of the ramp after the glutamate application were subtracted from ramp 2 (pink). **D** A comparison of rectification indices of the two ramps. Here the peak current at 40 mV was normalised to peak current at −60 mV. Open circles represent values of individual cells and bars represent the mean. **E** Average relative change in FRET during long (50 s) application of glutamate recorded at 40 mV is shown in the lower panel. The upper panel shows the corresponding currents recorded simultaneously. The coloured boxes show the areas of the trace which were compared spectrally. **F** Normalised FRET from an average of 7 frames acquired before the glutamate application (blue) and after 50 s of glutamate exposure (pink) indicated by the boxes in **E**. The FRET values were normalised to resting conditions, before glutamate application.

3.5 Insertion of circularly permuted GFP into AMPA receptors

Circularly permuted GFP (cpGFP) has previously been used in single wavelength sensors (marvin papers). The conformational changes of the domains fused to the cpGFP drive the reorganisation of the GFP chromophore producing a robust change in fluorescence in response to stimuli. To create a single wavelength reporter of AMPA receptor activity, cpGFP with linkers as described (Marvin et al., 2013) was genetically fused within the sites of the receptor shown to be permissive (Fig. 5) (see *Materials and methods*).

3.5.1 Functionality of AMPAR - cpGFP fusions

Initially, the functionality of AMPA receptors with a cpGFP inserted into either the I6 site of the intracellular M1M2 loop or the extracellular 383 and 391 positions (Fig. 41, left panel) was tested electrophysiologically. Average whole cell peak currents recorded from cells expressing the cpGFP fused AMPA receptors were: $I_{I6\ cpGFP} = 0.2 \pm 0.05$ nA, n = 4; $I_{383\ cpGFP} = 3.7 \pm 1.2$ nA, n = 5; $I_{391\ cpGFP} = 3.05 \pm 0.8$ nA, n = 5 (Fig 41 B). The low expression of the AMPA receptors with intracellularly inserted cpGFP can be due to the short linkers connecting the cpGFP to the M1M2 loop (2 amino acids), compared to the 9 and 12 amino acid linker used for the YFP and CFP insertions. The extracellular insertion sites showed surprising tolerance to the shortening of the linkers of the fused fluorescent protein, suggesting that this particular region is highly permissive.
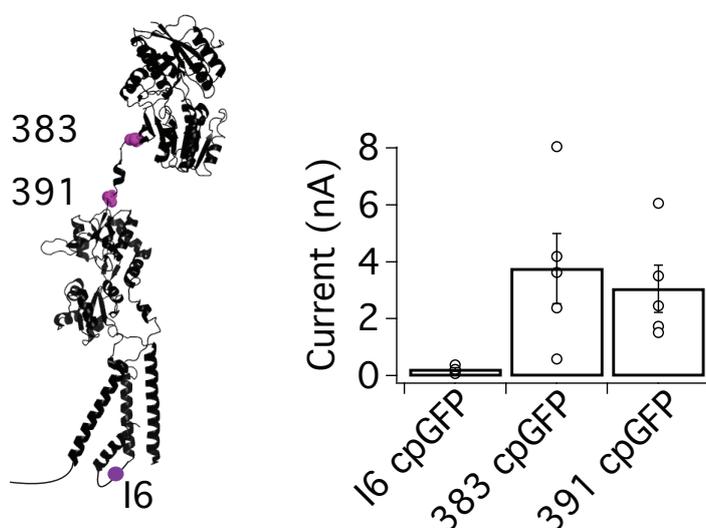
Figure 41 Membrane expression of AMPA receptors with cpGFP fusions The insertion sites used for fusion of cpGFP into an AMPA receptor subunit are shown as magenta spheres. The whole cell peak currents recorded from cells expressing the GluA2 I6 cpGFP, 383 cpGFP and 391 cpGFP are shown in a summarising bar graph. Open circles represent peak currents from individual cells and the bars represent the mean. The error bars show the standard deviation of the mean.

3.5.2 No change in cpGFP fluorescence could be recorded during receptor gating

To see if the structural rearrangements of the AMPA receptor during gating would translate into a change of fluorescence of the extracellularly and intracellularly inserted cpGFP, spectra were recorded at 50 Hz in presence (green traces, active) and absence (red traces, desensitising) of 100 µM CTZ during long (400 ms) applications of 10 mM glutamate (Fig. 42). Fluorescence emission spectra from cells expressing the GluA2 I6 cpGFP (Fig. 42, left), GluA2 383 cpGFP (Fig. 42, middle) and GluA2 391cpGFP (Fig. 42, right) showed no significant change in the the fluorescence peak intensity during application of glutamate. The GluA2 391cpGFP constructs showed a small glutamate dependent decrease in fluorescence in receptor active state (Fig. 42, left, green trace). Because of the high sensitivity of the GFP chromophore to its surrounding (Marvin et al., 2011; Marvin et al., 2013), it is not unconceivable that modifications of the linkers in the GluA2 391cpGFP construct or movement of the insertion within the region of the ATD-LBD linker could produce a promising construct for single wavelength reporter of AMPA receptor activity.
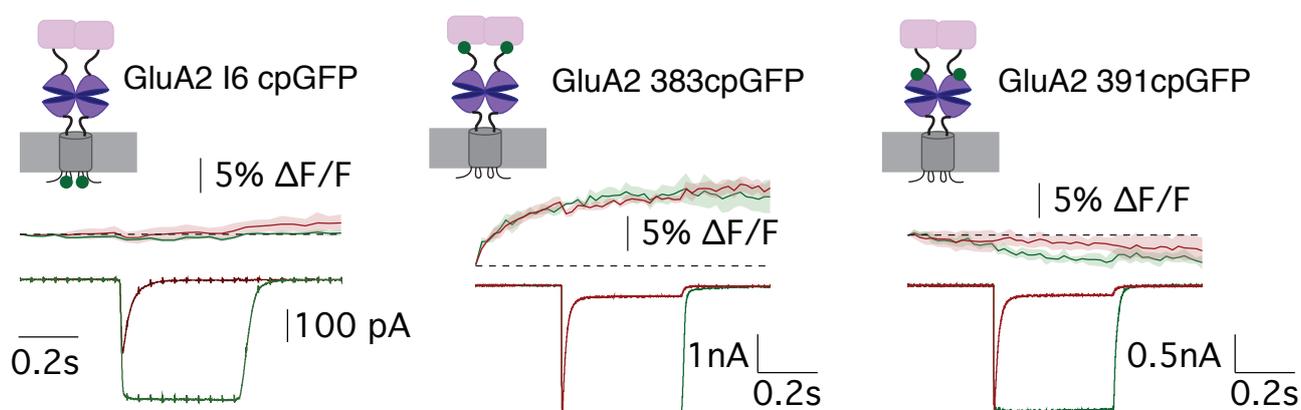
Figure 42 Spectral characterisation of AMPA receptors with cpGFP fusions cpGFP (presented here as green circles) was excited at 488 nm and fluorescence emission spectra were collected at 20Hz frequency from cells expressing the GluA2 I6cpGFP (left), GluA2 383cpGFP (middle) and GluA2 391cpGFP (right). The relative change in fluorescence normalised to baseline fluorescence before glutamate application is shown for each construct in presence (green traces) and absence (red traces) of 100 µM CTZ. Lower panels show the corresponding representative current recorded simultaneously with the fluorescence.

4. Discussion

4.1 Genetic insertion of fluorescent proteins within GluA2 subunits

4.1.1 Tolerance for fluorescent protein insertion varied within the GluA2 subunit

In the framework of this study variants of green fluorescent protein were introduced into several positions of a single GluA2 subunit to produce optically active receptors. The permissive sites were chosen among the one described previously (Sheridan et al., 2006) and from analysis of the full length structure (Sobolevsky et al., 2009). In the study of Sheridan et al. random insertions of GFP variants within three AMPA receptor subunits (A1, A2 and A4) were made. Targeted genetic fusion of fluorescent proteins described here uses identical linkers to connect the FPs within the GluA2 subunit, but alters the insertion sites that correspond to the described permissive positions (based on sequence alignments). Due to this there are some discrepancies between the permissiveness of certain sites in the GluA2 subunit as compared to the corresponding positions in the GluA1 and 4 subunits. Position 271, for instance, of the GluA2 subunit is located 4 amino acids downstream from a permissive site within the GluA1 subunit which was reportedly both bright and fully functional (Sheridan et al., 2006). This insertion site was chosen based on its location within a loop of the ATD of GluA2 and the poorly conserved sequence compared to the A1 and A4 subunits (data not shown). The 271 position in GluA2, despite producing bright fluorescence (Fig. 11), had no functional expression in whole cell patch clamp recordings (Fig. 28). Fluorescence intensity of the inserted FP is highly reliant on the folding of the chromophore and of the local structure around the insertion site. Additionally the linkers that encompass the FP within the target protein play a crucial role in enabling proper folding (Sheridan et al., 2006). Insertions with high fluorescence intensity, such as 271, can, however, still fail to produce functional ion channels. The lack of functional readout for receptors with a GFP variant inserted in the ATD at position 271 may be explained by several phenomena. Firstly, a high rate of intracellular retention of the fusion receptors, which is more evident for some insertion positions than others (Sheridan et al., 2006; Giraldez et al., 2005), can be the cause of a diminished surface expression and thus lower currents measured in cells expressing this particular construct. Secondly, insertion of a GFP variant into the ATD may lead to a misfolding of the domain and subsequently to a deficiency in receptor assembly (Ayalon and Stern-

Bach, 2001). Isolated ATDs and ATDs in the context of a full length receptor form tightly associated dimers (Jin et al., 2009; Sobolevsky et al., 2009). The dimer interface is formed between both the upper (L1) and lower (L2) lobes of the ATDs and buries about 1408 Å^2 of solvent-accessible area (Jin et al., 2009). Part of the L1-L1 interaction is achieved through contacts between the "flaps" of each subunit (residues 298-317) which are located on the very top of the L1 (Jin et al., 2009). Consequently, if insertion of a GFP variant in a position upstream of the "flap" region disrupts the points of contact at the interface, dimerisation and subsequent assembly of the receptor may be jeopardised, leading to diminished function, as seen for the 271 insertion site. In light of a resent study it is important to note, that although the ATDs facilitate the tetramerisation of the receptor, these domains are not necessary for the formation of a tetramer (Gan et al., 2016).

The 391 insertion site (Fig. 28) which is located at the C-terminal end of the linker connecting the ATD to the LBD has not previously been described. This position was chosen based on the assumption that linker regions of the receptor are highly permissive for inline fusion of fluorescent proteins and with the purpose of coming as close to the LBD as possible, to surpass the general intolerance of this domain for insertions of FPs (Sheridan et al., 2006). Interestingly this insertion allowed the formation of fully functional and fluorescent receptors (Fig. 28).

Insertion site 383 was chosen based on the corresponding permissive site in the GluA1 (Sheridan et al., 2006). This particular region of the ATD-LBD linker (6 residues: Leu378-Gly384) was deleted in the crystallisation trials to enhance construct stability (Sobolevsky et al., 2009), a modification seemingly without any functional effect, further demonstrating the permissiveness of the region.

4.1.2 Characterisation of insertion of different fluorescent protein variants into the GluA2 subunit

Whilst monomeric derivatives of the *Aequorea victoria* green fluorescent protein (GFP) such as Venus, mCerulean3 and mEGFP performed well as inline fusion proteins in AMPA receptor permissive sites (Fig 12 and 28), the mTagRFP-T (Shaner et al., 2008) insertion into the extracellular domains failed to produce any fluorescence or whole cell currents (Fig. 28). The lack of currents can be due to the origin of the protein, which was initially derived from *Entacmaea quadricolor* under the name eqFP578 and altered through multiple rounds of random and semi-random mutagenesis (Merzlyak et al., 2007; Shaner et al., 2008) to improve its overall performance.

The fact that insertion of mTagRFP-T into sites 383 and 391 didn't produce any fluorescence is puzzling, as GFP variants showed some degree of fluorescence when inserted virtually anywhere within a protein (Giraldez et al., 2005; Sheridan et al., 2006). In contrast, the labelling of stargazin with the mTagRFP-T fused C-terminally to the protein of interest produced fluorescent and functional constructs (Fig. 37). The variations fluorescence signals of FPs in different insertion sites are perhaps suggestive of the limits of use of this FP in inline fusions, as they may perturb chromophore maturation.

The maturation time of the various FPs may also influence the membrane expression of the receptors with fluorescent fusions. Various mutations have been introduced to the *Aequorea victoria* derived fluorescent proteins to optimise maturation at 37 degrees (Chudakov et al., 2010). The maturation of a fluorescent protein proceeds in two steps (Craggs et al., 2009) and has a halftime ranging from 40 min to 2 hours (Chudakov et al., 2010). First, the polypeptide chain must fold into the correct 3 dimensional structure, a process not considered to be rate limiting in the overall maturation of an FP. The folding is followed by cyclisation and oxidation of the chromophore. The latter is thought to be the slowest step in the FP maturation process. The timescale of the chromophore formation is irrelevant for the applications of FPs in present study, as the fluorescence recording takes place 48 - 72 hours post initial DNA transfection, giving the FPs sufficient time to mature. The folding of the FP on the other hand may be the crucial step in proper formation of functional fluorescent fusion proteins, as it should be timed with the folding of the target GluA2 polypeptide. The reported maturation rate of Venus (5.6×10^{-2} s^{-1}, Nagai et al., 2002) is faster than that of mEGFP (1.2×10^{-3} s^{-1}, Lizuka et al., 2011) and mCerulean3 (1.9×10^{-2} s^{-1}, Markwardt et al., 2011). This faster folding rate could explain the enhanced membrane expression of YFP fused receptors as compared to CFP and GFP fusions (Fig. 28)

4.2 Intracellular region of AMPA receptors

4.2.1 Ratiometric FRET

FRET and LRET techniques have been widely used to study protein interaction, assembly and co-localisation (see *Introduction 1.6*). Among others, structure function relationship of ion channels has been studied using these methods (Miranda et al., 2013, Zheng et al., 2000; Taraska et al., 2007)

with various labelling techniques (see *Introduction 1.6.4*). The focus of the present study has been on elucidating structural dynamics of AMPA receptors using FRET between fluorescent proteins genetically inserted at permissive sites within the GluA2 subunit. Despite being a widely popular technique, FRET has some underlying issues which make spectroscopic measurements challenging. One of these is the unavoidable crosstalk between the donor and acceptor channels. The excitation of the donor fluorophore will inevitably lead to some degree of direct acceptor excitation, because besides the necessary donor emission and acceptor absorption overlap, the absorption spectra of the donor and acceptor also display an overlap. Unmixing of the two channels is essential for a reliable measure of the uncontaminated energy transfer between the two fluorophores when measuring FRET using acceptor emission. A way to avoid the issue of the absorption overlap is to look exclusively at the donor by either measuring the lifetimes through fluorescence lifetime imaging (FLIM) or sensitised donor emission fluorescence. Another advantage of donor life time imaging is the independence of the measurement of the donor and acceptor concentrations in the test and control samples (Selvin et al., 1995). The FLIM FRET approach has beed used to study ion channel dynamics, of particular interest are the studies of NMDA receptors (Dore, 2014; Dore, 2015). Although relevant, these studies have been limited in temporal resolution and only addressed receptors with slower gating kinetics than the AMPARs. No reports on simultaneous optical and functional recording of ion channels using the FLIM technique exist to date, likely due to the complexity of the instrumentation and the technique. In the present study the ratiometric spectral FRET approach (Clegg et al., 1992; Zheng et al., 2002; Zheng et al., 2003) was used to study the structure-function relationship of AMPA receptors with voltage clamp fluorometry. Using ratios of extracted acceptor emission spectra from FRET samples and control samples bypasses the concern of nonuniform expression of genetically labelled donor and acceptor AMPAR subunits and errors in concentration between the samples do not lead to errors in FRET measurements.

4.2.2 Initial characterisation of FRET between intracellularly inserted fluorophores

Insertion of both YFP and CFP into a single subunit resulted in a receptor harbouring 4 FRET donor and acceptor pairs per tetramer. The insertion sites were intracellular, a region which has eluded all of the structures of iGluRs solved to date (See *Introduction* 1.2). In the double labelled construct, the YFP variant Venus was inserted in the intracellular loop connecting the M1 and M2

transmembrane helices and the CFP was positioned in the C-terminal tail of each subunit. This construct showed a robust FRET signal at steady state conditions (Fig. 14 and 15).

One possible limitation of measuring FRET between fluorescent proteins is the sheer size of the donor and acceptor molecules. The diameter of the beta-sheet barrel of the GFP molecule is 24 Å (Ormö et al., 1996) which – assuming the orientation of the donor and the acceptor is parallel – leads to a minimum separation of 24 Å between donor and acceptor chromophores. Because of the steep distance dependence of the FRET efficiency, the distances between donor and acceptor can be reliably resolved within the range of $0.5R_0 - 1.5R_0$ (Ishikawa-Ankerholdt et al., 2012). From this it follows that higher R_0 of the donor-acceptor pair will lead to better distance resolution, whereas FRET pairs with lower R_0 values will be faced with the size limitations as the donor and acceptor approach the critical distance. In the case of mCerulean3-Venus FRET pair, with the R_0 being 51 Å, the lower limit of the FRET resolution is at the limit at which further approach of the molecules would be structurally hindered (25.5 vs. 24 Å, respectively), which allows sufficient range of distances and motion to be monitored. According to the crystal structure, the width of the transmembrane domain is 55 Å (Sobolevsky et al., 2009). Based on the four fold symmetrical geometry of the AMPA receptor TMD and the relative distance of 58 Å between the donor and acceptor (calculated based on steady state FRET efficiency), the acceptor and donor fluorophores form 2 concentric rings around the central axis of the receptor. Because of the closer relative distance of the I6 position to the membrane, the YFP in the loop is likely positioned under the M3 transmembrane helix of each subunit. With the C-terminal tail being longer and more flexible, the I10 insertion may give a similar FRET while orbiting the loop along a 90º arc. The distances measured through DPA quenching, however, limit the location of I10 in a state dependent manner to be within 14-37 Å separation from the membrane, likely extending outwards from the central axis of the receptor.

4.2.3 Extracellular binding of positive allosteric modulator Cyclothiazide induces a change in FRET in the intracellular region of GluA2

In cells expressing the intracellularly double labelled GluA2 homomers there was a notable decrease in the apparent FRET between CFP and YFP in presence of the positive allosteric modulator CTZ (Fig. 16 and 17). This decrease in FRET efficiency suggests an increase in the

separation between the donor and acceptor molecules. As indicated by the lack of CTZ induced FRET change in double labelled constructs with a mutated CTZ binding site (Partin et al., 1996), the effect was specific to the extracellular binding of CTZ. Interestingly there was no glutamate dependent change in the FRET efficiency. These findings suggest that a distinct conformation of the intracellular regions of the receptor exists in presence of extracellular modulators and without ion flow. CTZ molecules bind extracellularly at the LBD D1-D1 lobe interface and block receptor desensitisation (Armstrong and Gouaux, 2000). Seen as the FRET change occurring between the C-terminal and the M1M2 loop is ligand independent, the CTZ binding alone is responsible for the transduction of the signal to the intracellular region. This transduction can be seen as a stabilisation of the receptor from a flexible resting state to a more rigid conformation. A similar finding has been reported for the NMDA receptor using a FLIM FRET approach to monitor agonist induced changes in the C-terminal domain organisation (Dore et al., 2015). In this study an increase in distance of approximately 10 Å was detected in presence of agonist NMDA and channel blockers between C-terminally attached GFP and mCherry molecules on separate subunits. This change showed how an extracellular signal propagates throughout the receptor and reaches the intracellular domains independently of ion flow and channel opening.

The binding of CTZ could be monitored both functionally and optically as the onset of desensitisation block and the decrease in FRET efficiency (Fig. 17 B). The time resolution of these recordings was limited by the fluorescence acquisition rates (1 frame every 1.3 seconds), which depended on the time of mechanical switching between the fluorescence filter cubes in the turret of the microscope. Due to the approximately 1 s delay in acquisition and the poor temporal resolution the onset of the fluorescence signal seems to precede the functional block of desensitisation by CTZ. In practice however, the functional relief of desensitisation had a time constant of 1.5 ± 0.1 s (Fig. 17 B, current trace) and began 50 ms after the application of CTZ and glutamate. Correspondingly the first acquired fluorescence frame, which was 300 ms long, contained a mixture of activation, desensitisation and CTZ binding signal.

The fluorescence signal did not return back to baseline immediately after the application of CTZ. This is consistent with the slow recovery from CTZ potentiation of AMPA receptors (approximately 15 seconds) (Partin et al., 1994; Partin et al., 1996).

Because the present study is focused on genetically labelled receptors and recordings in whole cells, part of the fluorescence signal originates from intracellularly retained receptors as mentioned

previously. The membrane expression of the labelled receptors had no correlation with the measured FRET efficiency (Fig. 19 A) confirming that the fluorescence signal is a mixture of membrane expressed and intracellular receptors. During whole cell recordings the glutamate should not penetrate the cell membrane, whereas CTZ, being highly lipophilic, might. There was a moderate correlation between the membrane expression of the labelled receptors and the FRET change occurring during extracellular application of glutamate and CTZ (Fig. 19 B), suggesting that although some signal might arise from intracellular compartments, the majority of the FRET change comes from receptors expressed at the membrane.

4.2.4 Quenching of YFP in intracellular positions I6 and I10

Intracellularly inserted YFP in positions I6 and I10 was quenched by addition of 5µM DPA to different extents (Fig. 20). DPA has been reported in multiple studies as a non-fluorescent quencher and a suitable FRET acceptor to CFP, GFP and YFP (see *Introduction 1.6.2*). The absorption spectrum of DPA is broad and extents far into the blue region of the light spectrum, which ensures the overlap with the emission of various fluorescent proteins. Due to this difference between the DPA molecules and the various FPs the quenching extent is expected to be distinct. This was clearly visible for the membrane attached GFP and YFP- tk constructs (Fig. 20 C) which were quenched by 70 and 50%, respectively, despite being attached at the same distance from the membrane.

The difference in quenching between the YFP in positions I6 and I10 is likely due to the difference in their separation from the plasma membrane and subsequently from the DPA. In all insertions the FP is attached to the receptor by unstructured flexible linkers of 9 and 12 amino acids on the 3' and 5' sites, respectively. The I6 position is located in the intracellular loop connecting the M1 and M2 transmembrane helices, at the end of the M1 sequence. This means that the YFP in this position is separated from the membrane by only the 9 amino acids N-terminal linker. The I10 position on the other hand is located in the C-terminal tail, 27 amino acids downstream of the last residue of the M4 transmembrane helix, and additional 9 amino acids of the linker separate the fluorophore from the membrane.

The C-terminal tail of the GluA2 subunit contains phosphorylation sites relevant for receptor trafficking and function and binds multiple regulatory and scaffolding proteins, implying a flexible nature of this region (see *Introduction 1.2.4*). The C-terminal tail may adopt some secondary

structure motifs in the membrane proximal region, but is likely to be disordered at the end of the sequence to accommodate the direct binding of phosphatases and scaffold proteins.

A major limitation of the genetic labelling approach, as discussed in the chapter above, is the intracellular retention of fluorescently labelled receptors. The background fluorescence reduces the degree of DPA quenching, as intracellularly retained receptors will not interact with DPA molecules (Sjulson et al., 2008). The total fluorescence F measured contains two components:

$$F = QF_M + F_{IC}$$

Where Q ($Q = F_{DPA}/F$) is the ratio of donor fluorescence with the acceptor present to donor fluorescence in absence of acceptor, F_M is the fraction of fluorescence arising from membrane expressed receptors and F_{IC} represents the fraction of intracellularly retained receptors (Sjulson, 2008). When the background fluorescence component is minimised the total measured fluorescence can be approximated to the population of membrane expressed receptors. Optimisation of membrane trafficking is thus a major concern for future experiments. Higher expression rates of genetically labelled receptors will also ultimately enable patch clamp fluorometry as apposed to whole cell voltage fluorometry, eliminating the intracellular background fluorescence all together. The variation in membrane trafficking and expression (Fig. 12) of the I6 and I10 labelled receptors might also contribute to the difference in the DPA dependent quenching. Intracellular retention also applies to the membrane targeted GFP and YFP-tk constructs (Sjulson et al., 2008), making comparisons of actual membrane distances complicated.

4.2.5 State dependent motions of the intracellular domains

Patch clamp fluorometry of AMPA receptors with single YFP fusions in the intracellular region revealed that both the I6 and I10 positions move relative to the membrane during receptor gating. The state dependent quenching of YFP by DPA showed that the intracellular region of GluA2 essentially adopts three distinct conformations: resting, desensitised and active. Interestingly, two of the states are characterised by a closed ion channel pore, the resting and desensitised states, with the distinction that agonist is bound in one state (desensitised) and no agonist is present in the other (resting).

In non-desensitising conditions both the I6 and I10 positions move closer to the membrane, as indicated by the increase in relative DPA quenching. While receptor activation is driven primarily by the ligand binding domain, the closure of the cleft following agonist binding exerts a force on the LBD – TMD connective linkers, which can result in an upward movement of the entire transmembrane domain (Sobolevsky et al., 2009, Jin et al., 2009). The apparent movement of the YFP in position I6 relative to the membrane can be partly attributed to this global structural rearrangement. Further speaking to the gating related movement of the I6 position are the concentration sensitivity of the fluorescence signal in non-desensitising conditions and the similar time-constants of fluorescence onset and decay to the rates of activation (Fig. 22). The slower fluorescence onset in desensitising conditions, as compared to the rate of receptor desensitisation seen in the current trace, can be caused by the superposition of the activation fluorescence onto the desensitisation signal.

The molecular mechanism of desensitisation involves the reorganisation of the interface between the upper lobes within the LBD dimers (see *Introduction 1.3.2*) and an apparent transition to a four-fold symmetry of the LBDs (Meyerson et al., 2014) which is thought to release the tension in the LBD-TMD linker region, allowing closure of the ion channel while preserving the agonist bound conformation of the LBD lobes. Based on the quenching profiles, the intracellular region seems to adopt a conformation distinct from the resting state during receptor desensitisation, with the decrease in DPA induced quenching of both the I6 and I10 insertion sites indicating a movement away from the membrane.

Interestingly, the gating process is thought be independent of the structural variability of the ATDs, as deletion of the amino terminal domains has little effect on receptor function (Pasternack et al.its, 2002). The effect of C-terminal deletion of AMPA receptors, on the other hand, results in a change of receptor kinetics and influences the membrane trafficking (Suzuki et al., 2005). Although the entire intracellular region is either deleted or unresolved in all full length crystal structures to date, the position of the M1M2 loop containing the I6 insertion site can be inferred due to its relatively short sequence. The orientation and membrane relative position of the C-terminal tail, being considerably longer, is however difficult to pinpoint. The four CTDs of the tetrameric receptor may assemble into a predefined structure or act as flexible linkers to allow direct binding of scaffold proteins to the polypeptide chain. The CTD is subjected to a number of post-translational modifications such as phosphorylation which modulates functional properties of the AMPA

receptors (Derkach et al., 1999; Banke et al., 2000; Jenkins et al., 2014; Kristensen et al., 2011). Additionally, palmitoylation of a C-terminal cysteine, located proximal to the last transmembrane helix is thought to be regulated by AMPA receptor agonists (Hayashi et al., 2005). The movement of the I10 position within the C-terminal tail is thus likely to happen following rearrangements of the membrane proximal region of the domain, allowing association and modification of the region.

The state dependent rearrangements of the M1M2 loop and the C-terminal domain, as monitored by single and double component FRET, suggest that this region is able to transmit structural information from the extracellular domains across the plasma membrane to report the functional state of the receptor.

As mentioned above some evidence of the involvement of the C-terminal domain in receptor gating mechanism already exist. To show that the effect is bidirectional, that is the extracellular and intracellular domains are causally linked, further studies need to be done. To use the approach described in this study, the deletion of the C-terminal tail is not an option, as it decreases the membrane expression of the receptors and diminishes the fluorescence signal, thus greatly limiting the data acquisition. Constraint of the C-terminal tail and/or the intracellular loops in the membrane could perhaps provide some information on the functional effects of this region on the gating properties of the receptor.

4.2.6 Determination of state dependent distances of YFP in position I6 and I10

The state dependent quenching of YFP in intracellular positions I6 and I10 can be used to assess the distances of the insertion sites relative to the membrane. Determination of the apparent distances is not a straight forward procedure and the next part will focus on quenching measurements in distinct conditions: i) fixed acceptor position and ii) fixed donor position.

Initially the movement of the domains was monitored at a steadily held membrane potential, at which the acceptor DPA molecules reside in the other leaflet of the cell membrane (Chanda et al., 2005a). Since the position of the acceptor DPA molecules is fixed, the change in the quenching must arise from the movement of the labelled regions of the receptor. Because of the sixth power dependence of the FRET efficiency on the distance between the donor and acceptor molecules the quenching of YFP will change rapidly around the R_0, a distance at which half maximal energy transfer occurs, and will be less pronounced when the donor molecule is positioned either closer or

further away than the R_0. Based on the initial quenching profile the YFP in position I6 (Fig. 20), where the FRET efficiency $(1 - Q)$ is roughly 60%, the distance of the insertion site to the DPA molecules in the outer leaflet of the membrane can be estimated to be less than the R_0 of the YFP - DPA FRET pair, which is 31 Å (Wang et al., 2010). Taking into account the preferential position of DPA molecules in the outer leaflet of the membrane at the holding potential of − 60 mV, the thickness of the membrane (app. 50 Å) and the size of the FP molecule itself, this distance does not seem realistic. To control the reliability of the DPA quenching effects, GFP and YFP with a truncated C-terminal and a short membrane anchoring sequence of the k-ras protein were used (Wang et al., 2010). These anchored fluorescent proteins have been used in the development and optimisation of a genetically encoded voltage sensor, hVos (Chanda et al., 2005; Wang et al., 2011; Sjulson et al., 2008).

During the optimisation of the hVos system (Wang et al., 2010) different anchoring strategies were used to bring the membrane anchored FPs to an optimal distance to the membrane for achieving highest possible voltage driven change in fluorescence. The linkers connecting the FP to the k-ras anchoring motif were shortened yielding the truncated constructs termed "-tk", which were used in this study as controls. In the truncated versions the N and C-terminal tails of the FP were shortened by 7 and 6 amino acids, respectively. The regular FP-tk was attached to a 14 amino acid sequence of the k-ras anchoring motif at the C-terminal tail. The estimated distance from the membrane mid-plane was between 40 and 50 Å. Anchoring the FP at both the N- and C-terminal showed better resolved voltage dependent fluorescence change by bringing the FP closer to the membrane. In the double anchored constructs the FP was labelled at the N-terminal by a 20 amino acid linker and at the C-terminal by a 10 amino acid linker. The distance of this construct to the membrane mid-plane was estimated to be 40 Å. By comparison, the YFP in the I6 insertion site of the GluA2 subunit was attached by its N-terminal tail without alteration of the native sequence (apart from the start codon, which was deleted) by a 9 amino acid linker to the last residue in the M1 transmembrane helix and by a 12 amino acid linker and 22 amino acids of the loop to the M2 transmembrane helix at the C-terminal. The number of amino acids connecting the body of the FP to the membrane is thus: 16 at the N-terminal and 34 at the C-terminal. Arguably, the doubly anchored FP in the study by Wang et al., would be a better choice to compare the distance from the membrane, as opposed to the single anchored -tk FP. This would explain the higher quenching efficiency of YFP in I6 position

compared to the YFP with a -tk motif (Fig. 20) suggesting that the I6 insertion site is slightly closer, despite the longer linkers.

While the change in the quenching of YFP in positions I6 and I10 during glutamate application should only arise from membrane expressed receptors, determination of distances based on an initial degree of quenching is too prone to uncertainties. The quenching by DPA does not account for possible localisation of DPA molecules in the membranes of intracellular organelles, the potential which is not known and cannot be controlled through voltage clamp, leading to high variability of the signal.

A more reliable way to determine the apparent distances of the fluorescent probes from the membrane takes advantage of the voltage sensitive nature of DPA molecules (Fernandez et al., 1983; Chanda et al., 2005a; Chanda et al., 2005b; Sjulson et al., 2008; Wang et al., 2010). The DPA is thought to travel 25 Å from the outer to the inner leaflet of the membrane upon hyperpolarising voltage pulses (Wang et al., 2010). The quenching curves of YFP in positions I6 and I10 following voltage ramps ranging from -120 to 120 mV confirm the sensitivity of the system (Fig. 24). The measured state dependent half quenching voltages of the YFP in the I6 and I10 insertion sites were similar to the one obtained for the membrane attached YFP-tk, but could not provide a reliable measure for the membrane relative distances due to the shallowness of the curves. The steepness of the slopes of the quenching curves was likely influenced by the fraction of the electric field travelled by DPA during voltage ramps, which was determined to be 0.6 (Fernandez, 1983). It is also influenced by the probabilistic nature of DPA distribution in the membrane leaflets, which ensures that at the hyperpolarising voltages the density of DPA in the inner leaflet of the membrane is non-zero (Fernandez et al., 1983). The change of the fluorescence during the ramp could be read out of the curves providing information on the positions of the insertion sites relative to the membrane in distinct receptor states. The maximal changes in fluorescence for the membrane attached FPs are described in the studies by Wang et al. and Sjulson et al.. During DPA translocation this change is limited by the fluorophore distance from the membrane and the R_0. At closer FP to membrane distances the change will not be large due to saturation of the signal by DPA at both the outer leaflet and the inner leaflet of membrane. At larger distances the change in fluorescence will be limited by the distance itself, as the quenching at hyperpolarising voltages will not be able to saturate. This reasoning explains the fact that the change is largest for the resting states of both I6 and I10 positions, smaller for the active state — as the fluorophores approach the membrane — and

also smaller for the desensitised state — as the insertions sites move further away from the membrane. According to the predicted maximal change in quenching of the membrane bound probes described by Wang et al., choosing a donor with a larger spectral overlap, i.e., larger R_0, and increasing the distance that separates the fluorophore from the membrane will result in a moderate increase in the sensitivity of the system. For a fixed position of fluorophore insertion, as is the case for receptor fusions, choosing an FP with a higher spectral overlap, such as GFP or CFP, would have likely led to a decrease in the maximal fluorescence change achieved by voltage driven translocation of DPA molecules across the membrane.

4.3 Extracellular domains of AMPA receptors

4.3.1 Kinetic characterisation of extracellularly labelled receptors

As discussed above, several positions within the extracellular domains of the GluA2 subunit were permissive for insertion of various fluorescent proteins (Fig. 28). The kinetic characteristics of the labelled homotetrameric receptors were assessed by fast perfusion outside out patch clamp recordings. The deactivation and desensitisation of the labelled receptors were only slightly slower than that of WT receptors. These findings are consistent with kinetic measurements of AMPA receptors lacking the amino terminal domain and the ATD-LBD linkers (Pasternack et al., 2002), where the authors did not find a large influence of the ATD deletion on AMPA receptor fast gating kinetics. Another study suggests a role for the amino terminal domain in stabilisation of the desensitised state, biosynthesis and membrane targeting (Möykkynen et al., 2014). The minor differences in the deactivation and desensitisation rates of the extracellular fused receptors could thus be due a general perturbation of the receptor structure and stability of the distinct states. The recovery from desensitisation of the labelled receptors was essentially unaffected. Taken together these results justify using the FP fused AMPA receptors as surrogates for wild-type in functional studies.

4.3.2 Quenching of extracellularly inserted GFP by DPA

Based on the dimensions of AMPA receptor extracellular domains (Sobolevsky et al., 2009; Meyerson et al., 2014; Yelshanskaya et al., 2015) quenching FRET experiments with DPA were done with GFP at the insertion sites 388 and 391 due to the higher R_0 of the GFP-DPA pair (37 Å, Wang et al., 2010) as compared to YFP-DPA pair (31 Å). The GFP in insertion site 391 was quenched to a higher degree than GFP in site 383 indicating a difference in the position of the attached fluorophore relative to the membrane (Fig. 30). Overall the degree of quenching by DPA was low compared to what was detected for the intracellular domains and the intracellularly membrane attached GFP. The distances were approximated by calculating the probability of GFP quenching by a sheet of DPA molecules residing in the plane nearest to the FP insertion (the outer membrane leaflet) and corrected for the background fluorescence arising from intracellularly retained receptors (with the assumption that the background signal is similar to intracellularly tagged AMPA receptors). The average separation of the 383 and 391 positions to the membrane was 70 and 50 Å, respectively. Due to the high distance dependence of FRET the top 5% of quenching efficiency lies on a mostly flat curve and thus the position of the 383 inserted GFP relative to the membrane varies over a large range of distances.

Recently, the crystal structure of the full length AMPA receptor in the resting state was solved by Dürr et al.. In the crystals the extracellular domains of the receptor are measured to be approximately 91 Å, taken from roughly the midpoint of the ATD dimer interface to the end of the LBD-TMD linkers (the membrane). Although there is no reliant way of knowing precise position of the inserted FPs, keeping in mind the lever effect of the linkers and the substantial volume of the fluorescent proteins, the distances calculated for the 383 and 391 insertions sites fit into the scale presented by the crystal structure, with the 383 position being located beneath the ATD midpoint and the 391 site being located above the LBD D1 lobe. It should be noted that the GluA2 construct used for the crystallographic studies has been heavily modified to enhance thermal stability of the protein. Among the modifications is the deletion of 6 residues within the ATD-LBD linker (Sobolevsky et al., 2009). Superposition of the crystal structure on the cryo-EM structure of the antagonist bound receptor showed a larger (approximately 8 Å) separation of the ATDs from the LBDs in the unmodified receptor (Meyerson et al., 2014), which may be explained by the deletions in the linker region. This difference, however, is irrelevant for the 383 and 391 distances measured

by DPA quenching, as the furthest measured insertion site is located downstream of the region subjected to deletions in crystallographic studies. In contrast the structure of heteromeric GluA2/GluA3 receptors displays a largely unseparated ATD and LBDs in a resting state (Herguedas et al., 2016).

4.3.3 Probing the gating motions of the extracellular domains

Large structural rearrangements of AMPA receptor amino terminal domains during receptor desensitisation have been proposed in two separate full length structural studies (Dürr et al., 2014; Meyerson et al., 2014). In the first study (Dürr et al., 2014) a full length structure of AMPA receptor bound to a partial agonist fluorowillardiine (FW) with a subatomic resolution (8 Å) was solved. Here the structural arrangement of the amino terminal domain compared to the receptor resting state (solved in the same study) was asymmetrically bent down toward the LBDs. The length of the extracellular domains – as measured from the ATD interface midpoint to the end of LBD-TMD linkers – was reduced in the desensitised receptor state to approximately 70 Å as compared to 90 Å in resting state. Images from cryo EM showed multiple classes of ATD arrangement in presence of FW, suggesting that the desensitised state of receptor adopts various conformations, with the extremely bent ATDs as one of them.

Another study showed (with a 21 Å resolution at best) that ATD dimer interfaces in desensitising conditions in presence of quisqualate adopted various conformations (Meyerson et al., 2014). The authors suggest a high conformational heterogeneity of the AMPA receptor ATDs during receptor desensitisation, based on the three different classes of molecules found all with different degrees of ATD dimer separations. The desensitised state of the kainate receptor, in contrast, does not exhibit a dissociation of the tetrameric structure on the level of the ATDs in the desensitised state, suggesting that this conformational arrangement, as infrequently visited as it might be, is AMPAR specific (Meyerson et al., 2014).

Considering the large changes of the ATDs proposed by the structural studies, FRET between the extracellularly inserted FPs and DPA would provide a sensitive measure of the conformational rearrangements during receptor gating – dependent on the measured position and the initial degree of quenching in the resting state. There was, however, no detectable change in the fluorescence of GFP inserted at position 383 or 391 under desensitising and non-desensitising conditions (Fig. 31).

There could be several explanations as to why no orthogonal movements of the extracellular domains during receptor gating are detected. Firstly, if the proposed "bending" arrangement of the ATDs is indeed attained, it could be transient in nature and occur faster than the fluorescence acquisition rates (20Hz, corresponding to 50 ms). A fast transition in which the ATDs are folded upon the membrane and revert to the normal arrangement, would therefore occur faster than the rate of recovery from desensitisation. This point may be answered by faster acquisition rates.

In addition to the structural information, the large scale rearrangements of the ATDs were supported by all-atom molecular dynamics simulations (Krieger et al., 2015). It was, however, not possible to accurately (or even approximately) determine the energy or frequency of such bending events from the simulations, and the rate of the proposed transitions is still unclear. The structural bending of the ATDs has also been proposed to be involved in the interaction and regulation of AMA receptor complexes with auxiliary subunits (Cais et al., 2014; Constals et al., 2015). Firstly, ATDs were proposed to form interactions with the extracellular portion of TARPs (Cais et al., 2014), which would require a large degree of structural rearrangement, as the TARP extracellular loop (which is important for receptor modulation (Priel et al., 2005; Tomita et al., 2005; Turetsky et al., 2005))) does not extend further than the D2 lobe of the LBDs (Twomey et al., 2016; Zhao et al., 2016). Secondly, the structural rearrangements of the ATDs were proposed to induce complex dissociation (Constals et al., 2015). According to these notions, the conformational rearrangements of the ATDs should be preserved in AMPA-TARP complexes. FRET between extracellularly-labelled AMPARs and TARPs in functional complexes, however, failed to show large transitions of the ATDs during desensitisation (Fig. 39).

An alternative explanation of the lack of optically detected ATD motions would be that the proposed transitions occur on a much slower timescale following sustained exposure to agonist. Based on the recordings shown in figures 31 and 39, the exposure to glutamate should exceed 500 ms.

As mentioned above, the conformational state in which the ATDs are fully separated may be rather rare, based on the heterogeneity of the crystal structures obtained to date, which means that it would also be difficult to capture optically because it wold correspond to a minor population of receptors.

4.3.4 Intra-receptor FRET between YFP and CFP in positions 383 and 391

To monitor FRET between the extracellular domains a mixture of GluA2 subunits labelled with either donor CFP or acceptor YFP in positions 383 and 391 were used (Fig. 32). The measured apparent FRET efficiency between CFP and YFP in different positions could be translated into donor – acceptor distances (Fig. 33) consistent with the dimensions of the AMPA receptor ligand binding and amino terminal domains (Sobolevsky et al., 2009). As described by Miranda et al. in 2013 the highest contribution of FRET likely comes from the closest neighbours of donor and acceptor fluorophores. In the case of the AMPA receptor the distances between the closest possible neighbouring CFP and YFP molecules mapped arbitrarily onto the domains correspond well to the measured distances during FRET recordings.

Despite being in close enough proximity for FRET to occur in both insertion sites, no state dependent change between CFP and YFP energy transfer was seen for either the 383 or 391 insertion site. This can be due a lack of lateral movement of the domains during receptor gating, although a transition from 2 - to 4-fold symmetry of the ligand binding domain during receptor desensitisation has been proposed (Meyerson et al., 2014).

4.3.5 FRET between acceptor labelled Stargazin and donor labelled GluA2

Stargazin molecules were labelled with a FRET acceptor mTagRFP-T extracellularly by creating Stargazin – Neto2 chimeras. The Neto2 transmembrane domain was chosen due to the lack of interaction with AMPA receptors (Zhang et al., 2009) and utilised to invert the cellular position of the N-terminal tail of Stargazin to face the exterior of the cell. The modulation of GluA2 receptors by stargazin was not interrupted suggesting that the stargazin chimera forms functional complexes with AMPA receptors.

Fluorescent labelling of Stargazin essentially serves multiple purposes. Firstly it provides a static receptor attached FRET reference point to monitor conformational dynamics of the GluA2 extracellular domains tagged with a FRET donor. Secondly it enables direct visualisation of receptor - TARP interaction and complex dynamics in real time.

Steady state FRET efficiency between GluA2 receptor with GFP in positions 383 and 391 and RFP-Stargazin (Fig. 38) allowed an approximation of donor acceptor distances in functional complexes. The distances between the donor in positions 383 and 391 to RFP acceptor were 64 and 57 Å, respectively. These distances are similar to the ones obtained through DPA quenching experiments (see *Discussion 4.3.2*) and are in agreement with the dimensions of the extracellular domains.

The stoichiometry of AMPAR – TARP complexes has been investigated in numerous studies (Hastie et al., 2013; Milstein et al., 2007; Kim et al., 2010). The general consensus is that the number of TARP molecules per AMPA receptor tetramer is highly variable. It has been reported that a single associated TARP is sufficient for the modulation of receptor kinetics (Kim et al., 2010). The stoichiometry varies from a single TARP molecule to four TARPs per complex at most (Kim et al., 2010; Milstein et al., 2007) and is dependent on the expression levels of the TARPs. The number of associated TARP molecules in complex with a receptor cannot be discerned from the FRET measurements, as a single acceptor is sufficient for FRET to occur.

4.3.6 Receptor - TARP complex dissociation

Several mechanisms of the dynamics of TARP and AMPA receptor complexes have been proposed (Semenov et al., 2012; Tomita et al., 2004; Morimoto-Tomita et al., 2009; Constals et al., 2015; Carbone and Plested, 2016). High concentrations and prolonged application of glutamate have been reported to induce complex dissociation on a millisecond time scale (Tomita et al., 2004; Morimoto-Tomita et al., 2009). By comparing a tandem AMPA receptor – stargazin complex and co-expression of AMPA with stargazin the authors propose that receptor desensitisation is responsible for the change in receptor modulation at high glutamate concentrations (Morimoto-Tomita et al., 2009). Recently published data, however, indicates that a co-expression of AMPA receptors and TARPs likely results in a mixed population of TARP-associated and "single" receptors at the cell membrane (Carbone and Plested, 2016). It is thus conceivable that the difference in the modulation of the tandem and receptors co-expressed with a TARP arises from the mixture of the TARPed and unTARPed complexes present in the recordings. Another observation in favour of glutamate driven complex dissociation was the increased mobility of desensitised AMPA receptors at the synapse of cultured rat hippocampal neurons (Constals et al., 2015). The authors suggest that conformational changes following receptor desensitisation, as proposed by the recent crystal structures (Dürr et al.,

2014; Meyerson et al., 2014), lead to AMPA – TARP dissociation and the subsequent release of AMPA receptors from the synapse. FRET experiments using fluorescently labelled AMPARs and TARPs, which enabled direct visualisation of the complexes, prolonged application of saturating concentrations of glutamate resulted in a mere 5% decrease in FRET efficiency between GluA2 with a GFP in position 391 and RFP-stargazin (Fig. 40). The decrease began to develop 30 seconds following the pulse and could potentially be attributed to a dissociation of a small fraction of receptor complexes, but on a timescale that exceeds any physiological relevance. The dissociated fraction was not detectable functionally, as there was no significant change in current rectification during ramps in the beginning and end of a 50 s glutamate pulse. In terms of physiological relevance, the presumed dissociation of AMPARs from their TARP complexes, which anchor the receptors at the postsynaptic density (Schnell et al., 2002; Bats et al., 2007, Opazo et al., 2010), is proposed to facilitate and increase the rate of the recovery of the synapse from a desensitisation-dependent depression resulting from sustained activation in the range of 10-100 Hz (Heine et al., 2008; Frischknecht et al., 2009). Depression of excitatory synaptic transmission following high frequency stimulation may be attributed to both pre- and postsynaptic factors. Among the postsynaptic responses, AMPA and Kainate receptor desensitisation and recovery from desensitisation is thought to play a key role in determining the time course of EPSCs (Colquhoun et al., 1992). The synaptic response to high frequency stimulation varies across different regions of the hippocampus, with a decrease of excitatory postsynaptic potential in dentate gyrus cells and an increase in CA3 and CA1 pyramidal cells (Alger and Taylor, 1976). AMPA receptor desensitisation and recovery are thus differentially regulated in the different brain regions, likely by the different distributions of TARPs (Tomita et al., 2003). Indeed, the various TARPs affect AMPAR desensitisation and recovery differently, with stargazin and other members of type I TARPs reducing the rate of receptor desensitization and speeding up the recovery from desensitisation (Priel et al., 2005; Turetsky et al., 2005) and gamma-5 TARP having the opposite effect on desensitisation (increased rates) (Kato et al., 2007). Since the recovery of the receptor is affected by the presence of TARPs, it is possible to speculate that dissociation of complexes does not occur during receptor desensitisation. Furthermore, structural rearrangements of the AMPAR ATDs during receptor desensitisation (Meyerson et al., 2014) are proposed to drive said dissociation (Constals et al., 2015). In present study, however, no such rearrangements were detected (Fig. 31 and *Discussion 4.3.3*). Newly released structures of full length AMPA receptors in complex with

stargazin (Twomey et al., 2016; Zhao et al., 2016), showing that the interaction sites within the complex are mainly concentrated at the interface between transmembrane domains and the extracellular loop of stg and the lower lobes of the LBDs, also speak to a lack of ATD-TARP interaction.

An alternative interactive dynamic of AMPA receptors and stargazin was proposed in the recent study by Carbone and Plested, where a two state model of stargazin conformation was described. The study suggests that modulation of AMPA receptors by stargazin can be segregated into different domain interactions. The relief of polyamine block, seen for TARPed AMPA receptors at positive membrane potentials, is thought to arise from transmembrane interactions, whereas modulation of receptor kinetics takes place at the extracellular domains. During prolonged exposure to glutamate, no change in relief of polyamine block was observed for the fluorescently labelled AMPAR–TARP complexes (Fig. 40), in agreement with the idea that different interaction sites within the complex are responsible for kinetic modulation (extracellular) and effects on pore pharmacology by stargazin (transmembrane).

To date, no direct visualisation of AMPA – TARP complexes has been described. The FRET data (Fig. 40) does not support dissociation of a large population of TARPed receptors, optically or functionally. Further studies of the complex dynamics need to be done to fully confirm this statement.

4.4 Insertion of circularly permuted GFP

Circularly permuted GFP (Baird et al., 1999; Marvin et al., 2011; Marvin et al., 2013) was inserted in three different positions of the GluA2 subunit: the intracellular I6 site and extracellular 383 and 391 sites (Fig. 41). Expression levels of fused receptors based on whole cell currents varied markedly between positions, highlighting the sensitivity of insertion regions. AMPA receptors with intracellularly inserted cpGFP showed significantly lower whole cell currents compared to the extracellularly tagged counterparts and wild-type receptors. The difference in membrane expression of cpGFP in I6 and YFP in identical position is likely due to the shortening of the linkers by which cpGFP and YFP are attached (2 vs. 9 amino acids on the N-terminal end, respectively). Two criteria determine the response efficacy of cpGFP to conformational rearrangements of the insertion site (Marvin et al., 2011; Marvin et al., 2013). First the ability of the insertion site of the host protein

must be able to transduce the global conformational change to the local environment of the cpGFP chromophore. With the large changes in the extracellular domains during AMPA receptor gating (Dürr et al., 2014; Meyerson et al., 2014) and the general tolerance of the ATD-LBD linker for FP insertion, the positions 383 and 391 seemed to be able to accommodate the first criteria. The movements of the intracellular region during gating (*Discussion* 3.2.5) also made it a target for inserting the cpGFP.

The linker connecting the cpGFP to insertion site was shown to be crucial for optimisation of single wavelength sensors, as random mutations produced variants of maltose (Marvin et al., 2011) and glutamate (Marvin et al., 2013) sensors with a ΔF/F ranging from 300 - 450%. The linker used for GluA2 cpGFP insertion was the same as described for the glutamate sensor iGluSnFR (Marvin et al., 2013) consisting of LV and NP residues on the N- and C-terminal ends of cpGFP, respectively.

During receptor gating cpGFP in position 391 exhibited a small glutamate dependent decrease in fluorescence (Fig. 42), suggesting that the structural rearrangements within the extracellular domains can be translated into a fluorescence signal. Although it is not possible to predict the influence of the linkers within individual insertion sites, their optimisation within the functional GluA2-cpGFP fusions could thus potentially yield single wavelength reporters of AMPA receptor activity.

5. Future perspectives – creating optical reporters of glutamate receptor activity

In the present study the permissiveness of AMPA receptors for genetic incorporation of fluorescent proteins has been described. Using the fluorescently labelled receptors allowed us to discern the structural rearrangements underlying the functional transitions of the receptor during the gating process.

With the fluorescently labelled AMPA receptor and the patch clamp fluorometry technique we have achieved the means of a direct optical readout of receptor gating motions in real time. Several questions about the AMPA receptor structural dynamics remain unanswered. How does heteromerisation of AMPA receptor subunits influence the domain arrangements and the conformational changes occurring during gating? In light of the recent structure of the full-length GluA2/A3 heteromer, the overall shape and architecture of the receptor might be different (Herguedas et al., 2016). These differences may be probed by fluorescent insertions within the different AMPAR subunits, based on the highly conserved features among them. Transitions of the intracellular and extracellular domains of the AMPAR in complex with the auxiliary subunits, may likewise be assessed. Additionally, AMPAR and TARP complex dynamics could be visualised in a physiologically relevant environment, such as cultured neurones and slice preparations, as the genetic incorporation surpasses several of the caveats associated with the chemical labelling techniques.

Through the course of this study the optical readout system has been simplified from a double wavelength FRET approach (CFP and YFP fusions) to two-component single wavelength approach (YFP and DPA) and finally to a single wavelength approach (cpGFP). A genetically encoded single wavelength reporter of AMPAR activity is a highly sought-after goal as it may be used as a potential sensor of excitatory neurotransmission in physiological and pathophysiological conditions, and may help to elucidate the molecular bases of the numerous processes the AMPA receptors are involved in.

Bibliography

Alger, B., & Teyler, T. (1976). Long-term and short-term plasticity in the CA1, CA3 and Dentate regions of the rat hippocampal slice. *Brain Research*, *110*, 463–480.

Anggono, V., & Huganir, R. L. (2012). Rgulation of AMPA receptor traffcking and synaptic plasticity. *Curr Opin Neurobiol. 22*(3), 461–469.

Aow, J., Dore, K., & Malinow, R. (2015). Conformational signaling required for synaptic plasticity by the NMDA receptor complex. *Proceedings of the National Academy of Sciences of the United States of America, 112* (47), 14711-14716.

Armstrong, N., & Gouaux, E. (2000). Mechanisms for Activation and Antagonism of an AMPA-Sensitive Glutamate Receptor : Crystal Structures of the GluR2 Ligand Binding Core, *Neuron, 28*, 165–181.

Armstrong, N., Jasti, J., Beich-Frandsen, M., & Gouaux, E. (2006). Measurement of Conformational Changes accompanying Desensitization in an Ionotropic Glutamate Receptor. *Cell*, *127*(1), 85–97.

Armstrong, N., Sun, Y., & Chen, G. (1998). Structure of a glutamate- receptor ligand-binding core in complex with kainate, *Nature, 395,* 913–917.

Ayalon, G., Segev, E., Elgavish, S., & Stern-bach, Y. (2005). Two Regions in the N-terminal Domain of Ionotropic Glutamate Receptor 3 Form the Subunit Oligomerization Interfaces That Control Subtype-specific Receptor Assembly. *The journal of Biological Chemistry, 280*(15), 15053–15060.

Ayalon, G., & Stern-bach, Y. (2001). Functional Assembly of AMPA and Kainate Receptors Is Mediated by Several Discrete Protein-Protein Interactions. *Neuron*, *31*, 103–113.

Baird, G. S., Zacharias, D. a, & Tsien, R. Y. (1999). Circular permutation and receptor insertion within green fluorescent proteins. *Proceedings of the National Academy of Sciences of the United States of America*, *96*(20), 11241–11246.

Banke, T. G., Bowie, D., Lee, H., Huganir, R. L., Schousboe, A., & Traynelis, S. F. (2000). Control of GluR1 AMPA Receptor Function by cAMP-Dependent Protein Kinase. *The Journal of Neuroscience*, *20*(1), 89–102.

Baranovic, J., Chebli, M., Salazar, H., Carbone, A. L., Faelber, K., Lau, A. Y., … Plested, A. J. R. (2016). Article Dynamics of the Ligand Binding Domain Layer during AMPA Receptor Activation. *Biophysj*, *110*(4), 896–911.

Barbour, B., Keller, B. U., Llano, I., & Marty, A. (1994). Prolonged Presence of G lutamate during Excitatory Synaptic Transmission to Ceiebellar Ptirkihje Cells, *Neuron, 12*, 1331–1343.

Bastiaens, P. I. H., & Squire, A. (1999). Fluorescence lifetime imaging microscopy : spatial resolution of biochemical processes in the cell, *Trends in Cell Biology, 9*, 48–52.

Bats, C., Groc, L., & Choquet, D. (2007). The Interaction between Stargazin and PSD-95 Regulates AMPA Receptor Surface Trafficking. *Neuron*, *53*, 719–734.

Bats, C., Soto, D., Studniarczyk, D., Farrant, M., & Cull-candy, S. G. (2012). Channel properties reveal differential expression of TARPed and TARPless AMPARs in stargazer neurons, *Nature Neuroscience, 15*(6).

Bedoukian, M. a, Weeks, A. M., & Partin, K. M. (2006). Different domains of the AMPA receptor direct stargazin-mediated trafficking and stargazin-mediated modulation of kinetics. *The Journal of Biological Chemistry*, *281*(33), 23908–21.

Birdsey-benson, A., Gill, A., Henderson, L. P., & Madden, D. R. (2010). Enhanced Efficacy without Further Cleft Closure : Reevaluating Twist as a Source of Agonist Efficacy in AMPA Receptors, *The Journal of Neuroscience, 30*(4), 1463–1470.

Blunck, R., Starace, D. M., Correa, A. M., & Bezanilla, F. (2004). Detecting rearrangements of shaker and NaChBac in real-time with fluorescence spectroscopy in patch-clamped mammalian cells. *Biophysical Journal*, *86*(6), 3966–3980.

Bowie, D., & Mayer, M. L. (1995). Inward rectification of both AMPA and kainate subtype glutamate receptors generated by polyamine-mediated ion channel block. *Neuron*, *15*(2), 453–462.

Bredt, D. S., & Nicoll, R. A. (2003). AMPA Receptor Trafficking at Excitatory Synapses, *Neuron, 40*, 361–379.

Brien, R. J. O., Kamboj, S., Ehlers, M. D., Rosen, K. R., Fischbach, G. D., Huganir, R. L., & Hughes, H. (1998). Activity-Dependent Modulation of Synaptic AMPA Receptor Accumulation, *Neuron, 21*, 1067–1078.

Burnashev, N., Monyer, H., & Seeburg, P. H. (1992). Divalent Ion Permeability of AMPA Receptor Channels Is Dominated by the Edited Form of a Single Subunit. *Neuron, 8*, 189–198.

Cais, O., Herguedas, B., Greger, I. H., Cais, O., Herguedas, B., Krol, K., … Greger, I. H. (2014). Mapping the Interaction Sites between AMPA Receptors and TARPs

Reveals a Role for the Receptor N-Terminal Domain in Channel Gating. *CellReports*, *9*(2), 728–740.

Carbone, A. L., & Plested, A. J. R. (2016). Superactivation of AMPA receptors by auxiliary proteins. *Nature Communications*, *7*, 1–12.

Cardullo, R. A., & Parpura, V. (2003). Fluorescence Resonance Energy Transfer Microscopy : Theory and Instrumentation, *72*, 415–430.

Cha, A., & Bezanilla, F. (1997). Characterizing Voltage-Dependent Conformational Changes in the Shaker K 1 Channel with Fluorescence. *Neuron*, *19*, 1127–1140.

Cha, A., & Bezanilla, F. (1998). Structural Implications of Fluorescence Quenching in the Shaker K 2 Channel. *J. Gen. Physiol.*, *112*(October), 391–408.

Cha, A., Ruben, P. C., George, A. L., Fujimoto, E., & Bezanilla, F. (1999). Voltage Sensors in Domains III and IV , but Not I and II , Are Immobilized by Na 1 Channel Fast Inactivation. *Neuron*, *22*, 73–87.

Cha, A., Snyder, G. E., Selvin, P. R., & Bezanilla, F. (1999). Atomic scale movement of the voltage-sensing region in a potassium channel measured via spectroscopy. *Nature*, *946*, 809–813.

Chanda, B., Asamoah, O. K., & Bezanilla, F. (2004). Coupling Interactions between Voltage Sensors of the Sodium Channel as Revealed by Site-specific Measurements The Journal of General Physiology. *The Journal of General Physiology*, *123*, 217–230.

Chanda, B., & Bezanilla, F. (2002). Tracking Voltage-dependent Conformational Changes in Skeletal Muscle Sodium Channel during Activation, *The Journal of General Physiology*, *120*, 629-645.

Chanda, B., Blunck, R., Faria, L. C., Schweizer, F. E., Mody, I., & Bezanilla, F. (2005). A hybrid approach to measuring electrical activity in genetically specified neurons. *Nature Neuroscience*, *8*(11).

Chanda, B., Kwame Asamoah, O., Blunck, R., Roux, B., & Bezanilla, F. (2005). Gating charge displacement in voltage-gated ion channels involves limited transmembrane movement. *Nature*, *436*(7052), 852–856.

Chang, Y., & Weiss, D. S. (2002). Site-specific fluorescence reveals distinct structural changes with GABA receptor activation and antagonism. *Nature Neuroscience*, *241*, 1163–1168.

Chen, L., Chetkovich, D. M., Petralia, R. S., Sweeney, N. T., Kawasaki, Y., Wenthold, R. J., Bredt, D. S., Nicoll, R. A. (2000). Stargazin regulates synaptic targeting of

AMPA receptors by two distinct mechanisms. *Nature, 408,* 936-943

Chen, L., Dürr, K. L., & Gouaux, E. (2014). X-ray structures of AMPA receptor -cone snail toxin complexes illuminate activation mechanism. *Science*, *345*.

Cho, C., St-gelais, F., Zhang, W., Tomita, S., & Howe, J. R. (2007). Two Families of TARP Isoforms that Have Distinct Effects on the Kinetic Properties of AMPA Receptors and Synaptic Currents, *Neuron, 55,* 890–904.

Choi, U. B., Kazi, R., Stenzoski, N., Wollmuth, L. P., Uversky, V. N., & Bowen, M. E. (2013). Modulating the intrinsic disorder in the cytoplasmic domain alters the biological activity of the N-methyl-D-aspartatesensitive glutamate receptor. *Journal of Biological Chemistry*, *288*(31), 22506–22515.

Chudakov, D. M., Matz, M. V, Lukyanov, S., & Lukyanov, K. A. (2010). Fluorescent Proteins and Their Applications in Imaging Living Cells and Tissues. *Physiological Reviews*, *90*, 1103–1163.

Chung, H. J., & Steinberg, J. P. (2003). Requirement of AMPA Receptor GluR2 Phosphorylation for Cerebellar Long-Term Depression, *Science, 300*, 1751–1756.

Clayton, A., Siebold, C., Gilbert, R. J. C., Sutton, G. C., Harlos, K., Mcilhinney, R. A. J., … Aricescu, A. R. (2009). Crystal Structure of the GluR2 Amino-Terminal Domain Provides Insights into the Architecture and Assembly of Ionotropic Glutamate Receptors. *Journal of Molecular Biology*, *392*(5), 1125–1132.

Clegg, R. M. (1995). Fluorescence resonance energy transfer, *6*, 103–110.

Clegg, R. M. (1996). THE HISTORY OF FRET : From conception through the labors of birth, 1–45.

Collingridge, G. L., Isaac, J. T. R., & Wang, Y. T. (2004). RECEPTOR TRAFFICKING AND SYNAPTIC PLASTICITY, *Nature Reviews Neuroscience, 5*, 952–962.

Colquhoun, B. Y. D., Jonas, P., & Sakmann, B. (1992). Action of brief pulses of glutamate on AMPA/Kainate receptors in patches from different neurones of rat hippocampal slices, *Journal of Physiology, 458,* 261–287.

Constals, A., Penn, A. C., Hosy, E., Choquet, D., Phillipat, A., Retailleau, N., & Hafner, A. (2015). Glutamate-Induced AMPA Receptor Desensitization Increases Their Mobility and Modulates Short-Term Plasticity through Unbinding from Stargazin. *Neuron, 85,* 787-803

Cooper, D. R., Dolino, D. M., Jaurich, H., Shuang, B., Ramaswamy, S., Nurik, C. E., … Landes, C. F. (2015). Conformational Transitions in the Glycine-Bound GluN1

NMDA Receptor. *Biophysj*, *109*(1), 66–75.

Cortese, M. S., Uversky, V. N., & Dunker, A. K. (2008). Intrinsic disorder in scaffold proteins : Getting more from less, *Progress in Biophysics and Molecular Biology 98*, 85–106.

Craggs, T. D. (2009). Gree fluorescent protein: structure, folding and chromophore maturation. *Chem. Soc. Rev*, *38*, 2865–2875.

Dahan, D. S., Dibas, M. I., Petersson, E. J., Auyeung, V. C., Chanda, B., Bezanilla, F., Dougherty, D.A., Lester, H. A. (2004). A fluorophore attached to nicotinic acetylcholine receptor betaM2 detects productive binding of agonist to the alpha-delta site. *Proceedings of the National Academy of Sciences*, *101*(27), 10195–10200.

Dale, R. E., Eisinger, J., & Blumberg, W. E. (1979). The orientational freedom of molecular probes. The orientation factor in intramolecular energy transfer. *Biophysical Journal*, *26*(2), 161–193.

Danysz, W., & Parsons, C. G. (2003). The NMDA receptor antagonist memantine as a symptomatological and neuroprotective treatment for Alzheimer's disease : preclinical evidence, *Int J Geriatr Psychiatry*, *18,* 23-32

Dawe, G. B., Musgaard, M., Aurousseau, M. R. P., Nayeem, N., Green, T., Biggin, P. C., … Biggin, P. C. (2016). Distinct Structural Pathways Coordinate the Distinct Structural Pathways Coordinate the Activation of AMPA Receptor-Auxiliary Subunit Complexes. *Neuron*, *89*(6), 1264–1276.

Derkach, V. A., Oh, M. C., Guire, E. S., & Soderling, T. R. (2007). Regulatory mechanisms of AMPA receptors in synaptic plasticity, *Nature Reviews Neuroscience, 8*, 101–113.

Derkach, V., Barria, A., & Soderling, T. H. R. S. (1999). Ca 2+⁻calmodulin-kinase II enhances channel conductance of alpha -amino-3-hydroxy-5-methyl-4-isoxazolepropionate type glutamate receptors. *Proceedings of the National Academy of Sciences*, *96*(March), 3269–3274.

Dev, K. K., Nishimune, A., Henley, J. M., & Nakanishi, S. (1999). The protein kinase C a binding protein PICK1 interacts with short but not long form alternative splice variants of AMPA receptor subunits, *Neuropharmacology, 38*, 635–644.

DiFranco, M., Capote, J., Quiñonez, M., & Vergara, J. L. (2007). Voltage-dependent dynamic FRET signals from the transverse tubules in mammalian skeletal muscle fibers. *The Journal of General Physiology*, *130*(6), 581–600.

Digregorio, D. A., Rothman, J. S., Nielsen, T. A., & Silver, R. A. (2007). Desensitization Properties of AMPA Receptors at the Cerebellar Mossy Fiber – Granule Cell Synapse, *The Journal of neuroscience, 27*(31), 8344–8357.

Dingledine, R., Borges, K., Bowie, D., & Traynelis, S. F. (1999). The glutamate receptor ion channels. *Pharmacol Rev, 51*(1), 7–61.

Dingledine, R., Hume, R. I., & Channels, N. G. R. (1992). Dingledine R , Hume RI & Heinemann SF . Structural determinants of barium permeation and rectification in non-NMDA glutamate receptor channels . *J Neurosci, 12* .

Dong, H., O'brien, R. J., Fung, E. T., Lanahan, A. A., Worley, P. F., & Huganir, R. L. (1997). GRIP: a synaptic PDZ domain-containing protein that interacts with AMPA receptors. *Nature, 386*.

Dong, H., Zhang, P., Song, I., Petralia, R. S., Liao, D., & Huganir, R. L. (1999). Characterization of the Glutamate Receptor-Interacting Proteins GRIP1 and GRIP2, *The Journal of neuroscience 19*(16), 6930–6941.

Dong, H., & Zhou, H.-X. (2011). Atomistic mechanism for the activation and desensitization of an AMPA-subtype glutamate receptor. *Nature Communications*, *2*, 354.

Dore, K., Aow, J., & Malinow, R. (2015). Agonist binding to the NMDA receptor drives movement of its cytoplasmic domain without ion flow. *Proceedings of the National Academy of Sciences*, *112*(47), 14705–14710.

Dore, K., Labrecque, S., Tardif, C., & Koninck, P. De. (2014). FRET-FLIM Investigation of PSD95-NMDA Receptor Interaction in Dendritic Spines ; Control by Calpain , CaMKII and Src Family Kinase. *PloS One*, *9*(11).

Du, M., Reid, S. A., & Jayaraman, V. (2005). Accelerated Publication Conformational Changes in the Functional Ionotropic Glutamate Receptor. *The Journal of Biological Chemistry*, *280*(10), 8633–8636.

Dürr, K. L., Chen, L., Stein, R. A., Zorzi, R. De, Folea, I. M., Walz, T., Gouaux, E. (2014). Structure and Dynamics of AMPA Receptor GluA2 in Resting , Pre-Open , and Desensitized States. *Cell 158,* 778-792

Erickson, M. G., Alseikhan, B. A., Peterson, B. Z., & Yue, D. T. (2001). Preassociation of Calmodulin with Voltage-Gated Ca 2+ Channels Revealed by FRET in Single Living Cells, *Neuron 31*, 973–985.

Fernández, J. M., Taylor, R. E., & Bezanilla, F. (1983). Induced capacitance in the squid giant axon. Lipophilic ion displacement currents. *The Journal of General*

Physiology, *82*(3), 331–346.

Frischknecht, R., Heine, M., Perrais, D., Seidenbecher, C. I., Choquet, D., & Gundelfinger, E. D. (2009). Brain extracellular matrix affects AMPA receptor lateral mobility and short-term synaptic plasticity. *Nature Publishing Group, 12*(7), 897–904.

Fukata, Y., Tzingounis, A. V, Trinidad, J. C., Fukata, M., Burlingame, A. L., Nicoll, R. A., & Bredt, D. S. (2005). Molecular constituents of neuronal AMPA receptors, *The Journal of Cell Biology* 169(3), 399–404.

Furukawa, H. (2012). Structure and function of glutamate receptor amino terminal domains, *J Physiol. 509*(1), 63–72.

Furukawa, T., Hoshino, S., & Kobayashi, S. (2003). Cerebral Edema , and Neurological Motor Deficits after Experimental Brain Injury in Rats, *journal of neurotrauma 20*(3), 269–278.

Gan, Q., Dai, J., Zhou, H.-X., & Wollmuth, L. P. (2016). The Transmembrane Domain Mediates Tetramerization of alpha-Amino-3-hydroxy-5-methyl-4-isoxazolepropionic Acid. *The Journal of Biological Chemistry, 291*(12), 6595–6606.

Geiger, J. R. P., Melcher, T., Koh, D., Sakmann, B., Seeburg, P. H., Jonas, P., & Monyer, H. (1995). Relative Abundance of Subunit mRNAs Determines Ca2+ Permeability of AMPA receptors in principal neurons and Interneurons in Rat CNS. *Neuron*, *15*, 193–204.

Giraldez, T., Hughes, T. E., & Sigworth, F. J. (2005). Generation of Functional Fluorescent BK Channels by Random Insertion of GFP Variants. *The Journal of General Physiology, 126*(5), 429–438.

Glauner, K. S., Mannuzzu, L. M., Gandhi, C. S., & Isacoff, E. Y. (1999). Spectroscopic mapping of voltage sensor movement in the Shaker potassium channel. *Nature, 402*(December), 813–817.

Gonzalez, J., Du, M., Parameshwaran, K., Suppiramaniam, V., & Jayaraman, V. (2010). Role of dimer interface in activation and desensitization in AMPA receptors. *PNAS, 107*(21), 9891-9896

Gonzalez, J., Rambhadran, A., Du, M., & Jayaraman, V. (2008). LRET Investigations of Conformational Changes in the Ligand Binding Domain of a Functional AMPA Receptor †, *Biochemistry 47,* 10027–10032.

Granger, A. J., & Nicoll, R. A. (2014). LTD expression is independent of glutamate

receptor subtype. *Front. Synaptic Neurosci.*, *6*(July), 1–5.

Hashimoto, K., Fukaya, M., Qiao, X., Sakimura, K., & Watanabe, M. (1999). Impairment of AMPA Receptor Function in Cerebellar Granule Cells of Ataxic Mutant Mouse Stargazer, *The Journal of Neuroscience 19*(14), 6027–6036.

Hastie, P., Ulbrich, M. H., Wang, H., Arant, R. J., Lau, A. G., & Zhang, Z. (2013). AMPA receptor / TARP stoichiometry visualized by single-molecule subunit counting, *PNAS 110*(13), 5163-5168.

Hayashi, T., Rumbaugh, G., & Huganir, R. L. (2005). Differential Regulation of AMPA Receptor Subunit Trafficking by Palmitoylation of Two Distinct Sites. *Neuron*, *47*, 709–723.

Heine, M., Groc, L., Frischknecht, R., Bé, J., Lounis, B., Rumbaugh, G., … Choquet, D. (2008). Surface Mobility of Postsynaptic AMPARs Tunes Synaptic Transmission. *Science*, *320*(April).

Herguedas, B., García-nafría, J., Cais, O., Fernández-leiro, R., Krieger, J., Ho, H., & Greger, I. H. (2016). Structure and organization of heteromeric AMPA-type glutamate receptors. *Science*, *352*(6285).

Hestrin, S. (1993). Different Glutamate Receptor Channels Mediate Fast Excitatory Synaptic Currents in Inhibitory and Excitatory Cortical Neurons, *Neuron 11*, 1083–1091.

Hollmann, M., Hartley, M., & Heinemann, S. (1991). Ca2 + Permeability of KA-AMPA-Gated Glutamate Receptor Channels Depends on Subunit Composition, *Science 252*.

Horne, A. J., Peters, C. J., Claydon, T. W., & Fedida, D. (2010). Fast and slow voltage sensor rearrangements during activation gating in Kv1 . 2 channels detected using tetramethylrhodamine fluorescence. *The Journal of General Physiology*, *136*(1), 83–99.

Horning, M. S., & Mayer, M. L. (2004). Regulation of AMPA Receptor Gating by Ligand Binding Core Dimers, *Neuron 41*, 379–388.

Hosokawa, T., Mitsushima, D., Hosokawa, T., Mitsushima, D., Kaneko, R., & Hayashi, Y. (2015). Stoichiometry and Phosphoisotypes of Hippocampal Report Stoichiometry and Phosphoisotypes of Hippocampal AMPA-Type Glutamate Receptor Phosphorylation. *Neuron*, *85*(1), 60–67.

Hume, R. I., Dingledine, R., & Heinemann, S. F. (1991). Identification of a Site in Glutamate Receptor Subunits That Controls Calcium Permeability. *Science 253*.

Inanobe, A., Furukawa, H., & Gouaux, E. (2005). Mechanism of Partial Agonist Action at the NR1 Subunit of NMDA Receptors, *Neuron 47*, 71–84.

Isaac, J. T. R., Ashby, M. C., & Mcbain, C. J. (2007). The Role of the GluR2 Subunit in AMPA Receptor Function and Synaptic Plasticity, *Neuron 54,* 859–871.

Ishikawa-Ankerhold, H. C., Ankerhold, R., Drummen, G. P. C., Biology, C., Zeiss, C., Gmbh, M., … Program, A. (2012). Advanced Fluorescence Microscopy Techniques—FRAP , FLIP , FLAP , FRET and FLIM. *Molecules*, *17*, 4047–4132.

Jackson, A. C., & Nicoll, R. A. (2011). The Expanding Social Network of Ionotropic Glutamate Receptors: TARPs and Other Transmembrane Auxiliary Subunits. *Neuron*, *70*(2), 178–199.

Jares-erijman, E. A., & Jovin, T. M. (2003). FRET imaging, *Nature Biotechnology 21*(11), 1387–1395.

Jenkins, M. A., Wells, G., Bachman, J., Snyder, J. P., Jenkins, A., Huganir, R. L., … Traynelis, S. F. (2014). Regulation of GluA1 a -Amino-3-Hydroxy-5-Methyl-4-Isoxazolepropionic Acid Receptor Function by Protein Kinase C at Serine-818 and Threonine-840. *Molecular Pharmacology*, *85*, 618–629.

Jin, R., Banke, T. G., Mayer, M. L., Traynelis, S. F., & Gouaux, E. (2003). Structural basis for partial agonist action at ionotropic glutamate receptors, *Nature Neuroscience 6*(8), 803–810.

Jin, R., Clark, S., Weeks, A. M., Dudman, J. T., Gouaux, E., & Partin, K. M. (2005). Mechanism of Positive Allosteric Modulators Acting on AMPA Receptors, *The Journal of Neuroscience 25*(39), 9027–9036.

Jin, R., Horning, M., Mayer, M. L., & Gouaux, E. (2002). Mechanism of Activation and Selectivity in a Ligand-Gated Ion Channel : Structural and Functional Studies of GluR2 and Quisqualate. *Biochemistry 41,* 15635–15643.

Jin, R., Singh, S. K., Gu, S., Furukawa, H., Sobolevsky, A. I., Zhou, J., … Gouaux, E. (2009). Crystal structure and association behaviour of the GluR2 amino-terminal domain. *The EMBO Journal*, *28*(12), 1812–1823.

Jonas, P., & Burnashevt, N. (1995). Molecular Mechanisms Controlling Calcium Entry through AMPA-Type Glutamate Receptor Channels, *Neuron 15*, 987–990.

Jones, M. V., & Westbrook, G. L. (1996). The impact of receptor desensitization on fast synaptic transmission. *Trends in Neurosciences*, *19*(3), 96–101.

Kalstrup, T., & Blunck, R. (2013). Dynamics of internal pore opening in K V channels probed by a fl uorescent unnatural amino acid. *Proceedings of the National*

Academy of Sciences of the United States of America, *110*(20), 8272–8277.

Karakas, E., & Furukawa, H. (2014). Crystal structure of a heterotetrameric NMDA receptor ion channel. *Science, 344*(6187).

Karakas, E., Simorowski, N., & Furukawa, H. (2011). Subunit arrangement and phenylethanolamine binding in GluN1/GluN2B NMDA receptors. *Nature, 475*(7355), 249–253.

Kato, A. S., Siuda, E. R., Nisenbaum, E. S., & Bredt, D. S. (2008). Article AMPA Receptor Subunit-Specific Regulation by a Distinct Family of Type II TARPs, *Neuron 1*, 986–996.

Kato, A. S., Zhou, W., Milstein, A. D., Knierman, M. D., Siuda, E. R., Dotzlaf, J. E., Bredt, D. S. (2007). New Transmembrane AMPA Receptor Regulatory Protein Isoform, gamma-7 , Differentially Regulates AMPA Receptors, *The Journal of Neuroscience27*(18), 4969–4977.

Kim, E., Sheng, M., Neuroscience, R., & Medical, H. H. (2004). PDZ DOMAIN PROTEINS OF SYNAPSES, *Nature reviews Neuroscience 5*(October).

Kim, K. S., Yan, D., & Tomita, S. (2010). Assembly and Stoichiometry of the AMPA Receptor and Transmembrane AMPA Receptor Regulatory Protein Complex. *The Journal of Neuroscience*, *30*(3), 1064–1072.

Kiskin, N., Krishtal, O., & Tsyndrenko, Ay. (1986). Excitatory a m i n o acid r e c e p t o r s in h i p p o c a m p a l n e u r o n s : kainate fails to d e s e n s i t i z e t h e m. *Neuroscience Letters*, *63*, 225–230.

Körber, C., Werner, M., Kott, S., Ma, Z., & Hollmann, M. (2007). The Transmembrane AMPA Receptor Regulatory Protein gamma-4 Is a More Effective Modulator of AMPA Receptor Function than Stargazin (gamma-2). *The Journal of Neuroscience*, *27*(31), 8442–8447.

Krieger, J., Bahar, I., & Greger, I. H. (2015). Structure, Dynamics, and Allosteric Potential of Ionotropic Glutamate Receptor N-Terminal Domains. *Biophysical Journal*, *109*(6),

Kristensen, A. S., Jenkins, M. a, Banke, T. G., Schousboe, A., Makino, Y., Johnson, R. C., … Traynelis, S. F. (2011). Mechanism of Ca2+/calmodulin-dependent kinase II regulation of AMPA receptor gating. *Nature Neuroscience*, *14*(6), 727–735.

Kusch, J., & Zifarelli, G. (2014). Patch-Clamp Fluorometry : Electrophysiology meets Fluorescence. *BPJ*, *106*(6), 1250–1257.

Lakhan, S. E., Caro, M., & Hadzimichalis, N. (2013). NMDA receptor activity in

neuropsychiatric disorders, *Frontiers in Psychiatry 4*(June), 1–7.

Lau, A. Y., Salazar, H., Blachowicz, L., Ghisi, V., Plested, A. J. R., & Roux, B. (2013). A Conformational intermediate in glutamate receptor activation. *Neuron*, *79*(3), 792–503.

Lee, C.-H., Lü, W., Michel, J. C., Goehring, A., Du, J., Song, X., & Gouaux, E. (2014). NMDA receptor structures reveal subunit arrangement and pore architecture. *Nature*, *511*(7508), 191–197.

Lee, H., Barbarosie, M., Kameyama, K., Bear, M. F., & Huganir, R. L. (2000). Regulation of distinct AMPA receptor phosphorylation sites during bidirectional synaptic plasticity, *Nature 405*(June), 955–959.

Lee, H., Takamiya, K., Han, J., Man, H., Kim, C., Rumbaugh, G., Huganir, R. L. (2003). Phosphorylation of the AMPA Receptor GluR1 Subunit Is Required for Synaptic Plasticity and Retention of Spatial Memory, *Cell 112*, 631–643.

Lerma, J., Morales, M., Ibarz, J. M., & Somohano, F. (1994). Rectification Properties and Ca2 + Permeability of Glutamate Receptor Channels in Hippocampal Cells, *European journal of neuroscience 6*, 1080–1088.

Letts, V. A., Felix, R., Biddlecome, G. H., Arikkath, J., Mahaffey, C. L., Valenzuela, A., … Frankel, W. N. (1998). The mouse stargazer gene encodes a neuronal Ca 2 + -channel γ subunit, *Nature Genetics 19*, 340–347.

Leuschner, W. D., Hoch, W., & Tu, D.-. (1999). Subtype-specific Assembly of alpha-Amino-3-hydroxy-5-methyl-4- isoxazole Propionic Acid Receptor Subunits Is Mediated by Their N-terminal Domains , *The Journal of Biological Chemistry 274*(24), 16907–16916.

Linden, D. J., & Connor, J. A. (1991). Participation of Postsynaptic PKC in Cerebellar Long-Term Depression in Culture. *Science 254 (*5038*),* 1656-1659 .

LISSIN, D. V., GOMPERTS, S. N., REED C. CARROLL, CHADWICK W. CHRISTINE, DANIEL KALMAN, MARINA KITAMURA, … ROBERT C.MALENKA. (1998). Activity differentially regulates the surface expression of synaptic AMPA and NMDA glutamate receptors. *Proceedings of the National Academy of Sciences*, *95*(June), 7097–7102.

Lissin, D. V, Carroll, R. C., Nicoll, R. A., Malenka, R. C., Zastrow, M. Von, & Francisco, S. (1999). Rapid, Activation-Induced Redistribution of Ionotropic Glutamate Receptors in Cultured Hippocampal Neurons, *The Journal of Neuroscience 19*(4), 1263–1272.

Lizuka, R., Yamagishi-shirasaki, M., & Funatsu, T. (2011). Kinetic study of de novo chromophore maturation of fluorescent proteins Normalized intensity Normalized intensity Normalized intensity. *Analytical Biochemistry*, *414*(2), 173–178.

Lu, W., Shi, Y., Jackson, A. C., Bjorgan, K., During, M. J., Sprengel, R., … Nicoll, R. A. (2009). Article Subunit Composition of Synaptic AMPA Receptors Revealed by a Single-Cell Genetic Approach. *Neuron*, *62*(2), 254–268.

Malinow, R., & Malenka, R. C. (2002). Ampa receptor trafficking and synapticplasticity. *Annu. Rev. Neurosci 25,* 103-126

Mannuzzu, L. M., Moronne, M. M., & Isacoff, E. Y. (1996). Direct Physical Measure of Conformational. *Science*, *271*.

Markwardt, M. L., Kremers, G., Kraft, C. A., Ray, K., Cranfill, P. J. C., Wilson, K. A., Day, R. N., Wachter, R. M., Davison, M.W., Rizzo, M. A. (2011). An Improved Cerulean Fluorescent Protein with Enhanced Brightness and Reduced Reversible Photoswitching. *PLoS ONE 6*(3).

Marvin, J. S., Borghuis, B. G., Tian, L., Cichon, J., Harnett, M. T., Akerboom, J., … Looger, L. L. (2013). An optimized fluorescent probe for visualizing glutamate neurotransmission. *Nature Methods*, *10*(2), 162–170.

Marvin, J. S., Schreiter, E. R., Echevarría, I. M., & Looger, L. L. (2011). A genetically encoded, high-signal-to-noise maltose sensor. *Proteins: Structure, Function and Bioinformatics*, *79*(11), 3025–3036.

Merzlyak, E. M., Goedhart, J., Shcherbo, D., Bulina, M. E., Shcheglov, A. S., Fradkov, A. F., … Chudakov, D. M. (2007). Bright monomeric red fluorescent protein with an extended fluorescence lifetime. *Nature Methods*, *4*(7), 555–557.

Meyerson, J. R., Kumar, J., Chittori, S., Rao, P., Pierson, J., Bartesaghi, A., … Subramaniam, S. (2014). Structural mechanism of glutamate receptor activation and desensitization. *Nature*, *514*(7522), 328–334.

Milstein, A. D., Zhou, W., Karimzadegan, S., Bredt, D. S., & Nicoll, R. A. (2007). TARP Subtypes Differentially and Dose-Dependently Control Synaptic AMPA Receptor Gating. *Neuron*, *55*, 905–918.

Minezaki, Y., Homma, K., & Nishikawa, K. (2007). Intrinsically Disordered Regions of Human Plasma Membrane Proteins Preferentially Occur in the Cytoplasmic Segment, *J. Mol. Biol. 368,* 902–913.

Miranda, P., Contreras, J. E., Plested, A. J. R., Sigworth, F. J., Holmgren, M., & Giraldez, T. (2013). State-dependent FRET reports calcium- and voltage-

dependent gating-ring motions in BK channels. *Proceedings of the National Academy of Sciences of the United States of America*, *110*(13), 5217–22.

Morimoto-tomita, M., Zhang, W., Straub, C., Cho, C., Kim, K. S., & Howe, J. R. (2009). Article Autoinactivation of Neuronal AMPA Receptors via Glutamate-Regulated TARP Interaction. *Neuron*, *61*(1), 101–112.

Mourot, A., Bamberg, E., & Rettinger, J. (2008). Agonist- and competitive antagonist-induced movement of loop 5 on the a subunit of the neuronal a 4 b 4 nicotinic acetylcholine receptor. *Journal of Neurochemistry*, 413–424.

Möykkynen, T., Coleman, S. K., Semenov, A., & Keinänen, K. (2014). The N-terminal domain modulates α-amino-3-hydroxy-5-methyl-4-isoxazolepropionic acid (AMPA) receptor desensitization. *The Journal of Biological Chemistry*, *289*(19),

Muroi, Y., Czajkowski, C., & Jackson, M. B. (2006). Local and Global Ligand-Induced Changes in the Structure of the GABA A. *Biochemistry*, *45*, 7013–7022.

Nagai, T., Ibata, K., Park, E. S., Kubota, M., & Mikoshiba, K. (2002). A variant of yellow fluorescent protein with fast and efficient maturation for cell-biological applications. *Nature Biotechnology*, *20*, 87–90.

Nakagawa, T., Cheng, Y., Ramm, E., Sheng, M., & Walz. (2005). Structure and different conformational states of native AMPA receptor complexes. *Nature*, *433*(February), 545–549.

Nicoll, R. A., & Tomita, S. (2006). Auxiliary Subunits Assist AMPA-Type. *Science*, *311*, 1253–1256.

Opazo, P., Labrecque, S., Tigaret, C. M., Frouin, A., Wiseman, P. W., Koninck, P. De, & Dsred, H. (2010). Article CaMKII Triggers the Diffusional Trapping of Surface AMPARs through Phosphorylation of Stargazin. *Neuron*, *67*(2), 239–252.

Ormo, M., Cubitt, A. B., Kallio, K., Gross, L. A., Tsien, R. Y., & Remingtont, S. J. (1996). Crystal Structure of the Aequorea victoria Green Fluorescent Protein, *Science 273*(5280), 1392-1395

Otis, T. S. (1996). Inhibition of Transmitter Release Shortens the Duration of the Excitatory Synaptic Current at a Calyceal Synapse, *Journal of neurophysiology 76*(5).

Otis, T., Zhang, S., & Trussell, L. O. (1996). Direct Measurement of AMPA Receptor Desensitization Induced by Glutamatergic Synaptic Transmission, *the Jpurnal of neuroscience 16*(23), 7496–7504.

Paoletti, P., & Neyton, J. (2007). NMDA receptor subunits : function and

pharmacology. *Current Opinion in Pharmacology 7,* 39-47

Parsons, C. G., Danysz, W., Dekundy, A., & Pulte, I. (2013). Memantine and Cholinesterase Inhibitors : Complementary Mechanisms in the Treatment of Alzheimer ' s Disease, *Neurotox Res 24,* 358-369

Parsons, C. G., & Gilling, K. (2007). Open Channel N -Methyl- d -Aspartate Receptor Blocker. *Methods in Molecular Biology*, *288*.

Partin, K. M., Fleck, M. W., & Mayer, M. L. (1996). AMPA receptor flip/flop mutants affecting deactivation, desensitization, and modulation by cyclothiazide, aniracetam, and thiocyanate. *The Journal of Neuroscience*, *16*(21), 6634–6647.

Partin, K. M., Patneau, D. K., & Mayer, M. L. (1994). Cyclothiazide Differentially Modulates Desensitization of Acid Receptor Splice Variants. *Molecular Pharmacology*, (46).

Passafaro, M., Piëch, V., & Sheng, M. (2001). Subunit-specific temporal and spatial patterns of AMPA receptor exocytosis in hippocampal neurons, *Nature Neuroscience 4*(9), 917–926.

Pasternack, A., Coleman, S. K., Jouppila, A., Mottershead, D. G., Lindfors, M., Pasternack, M., & Keina, K. (2002). alpha-Amino-3-hydroxy-5-methyl-4-isoxazolepropionic Acid (AMPA) Receptor Channels Lacking the N-terminal Domain, *the Journal of Biological Chemistry 277*(51), 49662–49667.

Pepperkok, R., Squire, A., Geley, S., & Bastiaens, P. I. H. (1999). Simultaneous detection of multiple green fluorescent proteins in live cells by fluorescence lifetime imaging microscopy. *Current Biology*, *9*.

Piston, D. W., & Kremers, G. (2007). Fluorescent protein FRET : the good , the bad and the ugly, *TRENDS in Biochemical Sciences 32*(9).

Pless, S. A., & Lynch, J. W. (2008). Illuminating the structure and function of cys-loop receptors. *Clinical and Experimental Pharmacology and Physiology 35*, *35*, 1137–1142.

Plested, A. J., & Mayer, M. L. (2009). AMPA receptor ligand binding domain mobility revealed by functional cross linking. *J Neurosci*, *29*(38), 11912–11923.

Priel, A., Kolleker, A., Ayalon, G., Gillor, M., Osten, P., & Stern-bach, Y. (2005). Stargazin Reduces Desensitization and Slows Deactivation of the AMPA-Type Glutamate Receptors, *J Neurosci, 25*(10), 2682–2686.

Puljung, M. C., & Zagotta, W. N. (2013). A Secondary Structural Transition in the C-helix Promotes Gating of Cyclic Nucleotide-regulated Ion Channels. *Journal of*

Biological Chemistry, *288*(18), 12944–12956.

Ramanoudjame, G., Du, M., Mankiewicz, K. a, & Jayaraman, V. (2006). Allosteric mechanism in AMPA receptors: a FRET-based investigation of conformational changes. *Proceedings of the National Academy of Sciences of the United States of America*, *103*(27), 10473–10478.

Rambhadran, A., Gonzalez, J., & Jayaraman, V. (2011). Conformational changes at the agonist binding domain of the N-methyl-D-aspartic acid receptor. *The Journal of Biological Chemistry*, *286*(19), 16953–7.

Rizzo, M. A., Springer, G. H., Granada, B., & Piston, D. W. (2004). An improved cyan fluorescent protein variant useful for FRET. *Nature Biotechnology*, *22*(4), 445–449.

Roche, K. W., Brien, R. J. O., Mammen, A. L., Bernhardt, J., & Huganir, R. L. (1996). Characterization of Multiple Phosphorylation Sites on the AMPA Receptor GluR1 Subunit, *Neuron 16*, 1179–1188.

Rosenmund, C., Stern-bach, Y., & Stevens, C. F. (1998). The Tetrameric Structure of a Glutamate Receptor Channel, *Science 280*, 1596-1599.

Rozov, A., Jerecic, J., Sakmann, B., & Burnashev, N. (2001). AMPA Receptor Channels with Long-Lasting Desensitization in Bipolar Interneurons Contribute to Synaptic Depression in a Novel Feedback Circuit in Layer 2 / 3 of Rat Neocortex, *The Journal of Neuroscience 21*(20), 8062–8071.

Rubio, M. D., Drummond, J. B., & Meador-woodruff, J. H. (2012). Glutamate Receptor Abnormalities in Schizophrenia : Implications for Innovative Treatments. *Biomol Ther 20*(1), 1–18.

Salussolia, C. L., Corrales, A., Talukder, I., Kazi, R., Akgul, G., Bowen, M., & Wollmuth, L. P. (2011). Interaction of the M4 Segment with Other Transmembrane Segments Is Required for Surface Expression of Mammalian alpha-Amino-3-hydroxy-5-methyl-4-isoxazolepropionic Acid (AMPA) Receptors, *The Journal of Biological Chemistry 286*(46).

Salussolia, C. L., Gan, Q., Kazi, R., Singh, P., Allopenna, J., Furukawa, H., & Wollmuth, L. P. (2013). A Eukaryotic Specific Transmembrane Segment is Required for Tetramerization in AMPA Receptors, *The Journal of Neuroscience 33*(23), 9840–9845.

Sasmal, D. K., & Lu, H. P. (2014). Single-Molecule Patch-Clamp FRET Microscopy Studies of NMDA Receptor Ion Channel Dynamics in Living Cells: Revealing the

Multiple Conformational States Associated with a Channel at Its Electrical Off State. *J. Am. Chem. Soc. 136*, 12998−13005

Sasmal, D. K., Yadav, R., Lu, H. P., Sasmal, D. K., Yadav, R., & Lu, H. P. (2016). Studies of NMDA Receptor Ion Channel Activation and Deactivation under Agonist Ligand Binding in Living Cells Single-Molecule Patch-Clamp-FRET-Anisotropy Microscopy Studies of NMDA Receptor Ion Channel Activation and Deactivation under Agonist Ligand Bind. *J. Am. Chem. Soc.*

Schauder, D. M., Kuybeda, O., Zhang, J., Klymko, K., Bartesaghi, A., Borgnia, M. J., Subramaniam, S. (2013). Glutamate receptor desensitization is mediated by changes in quaternary structure of the ligand binding domain. *Proceedings of the National Academy of Sciences*, *110*(15), 5921–5926.

Schnell, E., Sizemore, M., Karimzadegan, S., Chen, L., Bredt, D. S., & Nicoll, R. A. (2002). Direct interactions between PSD-95 and stargazin control synaptic AMPA receptor number. *Proceedings of the National Academy of Sciences*, *99*(21), 13902–13907.

Schorge, S., & Colquhoun, D. (2003). Studies of NMDA Receptor Function and Stoichiometry with Truncated and Tandem Subunits, *The Journal of Neuroscience 23*(4), 1151–1158.

Sekar, R. B., & Periasamy, A. (2001). Fluorescence resonance energy transfer (FRET) microscopy imaging of live cell protein localizations, *The Journal of Cell Biology*, *160*(5), 629–633.

Selvin, P. R. (1995). Fluorescence Resonance Energy Transfer. *Methods in Enzymology*, *246*, 300–334.

Semenov, A., Coleman, S. K., Korpi, E. R., Keina, K., & Mo, T. (2012). Autoinactivation of the Stargazin – AMPA Receptor Complex : Subunit-Dependency and Independence from Physical Dissociation. *PloS One*, *7*(11).

Shaner, N. C., Lin, M. Z., Mckeown, M. R., Steinbach, P. A., Hazelwood, K. L., Davidson, M. W., & Tsien, R. Y. (2008). Improving the photostability of bright monomeric orange and red fluorescent proteins. *Nature Methods*, *5*(6).

Shemiakina, I. I., Ermakova, G. V, Cranfill, P. J., Baird, M. A., Evans, R. A., Souslova, E. A., … Chudakov, D. M. (2012). A monomeric red fluorescent protein with low cytotoxicity. *Nature Communications*, *3*, 1204–1207.

Sheridan, D. L., Robert, a., Cho, C. H., Howe, J. R., & Hughes, T. E. (2006). Regions of ??-amino-5-methyl-3-hydroxy-4-isoxazole propionic acid receptor subunits that

are permissive for the insertion of green fluorescent protein. *The Journal Neuroscience*, *141*(2), 837–849.

Shi, S., Hayashi, Y., Esteban, A., & Malinow, R. (2001). Subunit-Specific Rules Governing AMPA Receptor Trafficking to Synapses in Hippocampal Pyramidal Neurons, *Cell 105*, 331–343.

Shi, S., Hayashi, Y., Petralia, R. S., Zaman, S. H., Wenthold, R. J., Svoboda, K., & Malinow, R. (1999). Rapid Spine Delivery and Redistribution of AMPA Receptors After Synaptic NMDA Receptor Activation, *Science 284*(June).

Shrestha, D., Jenei, A., Nagy, P., Vereb, G., & Szöll, J. (2015). Understanding FRET as a Research Tool for Cellular Studies. *Int. J. Mol. Sci. 16*, 6718-6756

Sirrieh, R. E., Maclean, D. M., & Jayaraman, V. (2013). Amino-terminal Domain Tetramer Organization and Structural Effects of Zinc Binding in the N -Methyl- D -aspartate (NMDA) Receptor, *The Journal of Biological Chemistry 288*(31), 22555–22564.

Sjulson, L., & Miesenbo, G. (2008). Rational Optimization and Imaging In Vivo of a Genetically Encoded Optical Voltage Reporter. *The Journal of Neuroscience*, *28*(21), 5582–5593.

Sobolevsky, A. I., Rosconi, M. P., & Gouaux, E. (2009). X-ray structure, symmetry and mechanism of an AMPA-subtype glutamate receptor. *Nature*, *462*(7274), 745–756.

Sommer, B., Kohler, M., Sprengel, F., & Seeburg, P. H. (1991). RNA Editing in Brain Controls of Ion Flow in Glutamate-Gated a Determinant Channels, *Cell 67*, 11–19.

Song, I., & Huganir, R. L. (2002). Regulation of AMPA receptors during synaptic plasticity, *TRENDS in Neurosciences 25*(11), 578–588.

Soto, D., Coombs, I. D., Kelly, L., Farrant, M., & Cull-candy, S. G. (2007). Stargazin attenuates intracellular polyamine block of calcium-permeable AMPA receptors, *Nature Neuroscience 10*(10).

Soto, D., Coombs, I. D., Renzi, M., Zonouzi, M., Farrant, M., & Cull-candy, S. G. (2009). Selective regulation of long-form calcium-permeable AMPA receptors by an atypical TARP , gamma -5, *Nature Neuroscience 12*(3), 277–286.

Straub, C., Hunt, D. L., Yamasaki, M., Kim, K. S., Watanabe, M., Castillo, P. E., & Tomita, S. (2011). Distinct functions of kainate receptors in the brain are determined by the auxiliary subunit Neto1. *Nature Neuroscience*, *14*(7), 866–873.

Straub, C., & Tomita, S. (2012). The regulation of glutamate receptor trafficking and function by TARPs and other transmembrane auxiliary subunits. *Current Opinion*

in Neurobiology, *22*(3), 488–495

Straub, C., Zhang, W., & Howe, J. R. (2011). Neto2 Modulation of Kainate Receptors with Different Subunit Compositions. *The Journal of Neuroscience*, *31*(22), 8078–8082.

Sukumaran, M., Shrivastava, I., Dutta, A., Bahar, I., & Greger, I. H. (2011). Dynamics and allosteric potential of the AMPA receptor N-terminal domain. *The EMBO Journal*, *30*(5), 972–982.

Sun, Y., Olson, R., Horning, M., Armstrong, N., Mayer, M., & Gouaux, E. (2002). Mechanism of glutamate receptor desensitization, *Nature 417,* 245–253.

Suzuki, E., Kessler, M., & T, A. C. A. (2005). C-terminal truncation affects kinetic properties of GluR1 receptors. *Mol. Cell. Neurosci*, *29*, 1–10.

Swanson, G. T., Kamboj, S. K., & Cull-candy, S. G. (1997). Single-Channel Properties of Recombinant AMPA Receptors Depend on RNA Editing , Splice Variation , and Subunit Composition, *The Journal of Neuroscience 17*(1), 58–69.

Swope, S., Hughes, H., & Huganir, L. (1992). Phosphorylation of ligand-gated ion channels: a possible mode of synaptic plasticity. *The FASEB Journal 6*(8), 2514–2523.

Taraska, J. W., & Zagotta, W. N. (2007). Structural dynamics in the gating ring of cyclic nucleotide-gated ion channels. *Nature Structural & Molecular Biology*, *14*(9), 854–60.

Tomita, S., Adesnik, H., Sekiguchi, M., Zhang, W., Wada, K., Howe, J. R., … Bredt, D. S. (2005). Stargazin modulates AMPA receptor gating and trafficking by distinct domains. *Nature*, *435*(7045),

Tomita, S., Chen, L., Kawasaki, Y., Petralia, R. S., Wenthold, R. J., Nicoll, R. A., & Bredt, D. S. (2003). Functional studies and distribution define a family of transmembrane AMPA receptor regulatory proteins, *The Journal of Chemical Biology 161*(4), 805–816.

Tomita, S., Fukata, M., & Nicoll, R. A. (2004). Dynamic Interaction of Stargazin-like TARPs with Cycling AMPA Receptors at Synapses, *Science 303*, 1508–1512.

Tomita, S., Shenoy, A., Fukata, Y., Nicoll, R. A., & Bredt, D. S. (2006). Stargazin interacts functionally with the AMPA receptor glutamate-binding module. *Neuropharpacology*, *52*, 87–91.

Trudeau, M. C., & Zagotta, W. N. (2004). Dynamics of Ca 2 ℰ -Calmodulin – dependent Inhibition of Rod Cyclic Nucleotide-gated Channels Measured by

Patch-clamp Fluorometry, *The Journal of General Physiology 124*.

Trussel, L., Zhang, S., & Ramant, I. M. (1993). Desensitization of AMPA Receptors upon Multiquantal Neurotransmitter Release. *Neuron*, *10*, 1185–1196.

Trussell, L. O., & Fischbach, G. D. (1989). Glutamate receptor desensitization and its role in synaptic transmission. *Neuron*, *3*(2), 209–218.

Turetsky, D., Garringer, E., & Patneau, D. K. (2005). Stargazin Modulates Native AMPA Receptor Functional Properties by Two Distinct Mechanisms, *The Journal of Neuroscience 25*(32), 7438–7448

Twomey, E. C., Yelshanskaya, M. V, Grassucci, R. A., Frank, J., & Sobolevsky, A. I. (2016). Elucidation of AMPA receptor − stargazin complexes by cryo − electron microscopy. *Science*, *353*(6294).

Walker, C. S., Jensen, S., Ellison, M., Matta, J. A., Lee, W. Y., Julita, S., … Maricq, A. V. (2009). A Novel Conus Snail Polypeptide Causes Excitotoxicity by Blocking Desensitization of AMPA Receptors. *Curr Biol. 19*(11), 900–908.

Wang, D., Zhang, Z., Chanda, B., & Jackson, M. B. (2010). Improved Probes for Hybrid Voltage Sensor Imaging. *Biophysical Journal*, *99*(7), 2355–2365.

Wenthold, J., Petralia, S., & Niedzielski, S. (1996). Evidence for Multiple Neurons Complexes in Hippocampal, *the Journal of Neuroscience 76*(6), 1982–1989.

Whitlock, J. R., Heynen, A. J., Shuler, M. G., & Bear, M. F. (2006). Learning Induces Long-Term Potentiation in the Hippocampus, *Science 313*, 1093–1098.

Wood, M. W., Vandongen, H. M. A., & Vandongen, A. M. J. (1995). Structural conservation of ion conduction pathways in K channels and glutamate receptors, *PNAS 92*, 4882–4886.

Xia, J., Chung, H. J., Wihler, C., Huganir, R. L., & Linden, D. J. (2000). Cerebellar Long-Term Depression Requires PKC-Regulated Interactions between GluR2 / 3 and PDZ Domain − Containing Proteins, *Neuron 28*, 499–510.

Xia, J., Zhang, X., Staudinger, J., & Huganir, R. L. (1999). Clustering of AMPA Receptors by the Synaptic PDZ Domain − Containing Protein PICK1, *Neuron 22*, 179–187.

Yelshanskaya, M. V., Li, M., & Sobolevsky, a. I. (2014). Structure of an agonist-bound ionotropic glutamate receptor. *Science*, *345*(6200).

Zacharias, D. A., Violin, J. D., & Newton, A. C. (2002). Partitioning of Lipid-Modified Monomeric GFPs into Membrane Microdomains of Live Cells. *Science*, *296*(May), 913–917.

Zachariassen, L. G., Katchan, L., Jensen, A. G., Pickering, D. S., & Plested, A. J. R. (2016). Structural rearrangement of the intracellular domains during AMPA receptor activation. *Proceedings of the National Academy of Sciences*.

Zeeuw, C. I. De, Hansel, C., Bian, F., Koekkoek, S. K. E., Alphen, A. M. Van, Linden, D. J., & Oberdick, J. (1998). Expression of a Protein Kinase C Inhibitor in Purkinje Cells Blocks Cerebellar LTD and Adaptation of the Vestibulo-Ocular Reflex, *Neuron 20*, 495–508.

Zhao, Y., Chen, S., Yoshioka, C., Baconguis, I., & Gouaux, E. (2016). Architecture of fully occupied GluA2 AMPA receptor-TARP complex elucidated by cryo-EM. *Nature*

Zheng, J., Trudeau, M. C., & Zagotta, W. N. (2002). Rod cyclic nucleotide-gated channels have a stoichiometry of three CNGA1 subunits and one CNGB1 subunit. *Neuron*, *36*(5), 891–896.

Zheng, J., Varnum, M. D., & Zagotta, W. N. (2003). Disruption of an intersubunit interaction underlies Ca2+-calmodulin modulation of cyclic nucleotide-gated channels. *The Journal of Neuroscience 23*(22), 8167–75.

Zheng, J., & Zagotta, W. N. (2000). Neurotechnique Nucleotide-Gated Channels Revealed by Patch-Clamp Fluorometry, *Neuron 28*, 369–374.

Zheng, J., & Zagotta, W. N. (2003). Patch-Clamp Fluorometry Recording of Conformational Rearrangements of Ion Channels. *Science Signaling*, *2003*(176), pl7.

Zimmermann, D., Kiesel, M., Terpitz, U., Zhou, a, Reuss, R., Kraus, J., … Sukhorukov, V. L. (2008). A combined patch-clamp and electrorotation study of the voltage- and frequency-dependent membrane capacitance caused by structurally dissimilar lipophilic anions. *The Journal of Membrane Biology*, *221*(2), 107–21.

Appendix

A1 Loading .spe waves from LightField software (Princeton instruments)

```
// Originally from Sjors Wurpel 2005
// This procedure file contains the LoadPrincetonSPE() function to
import binary winspec (.spe) files

// General load routine for Princeton binary files as written by e.g.
Winspec
// Code based on
http://www.sccs.swarthmore.edu/users/03/roban/temperature/conversion/
read_princeton.pro
// Reads both graphs and images
// Should work with all datatypes, but only type 3 (int) has been
tested
// Info from the 4100 byte header is processed and stored in wave
notes
// If there is calibration info available, a scaling wave is created


Function SpeLoader()

variable refnum
variable exp_sec
variable nx, ny, nframes, datatype
string wname
string wnameX, wnameY
string datestr, timestr, comment1, comment2, comment3, comment4,
comment5
string notestr, wavenote=""

open/r/Z=2/M="Press cancel if you're finished"/t=".spe" refnum as ""
if (V_flag!=0)
abort "abort"
endif

//Build wavename
FStatus refnum
wname=S_fileName[0,((strlen(S_fileName)-1)-4)] // remove last 4 chars
from filename
wname = Cleanupname(wname,0)

//Header info
FSetPos refnum, 10; FBinRead/B=3/F=4 refnum,exp_sec //exposure in
seconds
FSetPos refnum, 42; FbinRead/B=3/F=2 refnum, nx //number of x pixels
FSetPos refnum, 656; FbinRead/B=3/F=2 refnum, ny //number of y pixels
(=1 for graph)
FSetPos refnum, 1446; FbinRead/B=3/F=3 refnum, nframes //number of
frames
FSetPos refnum, 108; FbinRead/B=3/F=2 refnum, datatype //data type
float, long, uint, int
//Date-time
FSetPos refnum, 20; FReadLine/N=10 refnum, datestr //format DDMMMYYYY
(20Apr2005)
FSetPos refnum, 172; FReadLine/N=6 refnum, timestr //format HHMMSS
(161959)
//User Comments
FsetPos refnum, 200; Freadline refnum, comment1
FsetPos refnum, 280; Freadline refnum, comment2
```

```
FsetPos refnum, 360; Freadline refnum, comment3
FsetPos refnum, 440; Freadline refnum, comment4
FsetPos refnum, 520; Freadline refnum, comment5

//Step & Glue parameters
Variable glue, offset, scalefactor, final
FSetPos refnum, 76; FBinRead/B=3/F=2 refnum,glue //glue flag
FSetPos refnum, 78; FBinRead/B=3/F=4 refnum,offset //offset
FSetPos refnum, 82; FBinRead/B=3/F=4 refnum,final //final wavelength
FSetPos refnum, 90; FBinRead/B=3/F=4 refnum,scalefactor //scalefactor

//Grating parameters
Variable center, xpix, grooves
FSetPos refnum, 72; FBinRead/B=3/F=4 refnum,center //offset
FSetPos refnum, 6; FBinRead/B=3/F=2 refnum,xpix //scalefactor
FSetPos refnum, 650; FBinRead/B=3/F=4 refnum,grooves //scalefactor

//Calibration data
Variable polyx,offsetx, scalex0, scalex1, scalex2
FSetPos refnum, 3101; FBinRead/B=3/F=1 refnum,polyx //polynomial
number
FSetPos refnum, 3183; FBinRead/B=3/F=5 refnum,offsetx //offsetx
FSetPos refnum, 3263; FBinRead/B=3/F=5 refnum,scalex0 //scalefactor0
FSetPos refnum, 3271; FBinRead/B=3/F=5 refnum,scalex1//scalefactor1
FSetPos refnum, 3279; FBinRead/B=3/F=5 refnum,scalex2 //scalefactor2


Close refnum

print nx, ny,nframes

switch(datatype)
case 0: // float ?
GBLoadWave/O/Q/B=3/S=4100/T={2,4}/U=(nx*ny*nframes)/W=(1)/N=WStemp
(S_path+S_filename)
break
case 1: // long ?
GBLoadWave/O/Q/B=3/S=4100/T={32,4}/U=(nx*ny*nframes)/W=(1)/N=WStemp
(S_path+S_filename)
break
case 2: //uint ?
GBLoadWave/O/Q/B=3/S=4100/T={16+64,4}/U=(nx*ny*nframes)/W=(1)/N=WStem
p (S_path+S_filename)
break
case 3: //originally int, changed to unsigned integer
GBLoadWave/O/B=3/S=4100/T={16+64,4}/U=((nx*ny+1)*nframes)/W=(1)/N=WSt
emp (S_path+S_filename)
break
default:
abort "Unknown datatype"
endswitch


// redimension and create scaling waves
if (ny>1) // image(stack) file
        if (nframes == 1) // image
                redimension/N=(nx,ny) WStemp0
        else // 3D image stack with timestamp!!!
                redimension/N=(nx*ny+2, nframes) WStemp0
        endif
else // assume ny = 1
        redimension/N=(nx, nframes) WStemp0
endif
```

```
//Setscale
if (glue==1)
        Setscale/P x, offset*1E-9, scalefactor*1E-9, "m", WStemp0
else
        if(polyx==2)
                String Calibx = wname + "_x"
                Make/D/O/N = (xpix) $calibx = scalex0 + scalex1*(p+1)
+ scalex2*(p+1)^2
        else
                Print "Special Calibration - scale not made:
polynomial order", polyx
        endif
endif

//Rename loaded wave to cleaned-up filename
print "Dimensions of WStemp", dimsize(WStemp0,0), dimsize(WStemp0,1)
//This line for 2D 512x512
//Duplicate/O /R=[0,262143] WStemp0, $wname

Duplicate/O /R=[0,nx*ny] WStemp0, $wname
print "Dimensions of image slice", dimsize ($wname,0),
dimsize($wname,1)


redimension/N=(nx*ny*nframes) $wname

print "1D collapsed", dimsize($wname,0)

redimension/N=(nx,ny,nframes) $wname
print "3D exploded", dimsize($wname,0), dimsize($wname,1),
dimsize($wname,2)
KillWaves/Z WStemp0
edit $wname
print wname
//Store all parameters in wavenote
sprintf notestr, "File: %s\r", S_Filename ;wavenote+=notestr
sprintf notestr, "Path: %s\r", S_Path ;wavenote+=notestr
sprintf notestr, "Exposure: %g\r", exp_sec ;wavenote+=notestr
sprintf notestr, "Grating: %g\r", grooves ;wavenote+=notestr
sprintf notestr, "Frames: %g\r", nframes ;wavenote+=notestr
sprintf notestr, "Captured: %s %s\r", DateStr , TimeColon(Timestr)
;wavenote+=notestr
sprintf notestr, "Comment: %s -- %s -- %s -- %s -- %s\r",
Comment1,Comment2,Comment3,Comment4,Comment5
wavenote+=notestr
Note $wname, wavenote

End


Function/S TimeColon(timestr)
string timestr

string hh, mm, ss
hh=timestr[0,1]
mm=timestr[2,3]
ss=timestr[4,5]

return hh+":"+mm+":"+ss
End
```

```
///////////////////////////////////////////////////////////////////
////
//Complete Header info
//
//                                          Decimal Byte
//                                             Offset
//                                          -----------
//   SHORT    ControllerVersion               0  Hardware Version
//   SHORT    LogicOutput                     2  Definition of Output
BNC
//   WORD     AmpHiCapLowNoise        4  Amp Switching Mode
//   WORD     xDimDet                         6  Detector x dimension
of chip.
//   SHORT    mode                            8  timing mode
//   float    exp_sec                        10   alternitive
exposure, in sec.
//   SHORT    VChipXdim                      14  Virtual Chip X dim
//   SHORT    VChipYdim                      16  Virtual Chip Y dim
//   WORD     yDimDet                        18  y dimension of CCD or
detector.
//   char     date[DATEMAX]                  20  date
//   SHORT    VirtualChipFlag                30  On/Off
//   char     Spare_1[2]                     32
//   SHORT    noscan                         34  Old number of scans
– should always be –1
//   float    DetTemperature                 36  Detector
Temperature Set
//   SHORT    DetType                        40  CCD/DiodeArray type
//   WORD     xdim                           42   actual # of
pixels on x axis
//   SHORT    stdiode                        44  trigger diode
//   float    DelayTime                      46  Used with Async
Mode
//   WORD     ShutterControl                 50  Normal, Disabled
Open, Disabled Closed
//   SHORT    AbsorbLive                     52  On/Off
//   WORD     AbsorbMode                     54  Reference Strip or File
//   SHORT    CanDoVirtualChipFlag      56  T/F Cont/Chip able to do
Virtual Chip
//   SHORT    ThresholdMinLive               58  On/Off
//   float    ThresholdMinVal                60  Threshold Minimum
Value
//   SHORT    ThresholdMaxLive              64  On/Off
//   float    ThresholdMaxVal                66  Threshold Maximum
Value
//   SHORT    SpecAutoSpectroMode      70  T/F Spectrograph Used
//   float    SpecCenterWlNm                 72  Center Wavelength in
Nm
//   SHORT    SpecGlueFlag                   76  T/F File is Glued
//   float    SpecGlueStartWlNm              78  Starting Wavelength in
Nm
//   float    SpecGlueEndWlNm                82  Starting Wavelength in
Nm
//   float    SpecGlueMinOvrlpNm             86  Minimum Overlap in Nm
//   float    SpecGlueFinalResNm             90  Final Resolution in Nm
//   SHORT    PulserType                     94  0=None, PG200=1,
PTG=2, DG535=3
//   SHORT    CustomChipFlag                 96  T/F Custom Chip Used
//   SHORT    XPrePixels                     98  Pre Pixels in X
direction
//   SHORT    XPostPixels                    100  Post Pixels in X
direction
```

```
//   SHORT    YPrePixels                    102  Pre Pixels in Y
direction
//   SHORT    YPostPixels                   104  Post Pixels in Y
direction
//   SHORT    asynen                         106  asynchron enable
flag  0 = off
//   SHORT    datatype                       108  experiment datatype
//                                             0 =   FLOATING POINT
//                                             1 =   LONG INTEGER
//                                             2 =   INTEGER
//                                             3 =   UNSIGNED INTEGER
//---- SY 03-22-2004 ???? should be UINT16 or WORD or SHORT ????
//   SHORT    PulserMode                    110  Repetitive/Sequential
//   USHORT   PulserOnChipAccums            112  Num PTG On-Chip Accums
//   DWORD    PulserRepeatExp               114  Num Exp Repeats (Pulser
SW Accum)
//   float    PulseRepWidth                 118  Width Value for
Repetitive pulse (usec)
//   float    PulseRepDelay                 122  Width Value for
Repetitive pulse (usec)
//   float    PulseSeqStartWidth            126  Start Width for
Sequential pulse (usec)
//   float    PulseSeqEndWidth              130  End Width for
Sequential pulse (usec)
//   float    PulseSeqStartDelay            134  Start Delay for
Sequential pulse (usec)
//   float    PulseSeqEndDelay              138  End Delay for
Sequential pulse (usec)
//   SHORT    PulseSeqIncMode               142  Increments: 1=Fixed,
2=Exponential
//   SHORT    PImaxUsed                     144  PI-Max type controller
flag
//   SHORT    PImaxMode                     146  PI-Max mode
//   SHORT    PImaxGain                     148  PI-Max Gain
//   SHORT    BackGrndApplied               150  1 if background
subtraction done
//   SHORT    PImax2nsBrdUsed               152  T/F PI-Max 2ns Board
Used
//   WORD     minblk                        154  min. # of strips per
skips
//   WORD     numminblk                     156  # of min-blocks before
geo skps
//   SHORT    SpecMirrorLocation[2]         158  Spectro Mirror
Location, 0=Not Present
//   SHORT    SpecSlitLocation[4]           162  Spectro Slit Location,
0=Not Present
//   SHORT    CustomTimingFlag              170  T/F Custom Timing Used
//   char     ExperimentTimeLocal[TIMEMAX]  172  Experiment Local Time
as hhmmss\0
//   char     ExperimentTimeUTC[TIMEMAX]    179  Experiment UTC Time as
hhmmss\0
//   SHORT    ExposUnits                    186  User Units for Exposure
//   WORD     ADCoffset                     188  ADC offset
//   WORD     ADCrate                       190  ADC rate
//   WORD     ADCtype                       192  ADC type
//   WORD     ADCresolution                 194  ADC resolution
//   WORD     ADCbitAdjust                  196  ADC bit adjust
//   WORD     gain                          198  gain
//   char     Comments[5][COMMENTMAX]       200  File Comments
//   WORD     geometric                     600  geometric ops: rotate
0x01,
//                                               reverse 0x02, flip
0x04
```

```
//  char    xlabel[LABELMAX]            602  intensity display
string
//  WORD    cleans                      618  cleans
//  WORD    NumSkpPerCln                620  number of skips per
clean.
//  SHORT   SpecMirrorPos[2]            622  Spectrograph Mirror
Positions
//  float   SpecSlitPos[4]              626  Spectrograph Slit
Positions
//  SHORT   AutoCleansActive           642  T/F
//  SHORT   UseContCleansInst          644  T/F
//  SHORT   AbsorbStripNum             646  Absorbance Strip Number
//  SHORT   SpecSlitPosUnits           648  Spectrograph Slit
Position Units
//  float   SpecGrooves                650  Spectrograph Grating
Grooves
//  SHORT   srccmp                     654  number of source comp.
diodes
//  WORD    ydim                       656  y dimension of raw
data.
//  SHORT   scramble                   658
0=scrambled,1=unscrambled
//  SHORT   ContinuousCleansFlag       660  T/F Continuous Cleans
Timing Option
//  SHORT   ExternalTriggerFlag        662  T/F External Trigger
Timing Option
//  long    lnoscan                    664  Number of scans (Early
WinX)
//  long    lavgexp                    668  Number of Accumulations
//  float   ReadoutTime                672  Experiment readout time
//  SHORT   TriggeredModeFlag          676  T/F Triggered Timing
Option
//  char    Spare_2[10]                678
//  char    sw_version[FILEVERMAX]     688  Version of SW creating
this file
//  SHORT   type                       704   1 = new120 (Type II)
//                                            2 = old120 (Type I )
//                                            3 = ST130
//                                            4 = ST121
//                                            5 = ST138
//                                            6 = DC131 (PentaMax)
//                                            7 = ST133
//  (MicroMax/SpectroMax)
//                                            8 = ST135 (GPIB)
//                                            9 = VICCD
//                                           10 = ST116 (GPIB)
//                                           11 = OMA3 (GPIB)
//                                           12 = OMA4
//  SHORT   flatFieldApplied           706  1 if flat field was
applied.
//  char    Spare_3[16]                708
//  SHORT   kin_trig_mode              724  Kinetics Trigger Mode
/
//  char    Spare_4[436]               742
//  char    PulseFileName[HDRNAMEMAX]  1178  Name of Pulser File
with
//                                           Pulse Widths/Delays
(for Z-Slice)
//  char    AbsorbFileName[HDRNAMEMAX] 1298 Name of Absorbance File
(if File Mode)
//  DWORD   NumExpRepeats              1418  Number of Times
experiment repeated
```

```
//  DWORD   NumExpAccums              1422  Number of Time
experiment accumulated
//  SHORT   YT_Flag                   1426  Set to 1 if this file
contains YT data
//  float   clkspd_us                 1428  Vert Clock Speed in
micro-sec
//  SHORT   HWaccumFlag               1432  set to 1 if accum done
by Hardware.
//  SHORT   StoreSync                 1434  set to 1 if store sync
used
//  SHORT   BlemishApplied            1436  set to 1 if blemish
removal applied
//  SHORT   CosmicApplied             1438  set to 1 if cosmic ray
removal applied
//  SHORT   CosmicType                1440  if cosmic ray applied,
this is type
//  float   CosmicThreshold           1442  Threshold of cosmic ray
removal.
//  long    NumFrames                 1446  number of frames in
file.
//  float   MaxIntensity              1450  max intensity of data
(future)
//  float   MinIntensity              1454  min intensity of data
(future)
//  char    ylabel[LABELMAX]          1458  y axis label.
//  WORD    ShutterType               1474  shutter type.
//  float   shutterComp               1476  shutter compensation
time.
//  WORD    readoutMode               1480  readout mode,
full,kinetics, etc
//  WORD    WindowSize                1482  window size for
kinetics only.
//  WORD    clkspd                    1484  clock speed for
kinetics & frame transfer
//  WORD    interface_type            1486  computer interface
//                                          (isa-taxi, pci, eisa,
etc.)
//  SHORT   NumROIsInExperiment       1488  May be more than the 10
allowed in
//                                          this header (if 0,
assume 1)
//  char    Spare_5[16]               1490
//  WORD    controllerNum             1506  if multiple controller
system will
//                                          have controller number
data came from.
//                                          this is a future item.
//  WORD    SWmade                    1508  Which software package
created this file
//  SHORT   NumROI                    1510  number of ROIs used. if
0 assume 1.
//                                    1512 - 1630  ROI information
//  struct ROIinfo { //---- SY 03-22-2004 ???? should be WORD or
SHORT ????
//    unsigned int startx             left x start value.
//    unsigned int endx               right x value.
//    unsigned int groupx             amount x is binned/grouped in
hw.
//    unsigned int starty             top y start value.
//    unsigned int endy               bottom y value.
//    unsigned int groupy             amount y is binned/grouped in
hw.
//  } ROIinfoblk[ROIMAX]                 ROI Starting Offsets:
```

145

```
//                                              ROI  1 = 1512
//                                              ROI  2 = 1524
//                                              ROI  3 = 1536
//                                              ROI  4 = 1548
//                                              ROI  5 = 1560
//                                              ROI  6 = 1572
//                                              ROI  7 = 1584
//                                              ROI  8 = 1596
//                                              ROI  9 = 1608
//                                              ROI 10 = 1620
//  char     FlatField[HDRNAMEMAX]    1632  Flat field file name.
//  char     background[HDRNAMEMAX]   1752  background sub. file
name.
//  char     blemish[HDRNAMEMAX]      1872  blemish file name.
//  float    file_header_ver          1992  version of this file
header
//  char     YT_Info[1000]            1996-2996  Reserved for YT
information
//  LONG     WinView_id               2996  == 0x01234567L if file
created by WinX
//
//------------------------------------------------------------------
------------
//
//                    START OF X CALIBRATION STRUCTURE
//
//  double       offset              3000  offset for absolute
data scaling
//  double       factor              3008  factor for absolute
data scaling
//  char         current_unit        3016  selected scaling unit
//  char         reserved1           3017  reserved
//  char         string[40]          3018  special string for
scaling
//  char         reserved2[40]       3058  reserved
//  char         calib_valid         3098  flag if calibration is
valid
//  char         input_unit          3099  current input units for
//                                          "calib_value"
//  char         polynom_unit        3100  linear UNIT and used
//                                          in the "polynom_coeff"
//  char         polynom_order       3101  ORDER of calibration
POLYNOM
//  char         calib_count         3102  valid calibration data
pairs
//  double       pixel_position[10]  3103  pixel pos. of
calibration data
//  double       calib_value[10]     3183  calibration VALUE at
above pos
//  double       polynom_coeff[6]    3263  polynom COEFFICIENTS
//  double       laser_position      3311  laser wavenumber for
relativ WN
//  char         reserved3           3319  reserved
//  unsigned char new_calib_flag     3320  If set to 200, valid
label below
//  char         calib_label[81]     3321  Calibration label (NULL
term'd)
//  char         expansion[87]       3402  Calibration Expansion
area
//
//------------------------------------------------------------------
------------
//
```

146

```
//                         START OF Y CALIBRATION STRUCTURE
//
//  double        offset              3489  offset for absolute
data scaling
//  double        factor              3497  factor for absolute
data scaling
//  char          current_unit        3505  selected scaling unit
//  char          reserved1           3506  reserved
//  char          string[40]          3507  special string for
scaling
//  char          reserved2[40]       3547  reserved
//  char          calib_valid         3587  flag if calibration is
valid
//  char          input_unit          3588  current input units for
//                                          "calib_value"
//  char          polynom_unit        3589  linear UNIT and used
//                                          in the "polynom_coeff"
//  char          polynom_order       3590  ORDER of calibration
POLYNOM
//  char          calib_count         3591  valid calibration data
pairs
//  double        pixel_position[10]  3592  pixel pos. of
calibration data
//  double        calib_value[10]     3672  calibration VALUE at
above pos
//  double        polynom_coeff[6]    3752  polynom COEFFICIENTS
//  double        laser_position      3800  laser wavenumber for
relativ WN
//  char          reserved3           3808  reserved
//  unsigned char new_calib_flag      3809  If set to 200, valid
label below
//  char          calib_label[81]     3810  Calibration label (NULL
term'd)
//  char          expansion[87]       3891  Calibration Expansion
area
//
//                         END OF CALIBRATION STRUCTURES
//
//    ------------------------------------------------------------
------
//
//  char    Istring[40]               3978  special intensity
scaling string
//  char    Spare_6[76]               4018
//  SHORT   AvGainUsed                4094  avalanche gain was used
//  SHORT   AvGain                    4096  avalanche gain value
//  SHORT   lastvalue                 4098  Always the LAST value
in the header
//
********************************************************************
*********/
//                         /* 4100 Start of Data */
```

147

A2 Automated FRET calculation

```
function CalculateRatioA(inwave, nframes)
 //Use this function straight after loading the cross-section
spefile. it first redimensions the loaded file to have single spectra
as collumns in a 2D wave.
 //Then it finds the min value for EACH collumn and stores it in
another 2D wave. The matrixOp operation then subtracts the minValue
wave from the original
 //wave, giving the baselined wave. Finally, the wave is
redimensioned back to 3D form and is ready for averaging (Average3D
function)

wave inwave
variable nframes
variable cols
variable layers
variable rows
variable eps
variable ii
variable j

rows = dimsize(inwave, 0)
cols = dimsize(inwave, 1)
layers=dimsize(inwave, 2)
eps = layers/nframes
print "before redimension",
dimsize(inwave,0),dimsize(inwave,1),dimsize(inwave,2)

redimension/N= (rows*layers) inwave
redimension/N= (rows, layers) inwave

print "after redimension",
dimsize(inwave,0),dimsize(inwave,1),dimsize(inwave,2)
make/n=(rows,layers)/o wAvg

//baseline
            for(ii = 0 ; ii < layers ; ii += 1)

                        imagestats/G={1, 7 , ii, ii}  inwave
                        if(!V_flag)
                              wAvg[][ii] = V_avg
                        endif

            endfor


matrixop/O inwave=inwave-wAvg  //subtract baseline

redimension/N = (rows*layers)inwave
redimension/N = (rows, nframes, eps)inwave
print "final redimension",
dimsize(inwave,0),dimsize(inwave,1),dimsize(inwave,2)

DeletePoints/M=2 0,1, inwave   //delete first layer (first recorded
episode)

//Takes a 3Dinwave and seperates the even and odd layers
(corresponding to CFP and YFP exitation). Then averages each cell
over the existing number of layers.

variable Nrows = dimsize(inwave,0)
```

```
variable ncols = dimsize(inwave,1)
variable Nlayers= dimsize(inwave,2)/2
string wname
string GFP_ex
string RFP_ex

//create 2 new waves to store donor and acceptor excitation spectra
Make/O/N= (Nrows, ncols,nlayers )oddlayers
Make/O/N= (Nrows, ncols, nlayers)evenlayers

//seperate the layers
OddLayers[][][] = InWave[p][q][2 * r + 1]
EvenLayers[][][] = InWave[p][q][2 * r]

print "seperation odd",
dimsize(oddlayers,0),dimsize(oddlayers,1),dimsize(oddlayers,2)
print "seperation even",
dimsize(evenlayers,0),dimsize(evenlayers,1),dimsize(evenlayers,2)

//average of episodes
MatrixOP/O AvgOddCols=sumbeams(oddLayers)/Nlayers
MatrixOP/O AvgEvenCols=sumbeams(evenLayers)/Nlayers

display AvgOddCols[][0]
//rename the new seperated waves according to their excitation
wavelength
wname = nameofwave(inwave)
GFP_ex = wname +"_488"
RFP_ex= wname +"_561"

string excitation
variable wavelength = 2
prompt wavelength, "wavelength", popup, "gfp;rfp"
doprompt "wavelength of AvgOddCols", wavelength
if(V_flag)
        return 0                            //cancelled
endif

if (wavelength == 1)
        rename avgoddcols, $GFP_ex
        rename avgevencols, $RFP_ex
elseif(wavelength == 2)
        rename avgoddcols, $RFP_ex
        rename avgevencols, $GFP_ex
endif

//delete the first frame in each wave
DeletePoints/M=1 0,4, AvgOddCols
DeletePoints/M=1 0,4, AvgEvenCols

wave GFP_FRET = $GFP_ex
wave RFP_direct = $RFP_ex

DFREF dfr = root:

//Scaling of GFP (the 'pure' GFP wave (spectra) has to be loaded
beforehand)

wave gfp = dfr:gfp
wavestats/Q/R=(145,155) gfp
variable avg_GFP_alone = V_avg
print v_avg
```

```
variable i
variable avg_FRET
variable numCols =dimsize(GFP_FRET, 1)
variable numRows = dimsize(gfp,0)
variable scalingfactor
print numcols
print numrows

//create wave to store the scaling factors for the "pure" gfp spectra
make/O/n=(1,numcols) scalingFactors
            for(i=0; i<numCols; i+=1)
                    imagestats/G={110,120,i,i} GFP_FRET
                    if(!V_flag)
                            avg_FRET = V_avg/avg_GFP_alone
                            scalingFactors[i] = avg_FRET
                    endif
            endfor
edit scalingFactors

//make a scaling matrix(multiply the "pure" gfp spectra by the
scaling factors)

make/o/n=(numrows,numcols) scalingmatrix
make/o/n=(numrows,1) GFP_scaled
variable jj
for(jj=0;jj<numcols;jj+=1)
        gfp_scaled = scalingfactors[jj]*gfp
        scalingmatrix[][jj] = gfp_scaled[p]
endfor


edit rfp_direct
deletepoints/M=0 0,33, scalingmatrix
insertpoints/M=0 479,33, scalingmatrix

//subtract the scaled "pure"GFP from the the GFP-RFP mixture
Matrixop/o SubGFP=GFP_FRET-scalingmatrix

//RatioA
Matrixop/o RatioAw=SubGFP/RFP_direct
newwaterfall ratioAw

// average RatioA
variable z
make/o/n=(1,numcols) ratioAavg
        for(z=0;z<numcols;z+=1)
                imagestats/G={400,420,z,z} RatioAw
                        if(!V_flag)
                        ratioAavg[][z]=V_avg
                        endif
        endfor

matrixop/O ratioA=row(RatioAavg,0)
redimension /N=(numcols) RatioA
edit RatioA
display ratioA
string ratA = nameofwave(inwave) + "RatioA"
rename ratioA, $ratA

//The value for RatioA0 has to be loaded beforehand
wave RatioA0 = dfr:RatioA0
variable y
make/o/n=(1,numcols) FRETratio
```

```
for(y=0;y<ncols;y+=1)
        fretratio[][y] = RatioAavg[y]/RatioA0
endfor

//calculate FRET efficiency
matrixop/o FRETef = (56/81)*((Fretratio-1)*100)
matrixop/O FRETefficiency=row(FRETef,0)

//redimension the FRET Efficincy wave to be vertical
redimension /N=(numcols) FRETefficiency

string FRET = wname+ "_FRET_efficiency"
rename FRETEfficiency, $FRET

display FRETefficiency
edit FRETefficiency

end
```

```
Function CalculateRatioA0(inwave,nframes)
wave inwave
variable nframes
variable cols
variable layers
variable rows
variable eps
variable ii
variable j

rows = dimsize(inwave, 0)
cols = dimsize(inwave, 1)
layers=dimsize(inwave, 2)
eps = layers/nframes
print "before redimension",
dimsize(inwave,0),dimsize(inwave,1),dimsize(inwave,2)

redimension/N= (rows*layers) inwave
redimension/N= (rows, layers) inwave

print "after redimension",
dimsize(inwave,0),dimsize(inwave,1),dimsize(inwave,2)

make/n=(rows,layers)/o wAvg
                for(ii = 0 ; ii < layers ; ii += 1)

                        imagestats/G={1, 7 , ii, ii}  inwave
                        if(!V_flag)
                                wAvg[][ii] = V_avg
                        endif

        endfor


matrixop/O inwave=inwave-wAvg

redimension/N = (rows*layers)inwave
redimension/N = (rows, nframes, eps)inwave
print "final redimension",
dimsize(inwave,0),dimsize(inwave,1),dimsize(inwave,2)

DeletePoints/M=2 0,1, inwave

//Takes a 3Dinwave and seperates the even and odd layers
(corresponding to CFP and YFP exitation). Then averages each cell
over the existing number of layers.

variable Nrows = dimsize(inwave,0)
variable ncols = dimsize(inwave,1)
variable Nlayers= dimsize(inwave,2)/2
string wname
string GFP_ex
string RFP_ex


Make/O/N= (Nrows, ncols,nlayers )oddlayers
Make/O/N= (Nrows, ncols, nlayers)evenlayers

OddLayers[][][] = InWave[p][q][2 * r + 1]
EvenLayers[][][] = InWave[p][q][2 * r]

DeletePoints/M=2 0,5, oddlayers
DeletePoints/M=2 0,5, evenlayers
```

152

```
print "seperation odd",
dimsize(oddlayers,0),dimsize(oddlayers,1),dimsize(oddlayers,2)
print "seperation even",
dimsize(evenlayers,0),dimsize(evenlayers,1),dimsize(evenlayers,2)

MatrixOP/O AvgOddCols=sumbeams(oddLayers)/Nlayers
MatrixOP/O AvgEvenCols=sumbeams(evenLayers)/Nlayers

display AvgOddCols[][0]

wname = nameofwave(inwave)
GFP_ex = wname +"_488"
RFP_ex= wname +"_561"

string excitation
variable wavelength = 2
prompt wavelength, "wavelength", popup, "gfp;rfp"
doprompt "wavelength of AvgOddCols", wavelength
if(V_flag)
        return 0                                //cancelled
endif

if (wavelength == 1)
        rename avgoddcols, $GFP_ex
        rename avgevencols, $RFP_ex
elseif(wavelength == 2)
        rename avgoddcols, $RFP_ex
        rename avgevencols, $GFP_ex
endif

DeletePoints/M=1 0,1, AvgOddCols
DeletePoints/M=1 0,1, AvgEvenCols

wave rfp_488 = $GFP_ex
wave rfp_561 = $RFP_ex
 edit rfp_488
 edit rfp_561

duplicate/o rfp_488, RatioA0
RatioA0 = rfp_488/rfp_561

newwaterfall ratioA0
SetAxis bottom 375,410
setaxis left 0,1

edit ratioA0


end
```

A3 Automated distance calculation from FRET efficiencies

```
#pragma rtGlobals=3              // Use modern global access method and
strict wave access.
function FRETefficiency()
variable R0=52
make/o/N=1000 fx
setscale/I x 0, 110, "", fx
fx = 1/(1+(x/R0)^6)
display fx
end


function calc_E(inwave)
wave inwave
variable rows = dimsize(inwave, 0)
make/o/N=(rows) E_wave
E_wave = inwave
edit E_wave

make/o/N=(rows) r_wave
variable R0 = 52
r_wave = R0*((1-E_wave)/E_wave)^(1/6)
edit r_wave
end
```

A4 Automated analysis of DPA quenching data

```
function Spectra_YFP_DPA(inwave, nframes)
 //Use this function straight after loading the cross-section
spefile. it first redimensions the loaded file to have single spectra
as collumns in a 2D wave.
 //Then it finds the min value for EACH collumn and stores it in
another 2D wave. The matrixOp operation then subtracts the minValue
wave from the original
 //wave, giving the baselined wave. Finally, the wave is
redimensioned back to 3D form and is ready for averaging (Average3D
function)

wave inwave
variable nframes
variable cols
variable layers
variable rows
variable eps
variable ii
variable j

rows = dimsize(inwave, 0)
cols = dimsize(inwave, 1)
layers=dimsize(inwave, 2)
eps = layers/nframes
print "before redimension",
dimsize(inwave,0),dimsize(inwave,1),dimsize(inwave,2)

redimension/N= (rows*layers) inwave
redimension/N= (rows, layers) inwave

print "after redimension",
dimsize(inwave,0),dimsize(inwave,1),dimsize(inwave,2)


        make/n=(rows,layers)/o wAvg


            for(ii = 0 ; ii < layers ; ii += 1)

                        imagestats/G={19, 34 , ii, ii}  inwave
                        if(!V_flag)
                                wAvg[][ii] = V_avg
                        endif

            endfor


matrixop/O inwave=inwave-wAvg

end
```

A5 Automated calculation of donor quenching probability by DPA
(This procedure was written by Andrew Plested)

```
#pragma rtGlobals=3              // Use modern global access method and
strict wave access
#include <WMBatchCurveFitIM>
#include <KBColorizeTraces>

Function PQuench (u)
        //Function to be integrated Wang et al 2010 BJ appendix
        Variable u
        Variable result
        result = 1 / ( 1 + u^3)
        return result
End

Function Pinf (Rz, Rp, dens)
        // integral corresponding to no-quenching by an infinite
(10000Å) radius disk of DPA

        Variable Rz, Rp, dens   // dens is sigma, the area number
density of DPA molecules
        Variable lower = Rp^2 / Rz^2
        //printf "lower limit: %g\r", lower
        Variable integral = integrate1d (PQuench, lower, 10000)
        Variable prefactor = dens*pi*Rz^2
        //printf "density: %g\r", dens
        //printf "prefac: %g\r", prefactor
        //printf "integral: %g\r", integral
        return exp (-prefactor*integral)
End

Function P_MemQuench(innerfract, Ra, Rz, sigma)
        // probability of quenching by DPA in the membrane –
complement of product of no-quenching by 2 planes

        Variable innerfract, Ra, Rz, sigma     // sigma is density, Ra
is the probe distance from the inner plane
        Variable inner = Pinf(Rz, Ra, sigma * innerfract)
        Variable outer = Pinf(Rz, Ra+25, sigma * (1-innerfract)) //
outer plane is 25Å distant from FP.

        return 1-inner * outer
End

Function DPA_fract(V_mV, V0)

        Variable V_mV, V0
        // kt / e at 25ºC is 25.6 mV
        // working in mV
        //0.6 is the fraction of the e-field that DPA moves across,
in the giant axon Fernandez, Taylor and Bezanilla JGP 1983
        //in HEK it is 0.5
        Variable denom = 1 + exp (-0.5*(V_mV-V0)/25.6)
        return 1/denom
end

Function DPAexpt (V_mV, MaxDist,  DistInc, Rz, sigma, Prefix)
        //calculate F(V,Ra) and Pquench(V, Ra) for a given
fluorophore
        //sigma in katchan experiments is 12.5e-4
```

```
        Wave V_mV                // a wave of voltages in mV
        Variable MaxDist, DistInc, Rz, sigma  // Rz is the Rzero for
the fluorophore-DPA pair
        String Prefix            // to modify the output
        Variable Dist = 15
        Variable V0_DPA = 15
        //minimum distance for GFP is 15Å
        do
                if (Dist > MaxDist)
                        break
                endif
                printf "----------DISTANCE------: %g\r", Dist
                String outname = Prefix+"_P_" + num2str(Dist)
                //create the output for the DF/F waves
                String fluoname = Prefix+"_DF_" + num2str(Dist)

                Make/O/N=(numpnts(V_mV)) $outname
                Variable index = 0
                do
                        if (index == numpnts(v_mV))
                                break
                        endif
                        wave wOut = $outname
                        variable DPA_infract = DPA_fract(V_mV[index],
V0_DPA)
                        wOut[index] = P_MemQuench(DPA_infract, Dist,
Rz, sigma)

                        index += 1
                while (1)

                wOut = 1-wOut
                Duplicate/O wOut, $fluoname
                WAVE Fdest = $fluoname           // the final
destination for the normalised F values
                Fdest =  Fdest /  wOut[0]        //              division
is normalization to first value in series

                Dist += DistInc
        while (1)
end

Function DPAdistance (distance_points, V_mV, Rz, sigma, extra,
Prefix)
        //calculate Pquench(Ra) for a given fluorophore and voltage
        //extra is a flag to flip voltage and V0_DPA for
extracellular probes
        // because "inner" is taken as equivalent to near but this is
only true for intracellular probes!!
        //sigma in katchan experiments is 12.5e-4
        // distance points is a wave of Ra values in Angstroms

        Wave distance_points
        Variable V_mV            // pick the voltage (mV) - often -60mV
        Variable extra           // 0 = intracellular, 1 =
extracellular
        Variable  Rz, sigma      // Rz is the Rzero for the
fluorophore-DPA pair
        String Prefix            // to modify the output - default is
to overwrite...
        Variable Dist = 15
        Variable V0_DPA = 15
        Variable index = 0
        //minimum distance for GFP is 15Å
```

```
        if (extra == 1)
                V_mV = -V_mV
                V0_DPA = -V0_DPA
        endif

        String outname = Prefix+"_P_"
        Make/O/N=(numpnts(distance_points)) $outname
        wave wOut = $outname
                //create the output for the DF/F waves
        do
                if (index > numpnts(distance_points) - 1)
                        break
                endif
                printf "----------DISTANCE------: %g\r",
distance_points[index]

                variable DPA_infract = DPA_fract(V_mV, V0_DPA)
                printf "----------DPA near fraction------: %g\r",
DPA_infract

                wOut[index] = P_MemQuench(DPA_infract,
distance_points[index],  Rz, sigma)
                index += 1
        while (1)

        wOut = 1-wOut
end


Function DPA_Dist(w_mV, V0)
        //calculate DPA Distribution in the membrane at room
temperature
        Wave w_mV
        Variable V0    //The half maximal voltage for DPA
translocation
        //V0 for DPA is -15mV Fernandez, Taylor and Bezanilla JGP
1983
        //In HEK seems more like +15 mV
        // our data needs +70!!! NOPE we corrected it - due to an
adsorption of DPA, this value was overestimated

        String DPAname = "DPA_" + nameofwave(w_mV)
        Make/o/n=(numpnts(w_mV)) $DPAname
        Wave DPA_local = $DPAname
        Variable index = 0
        do
                if (index == numpnts(w_mV))
                        break
                endif

                DPA_local[index] = DPA_fract(w_mV[index], V0)
                index +=1
        while(1)
end
```

Acknowledgement